UNIVERSITY OF SOUTHAMPTON
Faculty of Engineering and the Environment

Investigations of Lymphatic Fluid Flow

by

Laura Jane Cooper

A thesis submitted in partial fulfilment for the
degree of Doctor of Philosophy

March 2016

UNIVERSITY OF SOUTHAMPTON

ABSTRACT

FACULTY OF ENGINEERING AND THE ENVIRONMENT
Engineering Sciences

Doctor of Philosophy

by Laura Jane Cooper

The lymphatic system returns fluid to the blood stream from the tissues to maintain tissue fluid homeostasis. The collecting lymphatic vessels actively pump fluid against a body scale pressure gradient, i.e., from tissue interstitial space to the venous side of the blood circulatory system. The collecting lymphatic vessels pass the lymphatic fluid to lymph nodes that filter the lymph before it is returned to the circulatory system.

This thesis presents work undertaken to create a fluid structure interaction model of a lymph node with afferent and efferent lymphatic vessels. The model is built in COMSOL Multiphysics, a commercial finite element software.

Four pieces of novel work are presented in this thesis. Firstly, an optimisation method used to approximate the material properties for the collecting lymphatic vessel from the pressure diameter behaviour. Secondly, model of the collecting lymphatic valve with surrounding wall used to investigate valve closing behaviour. Thirdly, an image based model of a lymph node where the material properties are optimised to experimental data and based on selective plane illumination microscopy images. Finally, an image based model of a lymph node based on computed tomography images that shows how the structure within the node affects the fluid flow pathways.

Contents

List of Figures

List of Tables

Academic Thesis: Declaration of Authorship

I, Laura Jane Cooper, declare that this thesis, 'Investigations of Lymphatic Fluid Flow', and the work presented in it are my own and has been generated by me as the result of my own original research. I confirm that:

1. This work was done wholly or mainly while in candidature for a research degree at this University;
2. Where any part of this thesis has previously been submitted for a degree or any other qualification at this University or any other institution, this has been clearly stated;
3. Where I have consulted the published work of others, this is always clearly attributed;
4. Where I have quoted from the work of others, the source is always given. With the exception of such quotations, this thesis is entirely my own work;
5. I have acknowledged all main sources of help;
6. Where the thesis is based on work done by myself jointly with others, I have made clear exactly what was done by others and what I have contributed myself;
7. Either none of this work has been published before submission, or parts of this work have been published as:
    - Modelling the Mechanical Behaviour of Collecting Lymphatic Vessels, L. J. Cooper, J. P. Scallan, J. P. Heppell, G. F. Clough, B. Ganapathisubramani and T. Roose, Virtual Physiological Human Conference Proceedings 2014, Paper #34.
    - Imaged Based Modelling of Fluid Flow through Lymph Nodes, L. J. Cooper, G. F. Clough, B. Ganapathisubramani and T. Roose, 4th International Conference on Computational and Mathematical Biomedical Engineering Proceedings 2015, 452-455.
    - An Image Based Model of Fluid Flow Through Lymph Nodes, L. J. Cooper, J. P. Heppell, G. F. Clough, B. Ganapathisubramani and T. Roose, Bulletin of Mathematical Biology. Bulletin of Mathematical Biology, 2016, 78(1):52-71, doi: 10.1007/s11538-015-0128-y (Epub 21 Dec 2015).

Signed:

Date:

Acknowledgements

I would like to thank my supervisors Professor Tiina Roose, Professor Bharathram Ganapathisubramani and Professor Geraldine Clough for their advice, support and patience during the creation of this thesis. To the members of the Bioengineering Sciences Research Group, Aerodynamics and Flight Mechanics Group and Engineering Sciences, I would like to say thank you for the distraction of tea, cake and conversation. Thank you to the staff at the μ-VIS centre for Computed Tomography for sharing their knowledge of high resolution imaging and high performance computing. I would also like to acknowledge the use of the IRIDIS High Performance Computing Facility in the completion of this work.

Thank you also to those outside of Southampton University who have shared their knowledge, data and videos with me, Doctor Joshua Scallan, Professor Taija Makinen, Jürgen Mayer, Professor Micheal Davis and Doctor Kenton Arkill.

Finally, thank you to my friends and family for all their encouragement, support and willingness to read and listen.

Funding for this research was awarded by the Institute for Life Science at the University of Southampton and supplemented with a studentship awarded by the Faculty of Engineering and the Environment.

Chapter 1

Introduction

The immune system protects the body from disease by killing pathogens, for example viruses, bacteria, parasites or fungi, that breach the body's physical defence barriers, such as the skin and mucous membranes. Lymph nodes are lymphoid organs where immune cells can gather to communicate information about and activate the necessary response to a particular threat [Sompayrac, 2012].

The lymph nodes are components of the lymphatic system, a unidirectional drainage network, with the primary function of maintaining fluid homoeostasis in the tissues. The immune cells are transported between lymph nodes along with lymph, i.e. the fluid in the lymphatic system, through collecting lymphatic vessels. Lymphocytes, a type of immune cell, enter the lymph node, remain there for a period of time, and then leave to continue circulating around the body. The movement of lymphocytes is an important aspect in immune response. However the impact of the lymph flow on the transport of these immune cells is not well understood [Nagai et al., 2008]. A contributing factor to this lack of knowledge is the difficulty of conducting experiments on the lymphatic system due to the size and fragility of the vessels and nodes that it is made up of.

In the next section 1.1, an overview of the lymphatic system will be given. This provides background information that will be used to motivate and define the aim of the work presented in this thesis.

1.1 The Lymphatic System

The lymphatics drain fluid away from the interstitium, filter it through lymph nodes and transport it back into the circulatory system via a junction with one of the veins in the neck. The fluid pressure in the interstitial space is often lower than the pressure in the veins of the neck [Aukland and Reed, 1993]. In order to absorb

and transport fluid away from the tissues, the lymphatic system must work against pressure gradients produced by the interstitial fluid, gravity and the venous system [Nipper and Dixon, 2011].

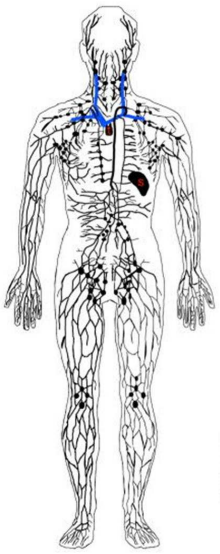

Figure 1.1: The lymphatic system of the human body. Blue lines indicate the major veins where lymph is returned to the blood stream. From Butler et al. [2009] ©2009 Wiley-Liss, Inc. Permission to reproduce this figure has been granted by John Wiley and Sons.

1.1.1 Interstitial Space

The tissues of the body are made up of cells held within an extracellular matrix (ECM). The interstitial space is the area around the blood and lymphatic vessels, which is filled with a gel like substance called interstitium. This gel contains interstitial fluid, which has left the capillaries by extravasation to deliver nutrients to the cells [Swartz and Fleury, 2007]. The interstitial fluid has a similar composition to plasma, but with a different protein concentration [Abramson and Dobrin, 1984]. As the protein concentration of plasma in the blood is higher than in the interstitial fluid, it is impossible for the proteins in the interstitial fluid to return to the blood by ultrafiltration. Therefore, the role of the lymphatic system is to remove this fluid and protein solution from the interstitium [Földi et al., 2003; Aukland and Reed, 1993].

1.1.2 Lymph

The formation of lymph - the fluid in the lymphatic vessels - occurs when the interstitial fluid, plasma proteins and cells from the interstitium enter the initial lymphatics vessels [Abramson and Dobrin, 1984]. Lymph is generally a clear fluid, except for chyle which is milky white because the lymph is mixed with lipids absorbed

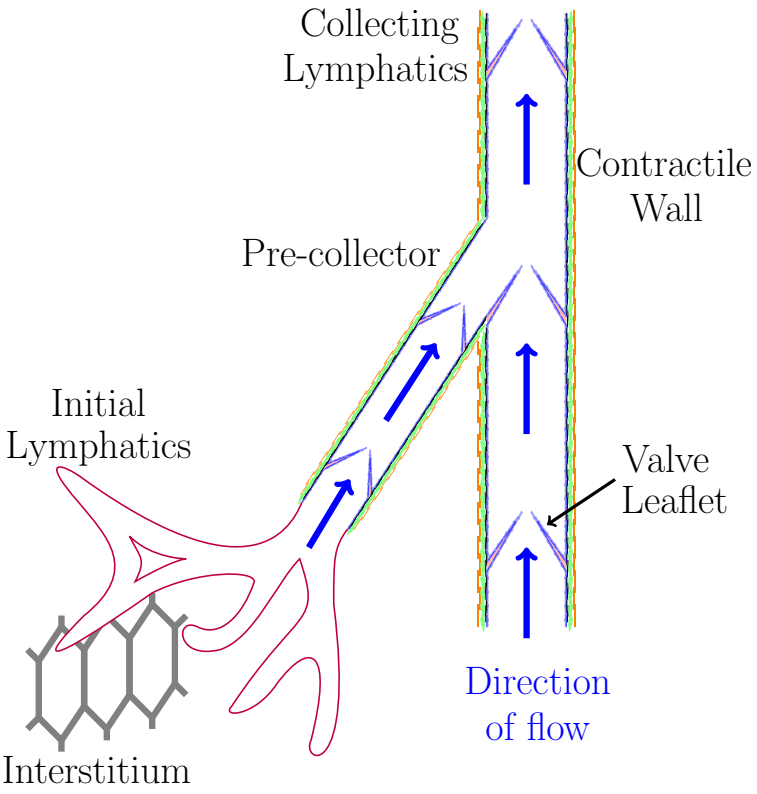

Figure 1.2: Schematic of a section of the lymphatic system (not to scale). Fluid is absorbed from the interstitium by the initial lymphatics. Once within the lymphatic vessels this fluid is called lymph. The lymph is transported from the initial lymphatics to increasingly larger vessels, which have contractile walls to propel the lymph forward and valves to reduce the amount of backward flow. These collecting lymphatic vessels transport the lymph through the body and return it to the blood stream.

in the small intestine [Földi et al., 2003]. The density of lymph is about 1000 kgm^{-3} [Mazzoni et al., 1987] and the dynamic viscosity is between 1.5×10^{-3} and 2.2×10^{-3} cP [Dixon et al., 2006; Burton-Opitz and Nemser, 1917].

1.1.3 Initial Lymphatics

The initial lymphatics are microscopic blind ended vessels, approximately 10-60 μm in diameter [Swartz and Skobe, 2001]. The walls are a single layer of endothelial cells with an incomplete basement membrane, a flexible sheet that separates the endothelial cells from the surrounding tissue. The cells are tethered to the ECM at local attachment points connecting the basement membrane to fibres in the tissue [Schmid-Schönbein, 1990; Swartz and Skobe, 2001]. As the volume of fluid in the interstitium increases the ECM swells. The fibres then pull the cells apart increasing the volume of the vessel and opening the gaps between the endothelial cells, see Figure 1.3. This creates a pressure gradient that causes interstitial fluid, particles and proteins to flow into the vessel [Ikomi et al., 2012]. As the pressure gradient decreases

the gaps between the cells close, stopping fluid returning to the surrounding tissue [Swartz and Skobe, 2001].

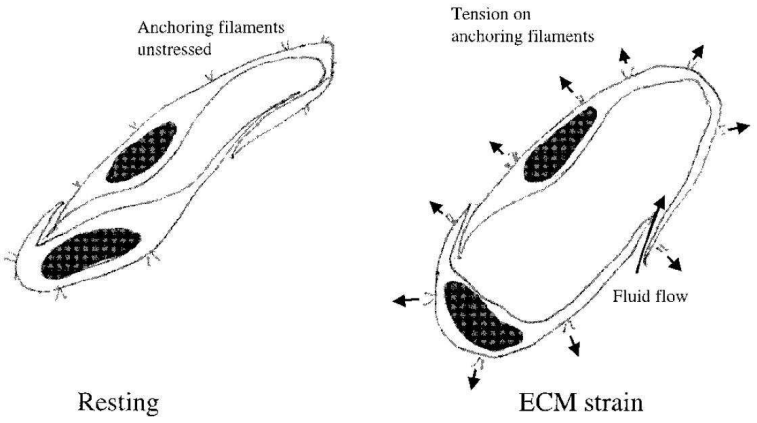

Figure 1.3: Diagram illustrating the mechanism that allows lymph to be absorbed into the primary lymphatics from Swartz and Skobe [2001]. Fluid collects in the interstitial space causing the extracellular matrix (ECM) to expand. This tensions the fibres connecting the surrounding tissue to the basement membrane of the endothelial cells that form the wall of the vessel. This separates the cells, creates a pressure difference with lower pressure inside the initial vessels than in the tissues, and so the fluid flows into the lumen of the initial lymphatic. ©2001 Wiley-Liss, Inc. Permission to reproduce this figure has been granted by John Wiley and Sons.

1.1.4 Collecting Lymphatics

As lymph flows downstream, the initial lymphatic vessels drain into the collecting lymphatics. They are formed of a chain of lymphangions, sections of lymphatic vessel with a valve at either end [Schmid-Schönbein, 1990; Stücker et al., 2008]. Once in the collecting lymphatics, lymph is transported through the vessels by both active and passive mechanisms. Lymph is actively pumped as smooth muscle cells in the walls cause the lymphangions to contract. The valves between the segments minimise the amount of back flow [Schmid-Schönbein, 1990]. Lymph is moved passively due to lymph formation, gravity, pumping of nearby blood vessels and movements from surrounding muscles and tissues [Davis et al., 2011; Nipper and Dixon, 2011].

The collecting lymphatics deliver the lymphatic fluid to lymph nodes through afferent vessels and drain the lymph away from the node through efferent lymph vessels [Földi et al., 2003]. The majority of the fluid then returns to the circulatory system either via the right lymphatic duct or the thoracic duct, which empty into veins in the neck [Földi et al., 2003].

The collecting lymphatic wall consists of several components, which are summarised in figure 1.4.

- Endothelial cells: flat cells found lining the inner surface of lymphatic vessels, blood vessels and heart chambers.
- Basement membrane: a fibrous flexible sheet that separates the endothelial cells from the surrounding wall components.
- Elastin: an extensible protein that can return to its original shape after being stretched.
- Smooth muscle cells: these cells contract and relax in response to stimuli causing the collecting lymphatic walls to contract and propel fluid through the vessels.
- Collagen: an inextensible protein that can resist large strains. Bundles of collagen fibres and collagen networks are deformable.

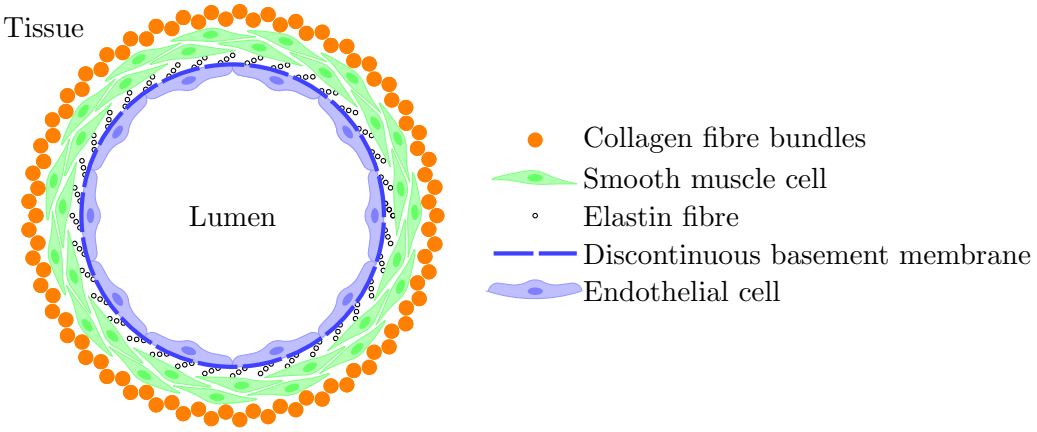

Figure 1.4: Sketch of typical collecting lymphatic wall structure, not to scale.

The lumen, the hollow centre of the vessel that is filled with fluid, of the collecting lymphatic vessel is lined with one layer of endothelial cells, which have a discontinuous basement membrane. This is connected to a layer of smooth muscle cell and elastin and finally a layer of collagen fibre bundles [Gnepp and Green, 1980; Arkill et al., 2010; Margaris and Black, 2012; Rahbar et al., 2012].

1.1.5 Lymph Nodes

A human has about 600 to 700 lymph nodes [Földi et al., 2003]. They filter the lymph, removing harmful material so that it is not returned to the blood stream, and provide a site for interaction between different immune cells. Lymphocytes enter the lymph node through the afferent lymphatic vessels or through the blood vessel walls. The lymph nodes also regulate the protein concentration of the lymph [Földi et al., 2003].

Nodes have a high resistance to the lymphatic flow, which is dependent on the pressure in the afferent and efferent lymphatic vessels; the size of the node; the flow

rate and blood pressure [Schmid-Schönbein, 1990]. The flow in the lymph nodes affects the behaviour of the cells within the nodes and the morphology of the reticular cell network, which forms the underlying structure of the lymph node [Tomei et al., 2009].

1.1.6 Lymphatic System Dysfunction

If the downstream collecting lymphatics are blocked, this can affect the initial vessels. As the collecting lymphatics downstream are unable to remove the fluid, it collects in the initial lymphatics increasing the pressure in the vessels. The vessels distend and the endothelial cells are pulled apart so they no longer overlap, which prevents the fluid being drained away from the tissue, so it accumulates causing oedema [Schmid-Schönbein, 1990; Davis et al., 2011]. The causes of lymphoedema can be blockages of the collecting vessels, such as after the removal of downstream vessels during surgery, the result of a parasitic infection, e.g. lymphatic filariasis, or malfunctioning collecting valves due to a genetic condition. An example of this is lymphedema-distichiasis syndrome, which causes the valves to develop incorrectly, as seen in figure 1.5 [Bazigou et al., 2009].

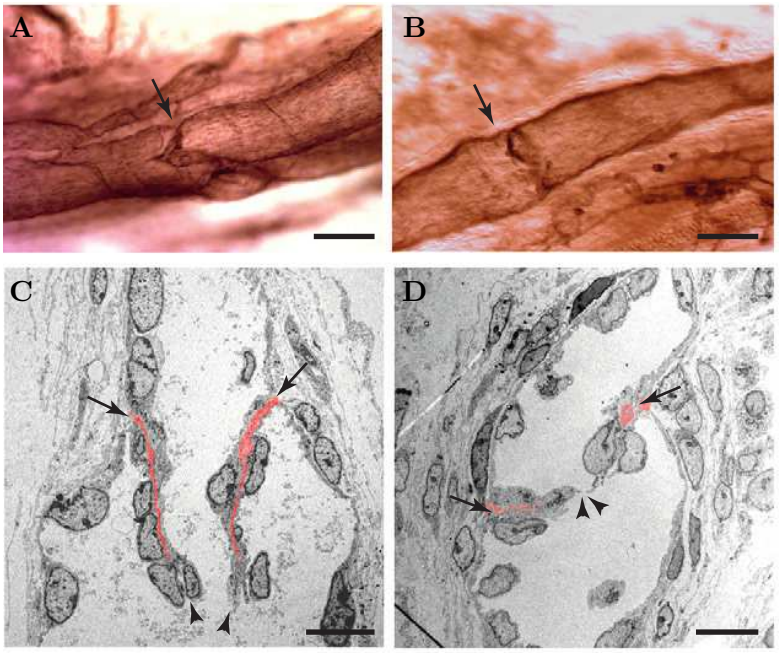

Figure 1.5: Images comparing healthy and deformed collecting valves from genetically different mice [Bazigou et al., 2009]. The valves in A and C have formed normally and in B and D are deformed. The misshapen valves are from mouse embryos deficient in a gene that encodes a protein found in the endothelial cells of the valve leaflets. The deformed valves are shorter than the healthy valves and cannot effectively prevent reverse flow. In A and B, scale bar = 50 μm; in C and D, scale bar = 10 μm. Reprinted from Bazigou et al. [2009] ©2009, with permission from Elsevier.

Mihara et al. [2012] have studied the macroscopic anatomy of collecting lymphatic vessels from patients at different stages of limb lymphoedema. They separated the vessels into four types:

- Normal: several layers of contractile smooth muscle cells, endothelial cells that extended into the lumen of the vessel and some collagen fibres.
- Ectasis: dilated lumen, thin layers of contractile smooth muscle cells and a smooth layer of endothelial cells.
- Contraction: thick layer of synthetic smooth muscle cells (do not contract but instead produce more smooth muscle cells and collagen fibres), narrowing of lumen, increased thickness of collagen fibre layer.
- Sclerosis: Lumen narrowed so almost blocked or completely blocked, collagen fibres so numerous that they push past the endothelial cells and extend into the lumen, very thick wall.

The types of vessel are summarised in figure 1.6.

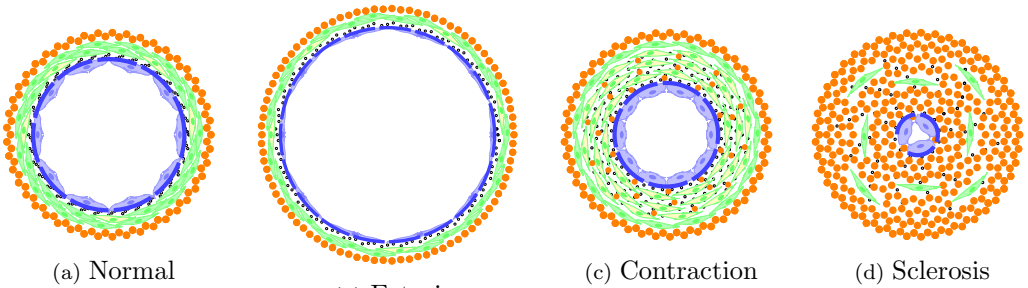

(a) Normal (b) Ectasis (c) Contraction (d) Sclerosis

Figure 1.6: Sketches of types of lymphatic vessels found in lymphoedema patients. Based on descriptions and images in Mihara et al. [2012].

Mihara et al. [2012] found that in early stages of lymphoedema, when it is still reversible, the majority of the patients vessels were of the type normal or ectasis with a small amount of contraction vessels. However, at late stages, when the disease cannot be reversed, all or almost all of the vessels were contraction or sclerosis.

1.2 Motivation and Hypothesis

The lymphatic system transports fluid along with particulate matter away from the tissues and returns it to the blood stream. The effective transport of fluid in the lymphatic system is important for preventing lymphoedema. Improving our understanding of the fluid behaviour within the lymphatic system may lead to insights into new ways of treating lymphoedema. It may also contribute to knowledge about

how the lymphatics transports waste, immune cells, and proteins around the body [Margaris and Black, 2012].

Due to the size of the lymphatic vessels and viscosity of the fluid, the valves must function mainly due to the hydrodynamic forces. The fragility and size of the collecting lymphatic vessels make physical study difficult. Therefore a computational model that can recreate the physical phenomenon would be useful for investigating valve function in more detail. A computational model of a colleting lymphatic vessel could be used to model how the changing the material properties of the wall and the size of the lumen affect the fluid flow. This would be useful for investitating how the changes to lymphatic vessels that occur during lymphoedema, as discussed in section 1.1 and sketched in figure 1.6, affect the efficiently of lymph transport. Examples of changes that could be made and compared to one another are: making the wall less compliant, increasing or decreasing the size of the lumen, making the wall thicker or decreasing the amount of smooth muscles cells. Understanding more about these effects could identify possible avenues for intervention to prevent the disease from worsening.

Lymph nodes are similarly difficult to study experimentally. To track the passage of flow through a lymph node, the fluid has to be seeded with particles. However, the lymph node filters particulate matter, causing particles not to follow the flow pathways but instead directs the particles to areas of the node where foreign particulate matter is stored and broken down.

This thesis aims to test the hypothesis that from the currently available experimental data it is possible to construct a three dimensional fluid structure interaction model of fluid flow entering a lymph node through an afferent lymphatic vessel and leaving through an efferent vessel. The model will be used to investigate the effect of different flow dynamics on the lymphatic vessels, the flow within the lymph node and provide information about how the fluid flow may affect immune response. Creating the model requires the gathering of relevant literature, which indicates in which areas further experimental data is required.

The advantage of creating a computer model is that it can bring together all the data that have been accumulated from different experimental methods. Experiments *in vivo* have a more realistic environment but allow the research less control over all the individual aspects that occur, e.g. conducting experiments of lymphatic vessels *in vivo* will be affected by the behaviour of the surround tissue such as muscle movements and the pulsating flow in the blood vessels. It can also be difficult to visualise the object of interest within the body of a living organism and can cause distress to the test subject, whether human or animal. Experiments carried out *ex vivo* can result in important aspects being lost, e.g. in lymphatic research it is not possible to study passive mechanisms and behaviour *ex vivo*. It can also be difficult to isolate

individual effects experimentally. With a computational model it is possible to bring together all known and suspected aspects that may affect the behaviour. Data from *in vivo* and *ex vivo* experiments can be brought together in the same model and the user can have complete control over all the mechanisms involved. The model can be used to systematically investigated the significance of each factor. The model of the collecting lymphatic vessels and lymph nodes that will be created in this thesis, will enable the identification of the most significant traits and so will highlight areas that require further experimental investigation to be carried out. This will also reduce the number of animals and human participants required for experimentation as the areas of investigation will be more specifically targeted and potential sources of error identified before hand.

The model is created by separating it into three components that can be brought together; the lymphatic vessel wall, valve and lymph node:

- A cylindrical model of an idealised lymphatic vessel will be created without the valve. Appropriate material properties for modelling the vessel wall will be found to ensure the model produces realistic biological behaviour. This model could be used in investigate the effect of a thickening lymphatic wall, as seen in cases of irreversible lymphoedema, and when connected to the lymph node model the affect of the vessel behaviour on the fluid flow through the node can be observed.
- An idealised collecting lymphatic valve will be modelled surrounded by the lymphatic vessel that is developed. This will allow investigation into the relationship between the valve and the wall. When connected to the lymph node model it will be possible to observe a functioning or malfunctioning valve affects the fluid flow pathways through the node.
- A model of a lymph node will be created based on high resolution images. Using an image based model will improve our understanding of how the structure of the lymph node affects the pathways of fluid flow through the node. After gaining an insight into flow on the scale of the whole node, sections of the node could be studied in more detail, i.e. subcapsular sinus or follicles.

In order to solve the governing equations on 3D domains discretisation must be used. Many methods available, here three popular methods will be considered: finite difference analysis (FDA), finite volume method (FVM) and finite element method (FEM). FDA replaces the partial derivatives in the governing equations with truncated series expansions. Increasing the terms in the expansion improves the accuracy of the solution, but dramatically increases the required computational resources. Another disadvantage of FDA is that for irregular geometries the series expansions must be transformed and this causes many problems. FVM uses the

assumption that the dependent variables are piecewise linear and integrates the equations over a volume. The flux is calculated between neighbouring nodes so for irregular geometries this requires many fluxes to be calculated. The advantage of using fluxes is that they are understandable in a physical sense. FEM integrates the equations over an element after multiplying them with a weight function. This function as the same form as the shape functions that are used to represent the dependent variables. The method is not disadvantaged when used applied to an irregular geometry. This makes it the prefered choice for this project.

It is necessary to use different physics to model all three elements and therefore each component is modelled using COMSOL Multiphysics, a commercial finite element software, that allows the user to incorporate different physical phenomenon into their model and solve these physics simultaneously using the finite element method (FEM), also known as finite element analysis (FEA). Boundary value problems for differential equations can be very difficult to solve analytically. COMSOL Multiphysics is a good platform for these simulations since it has many built in definitions, equations and settings as well as offering the possibility of adaptation and entering custom formulae.

The remaining chapters in this thesis describe the work carried out. In chapter 2 the literature relating to the collecting lymphatic wall is reviewed and a material model is developed that reproduces the behaviour of the passive collecting lymphatic wall observed experimentally. The results of this model are presented and compared to similar models in the literature. Chapter 3 contains a review of the behaviour of collecting lymphatic valves. Three models are developed and the results compared to experimental data to assess their validity. The chapter concludes with a comparison of the model to previous models of collecting lymphatic valves. In chapter 4, the structure of the lymph node is reviewed along with experimental data related to the fluid flow dynamics. A model based on images created using selective plane microscopy is presented and used to estimate parameters that are not available experimentally. The validity of the parameter values found are assessed by comparison to the relevant literature. In chapter 5, improvements to the model in chapter 4 are made by using high resolution x-ray computed tomography images and the sensitivity of the model to some parameters is investigated. The results of the model are compared and discussed. In the final chapter 6, the main conclusions are presented and the future work is discussed.

Chapter 2

Development of a Non-linear Material Model for Collecting Lymphatic Vessel Walls

In order to construct a biologically realistic model of a collecting lymphatic vessel, it is necessary to have an appropriate material model for the wall of the vessel. This is to ensure that the behaviour of the wall reflects the behaviour seen in experiments over a range of different initial conditions. The collecting lymphatic vessels display non-linear behaviour, therefore in this chapter, a detailed description of the collecting lymphatics is presented, followed by an example of a non-linear material model that has been used to model biological tissues. The methods used to parametrise the material model are described and the results are compared to example values from the literature. Finally, the results are discussed and ideas for future work are presented.

2.1 Literature Review

The collecting lymphatic vessels are formed of chains of lymphangions, a segment of lymphatic vessel, that actively pump to transport the fluid through the lymphatic system. The lymphangions are divided by collecting lymphatics valves that reduce the amount of back flow. This section begins with a review of lymphatic valve spacing, to investigate how the length of the lymphangions vary. The section continues with a review of the structure and function of the walls to understand more about the behaviour of the collecting lymphatic vessel walls. It is important to consider these experimental observations of the lymphatic vessels during the creation of the model so that the geometry and behaviour are realistically reproduced. Following this, estimated material parameters are presented for both the lymphatic fluid and the vessel wall. In section 2.1.6, previous approaches to model the collecting lymphatic

vessels are presented. Finally, a strain energy function is reviewed for its potential use in the model as a material model of the collecting lymphatic wall.

2.1.1 Valve Spacing

A review of the spacing between collecting lymphatic valves was carried out. The spacing and number of valves is species and organ specific [Shepro, 2005]. For example, birds have a lot of valves, but less than mammals, and hedgehogs have larger valve spacing than other mammals [Kampmeier, 1969]. The thoracic duct of the cat has more valves than the thoracic duct of the dog [Kampmeier, 1969]. There are fewer valves in the mesenteric vessels than skeletal muscle vessels [Shepro, 2005]. The results are summarised in table 2.1.

In humans the lymphangion length is approximately 3 to 10 times the diameter of the vessel [Földi et al., 2003]. The distances between valves can be irregular [Kampmeier, 1969; Zuther, 2009]. In the large collecting vessels from the fingers to the armpit of an adult human there are 60 to 80 valves and there are 80 to 100 valves from the toes to the groin giving an average of one valve every centimetre [Kampmeier, 1969].

In the adult human thoracic duct, the main collecting lymphatic vessel which drains into the subclavian vein in the neck, 6 to 12 valves have been seen with the most competent valve at or near the junction with the vein [Kampmeier, 1969]. The valves in the human thoracic duct are usually near vessels emptying into the duct [Kampmeier, 1969].

2.1.2 Collecting Lymphatic Wall Structure

The structure of the collecting lymphatics influence how they function. This structure has been described by several authors including Gnepp and Green [1980]; Skalak et al. [1984]; Mazzoni et al. [1987]; Arkill et al. [2010] and Rahbar et al. [2012]. Different microscopy techniques were employed, such as scanning electron microscopy (SEM), transmission electron microscopy (TEM) [Gnepp and Green, 1980; Skalak et al., 1984; Mazzoni et al., 1987] and multimodal nonlinear microscopy [Arkill et al., 2010; Rahbar et al., 2012], to investigate the micro-structure of the collecting lymphatics.

Gnepp and Green [1980] conducted an ultrastructural SEM study of the thoracic duct and collecting lymphatics in dogs. They measured the smooth muscle layer to be about 25 to 70 μm thick and the elastin layer to be approximately 5 μm [Gnepp and Green, 1980]. The thoracic duct wall was mainly made up of smooth muscle cells with some elastin fibres. The collecting lymphatics consisted of elastin fibres with some smooth muscle cells, although the amount of each was found to be very variable between vessels [Gnepp and Green, 1980].

Species	Vessel Type	Valve Spacing (mm)	Vessel Diameter (mm)	Spacing to Diameter Ratio	Reference
Adult Human	Precollector	2 to 3			[Földi et al., 2003]
	Collector	6 to 8 (up to 20)	100 to 600	3 to 10	[Földi et al., 2003]
	Caudal Part of Thoracic Duct	60 to 100			[Földi et al., 2003]
4.3 month human fetus	Thoracic duct	1 to 1.25			[Kampmeier, 1969]
Mid-intrauterine life human fetus	Thoracic duct	0.5 to 10			[Kampmeier, 1969]
130 mm human fetus	Thoracic duct	0.64 to 0.8			[Kampmeier, 1969]
New born human at term	Thoracic duct	4 to 5			[Kampmeier, 1969]
Dog	Thoracic duct	10 to 30			[Kampmeier, 1969]
Rat	Spinotrapizus muscle	0.3	0.02	15	[Mazzoni et al., 1987]
	Spinotrapizus muscle	0.06	0.013	4.62	[Mazzoni et al., 1987]
	Mesenteric	1.3	0.133	9.77	[Davis et al., 2011]
	Mesenteric	1.16 ± 0.66	0.08 to 0.22	2.27 to 22.75	[Scallan et al., 2013]
Mouse	Mesenteric	0.425	0.075	5.67	[Bazigou et al., 2009]
	Mesenteric	0.35	0.05	7	[Bazigou et al., 2009]
	Mesenteric, 18.5 day embryo	2.3 to 2.5	0.83 to 1.17	1.97 to 3.01	[Bazigou et al., 2009]
	Mesenteric	1.4			[Bazigou et al., 2009]

Table 2.1: Summary of valve spacing in different lymphatic vessels from different species. Information gathered from descriptions and measured from figures in literature. Some spaces are empty because this information was not present in the literature.

Mazzoni et al. [1987] looked at the lymphatics in the spinotrapizus muscle of the rat, which is the skeletal muscle across the back of the shoulders. It is a thin sheet of flat muscle. The lymphatics in this area are irregularly shaped and have no smooth muscle cells in the walls [Mazzoni et al., 1987]. This may be because the vessels are able to perform efficiently using only passive mechanisms without the need for spontaneous contractions as the skeletal muscle is very active. The lymphatics are often close to blood vessels and so can be stretched or compressed by the motion of nearby arterioles or muscle fibres [Mazzoni et al., 1987; Skalak et al., 1984].

Rahbar et al. [2012] imaged rat mesenteric collecting lymphatics at a valve and at positions upstream and downstream of it. The vessel was pressurised to 2 cmH_2O and 7 cmH_2O. They found that the thickness of the elastin layer was reduced at the higher pressures, the average thickness decreased from 11.1 μm to 8.3 μm. They also expected the collagen layer to decrease, but found that the average remained almost constant, which they believe could be due to the resolution of their equipment.

In the previous paragraphs, the structure and geometry of the collecting lymphatic vessel wall has been described. In the literature cited, the composition of the ultrastructure of the collecting lymphatic walls varies between the species and location. There is only a small amount of information about the thickness of each layer within the wall, particularly the amount of collagen and elastin fibres. In the next section, the function of the wall is reviewed. This relates how the structure contributes to the function of the vessel.

2.1.3 Vessel Wall Function

Vessels isolated from different regions of the body have been shown to behave differently. For example, the mesenteric lymphatics, vessels from the tissue surrounding some of the small intestine, pump more strongly than the thoracic duct and react differently to increased shear stress [Nipper and Dixon, 2011]. As shear stress increases the mesenteric lymphatics continue to pump where as the amplitude and frequency of contractions decrease in the thoracic duct [Nipper and Dixon, 2011].

Experiments have been carried out by Scallan et al. [2013], Davis et al. [2011] and Quick et al. [2007] amongst others, which aim to understand the physiology of the collecting lymphatics. Lengths of collecting lymphatic vessels are excised and manipulated using mechanical and biological methods [Nipper and Dixon, 2011; Moriondo et al., 2010]. Extracting the vessels from the tissue removes the possibility of constraints or influence from the surrounding tissue, which are considered to have little effect on the lymph flow in collecting lymphatic vessels under physiological conditions [Macdonald et al., 2008]. However, this restricts the type and kind of information that can be obtained about the passive mechanisms which assist lymph

transport. The information from the experiments is not applicable to some lymphatic vessels, such as those found in skeletal muscle, which only use passive mechanisms [Skalak et al., 1984].

The vessels are described as active when they are contracting and passive when they are not. During experiments the vessels are often placed in baths of physiological saline solution (PSS) to stop them drying out and provide the nutrition they need to continue to function outside the body. However, the smooth muscle cells require calcium to function. Therefore, Ca^{2+}-free PSS is substituted for the usual PSS in experiments to allow the investigation into the passive behaviour of the vessels [Davis et al., 2011].

2.1.3.1 Passive Behaviour

The passive diameter change of collecting lymphatic vessels to changes in pressure have been investigated and have been found to display nonlinear behaviour. At low pressures the vessels are highly extensible, however as the pressure rises the stiffness rapidly increases. Davis et al. [2011] and Rahbar et al. [2012] observed that in rat mesenteric lymphatics this sharp change occurs at about 5 cmH_2O. This can be seen in figure 2.1. The plots show how the diameter changes as the pressure increases at various locations along a lymphatic vessel. When the pressure is above 5 cmH_2O, the gradient of the curve is much steeper than before 5 cmH_2O. The graphs are all very similar, implying the behaviour is over the whole lymphangion length. Similar behaviour has been observed in bovine lymphatics [Ohhashi et al., 1980; Macdonald et al., 2008].

Arkill et al. [2010] investigated the structure of the walls of collecting lymphatics from bovine mesentry. The authors changed the pressure within the vessel and the longitudinal tension. Arkill et al. [2010] measured the fibre directions in four states: 1) no tension and intraluminal pressure of 0 Pa; 2) tension and intraluminal pressure of 0 Pa; 3) tension and intraluminal pressure of 1500 Pa and 4) tension and intraluminal pressure of 3000 Pa, to compare how the structure was altered.

In the initial state, which will be called state one, when the vessel was completely relaxed and the pressure inside the lumen 0 Pa, the vessels, which had a 2 mm diameter, had walls about 30 μm thick. The elastin fibres were found to occur singly, had diameter 1 μm and mainly ran straight along the vessel length, implying that the elastin fibres were tensioned even when the vessel was relaxed. The tension might be necessary because elastin has a low bending modulus. The collagen spiralled around and along the vessel's length in two layers. The collagen layer nearest the smooth muscle cells was composed of bundles of fibres with a diameter of 15 to 25 μm. Near

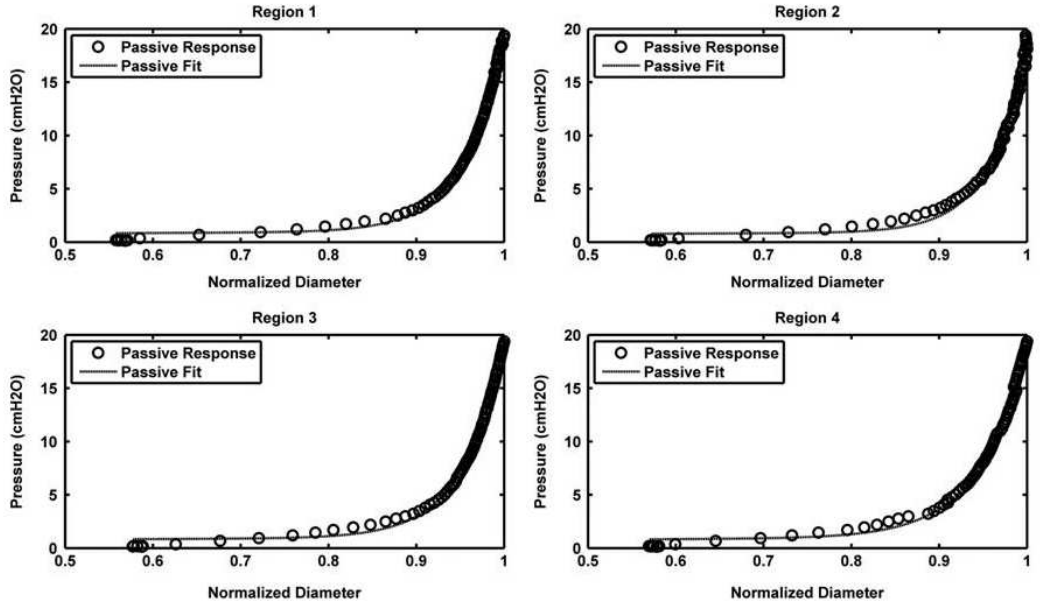

Figure 2.1: Pressure diameter curves for a lymphatic vessel from Rahbar et al. [2012]. Region 1: 260 μm upstream of valve. Region 2: 170 μm upstream of valve. Region 3: at valve. Region 4: 200 μm downstream of valve. The diameter is normalised with respect to the maximum diameter at 20 cmH_2O. Comparison of the graphs shows that there is little variation in the passive behaviour of the lymphangion between positions.

the outer surface of the wall the bundles had a 2 to 5 μm diameter. A graph showing the angle of the fibres is plotted in figure 2.2a.

In state 2, when the vessel was tensioned to the *in-situ* length, the vessel was about twice as long as the relaxed vessel. The collagen fibres rotated in the same direction as the strain. The elastin fibres also turned, but to a lesser extent, as can be see in figure 2.2b [Arkill et al., 2010].

Arkill et al. [2010] showed that as the tensioned vessel was pressurised to physiological values, the thickness of the wall halved. At 15 cmH_2O the collagen and elastin fibres turned to lie at about $\pm 40^\circ$ angle as measured with respect to the longitudinal axis, see figure 2.2c. This enabled the fibres to bear stresses in both the longitudinal and tangential directions. Arkill et al. [2010] state that at these pressures the material of the lymphatic walls is approximately isotropic. Increasing the pressure to 30 cmH_2O did not significantly increase the fibre angle, see figure 2.2d.

The findings from Arkill et al. [2010] appear to support the idea that at lower strains the elastin fibres take the load so the vessel can distend relatively easily and then at higher strains the collagen takes over, resisting extreme distension of the vessel [Macdonald et al., 2008; Arkill et al., 2010].

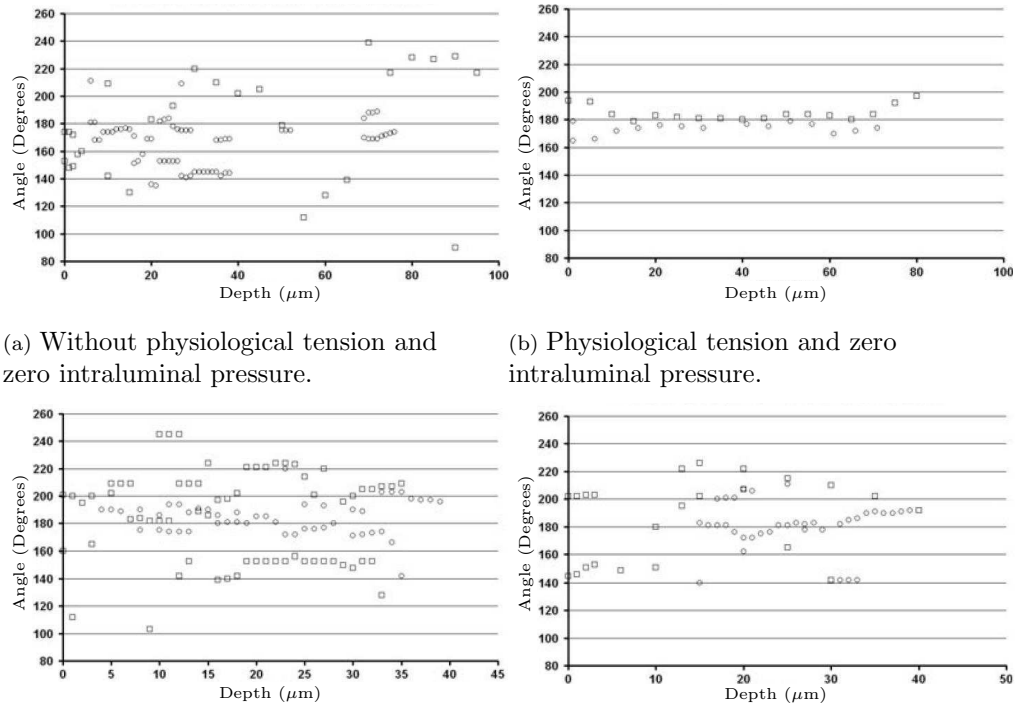

(a) Without physiological tension and zero intraluminal pressure.

(b) Physiological tension and zero intraluminal pressure.

(c) Physiological tension and 1500 Pa intraluminal pressure.

(d) Physiological tension and 3000 Pa intraluminal pressure.

Figure 2.2: Fibre angles measured with respect to the longitudinal direction of a bovine mesenteric collecting lymphatic vessel walls from Arkill et al. [2010]. Circles are elastin fibres, squares are collagen fibres. The mean and standard deviation are presented in table 2.8.

2.1.3.2 Active Behaviour

The smooth muscle cells within the collecting lymphatic vessel walls contract and relax in response to stimuli. This causes the vessels to pump fluid around the body. The terminology to describe the pump cycle of a lymphangion is based on phrases used to describe the phases of filling and pumping by the heart [Burton, 1972; Rowan, 1981; Schmid-Schönbein, 1990; Caro et al., 2012]:

- Systolic: Contraction phase, when fluid is pumped out.
- Diastole: Filling phase, when fluid flows in.

The collecting lymphatics are able to deal with rapidly changing loads and the efficiency of lymph transport can be improved by optimising different aspects of the vessel's pumping behaviour [Nipper and Dixon, 2011]. The strength and frequency of the contractions are affected by the pressure in the vessel, the volume of lymph, the wall shear stress, wall tension, vibrations, the rate of deformation and the

rate and volume of flow in the lymphatic [Nipper and Dixon, 2011; Gashev et al., 2002, 2004; Ohhashi, 2004]. For example, Gashev et al. [2004] shows that as the intraluminal pressure was increased from 1 cmH_2O to 9 cmH_2O cervical lymphatic vessels contracted approximately 6.25 times more at higher pressure than at lower pressures. The endothelial cells lining the vessel lumen produce nitric oxide, an agent that regulates vasodilation, to regulate the contractions [Ohhashi, 2004].

Collecting lymphatics have been shown to constrict, the diameter over the whole pumping cycle decreases, in response to a intraluminal pressure increase. Scallan et al. [2013] show that this constriction is in part a decrease in diastolic diameter, which is frequency-dependent, and a myogenic constriction, the diameter decreases as the pressure increases. Even though the lymphangion upstream of the valve does not experience the pressure increase caused by the accumulation of fluid in the downstream lymphangion, the constriction still occurs in the upstream lymphangion. Scallan et al. [2013] believe that the reason for this phenomena is to ensure that the valve will still close while the lymphatic vessels are pumping. This should prevent fluid flowing backwards into the initial lymphatics.

During contraction, excised vessels twist and buckle, particularly at higher pressures [Macdonald et al., 2008; Davis et al., 2011]. This means than experiments are usually carried out with the lymphatic vessels tensioned. Excised vessels can be about half their in-situ length. This implies that the vessels are under constant tension *in vivo* [Arkill et al., 2010].

In this section, the function of the collecting lymphatics was reviewed. The vessels are adapted to their environment and are able to react to changes in flow behaviour and quantity. The experiments that have been carried out show some difficulties when studying the lymphatics *ex vivo* and some aspects of the set up may affect the behaviour. These should be taken into consideration when comparing the results of a computational model with experimental data.

In order to computationally model the collecting lymphatics, it is necessary to be able to characterise the material properties using equations and appropriate parameters. In the next section fluid in the lymphatics is characterised using the Reynolds number and the methods for characterising the material of the wall are reviewed.

2.1.4 The Mechanics of the Collecting Lymphatics

2.1.4.1 Reynolds Numbers in Secondary Lymphatics

The Reynolds number, Re, is the ratio of the inertial fluid forces to viscous fluid forces. When the Reynolds number is small the viscous forces dominate the fluid flow. It has been noted that the Reynolds number in the collecting lymphatics is small due

to the viscosity of the flow and the size of the vessels [Schmid-Schönbein, 1990]. It is assumed (as in Reddy et al. [1975] and Rahbar and Moore [2011]) that the fluid is Newtonian, i.e. the viscous stresses are proportional to the local strain rate, and that the fluid does not contain solid particles. Similar assumptions have been made when modelling blood in the circulatory system [Caro et al., 2012].

Reynolds numbers were collected from the literature, either directly or calculated using the classic formula for the Reynolds number,

$$Re = \frac{UL}{\nu}, \tag{2.1}$$

where U is the characteristic velocity scale, L is the characteristic length scale and ν is the kinematic viscosity calculated by

$$\nu = \mu/\rho_f,$$

where ρ_f is the density of the fluid and μ is the dynamic viscosity [Acheson, 1990]. Unless otherwise stated, it is assumed $\mu = 1.5$ cP [Dixon et al., 2006] and $\rho_f = 998$ kgm^{-3} [Macdonald et al., 2008] as this information was only included in a few papers. This gives a kinematic viscosity of 1.503×10^{-6} m^{2}s^{-1}. We also assume that the lymphangions are cylindrical for the purpose of calculating the velocity by dividing the flow rate by the area.

Mazzoni et al. [1987] estimate a Reynolds number to be 0.0025 for the collecting lymphatics in the spinotrapizus muscle of the rat from a mean velocity of 0.1 mm/s, characteristic diameter 50 μm, lymph viscosity 2 cP and density 1 g/cm^3.

In Olszewski and Engeset [1980] measured the pressure of the lymphatics in the human leg. The diameter of the vessels were between 0.1 and 0.4 mm. Measurements were taken 2 and 5 days after the vessels had been cannulated and the wound had partially healed. The flow rate recorded, when the volunteers were lying down and keeping their legs and feet still, was 0.25 ± 0.04 ml/h, and when they were flexing their feet it was 0.57 ± 0.015 ml/h. Using a diameter of 0.25 mm gave $Re = 0.235$ when there was no movement and Re =0.537 when the feet were being flexed.

More recently, Dixon et al. [2006] recorded contraction cycles of mesenteric lymphatic vessels in a rat using high-speed video equipment. The rat was anaesthetised and a loop of small intestine was positioned under a microscope. They recorded the lymphatic flow for 30 second intervals and saved the footage for later analysis. Amongst other things this was used to measure the mean diameter, 91 ± 9.0 μm, and average volume flow rate, 13.95 ± 5.27 μL/h. This gives Re =0.0361.

In an experiment by Meisner et al. [2007] bovine mesenteric vessels, with no valves, were placed into a bath. A bypass was set up, with a stopcock at each end, so that

the fluid was directed through the vessel or through the bypass to keep the volume of fluid constant. The inlet pressure was set at 4 mmHg and luminal flow was controlled at 10 ml/h using a syringe pump. A micro-syringe was used to extract or insert fluid after it had left the vessel to vary the volume. They measured the pressure and diameter at ten volumes in a random order. The minimum diameter 1.8 mm and the controlled flow rate 10 ml/h give Re =1.307.

Quick et al. [2007] took bovine post-nodal mesenteric lymphatic vessels containing two valves and submerged them in a tubular organ bath so they had an external pressure of 1 mmHg. A video dimension analyser was used to record the diameter and a flow meter was used to measure the flow out of the lymphangion. Each end of the lymphatic vessel segment was collected to a fluid reservoir. Changing the height of these reservoirs altered the pressure at the ends of the lymphatic segment so that velocity and direction of the flow through the vessel could be controlled, i.e. if the pressure gradient was negative, the inlet pressure was less than the outlet pressure and vice versa. By reading the pressure and diameter values from the graphs in figure 2.3, it can be seen that when the pressure gradient was -1.5 mmHg, the diameter was approximately 1.7 mm and the flow rate was 0.6 ml/min. This gives $Re = 4.983$. When the pressure gradient was 1.5 mmHg, the diameter was approximately 1.8 mm and the flow rate 2.9 ml/min. This gives $Re = 22.747$.

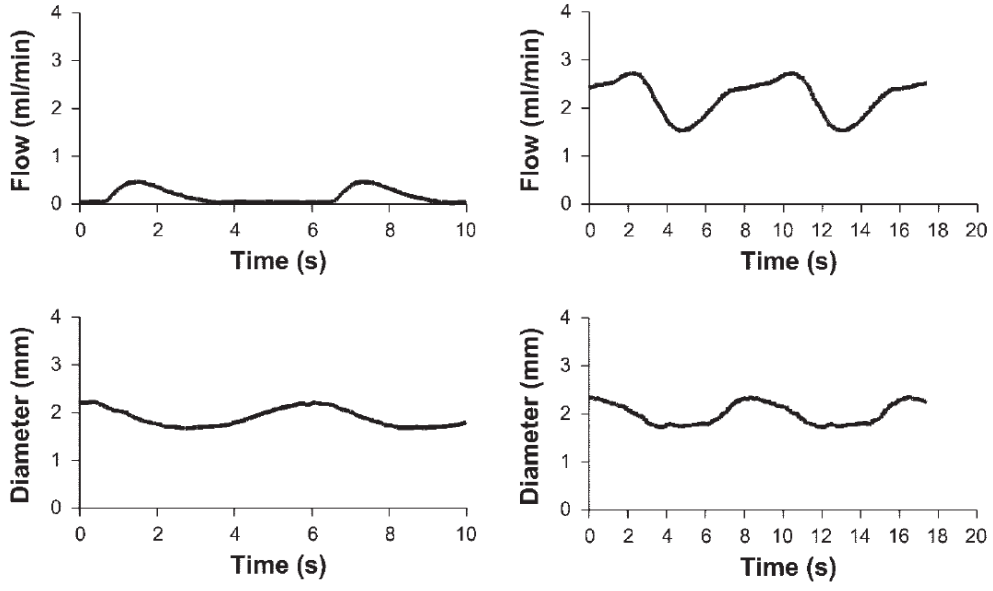

(a) Pressure gradient -1.5 mmHg

(b) Pressure gradient 1.5 mmHg

Figure 2.3: Graphs from Quick et al. [2007] showing flow rate and diameter for pumping bovine lymphatics with different pressure gradients. ©2007, The American Physiological Society. Permission not required.

In another paper, Quick and his colleges describe a similar experiment [Quick et al., 2009]. It had the same set up as Quick et al. [2007] but this time the inlet pressure

was kept constant and the outlet pressure was adjusted. When the pressure gradient was -1 cmH_2O, inlet pressure was less than outlet pressure, the minimum flow rate was approximately 4 ml/min, when the diameter was 4 mm. This gives Re =14.119. When the pressure gradient was 1 cmH_2O, inlet pressure was greater than outlet pressure, the minimum flow rate was approximately 8 ml/min. when the diameter was 4 mm. This gives Re =28.238.

The review above shows that Reynolds numbers over a range of magnitudes up to order 10 are possible in the secondary lymphatics depending on species and location, with larger animals having a higher Reynolds number. In order to measure the flow rate within the vessels experimentally, all the techniques described above were invasive in some way, i.e. cannulating vessels, anaesthetising the animal or extrating the vessels from their environment entirely. This will effect the behaviour of the lymphatic vessels. Despite this interference, the values of the Reynolds numbers calculated are considered to be of the correct order of magnitude. Having a good approximation of the Reynolds number for the model is important because it is necessary to define the equations that are most appropriate to model the fluid behaviour. Knowing the order of magnitude of the Reynolds number is considered sufficient for the selection of the equations as the values reported here are always in the pre-turbulent range, so the flow can be considered laminar. The information in this section has been summarised in table 2.2.

The low Reynolds numbers found are consistent with the descriptions in literature and indicate that the viscous forces dominate [Schmid-Schönbein, 1990], As well as knowing the properties of the fluid, we need to characterise the material properties of the collecting lymphatic vessels. This is considered in the next subsection 2.1.4.2.

2.1.4.2 Material Properties of Collecting Lymphatic Vessel

The Young's modulus, E, is the ratio of stress to strain forces and gives an indication of the elasticity of a material.

$$E = \frac{\text{tensile stress}}{\text{tensile strain}}.$$

This has been used to evaluate the mechanical properties of the collecting lymphatic wall. However, in the literature it has been estimated to range from 1200 Pa [Macdonald et al., 2008] to 1.1×10^6 Pa [Reddy et al., 1975]. This may be due to size, location, age and activity of the vessel used in these studies [Macdonald et al., 2008].

Ohhashi et al. [1980] calculated Young's moduli between 4200 Pa and 27000 Pa. They assumed the material was Hookean and used the equation from Azuma and Oka [1971] for the Young's modulus of a blood vessel wall in equilibrium calculated from

Species and location	Vessel diameter (mm)	Flow Rate (ml/h)	Mean Velocity (mm/s)	Reynolds Number	Reference
Rat, spinotrapizus muscle	0.05	7.07×10^{-3}	0.1	2.5×10^{-3}	[Mazzoni et al., 1987]
Human, leg, no movement, in situ	0.25	0.25	1.41	0.235	[Olszewski and Engeset, 1980]
Human, leg, feet flexed, in situ	0.25	0.57	3.23	0.537	[Olszewski and Engeset, 1980]
Rat, mesentry, in situ	9.1×10^{-2}	1.39×10^{-2}	0.596	3.61×10^{-2}	[Dixon et al., 2006]
Bovine, mesentry, isolated	1.8	10	1.09	1.31	[Meisner et al., 2007]
Bovine, mesentry, isolated	1.7	36	4.41	4.98	[Quick et al., 2007]
Bovine, mesentry, isolated	4	240	5.31	14.1	[Quick et al., 2009]
Bovine, mesentry, isolated	4	480	10.6	28.2	[Quick et al., 2009]

Table 2.2: Table of Reynolds numbers calculated for collecting lymphatics. The vessels were assumed to be cylindrical for calculating the velocity by dividing the flow rate by the area. The dynamic viscosity was assumed to be 1.5 cP [Dixon et al., 2006] and the density to be 998 kgm^{-3} [Macdonald et al., 2008], except for the value from [Mazzoni et al., 1987] where the viscosity and density were assumed to be 2 cP and 1 g/cm^3 respectively.

measurements taken at two states of mechanical stress. Each state has a different internal and external pressure. Azuma and Oka [1971] equation is given by,

$$E = \frac{(P_{12}r_{12} - P_{22}r_{22})\left(r_{21}^2 - r_{11}^2\right) - (P_{11}r_{11} - P_{21}r_{21})\left(r_{22}^2 - r_{12}^2\right)}{(r_{22} - r_{21})(r_{21} - r_{11})\left[(r_{22} + r_{12}) - (r_{21} + r_{11})\right]}, \tag{2.2}$$

where, for state one, r_{11} is the internal radius at internal pressure P_{11}, r_{21} is the external radius at external pressure P_{21}, and for state two in equilibrium, r_{12} is the internal radius at internal pressure P_{12}, r_{22} is the external radius for external pressure P_{22} [Azuma and Oka, 1971]. This equation was derived from the mean circumferential stress, τ_1, for state one, which can be calculated by

$$\tau_1 = \frac{T_1}{r_{21} - r_{11}}, \tag{2.3}$$

$$= \frac{P_{11}r_{11} - P_{21}r_{21}}{r_{21} - r_{11}}, \tag{2.4}$$

where T_1 is the state one tension. τ_1 can also be calculated by

$$\tau_1 = E\frac{(r_{21} + r_{11}) - (r_2 + r_1)}{(r_2 + r_1)}, \tag{2.5}$$

where r_1 is the internal radius as internal pressure $P_{1j} \rightarrow 0$ and r_2 is the external radius as external pressure $P_{2j} \rightarrow 0$. This leads to

$$\frac{P_{11}r_{11} - P_{21}r_{21}}{r_{21} - r_{11}} = E\frac{(r_{21} + r_{11}) - (r_2 + r_1)}{(r_2 + r_1)}. \tag{2.6}$$

Doing the same for state two means that $(r_2 + r_1)$ can be cancelled out. The resulting equation, rearranged for E, is equation (2.2). This means that the vessel under no stress does not need to be considered in order to calculate the Young's modulus [Azuma and Oka, 1971].

Macdonald et al. [2008] measured the external diameter of a lymphatic vessel while changing the intraluminal pressure, the pressure in the lumen, from 0 to 1500 Pa. They found that the diameter expands linearly as the pressure increases until it transitions sharply to a state where the vessel stops expanding [Macdonald et al., 2008; Davis et al., 2011]. At a strain of 1.1 ± 0.4, the Young's modulus dramatically increased [Macdonald et al., 2008]. Macdonald et al. [2008] suggest that initially the smooth muscle cells and elastin are taking the majority of strain, then as the strain increases the collagen takes more of the strain causing the Young's modulus value to increase.

Macdonald et al. [2008] used the equation for a thick walled tube to estimate the Young's modulus, i.e.,

$$\Delta P = \frac{E}{2(1-\sigma^2)}\Delta b \frac{b^2 - a^2}{a^2 b}, \tag{2.7}$$

where ΔP is the difference between the pressure on the inside and on the outside, σ is the Poisson ratio, E is the Youngs modulus, Δb is the change in the outer radius, b is the outer radius, a is the inner radius calculated as the outer radius minus the thickness of the wall.

The assumptions made to derive this equation are that the material is Hookean and the length of the tube does not change as it is inflated [Bergel, 1961]. Macdonald et al. [2008] calculated a Young's modulus for the period where the lymphangion expands, before the transition at strain 1.1±0.4, as 1200 Pa, however it was difficult to measure the wall thickness which introduced an uncertainty of ±700 Pa to this value.

Since values of Young's moduli for the wall presented in the literature vary over a large range and the only values found for the Young's modulus of the valve have been estimated for computational models not measured by mechanical testing, both of these values have been calculated based on images.

Equations (2.2) and (2.7) were applied to data from Macdonald et al. [2008], for bovine mesenteric vessels increasing the pressure from 0 to 215 Pa, and Davis et al. [2011], for rat mesenteric vessels the pressure changing from 19.6 to 36.3Pa. For equation (2.7) we assumed that the wall thickness was 0.7 times the initial inner radius, a, so the outer radius, b, could be calculated as

$$b = 1.7a. \tag{2.8}$$

It was also assumed that the vessels were incompressible, i.e. the Poisson ratio of the wall was assumed to be 0.5. Both sets of data resulted in much lower Young's moduli being calculated by equation (2.7): $E_w = 481.5$ Pa for bovine and $E_w = 8.67$ Pa for rat, than equation (2.2): $E_w = 1283.4$ Pa for bovine and $E_w = 33494.3$ Pa for rat. Compared to the Young's modulus of an endothelial cell which is 1000 Pa [Ohashi and Sato, 2005], the values calculated from equation (2.7) do not appear to be realistic as they are too small. The values calculated from equation (2.2) seem to be more realistic and more in keeping with values from the literature.

However, both (2.2) and (2.7) assume the elasticity is Hookean. This is probably not the case because it is known that the length of the vessel changes as the tube is inflated because the lymphangion twists and buckles [Macdonald et al., 2008].

Quick et al. [2007] used time-varying elastance to estimate Young's modulus,

$$E(t) = \frac{P(t)}{V(t) - V_0}, \tag{2.9}$$

where $P(t)$ is the pressure, $V(t)$ is the volume and V_0 is the volume when the pressure is zero. This was used by Suga et al. to relate ventricular chamber pressure and chamber volume in the heart [Quick et al., 2007; Suga and Sagawa, 1972].

2.1.5 Summary of the Mechanics of Collecting Lymphatics

The low Reynolds numbers calculated are always in the pre-turbulent range, so the flow can be considered as laminar and that the viscous forces dominate. Therefore it is suitable to assume that the behaviour of a solid mechanics model of the wall will be similar to the behaviour of a fluid structure interaction model. In the next section, 2.1.6, previous computational models, which have utilised the Young's modulus to model the material properties of the wall, are reviewed.

2.1.6 Computational Models of Collecting Lymphatics

Since the 1970's there have been several attempts to model aspects of the lymphatic system. This section reviews models of the collecting lymphatics, to examine the strengths and weaknesses of previous models, in order to avoid repetition and expand upon them.

Reddy et al. [1975] created a one-dimensional model of a chain of lymphangions by assuming Stoke's flow for an incompressible Newtonian fluid in a flexible cylinder with elastic walls. The walls were assumed to be much thinner than the length of the vessel. They assumed Poiseuille flow throughout, except at the valves, and that the radius and pressure were the same throughout the lymphangion. The valves were assumed to resist the flow and not allow negative flow rates. Reddy et al. [1975] included a strain threshold for the wall in their model which, when reached, initiated the active contractions of the lymphangion. The duration of the contraction and relaxation phases were both assumed to be 0.5 seconds for all the lymphagions. The results matched the available experimental data at the time although many of the assumptions were not realistic when considering the current knowledge of the system. For example, it is possible for different lymphangions and even regions within the same lymphangion to behave differently [Reddy et al., 1975]. It has since been shown that lymphangions contract without reaching a certain strain threshold [Gashev, 2002], therefore their condition of when the lymphangion should contract is incorrect.

Reddy et al. [1977] built upon their earlier model of a single lymphangion to create a simple model for the main lymphatic vessels of the body. The behaviour of the initial lymphatics was lumped into one section draining into the collecting lymphatics. The lymph nodes were modelled as lymphangions. The ratio of nodes to lymphangions was assumed to be small. Reddy et al. [1977] used the law of mass action to model

the rate of radial change as equal to the difference between the fluid flowing in and that flowing out divided by the surface area. The input parameters were the boundary conditions from the pressure in the jugular vein, arterial and venous capillary ends, the protein concentrations and the external pressure in the lymphangions. The model by Reddy et al. [1977] agreed with the available experimental data at the time. The model showed that the transport of lymph was affected by the rate of distension of the vessels [Reddy et al., 1977]. The advantages of this model were that it was relatively simple and could model a network of vessels. The disadvantages were the unrealistic assumptions. For example, the vessels all behave the same and the valves do not allow back flow. This backflow has been measured by Zawieja [2009] by tracking lymphocytes passing through a lymphatic vessel and calculating their velocity, see figure 2.4.

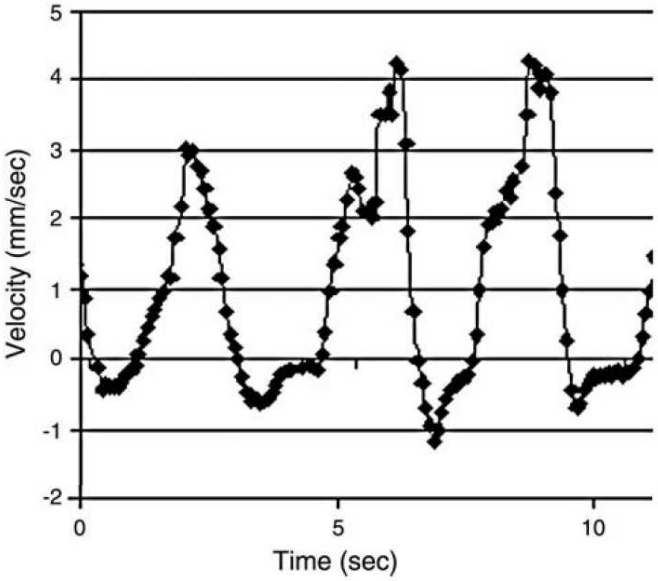

Figure 2.4: Velocity of lymphatic flow calculated from lymphocyte velocity and vessel diameter changes during three contraction cycles. Adapted from Zawieja [2009]. Note the negative flow velocity, which occurs just before the valve closes. ©2009, Mary Ann Liebert, Inc. Permission to used this figure granted by Mary Ann Liebert, Inc.

Macdonald et al. [2008] adapted the model by Reddy et al. [1975]. Macdonald et al. [2008] included vessel bending and damping terms and created a wall model that accounted for changes in the mechanical properties of the wall for the active and passive behaviour. In the passive mode the wall acts as an elastic membrane in this model. The active behaviour is modelled using a time varying Young's modulus. A minimum and maximum Young's modulus are calculated from experimental data to represent the wall in relaxed state, E_{rel}, and contracted state, E_{con}. A time dependent contraction function, ζ is used to increase or decrease the Young's modulus within

these limits. This is implemented using the equation,

$$E = E_{\text{rel}} + (E_{\text{con}} - E_{\text{rel}})\zeta(t) \quad \text{where} \quad \zeta \in [0, 1] \tag{2.10}$$

where E is the varying Young's modulus [Macdonald et al., 2008] and t is time. The values for E_{rel} and E_{con} were found using the thick walled tube equation (2.7). Two contraction functions were tried: a sine wave and a sine wave with a relaxation period. Macdonald et al. [2008] modelled a 2 cm lymphangion with an unstretched radius of 1.25 mm as six computational cells. The first and last were valve models, the behaviour of which was defined as an input. Each cell had a length three times longer than the diameter. The model did not include changes in the length or tension of the vessel during pumping. This model is an improvement of the model by Reddy et al. [1975] as it includes more realistic passive wall behaviour using two Young's moduli and splitting the lymphangion into separate sections allows each cell to behaviour differently. However this model is one dimensional.

Bertram et al. [2011] modelled a one dimensional connected series of contractile vessel segments with a valve separating each segment and a pressure reservoir at each end of the chain. The passive diameter of the wall of the collecting lymphatic vessels was related to the transmural pressure, p_{tm},

$$p_{tm} = P_d \left(e^{D/D_d} - (D_d/D)^3 \right), \tag{2.11}$$

where P_d and D_d are parameters defined by the authors to control the behaviour of the wall and D is the diameter of the lymphangion. A second term was added to incorporate vessel pumping. In order to find values of P_d and D_d that yielded experimentally observed behaviour, the equation was fitted to experimental data [Bertram et al., 2013b]. The pressure-diameter relationship was extrapolated to extend the model to function under negative transmural pressure, that had not been investigated experimentally. This model does result in biologically realistic behaviour of the pressure-diameter relation of the lymphatic vessel wall. However, the equation used has been chosen due to being able to match the data and no underlying explanation related to the structure of the vessel can be deduced.

Rahbar and Moore [2011] constructed a simplified three dimensional model of a lymphangion as a contractile cylinder with constant radius and an inlet and outlet at each end. The lymph was modelled as an incompressible Newtonian fluid with the density and dynamic viscosity as 0.997 g/cm^3 and 0.9 cP respectively. The model showed how the fluid was affected by the wall behaviour and showed that Poiseuille flow was maintained during all stages of the contraction cycle [Rahbar and Moore, 2011]. However, by defining the movement of the wall, it was not possible to use the model to investigate how the fluid affected the wall behaviour.

2.1.6.1 Summary

In this section, it has been shown that while various models of the collecting lymphatics have been attempted, many of these have been one-dimensional [Reddy et al., 1975; Macdonald et al., 2008; Bertram et al., 2011]. These models are able to represent the overall behaviour of a lymphatic vessel or network of them but the models are unable to show how the deformation of the vessel impacts on the flow. A three-dimensional model has been produced to take into account the behaviour of the wall [Rahbar and Moore, 2011], however the motion of the wall was prescribed and therefore it was not possible to explore how the fluid affected the vessel wall.

The range of values found in the literature for the Young's modulus may be caused by the clearly non-linear behaviour of collecting lymphatic wall, see figure 2.1. Therefore, using the Young's modulus in a computational model to determine how the vessel will behave when forces are applied to them will lead to results that do not reflect the experimental data. Bertram et al. [2011] presented a pressure-diameter relationship that can reproduce the experimental data, however it is not based on the underlying structure of the vessel wall and can give no indication as to why the vessel wall behaves as it does.

Other biological vessels, such as arteries and veins, have been modelled using strain energy functions to define the non-linear material properties, which are developed from an understanding of the material's structure. In the next section, 2.1.7, an example of a strain energy function is reviewed.

2.1.7 Strain Energy Functions

A strain energy function (SEF) relates the energy stored due to the strain in a solid to it's deformation. Differentiating the SEF by each of the strains results in the expression for stress in each direction. The SEF presented by Holzapfel et al. [2000] has been used to model arteries and veins, which have a structure similar to lymphatic vessels. In this section the SEF is presented, it's linear limit found and its application in computational models is reviewed.

2.1.8 Holzapfel-Gasser-Ogden Strain-Energy Function

Holzapfel et al. [2000] developed a strain-energy function for modelling the behaviour of the wall of an artery. The artery was modelled as a thick-walled cylinder consisting of two nonlinearly elastic layers that represented the media and adventitia layers of the arterial tissue. The media layer of an artery is made up of collagen, elastin and smooth muscle cells, although in different quantities to the lymphatic vessels. Arteries

also demonstrate the same exponential passive pressure-diameter curves. The Holzapfel-Gasser-Ogden (HGO) SEF aims to model the behaviour of the arterial wall under strains caused by inflation, extension and twisting.

The SEF from Holzapfel et al. [2000] takes the form

$$W = \underbrace{\frac{c}{2}\left(I_1 - 3\right)}_{\text{(A)}} + \underbrace{\frac{k_1}{2k_2}\left(\exp\left[k_2\left(I_4 - 1\right)^2\right] - 1\right) + \frac{k_1}{2k_2}\left(\exp\left[k_2\left(I_6 - 1\right)^2\right] - 1\right)}_{\text{(B)}}, \quad (2.12)$$

where c, k_1 and k_2 are material parameters. Term (A) is a neo-Hookean model that describes the isotropic properties of the material. The elastic constant c is greater than 0 and has units of stress (Pa). Term (B) models the anisotropic behaviour of the material, assumed to be a result of the presence of collagen fibres, increasing the stiffness as the strain increases. Parameters k_1 and k_2 are greater than 0; k_1 has units of stress (Pa) and k_2 is dimensionless [Holzapfel et al., 2000]. The I terms are invariants of a modified right Cauchy-Green tensor $\overline{\boldsymbol{C}} = J^{2/3}\boldsymbol{C}$ where $\boldsymbol{C}$ is the right Cauchy-Green tensor and J is the determinant of the deformation gradient. The invariants are given by,

$$I_1 = \mathrm{tr}\overline{\boldsymbol{C}}, \quad (2.13)$$

$$I_4 = \overline{\boldsymbol{C}} : \boldsymbol{A}_1, \quad (2.14)$$

$$I_6 = \overline{\boldsymbol{C}} : \boldsymbol{A}_2, \quad (2.15)$$

where $\boldsymbol{A}_1 = \boldsymbol{a}_1 \otimes \boldsymbol{a}_1$ and $\boldsymbol{A}_2 = \boldsymbol{a}_2 \otimes \boldsymbol{a}_2$; $\boldsymbol{a}_1$ and $\boldsymbol{a}_2$ are vectors that represent the directions of the collagen fibres. In cylindrical coordinates they are written as

$$\boldsymbol{a}_1 = \begin{pmatrix} 0 \\ \cos\beta_1 \\ \sin\beta_1 \end{pmatrix}, \quad \text{and} \quad \boldsymbol{a}_2 = \begin{pmatrix} 0 \\ \cos\beta_2 \\ -\sin\beta_2 \end{pmatrix}, \quad (2.16)$$

where β is the angle between the circumferential direction and the fibres, as shown in figure 2.8. It is assumed that the collagen fibres are active when extended, i.e. when $I_4, I_6 > 1$, but inactive when compressed, i.e. when $I_4, I_6 < 1$. Taking $\beta_1 = \beta$ and $\beta_2 = -\beta$, we can write the invariants as

$$I_1 = \lambda_\theta^2 + \lambda_z^2 + \lambda_r^2, \quad (2.17)$$

$$I_4 = \lambda_\theta^2 \cos^2(\beta) + \lambda_\theta^2 \sin^2(\beta), \quad (2.18)$$

$$I_6 = \lambda_\theta^2 \cos^2(-\beta) + \lambda_\theta^2 \sin^2(-\beta), \quad (2.19)$$

where λ_θ, λ_z, and λ_r are the stretch ratios in the principle directions.

Holzapfel et al. [2000] assumes that the material in incompressible. This implies that the third invariant $I_3 = \det\overline{\boldsymbol{C}} = 1$. However, this is not realistic for lymphatic vessels,

since we know from experiments by Arkill et al. [2010]; Rahbar et al. [2012] that the thickness of the walls of the vessels decrease as the vessel distends, for more detail of these experiments see section 2.1.2 and 2.2.2.2. We include a term to model the compressible behaviour from Doll and Schweizerhof [2000],

$$m\left(\sqrt{I_3}-1\right)\ln\left(\sqrt{I_3}\right), \tag{2.20}$$

where m is a material parameter and

$$I_3 = \lambda_\theta^2\lambda_z^2\lambda_r^2. \tag{2.21}$$

Therefore the SEF can be written as

$$\begin{aligned} W = \frac{c}{2}\left(I_1-3\right) + \frac{k_1}{2k_2}\left(\exp\left[k_2\left(I_4-1\right)^2\right]-1\right) + \frac{k_1}{2k_2}\left(\exp\left[k_2\left(I_6-1\right)^2\right]-1\right) \\ + m\left(\sqrt{I_3}-1\right)\ln\left(\sqrt{I_3}\right). \end{aligned} \tag{2.22}$$

2.1.8.1 Linear Limit of Holzapfel-Gasser-Ogden Strain Energy Function

The HGO SEF, in Cartesian coordinates with an added function for compressibility can be rewritten as,

$$\begin{aligned} W &= \frac{c}{2}\left(I_1-3\right) + \frac{k_1}{k_2}\left(\frac{1}{2}\left(\exp\left[k_2\left(I_4-1\right)^2\right]-1\right) + \frac{1}{2}\left(\exp\left[k_2\left(I_6-1\right)^2\right]-1\right)\right) \\ &\quad + m\left(\sqrt{I_3}-1\right)\ln(\sqrt{I_3}), \end{aligned} \tag{2.23}$$

$$\begin{aligned} &= \frac{c}{2}\left(I_1-3\right) + \frac{K}{2}\left(\exp\left[k\left(I_4-1\right)^2\right] + \exp\left[k\left(I_6-1\right)^2\right] - 2\right) \\ &\quad + m\left(\sqrt{I_3}-1\right)\ln(\sqrt{I_3}), \end{aligned} \tag{2.24}$$

where $K = \frac{k_1}{k_2}$ kPa, $k = k_2$ (no units) and m kPa are parameters usually found by data fitting. The invariants of the Cauchy strain tensor are,

$$I_1 = \lambda_x^2 + \lambda_y^2 + \lambda_z^2, \tag{2.25}$$

$$I_3 = \lambda_x^2\lambda_y^2\lambda_z^2, \tag{2.26}$$

$$I_4 = \lambda_x^2\cos^2\beta + \lambda_y^2\sin^2\beta, \tag{2.27}$$

$$I_6 = \lambda_x^2\cos^2\left(-\beta\right) + \lambda_y^2\sin^2\left(-\beta\right), \tag{2.28}$$

so $I_4 = I_6$, and λ_x, λ_y, λ_z are stretch ratios. Green's strains, defined as

$$E_x = \frac{1}{2}\left(\lambda_x^2 - 1\right), \tag{2.29}$$

$$E_y = \frac{1}{2}\left(\lambda_y^2 - 1\right), \tag{2.30}$$

$$E_z = \frac{1}{2}\left(\lambda_z^2 - 1\right), \tag{2.31}$$

are substituted into equation (2.24) giving,

$$\begin{aligned} W = {} & c\left(E_x + E_y + E_z\right) + K\left(\exp\left[k\left(2E_x\cos^2\beta + 2E_y\sin^2\beta\right)^2\right] - 1\right) \\ & + \frac{1}{2}m\left(\sqrt{\left(2E_x+1\right)\left(2E_y+1\right)\left(2E_z+1\right)} - 1\right)\ln\left(\left(2E_x+1\right)\left(2E_y+1\right)\left(2E_z+1\right)\right). \end{aligned} \tag{2.32}$$

Differentiating equation (2.33) by strains gives,

$$\begin{aligned} \sigma_{xx} = \frac{\partial W}{\partial E_x} = {} & c + 4Kk\left(2E_x\cos^2\beta + 2E_y\sin^2\beta\right)\cos^2\beta\exp\left[k\left(2E_x\cos^2\beta + 2E_y\sin^2\beta\right)^2\right] \\ & + \frac{m}{2}\frac{\left(2E_y+1\right)\left(2E_z+1\right)\ln\left(\left(2E_x+1\right)\left(2E_y+1\right)\left(2E_z+1\right)\right)}{\sqrt{\left(2E_x+1\right)\left(2E_y+1\right)\left(2E_z+1\right)}} \\ & + \frac{m\left(\sqrt{\left(2E_x+1\right)\left(2E_y+1\right)\left(2E_z+1\right)} - 1\right)}{2E_x+1}, \end{aligned} \tag{2.33}$$

$$\begin{aligned} \sigma_{yy} = \frac{\partial W}{\partial E_y} = {} & c + 4Kk\left(2E_x\cos^2\beta + 2E_y\sin^2\beta\right)\sin^2\beta\exp\left[k\left(2E_x\cos^2\beta + 2E_y\sin^2\beta\right)^2\right] \\ & + \frac{m}{2}\frac{\left(2E_x+1\right)\left(2E_z+1\right)\ln\left(\left(2E_x+1\right)\left(2E_y+1\right)\left(2E_z+1\right)\right)}{\sqrt{\left(2E_x+1\right)\left(2E_y+1\right)\left(2E_z+1\right)}} \\ & + \frac{m\left(\sqrt{\left(2E_x+1\right)\left(2E_y+1\right)\left(2E_z+1\right)} - 1\right)}{2E_y+1}, \end{aligned} \tag{2.34}$$

$$\begin{aligned} \sigma_{zz} = \frac{\partial W}{\partial E_z} = {} & c + \frac{m}{2}\frac{\left(2E_x+1\right)\left(2E_y+1\right)\ln\left(\left(2E_x+1\right)\left(2E_y+1\right)\left(2E_z+1\right)\right)}{\sqrt{\left(2E_x+1\right)\left(2E_y+1\right)\left(2E_z+1\right)}} \\ & + \frac{m\left(\sqrt{\left(2E_x+1\right)\left(2E_y+1\right)\left(2E_z+1\right)} - 1\right)}{2E_z+1}. \end{aligned} \tag{2.35}$$

Assuming isotropic (i.e. $K = 0$),

$$\sigma_{xx} = c + \frac{m}{2}\frac{(2E_y+1)(2E_z+1)\ln\left((2E_x+1)(2E_y+1)(2E_z+1)\right)}{\sqrt{(2E_x+1)(2E_y+1)(2E_z+1)}} + \frac{m\left(\sqrt{(2E_x+1)(2E_y+1)(2E_z+1)}-1\right)}{2E_x+1}, \tag{2.36}$$

$$\sigma_{yy} = c + \frac{m}{2}\frac{(2E_x+1)(2E_z+1)\ln\left((2E_x+1)(2E_y+1)(2E_z+1)\right)}{\sqrt{(2E_x+1)(2E_y+1)(2E_z+1)}} + \frac{m\left(\sqrt{(2E_x+1)(2E_y+1)(2E_z+1)}-1\right)}{2E_y+1}, \tag{2.37}$$

$$\sigma_{zz} = c + \frac{m}{2}\frac{(2E_x+1)(2E_y+1)\ln\left((2E_x+1)(2E_y+1)(2E_z+1)\right)}{\sqrt{(2E_x+1)(2E_y+1)(2E_z+1)}} + \frac{m\left(\sqrt{(2E_x+1)(2E_y+1)(2E_z+1)}-1\right)}{2E_z+1}. \tag{2.38}$$

Expanding in a Taylor series and only taking the first two terms, results in a standard linear stress-strain relation for Hooke's Law for an isotropic material [Fung and Tong, 2005],

$$\sigma_{xx}: \quad c + 2mE_x + 2mE_y + 2mE_z = \lambda(E_x + E_y + E_z) + 2GE_x, \tag{2.39}$$

$$\sigma_{yy}: \quad c + 2mE_x + 2mE_y + 2mE_z = \lambda(E_x + E_y + E_z) + 2GE_y, \tag{2.40}$$

$$\sigma_{zz}: \quad c + 2mE_x + 2mE_y + 2mE_z = \lambda(E_x + E_y + E_z) + 2GE_z. \tag{2.41}$$

This implies $c = 0$, $G = 0$ and $2m = \lambda$ in the linear limit of the strain energy function. This tells us that the primary linear response assumed in HGO is volumetric stress in response to the volumetric strain, but that the strain is negligible at the linear limit. Holzapfel et al. [2000] have built residual stress of the material into their strain energy function in the form of c. λ can be written as,

$$\lambda = \frac{E\nu}{(1+\nu)(1-2\nu)} \tag{2.42}$$

where E is the Young's modulus and ν is Poisson's ratio. Therefore, the HGO SEF can be written as,

$$W = \frac{c}{2}(I_1 - 3) + \frac{K}{2}\left(\exp\left[k(I_4-1)^2\right] + \exp\left[k(I_6-1)^2\right] - 2\right) + \frac{E\nu}{2(1+\nu)(1-2\nu)}\left(\sqrt{I_3}-1\right)\ln(\sqrt{I_3}). \tag{2.43}$$

2.1.8.2 Applications of Holzapfel-Gasser-Ogden Strain Energy Function

The HGO SEF has been used to model various biological tissues. A review some of these models is presented here. The values of the parameters used are shown in table 2.3 for comparison.

Holzapfel et al. [2000] modelled a carotid artery from a rabbit. They found different parameter values for the adventitia and media, layers of the artery wall, the value of c for the media was assumed to be ten times stiffer than the value of c for the adventitia as they knew the media should be stiffer than the adventitia.

Auricchio et al. [2014] used the SEF to model an aortic valve implant in an aorta root specific to a patient. They believe that a patient specific model would be useful for planning operations. It was hoped that including a more accurate material model for the leaflets would provide a better representation of the real effects of the implant. The stentless implant valve leaflets, which they were modelling, are made from bovine pericardium. Although this material has anisotropic mechanical properties, the fixation process may affect this. Therefore the authors decided to compare the leaflet behaviour modeled by the Holzapfel et al. [2000] SEF to an isotropic hyperelastic model. The image based model of an aortic root was constructed based on a cardiac computed tomography-angiography from a patient. Matlab and Abaqus were used to process the images and create a 3D finite element model. The geometry of the stentless valve was modelled on an implant called Labrosse, however the dimensions for this particular implant were not available, so they used the dimensions of the Freedom Solo valve implant and assumed that it was the same as a healthy human valve [Auricchio et al., 2014]. Auricchio et al. [2014] modelled the aortic root material as an incompressible Mooney-Rivlin model. They compared two models for the valve leaflets: firstly, they used a hyperelastic incompressible model with Young's modulus 8 MPa, Poisson's ratio 0.49 and density 1100 kg/m^3; secondly they used the HGO SEF. Auricchio et al. [2014] imposed a local vector system of $\boldsymbol{e}_1$, in the base-to-apex direction, $\boldsymbol{e}_2$, in the pericardium plane orthogonal to $\boldsymbol{e}_1$ and $\boldsymbol{e}_3 = \boldsymbol{e}_1 \times \boldsymbol{e}_2$. The fibres were considered to be organised symmetrically and $\pm\beta$ represented the angle from the base-to-apex direction to the fibre. Since the fibre angle of the leaflets was unknown it was treated as an unknown parameter. Auricchio et al. [2014] had four unknown parameters, c, k_1, k_2 and β. They repeated their optimisation for a range of initial parameters because the final result depended on the initial guess. The optimal values were found to be $c = 20.1$ kPa, $k_1 = 54.62$ kPa, $k_2 = 30.86$ and $\beta = 29.8\,\text{deg}$. They used this model to look at how the fibres affected the leaflets. Comparing the isotropic and anisotropic models, they found that the fibres cause the stress to be more uniformly aligned in the direction of the fibres resulting in smaller stress values overall. They found that the isotropic model had folds that were not biologically realistic whereas the anisotropic model displayed behaviour that agreed with previous computational studies. Auricchio et al. [2014] concluded that the material model chosen had a significant effect on numerical simulations.

Zulliger et al. [2004] used the SEF from Holzapfel et al. [2000] as a basis for creating their own SEF. They incorporated the density, mechanical properties and distribution of the collagen and elastin fibres. They found that their SEF resulted in a better fit to

the experimental data compared to the SEF from Holzapfel et al. [2000], however they required additional experiments to measure the necessary information. They used two equations to collect the information needed for the fitting,

$$P = \int_{r_i}^{r_o} (\sigma_\theta - \sigma_r) \frac{1}{r} \mathrm{d}r, \tag{2.44}$$

where P is the intraluminal pressure, r_o and r_i are the outer and inner radii respectively, σ_θ and σ_r are the local wall stresses in directions θ and r and r is the radius of the wall.

$$F_z = \int_{r_i}^{r_o} \sigma_z 2\pi r \mathrm{d}r - P\pi r_i^2, \tag{2.45}$$

where F_z is axial force, σ_z is the local wall stress in direction z. The initial diameter was estimated so that the radius at 1.98 kPa for 100% *in vivo* stretch closely matched the experimental data. The initial stretch required for 100% *in vivo* length is also unknown. Therefore λ_z was estimated so that the force required for the stretch at 1.98 kPa for 100% *in vivo* stretch was close to the experimental data. This initial diameter, 860 mm and stretch, $\lambda_z = 1.21$ of the untensioned vessel, were then fixed for the kriging procedure. $\lambda_z = 1.21$ was assumed to be 100% of the *in vivo* length. The fibre angle was fixed to 39.8°.

Cornejo et al. [2014] applied the SEF to patient specific aneurysmal cerebral arteries to compare the wall stress between a nonlinear isotropic model and the anisotropic model. They found that the anisotropic model resulted in a higher maximum stress than the isotropic model.

Sunbuloglu et al. [2013] carried out experiments to estimate the parameters for the SEF. They used one form of the SEF for the pure elastic energy, Ψ_e, and another to model the viscoelastic energy, Ψ_v.

$$\Psi_e = C_1^e (I_1^e - 3) + \frac{C_2^e}{\alpha^e} \left[\exp\left(\alpha^e (I_4 - 1)^n\right) + \exp\left(\alpha^e (I_6 - 1)^n\right) - 2\right], \tag{2.46}$$

$$\Psi_v = C_1^v (I_1^v - 3) + \frac{C_2^v}{\alpha^v} \left[\exp\left(\alpha^v (I_4 - 1)^n\right) + \exp\left(\alpha^v (I_6 - 1)^n\right) - 2\right], \tag{2.47}$$

where n is the elastic hardening power, set to be 2.5. They also included an equation for the dissipative potential, with parameters for fibre-resolved and isotropic viscosities and rate-hardening. They carried out experiments on ovine pulmonary arteries assuming that the behaviour of the vessel was homogeneous. The results from these experiments were used to estimate the parameters. They ran an experiment with a static test with a 10 N extension force and 15 kPa pressure to estimate C_1^e, C_2^e and α^e. They ran a dynamic test with 20° torsion, 1 to 11 N extension at 4 Hz and and 10 kPa pressure to estimate C_1^v, C_2^v, α^v and the parameters for the dissipative potential. The parameters listed in table 2.3 are the static parameters [Sunbuloglu et al., 2013].

Sunbuloglu et al. [2013] compared the model to experimental data for the tangential deformation gradient over time, the axial force against the axial strain, the pressure against the circumferential strain and torsion against time. The model matched the experiments reasonably well although it underestimated the tangential deformation gradient. Sunbuloglu et al. [2013] believe their procedure could be used to fit parameters for different materials however as the experiments are performed the behaviour of the material changes. This limits the number of times the experiments can be repeated.

Badel et al. [2013] used the HGO SEF to model a porcine vein. They created a computational model of a cylinder (6.5 mm diameter, 30 mm long, 0.3 mm wall thickness) and applied different amounts of axial stretch to it. They then increased the pressure (up to 100 mmHg) in the lumen in order to see how much the vessel buckled. They varied the angle of the fibres, finding that as the angle increased the vessel buckled to a lesser extent. They scaled the parameters c and k_1 to show that the vessel buckled less if the vessel was stiffer.

Sokolis [2013] carried out a parameter optimisation study for porcine jugular veins comparing the model to the pressure-radius-force data that they had obtained from experiments. They compared different SEFs. Although the SEF from Holzapfel et al. [2000] could reasonably accurately recreated the pressure-diameter data, it was unable to match the force data.

The HGO strain energy function has been used to model blood vessels. In subsection 2.1.10, lymphatic vessels are compared to blood vessels to try and approximate how the parameters for the SEF for the lymphatic vessels may differ due to the structural and behavioural differences between the types of vessels.

In table 2.3, it can be seen that, in general, the value of the parameters c, k_1 and k_2, are one or two orders of magnitude higher for arteries than for veins. All the values of E and ν are zero, as all these examples were assumed to be incompressible.

2.1.9 Summary

Strain energy functions have been used to model biological tissues because they are able to model highly nonlinear behaviour that is typical of soft tissues. In the next section 2.1.10 the structure and behaviour of lymphatic vessels are compared to blood vessels. This enables a prediction to be made as to how the parameters for the HGO SEF may be different for the lymphatics when compared with blood vessels. The values may also differ due to the species and vessel size and location.

Species	Tissue	c (kPa)	k_1 (kPa)	k_2	Initial Internal Diameter (μm)	β (degrees)	Reference
Rabbit	Adventita of carotid artery	0.3	0.5620	0.7112	970 to 1690	62	[Holzapfel et al., 2000]
Rabbit	Media of carotid artery	3	2.3632	0.8393	710 to 1430	29	[Holzapfel et al., 2000]
Human prosthetic	Aortic valve leaflet	20.1	54.62	30.86	n/a	29.8	[Auricchio et al., 2014]
Rat	Carotid artery	44.24	0.206	1.465	860	39.76	[Zulliger et al., 2004]
Human patient specific	Aneurysmal cerebral arteries	0.5	1.1	5	600	2, 45, 60	[Cornejo et al., 2014]
Sheep	Pulmonary artery	16.09	1.22	10.94		54	[Sunbuloglu et al., 2013]
Sheep	Pulmonary artery	21.38	1.81	18.12		54	[Sunbuloglu et al., 2013]
Sheep	Pulmonary artery	29.46	0.85	8.69		54	[Sunbuloglu et al., 2013]
Sheep	Pulmonary artery	27.71	4.49	4.47		54	[Sunbuloglu et al., 2013]
	Vein	1	5.6	2.9	6500	25	[Badel et al., 2013]
Pig	Jugular vein	0.643	0.185	0.569		36.9	[Sokolis, 2013]
Pig	Jugular vein	1.262	1.077	0.985		42.63	[Sokolis, 2013]
Pig	Jugular vein	0.977	0.155	1.637		42.69	[Sokolis, 2013]
Pig	Jugular vein	2.059	0.082	3.651		56.15	[Sokolis, 2013]
Pig	Jugular vein	1.810	0.113	2.532		41.6	[Sokolis, 2013]
Pig	Jugular vein	2.350	0.592	2.893		49.96	[Sokolis, 2013]
Pig	Jugular vein	0.838	0.255	0.532		44	[Sokolis, 2013]

Table 2.3: Parameter values used for the strain energy function. E and ν are not shown as the material was assumed to be incompressible.

2.1.10 Comparison to Blood Vessels

Lymphatic vessels have been compared to blood vessels, which have a different structural composition [Nipper and Dixon, 2011]. The structure of smooth muscle, elastin and collagen networks in the lymphatic walls are not present in blood vessels [Gnepp and Green, 1980; Arkill et al., 2010]. This may be because the vessels are adapted for the different luminal pressures that they have to withstand. It is not necessary for blood vessel walls to spontaneously contract, since the heart pumps the blood around the body. Blood vessels experience mainly radial stess. In comparison, the lymphatic walls have to actively pump the lymph which creates longitudinal as well as radial stresses [Arkill et al., 2010]. Lymphatic and blood vessels exhibit different pressure diameter relationships, as shown in figure 2.5 [Rahbar et al., 2012].

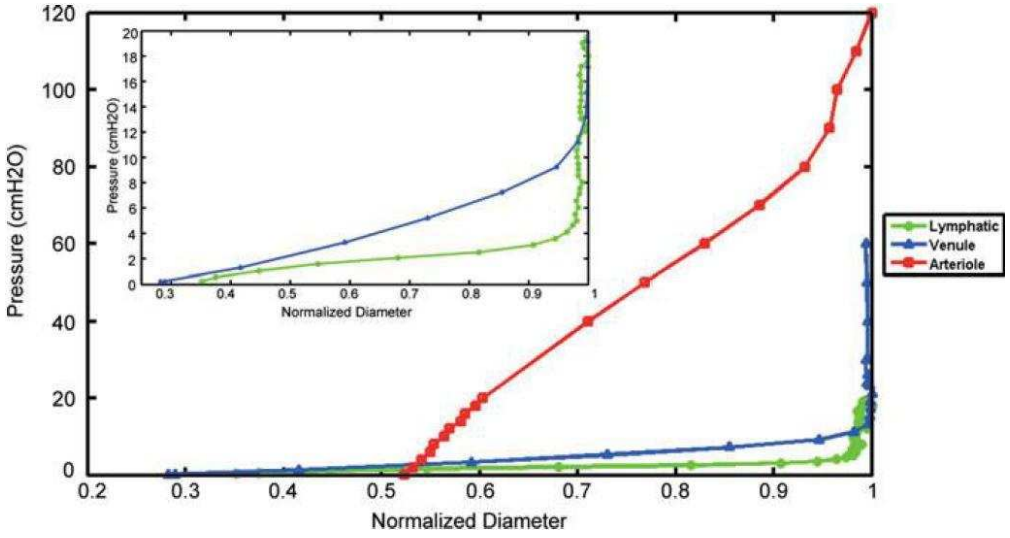

Figure 2.5: Pressure diameter comparisons for an arteriole, venule and lymphatic vessel from a rat [Rahbar et al., 2012]. Diameter normalised by maximum diameter, which was 267 μm for the lymphatic. ©2012, Mary Ann Liebert, Inc. Permission to use this figure granted by Mary Ann Libert, Inc.

There are much higher forces present in the vascular system than the lymphatic system. Blood moves relatively quickly compared to lymph, a comparison of values can be seen in table 2.4. Due to the slower velocities of the lymphatic system, the Reynolds number is a lot lower than in the vascular system.

Mean Flow	Cardiac	Mesenteric
Lymph	3.0 ml/hour	0.015 ml/min/100g
Blood	40 ml/hour	50 ml/min/100g

Table 2.4: Comparison of mean blood and lymph flows [Abramson and Dobrin, 1984; Miller et al., 1964; Lanciault and Jacobson, 1976; Vatner and McRitchie, 1975].

2.1.10.1 Summary

As can been seen in figure 2.5, the lymphatic vessels behave similarly to venules. Thus, it is expected that the parameters of the HGO SEF for lymphatic vessels to be more similar to veins than arteries. This means that the expected values of c would be of order 10^{-1} to 1 (kPa), k_1 of order 10^{-1} (kPa) and k_2 of order 10^{-1} to 1 (no units). However, it is unknown how including the compressibility term with parameters E (kPa) and ν will effect the final results.

2.2 Methods

2.2.1 Geometry

To estimate the geometry of the collecting lymphatic wall, two videos, 40_hires_3 and 40_hires_4, by Taija Makinen and colleagues at Cancer Research UK were used to obtain measurements for the geometry of mouse lymphatics. The vessels were isolated and then fixed. During the fixation process the lymphatic vessels become flattened. 40_hires_3 describes a rotating lymphatic valve from the side, see snapshots in figure 2.6a-2.6d, i.e. the buttress connection to the wall is straight on. 40_hires_4 describes a rotating valve from the front, see snapshots in figure 2.6e-2.6i, i.e. the leaflet of the valve is seen straight on. Measurements of the geometry of lymphatic vessels were made from some of the frames using ImageJ software. The measurements taken from these images can be seen in table 2.5.

	Side							Front			
Figure	2.6a	2.6c	2.6b	2.6d	2.6e	2.6f	**Mean**	2.6g	2.6h	2.6i	**Mean**
Downstream width (μm)	69.6		66.5				**68.0**	95.8	95.0	73.1	**88.0**
Upstream width (μm)	37.8		35.3		34.9	33.6	**35.4**	57.8	54.0	53.4	**55.1**
Thickness without valve (μm)		6.6		7.6			**7.1**				

Table 2.5: Measurements from images in figure 2.6. The white lines in figure 2.6 show the approximate position where the measurements were taken using ImageJ. These measurements form the basis for the geometry of the model of the collecting lymphatic valve and surrounding vessels. The mean values for the front and side measurements are also recorded. All measurements are accurate to one decimal place. The empty values could not be measured from the particular image.

In the images in figure 2.6, the wall thickness, h_w^{im}, was set to be half the flattened vessel thickness. This provided the wall thickness to external diameter ratio of the vessel. This ratio was used to estimate the wall thickness for the vessels in the experiments by scaling the wall thickness, h_w, to the initial internal diameter, D_0.

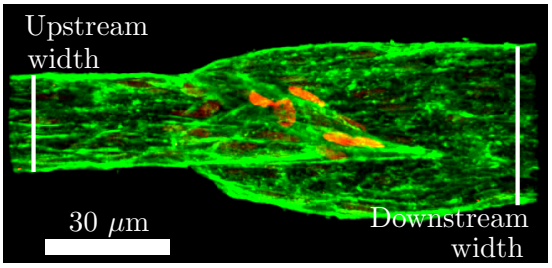

(a) 40_hires_3, frame 1

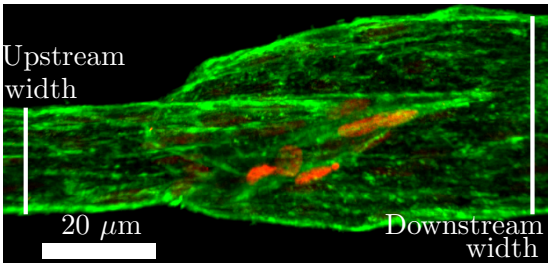

(b) 40_hires_3, frame 76

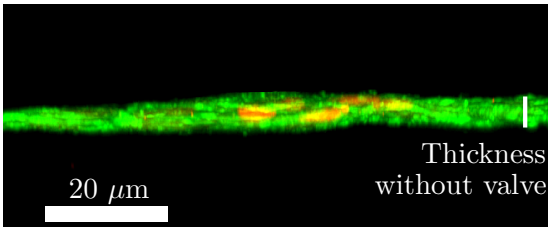

(c) 40_hires_3, frame 53

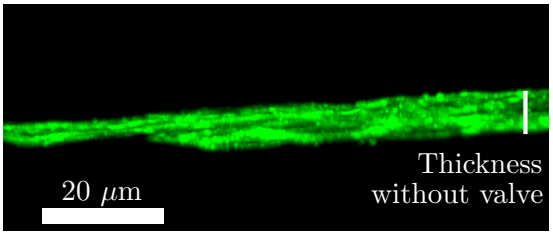

(d) 40_hires_3, frame 85

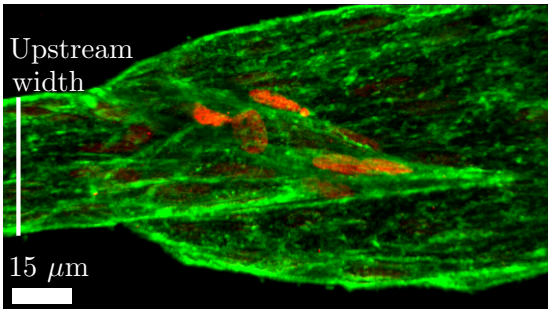

(e) 40_hires_3, frame 351

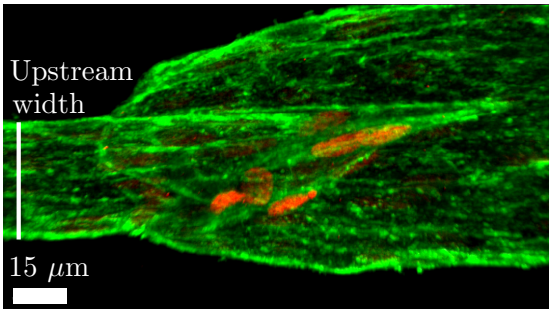

(f) 40_hires_3, frame 431

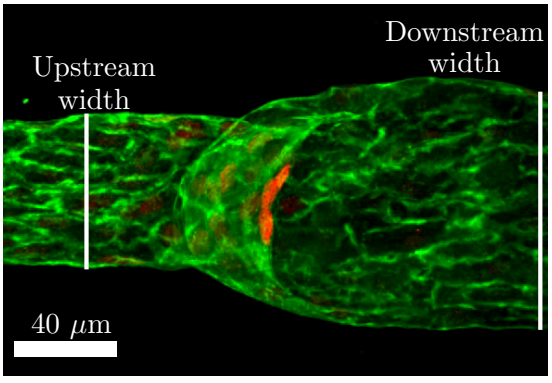

(g) 40_hires_4, frame 4

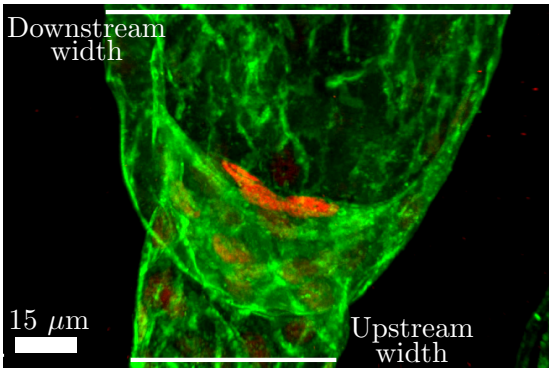

(h) 40_hires_4, frame 60

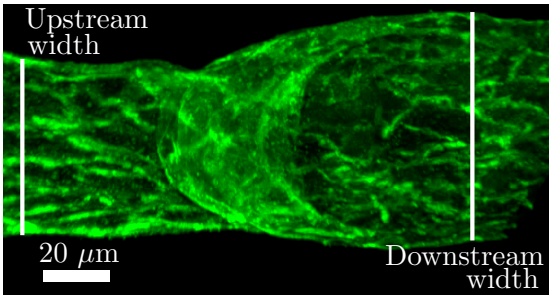

(i) 40_hires_4, frame 241

Figure 2.6: Frames from videos 40_hires_3 and 40_hires_4 by Taija Makinen and colleagues at Cancer Research UK of mouse lymphatic vessels. The white lines show the approximate position where the measurements were taken using ImageJ.

The wall thickness was calculated as,

$$h_w = D_0 \frac{h_w^{im}}{D_0^{im}}, \tag{2.48}$$

where D_0^{im} is the internal diameter from the images calculated as

$$D_0^{im} = D_{ext}^{im} - h_w^{im}, \tag{2.49}$$

where D_{ext}^{im} is the external diameter measured from the image. The length, L, was calculated to be,

$$L = 7D_0, \tag{2.50}$$

because the lymphangion length to diameter ratios reported in the literature were between 3 and 10 [Földi et al., 2003].

As well as constructing a biologically realistic geometry, data measured in experiments was used to optimise the parameters. Different data sets were used: pressure-diameter and pressure-force data from Zulliger et al. [2004] and mouse and rat lymphatic pressure-diameter data provided by Joshua Scallan at University of Missouri School of Medicine. This is presented in the next section.

2.2.2 Experimental Data

The Kriging procedure, which will be described in section 2.2.5.2, and HGO SEF were evaluated by using it to fit data published by Zulliger et al. [2004] for arteries and comparing the results to those presented by the authors. Zulliger et al. [2004] used an adapted version of the HGO SEF to model the pressure-diameter behaviour. This comparison may lead to an insight as to the effect of the additional compressible term and if the Kriging procedure and the SEF equation (2.43) were capable of accurately modelling the force data as well as the pressure-radius data.

Using DataThief, experimental data for both the pressure-radius curve and the axial force was obtained for rat carotid arteries from Zulliger et al. [2004]. Figure 2.7 shows the experimental data with the model fits presented in Zulliger et al. [2004] using the parameters in table 2.9. It can be seen that the model fits the data well, except for the force at 130% of the *in vivo* stretch. There was some variation in the pressures measured for the data points as using DataThief gave an accuracy of ± 0.2 kPa, but this is considered as small over the whole range of 30 kPa. The mean of the pressures collected was calculated and this was assumed to be the pressure at which the measurements of radius and force were conducted. The data points used are those with error bars in figure 2.7.

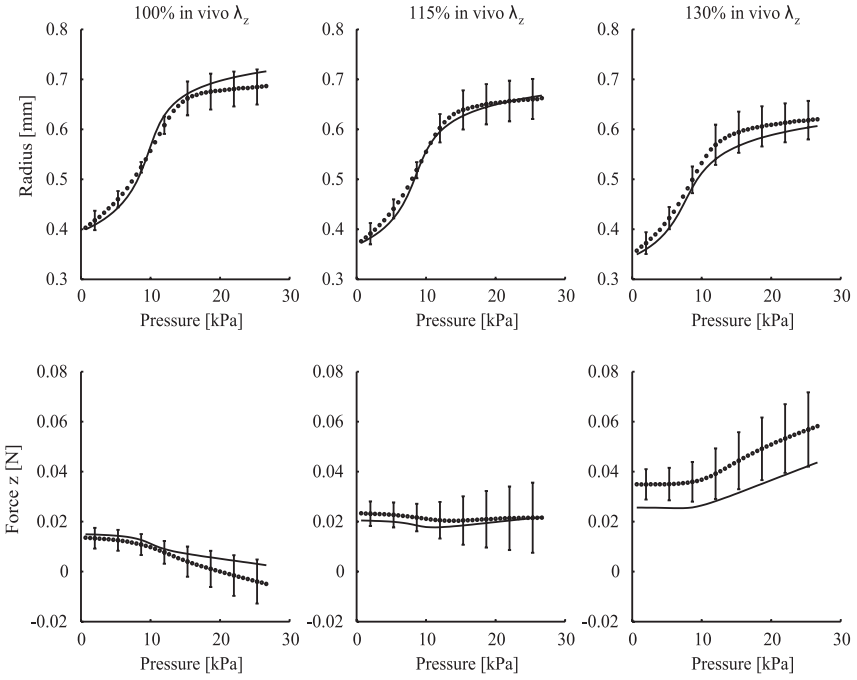

Figure 2.7: Graphs show experimental data (circles) for left cartoid relaxed arteries from 8 week old Wistar rats. Error bars show standard deviation of experimental data. The black line is the model results. The three upper graphs show pressure-diameter curves and the lower three the axial force applied. Reprinted from Zulliger et al. [2004] ©2004, with permission from Elsevier

In order to find parameters for the nonlinear material models that resulted in realistic biological behaviour for the collecting lymphatic wall model, experimental data was provided by Joshua Scallan, School of Medicine, University of Missouri. He produced passive pressure-diameter data for isolated mouse and rat mesenteric lymphatics. Information about the angle of the fibres in the collecting lymphatic wall was also used based on the measurements presented in Arkill et al. [2010].

2.2.2.1 Passive Pressure-Diameter Data

The experiments were carried out by mounting sections of lymphatic vessels between two pipettes. The pressure of each pipette would then be controlled. The pressure in both pipettes was raised to 10 cmH_2O for the mouse lymphatics and to 12 cmH_2O for the rat lymphatics. This caused the vessel to distend and buckle. The pipettes were then moved apart until the vessel was straight. After this the pressure in both pipettes was lowered. This prevented the vessel from moving so that the diameter could be measured as the pressure in both pipettes was gradually increased. The straightening of the vessel increased the length by approximately 30%, to about the same as the *in situ* length. [Scallan, personal communication]. These data are summarised in tables 2.6 and 2.7.

Mouse	32812	32912	33012	40212a	40212b	40512	60112	61412	61512
Pressure	**Diameter (μm)**								
0.5						73	68	71	51
1	69	80	76	83	99	81	73	78	65
2	73	84	85	93	106	84	77	85	74
3	75	85	90	96	108	85	78	88	79
5	76	87	92	99	112	86	80	91	85
7	77	88	93	101	114	86	81	93	88
10	78	89	94	102	115	86	81	95	90
12	78	90	95	103	116	86		96	90

Table 2.6: Summary of passive pressure-diameter curves for mouse lymphatic vessels from Joshua Scallan, School of Medicine, University of Missouri.

Rat	11912	20212	20612	20912a	20912b	21312a	21312b	21412	22012	22212
Pressure	**Diameter (μm)**									
0.5		116	110	133	123	114	89	115	122	125
1	168									
2	188	159	129	174	172	163	174	154	148	165
4	199	167	134							
6	204	169	136	183	182	178	184	165	154	176
8	208	170	138	185	185	181	185	168	156	178
12	211	170	140	186	186	187	186	169	159	180
14	214	172	141	186	186	189	187	170	160	182

Table 2.7: Summary of passive pressure-diameter curves for rat lymphatic vessels from Joshua Scallan, School of Medicine, University of Missouri.

2.2.2.2 Fibre Angles For Holzapfel-Gasser-Ogden Strain Energy Function

The HGO SEF required the angle of the collagen fibres as a model input. The data from Arkill et al. [2010] was used to find an approximate value for the fibre angle, a necessary input for the HGO SEF. Arkill et al. [2010] take 180° as being parallel to the longitudinal direction of the vessel. However, it is more useful to know the angle from the circumferential direction for use with the HGO SEF, see section 2.1.8. This was calculated as $\beta = 90° - |180° - \alpha|$, where α is the angle taken from the graphs in figure 2.2 using DataThief software (downloaded from http://datathief.softpedia.com/). The mean and standard deviation of β at different pressures and tensions are summarised in table 2.8.

Vessel	**Mean β (degrees)**	**Standard Deviation (degrees)**
0 Pa Transmural pressure, no tension	55	21
0 Pa Transmural pressure, with tension	85	6
1500 Pa Transmural pressure, with tension	60	16
3000 Pa Transmural pressure, with tension	63	12

Table 2.8: Table of mean values of collagen fibre angles as measured by Arkill et al. [2010]. The data was obtained from figure 2.2 using DataThief.

Arkill et al. [2010] show that the fibre angle changes as the pressure increases. A linear function was fitted to the normalised pressure to mean fibre angle shown in

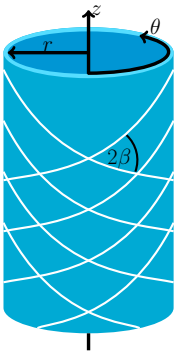

Figure 2.8: Diagram to show angle β. The white lines represent the collagen fibres. The black z-axis corresponds to 180° as measured by Arkill et al. [2010].

table 2.8 using data from Arkill et al. [2010], see figure 2.9. Therefore, β is set equal

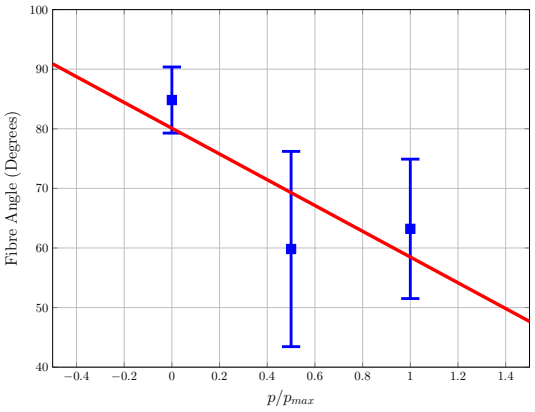

Figure 2.9: Fibre angle vs normalised pressure. The blue squares represent the mean and the error bars the standard deviation. The red line represents the linear fit to the data

to this function,

$$\beta = -21.61\frac{p}{p_{max}} - 80.09. \tag{2.51}$$

The fibre angles in mouse mesenteric lymphatics have not been measured. Therefore it is assumed that mean fibre angles estimated from Arkill et al. [2010] are consistent across all species. Two cases will be considered. In the first case the fibre angle will be assumed constant, as in Holzapfel et al. [2000]. The constant fibre angle is assumed to be $\beta = 60°$, the value of the mean fibre angle for 1500 Pa from table 2.8. This is the value of the fibre angle at higher pressures, which is when the collagen fibres take the strain. In the second case, a variable fibre angle will be considered using a linear fit to relate the fibre angle to the pressure, i.e. as the pressure increases, β decreases.

2.2.3 Strain Energy Functions in COMSOL Multiphysics

In the previous section 2.1.7, a SEF was reviewed. In this section, the implementation of the SEF in COMSOL Multiphysics is presented.

COMSOL Multiphysics has many inbuilt SEFs, however the SEF by Holzapfel et al. [2000] is not one of them. An example where the HGO SEF has been implemented in COMSOL is available on COMSOL Multiphysics website[1]. The model presented here is based on this example. To input the HGO SEF into COMSOL Multiphysics, I_4 and I_6 had to be included as variables. This was done by creating variables for each component of the vectors that define the direction of the collagen fibres, equation (2.16). A second set of variables was created to define I_4 and I_6 and each component of the strain energy function. The parameters c (kPa), k_1 (kPa), k_2S (no units) and E (kPa) and ν (no units) from equation (2.43) had to be defined.

The parameters listed above are necessary to define the material properties of the lymphatic vessel and valve. It is unknown what values these parameters should take for the material model to reproduce the behaviour of passive collecting lymphatic vessels in experiments. In order to find suitable parameters an iterative algorithm called Kriging, which is presented later in subsection 2.2.5, is used to optimise these parameters so that model behaviour reflects the experimental data in tables 2.6 and 2.7. This algorithm interpolates known function values to estimate other optimal parameters sets. It requires the model to be run many times, so to lower the computational time necessary for this process a 2D dimensional axisymmetric model of the vessel wall was built in COMSOL Multiphysics.

2.2.4 2D Finite Element Wall Model

The vessel wall is modelled as a rectangle in a two dimensional axisymmetric model, see figure 2.10a. The solution can then be rotated to form a full cylinder. This makes the model inexpensive to compute, even with a fine mesh. The number of mesh elements depends on the wall thickness. The width of the rectangle had a minimum of 4 elements across it for all models. The total number of elements ranged from 1218 to 5058.

The internal diameter of the vessel was not measured experimentally at intraluminal pressure 0 cmH_2O, which is the gauge pressure. It is unknown what diameter the stress free vessel has. This information in needed for the initial condition of the model. Therefore the initial diameter D_0 (μm) was included as an unknown parameter for the model. β is assumed to be 60 degrees for the fixed fibre angle model and equal to equation (2.51) for the variable fibre angle model. The Poisson's ratio ν is assumed

[1] `http://www.comsol.com/model/arterial-wall-mechanics-14499`

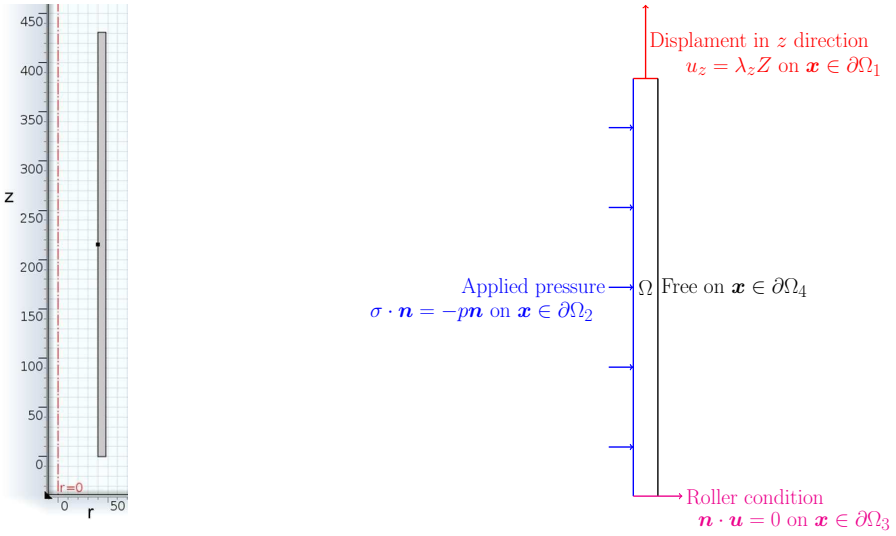

(a) 2D model geometry used for Kriging procedure to find parameters.

(b) Sketch of model to show boundary conditions. Not to scale.

Figure 2.10: 2D finite element model for use in Kriging

to be 0.2. There were a total of five unknown parameters for the model: c (kPa), $K = k_1/k_2$ (kPa), k (no units), E (kPa) and D_0 (μm). Several factors are neglected in the model: growth, inertial forces, gravity and external pressure.

The equations for the force balance are,

$$-\boldsymbol{\nabla} \cdot \boldsymbol{\sigma} = \boldsymbol{F}_v, \tag{2.52}$$

where $\boldsymbol{\sigma}$ is the stress tensor and $\boldsymbol{F}_v$ is the volume force vector. $\boldsymbol{\sigma}$ is related to the second Piola-Kirchhoff stress, S, by

$$\boldsymbol{\sigma} = J^{-1}\boldsymbol{U}\boldsymbol{S}\boldsymbol{U}^T, \tag{2.53}$$

where $\boldsymbol{U}$ is the deformation gradient given by,

$$\boldsymbol{U} = \nabla \boldsymbol{u} + \boldsymbol{I}, \tag{2.54}$$

with $\boldsymbol{u}$ the displacement gradient and $\boldsymbol{I}$ the identity matrix. The volume ratio between the initial and current configuration is

$$J = \det(\boldsymbol{U}). \tag{2.55}$$

The second Piola-Kirchhoff stress is related to the SEF by differentiating by the strains

$$\boldsymbol{S} = \frac{\partial W}{\partial \epsilon}, \tag{2.56}$$

where W is the SEF, equation (2.43), and the strains are related to the deformation gradient by

$$\epsilon = \frac{1}{2}\left(\boldsymbol{F}^T\boldsymbol{F} - \boldsymbol{I}\right). \tag{2.57}$$

Assuming that the same coordinates are used for the original and the deformed body and that the frame of reference for the deformed body can be contorted so that the coordinates of a particle have the same coordinates both in the original and deformed configurations, then Green's strain tensor is equal to the Cauchy strain tensor, ϵ.

2.2.4.1 Boundary Conditions

We applied a prescribed displacement boundary condition to the top end of the rectangle, see figure 2.10b. This resulted in elongation of the wall by a third, which was approximately the amount the vessels were displaced by when straightened before the experiments and stretch the vessel to its *in vivo* length [Scallan, personal communication], i.e. the following equation was applied,

$$u_z = \lambda_z Z \quad \text{on} \quad \boldsymbol{x} \in \partial\Omega_1, \tag{2.58}$$

where u_z is the component of $\boldsymbol{u}$ in the z direction, λ_z is the amount of axial stretch, in our case $\lambda_z = 1.3$, and Z is the material coordinate, i.e. the coordinate in the z direction given by the initial configuration. A boundary load was applied to the inner boundary of the rectangle.

$$\boldsymbol{\sigma}\cdot\boldsymbol{n} = -p\boldsymbol{n} \quad \text{on} \quad \boldsymbol{x} \in \partial\Omega_2, \tag{2.59}$$

where $\boldsymbol{n}$ is the vector in the normal direction to the boundary, outwards of the domain, and p is the pressure applied to the boundary. The values for p were the values of the fluid pressure at which the diameter of the vessel was measured in experiments. A roller boundary condition is applied to the base of the rectangle, which prevents movement in the normal direction, but allows movement in the radial direction.

$$\boldsymbol{n}\cdot\boldsymbol{u} = \boldsymbol{0} \quad \text{on} \quad \boldsymbol{x} \in \partial\Omega_3. \tag{2.60}$$

The external boundary is not constrained, i.e. stress free.

For the 2D model, COMSOL completed it's calculations in approximately 10 to 90 seconds depending on the parameter values. This was much quicker than running a 3D model but still resulted in the same pressure-diameter behaviour. Therefore this model could be used in the Kriging algorithm, which is described in the next subsection 2.2.5, to estimate the material properties.

2.2.5 Parameter Optimisation Using Kriging

Kriging is an iterative method from geostatistics [Krige, 1951]. Known function values are interpolated to estimate the optimal parameter set that fits the model to the observed data. Kriging is used to find the parameters for the HGO SEF with constant fibre angle for an artery using experimental data published in Zulliger et al. [2004] to evaluate how well it works, what the impact of including the compressible term is and to find parameters for the HGO SEF with constant and variable fibre angles for the experimental data summarised in tables 2.6 and 2.7. In this section, the general Kriging algorithm will be described, followed by the procedure used for finding the parameters.

2.2.5.1 Kriging Algorithm

The Kriging algorithm uses surrogate modelling, a model created to attempt to fill the gaps within a data set, e.g. curve fitting, to estimate the value the model will have for given parameters, based on the results from running the model for the random parameters that make up a vector of random points or a Latin hypercube. A Latin hypercube is a way of generating random initial points in a multidimensional parameter space. The algorithm for doing this aims to create a Latin hypercube that best fulfils the maximin criteria, i.e. the process where the minimum distance between any two points is maximised [Morris and Mitchell, 1995]. The model is evaluated for each of these parameter sets and the error calculated.

Next, the negative natural logarithm is minimised by searching for the minimum using a genetic algorithm. A genetic algorithm begins with an initial population of possible solutions each resulting in an objective function value, or error value in this case. The parameters sets that result in these solutions are encoded as binary strings. Three operations are then carried out. Firstly, reproduction. The strings are copied with respect to their objective function value, e.g. strings that represent the parameter sets that give smaller error values are more likely to be copied than strings with higher error values. These copied strings create a new population. Secondly, crossover takes place. The strings in the new population are divided into pairs at random. Then, for each pair a random integer position, i, along the string is selected. The characters in the two strings in the position $i + 1$ to the end are swapped creating two new strings. Finally, mutation occurs. Occasional changes of the newly created binary strings are made at random, i.e. change a 0 to a 1. This takes place relatively infrequently (1 in 1000 chance of a mutation occurring). These new strings can be decoded to form parameters sets that can be evaluated [Goldberg, 1989].

The genetic algorithm is implemented to estimate the possible parameter combination that would result in the lowest error based on the points that have already been

calculated. This parameter combination is then input into the model and the result is computed to find the actual value of the error. The process is repeated until the convergence criteria are met, i.e. the value of the error falls below a threshold, or a set number of iterations are reached for which there has been no change of the minimum value. This means that the parameter values tested are more likely to give better results rather than randomly choosing parameters to test. This reduces the number of times the full model has to be run.

2.2.5.2 Kriging Procedure

A function was written in MATLAB that ran the model and then calculated the error between the model results and the experimental data. Different error terms were used. For the artery data from Zulliger et al. [2004], the force in the axial direction is calculated as

$$F_z = \int_{r_i}^{r_o} \sigma_z 2\pi r \mathrm{d}r - P\pi r_i^2, \tag{2.61}$$

where r_o mm is the outer radius, r_i mm is the inner radius, σ_z Pa is the stress in the axial direction, r mm is the radius, P is the intraluminal pressure. The error, F_{zul}, was calculated as

$$F_{zul} = \frac{1}{2}\frac{1}{MN}\left(\frac{\sum_{i,j}^{M,N}\left(r_{ij}-\overline{r}_{ij}\right)^2}{r_{MN}^2} + \frac{\sum_{i,j}^{M,N}\left(f_{ij}-\overline{f}_{ij}\right)^2}{f_{MN}^2}\right), \tag{2.62}$$

where M is the number of different pressures, N is the number of axial stretchs, r_{ij} and f_{ij} are the experimental radii and forces measured and $\overline{r}_{ij}$ and $\overline{f}_{ij}$ are the model equivalents. For the mean of the mouse lymphatic pressure diameter data the error was calculated as

$$F_m = \sum_{i=1}^{n} \frac{\left(X_i^m - \overline{X}_i^m\right)^2}{nS_i^2}, \tag{2.63}$$

where X_i^m are mean experimental results, $\overline{X}_i^m$ are the model results, n is the number of data points and S_i is the standard deviation of the diameter change for each data point. For the individual mouse and rat pressure diameter data the error was calculated as

$$F_i = \frac{\sum_{i=1}^{n}\left(X_i - \overline{X}_i\right)^2}{nX_n^2}. \tag{2.64}$$

where X_i are the experimental results, $\overline{X}_i$ are the model results, n is the number of data points and X_n is the maximum experimental diameter value. The Kriging procedure was implemented in order to minimise the error. For the mean experiments the stop condition was that all the model results were within one standard deviation of diameter changes to the mean. For the individual experiment, the stop condition was when the error, i.e., F_i in equation (2.64), was less than 1×10^{-4}.

The Kriging procedure used here is an algorithm implemented in MATLAB using code based on the scripts published in Forrester et al. [2008]. For the artery data the following procedure was used:

1. Assign upper and lower bounds.
2. Run the Kriging algorithm for all parameters.
3. If the error, F_{zul} from equation (2.64), is above the defined error threshold the bounds are adjusted.
4. Steps 2 and 3 are repeated until the error, F_{zul}, is below the threshold.

The bounds were estimated based on the values presented in Zulliger et al. [2004].

For the lymphatic mouse data it was difficult to define appropriate parameter bounds. Therefore, a different procedure was implemented for the mean mouse data, the first lymphatic data used:

1. Set parameters are set to $K, k = 0$, m and D_0 as best guesses and the number of points in the Latin hypercube to 10.
2. Find the value for c which results in the best match for the first three points (diameters corresponding to 0.5, 1 and 2 $\mathrm{cmH_2O}$).
3. Hold c fixed to the value found in step 2, run Kriging to find good approximations of K and k
4. Hold K and k fixed to the values found in step 3, run Kriging to find good approximations of c and D_0.
5. Hold c, K, k and D_0 fixed, run Kriging to find good approximation of E.
6. Run the Kriging algorithm for all five parameters simultaneously with 20 points in the Latin hypercube. The bounds are set to 10% above and below the values found in steps 2 to 5.
7. Check to see if any of the best values for the parameters minimise to a limit. If necessary adjust the bounds and repeat the Kriging algorithm.
8. Repeat step 7 until stop condition reached.

The idea of the steps 2 to 5 are intended to get the variables into the right ball park before trying to find all the parameters together. This is done to help speed up the process because the bounds on the parameter values are not certain. Otherwise the initial bounds would need to be quite large, more points would be required in the Latin hypercube and more iterations would be needed.

For the individual lymph vessel data, the same procedure was used as for the artery data with bounds based on the parameter values from fitting the average data and the error value F_i. The Kriging procedure used was the same for both the constant and variable fibre angle, however it was more difficult to fit the data well using the variable fibre angle. The error threshold was 1×10^{-4} for the constant fibre angle and 1×10^{-3} for the variable fibre angle for both rats and mice. The results of all the fittings are shown in section 2.3.

2.3 Results

In this section the results from the parameter fitting using the methods described above will be presented. The parameters found are compared to the literature values.

2.3.1 Artery Data

Using the kriging procedure to find all the parameters resulted in good fits for the Zulliger et al. [2004] data, see figure 2.11. The initial diameter was set to 860 mm. The parameters found were $c = 55$ kPa, $k_1 = 1.74 \times 10^{-3}$, $k_2 = 33.8$ and $E = 173.52$ kPa. The pressure-radius curves do not have such a well defined S shape as the Zulliger et al. [2004] fits in figure 2.7, but still fit the data well. The pressure-force curves also show a good fit, in particular for 130% axial stretch the fit is better than the Zulliger et al. [2004] model. This shows the algorithm and procedures described above are effective for optimising the parameters to the experimental data.

Comparing the parameters found using the Kriging algorithm to those found by Zulliger et al. [2004], shown in table 2.3, show that the value of c is the same order of magnitude, where as k_1 is two orders of magnitude smaller and k_2 is two orders of magnitude larger than the corresponding values found by Zulliger et al. [2004].

2.3.2 Lymphatic Data with Constant Fibre Angle

Figure 2.12 compares how the fibres are arranged at the lowest internal pressure for the mouse vessels, 0.5 cmH_2O, to how they are arranged at an internal pressure of 12 cmH_2O. In both images the fibre angle is the same for the constant fibre angle case.

Figure 2.13 shows that the model is able to achieve a good match with the mean experimental data, equation (2.63) gave an error of $F_m = 1.48$. Initially it was difficult to estimate the bounds for parameter values for K and E. For the parameter optimisation for the mean data, equation (2.64) gave an error of $F_i = 2.98 \times 10^{-4}$. Therefore the error threshold, i.e. the maximum value for the error, for the individuals

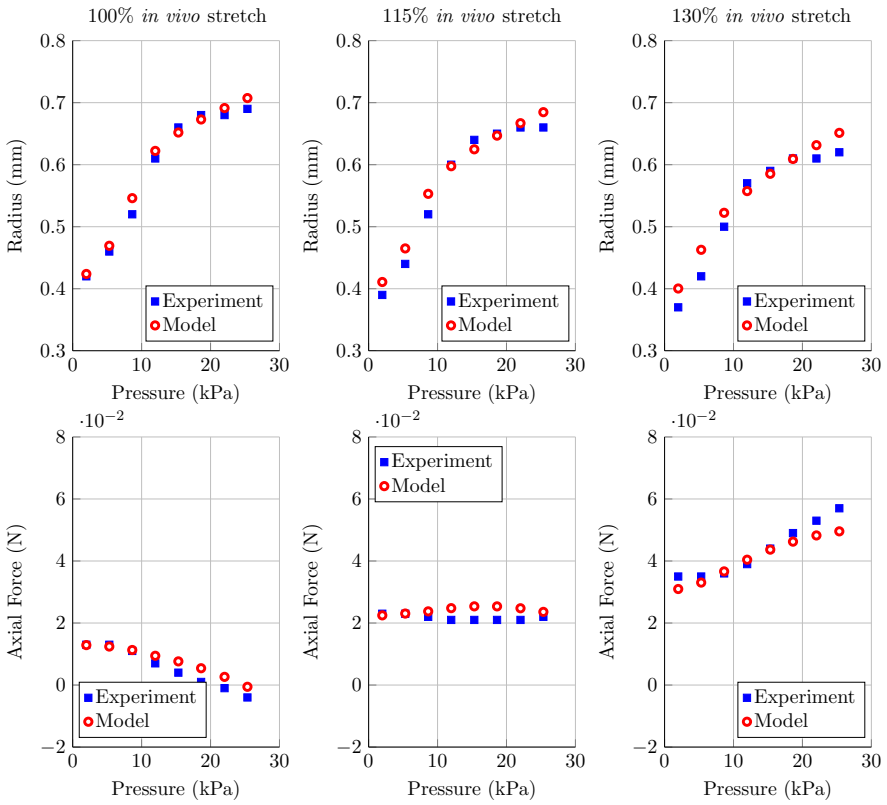

Figure 2.11: Comparison of model and experimental data from using parameters found by kriging procedure.

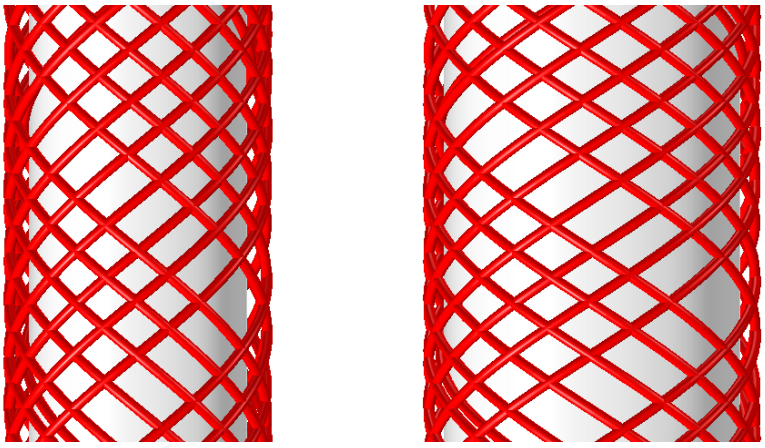

(a) Internal pressure 0.5 cmH_2O (b) Internal pressure 12 cmH_2O

Figure 2.12: Constant fibre angle at two different internal pressures.

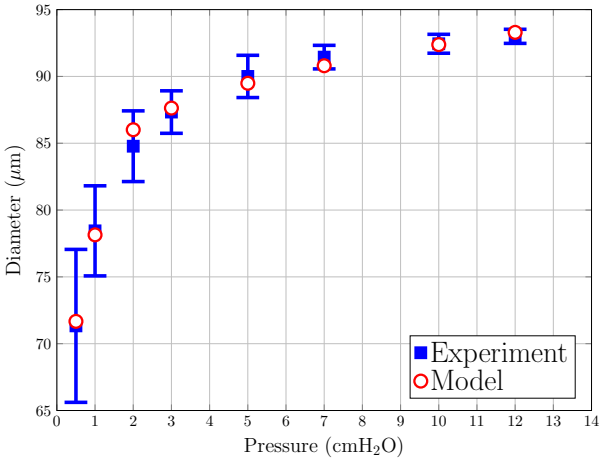

Figure 2.13: Comparison of model to mean difference experiments using Holzapfel et al. [2000] SEF. Parameter values: $c = 0.8334$ kPa, $k_1 = 2.505 \times 10^{-17}$, $k_2 = 115.6$, $m = 82.93$ kPa, $D_{int} = 76.31$ μm.

was set to 1×10^{-4}. Table 2.9 shows the values of the parameters used for the mean and each of the vessels. Figure 2.14 shows each of the vessels individually.

	c (kPa)	k_1 (kPa)	k_2	E (kPa)	D_0 (μm)
Mean Data	0.8334	2.505×10^{-17}	115.6	597.1	76.31
Mouse a	1.341	1.464×10^{-19}	146.0	7152	70.64
Mouse b	0.5736	1.115×10^{-19}	111.4	721.1	69.0
Mouse c	1.469	5.49×10^{-17}	109.5	3744	80.13
Mouse d	1.25	6.298×10^{-15}	94.81	3335	85.0
Mouse e	1.484	2.981×10^{-16}	119.2	3272	102.6
Mouse f	0.9509	4.293×10^{-17}	132.0	36010	80.44
Mouse g	0.8750	6.001×10^{-13}	93.76	11620	72.19
Mouse h	0.950	1.021×10^{-13}	90.68	625.5	77.54
Mouse i	0.3541	4.6553×10^{-3}	7.360	295.4	49.16
Rat a	0.8182	8.740×10^{-15}	87.40	360.1	160
Rat b	0.8350	8.336×10^{-19}	85.50	2025	121.9
Rat c	0.5566	5.591×10^{-14}	91.58	509.0	113.40
Rat d	0.7637	5.239×10^{-13}	69.85	1837	141.7
Rat e	0.6111	1.711×10^{-14}	59.18	697.5	125.1
Rat f	0.6725	9.567×10^{-14}	56.25	288.0	120.0
Rat g	0.7149	8.779×10^{-14}	25.82	3387	97.50
Rat h	0.9917	6.064×10^{-13}	61.67	1754	123.7
Rat i	0.6813	5.871×10^{-13}	77	1382	125.6
Rat j	0.8562	2.261×10^{-13}	67	2637	133.1

Table 2.9: Table of parameter values found by the data fitting procedure described in section 2.2.5 for constant fibre angle.

The values of c for mice and rat lymphatic vessels are similar to the c values found by Sokolis [2013] for porcine veins, but most of the other values are very different. In particular the majority of the values found for k_1 is more than 10 orders of magnitude smaller than the literature values. This corresponds to larger values of k_2. The values found for the Young's modulus E are three orders of magnitude larger than the values found for lymphatics in the literature.

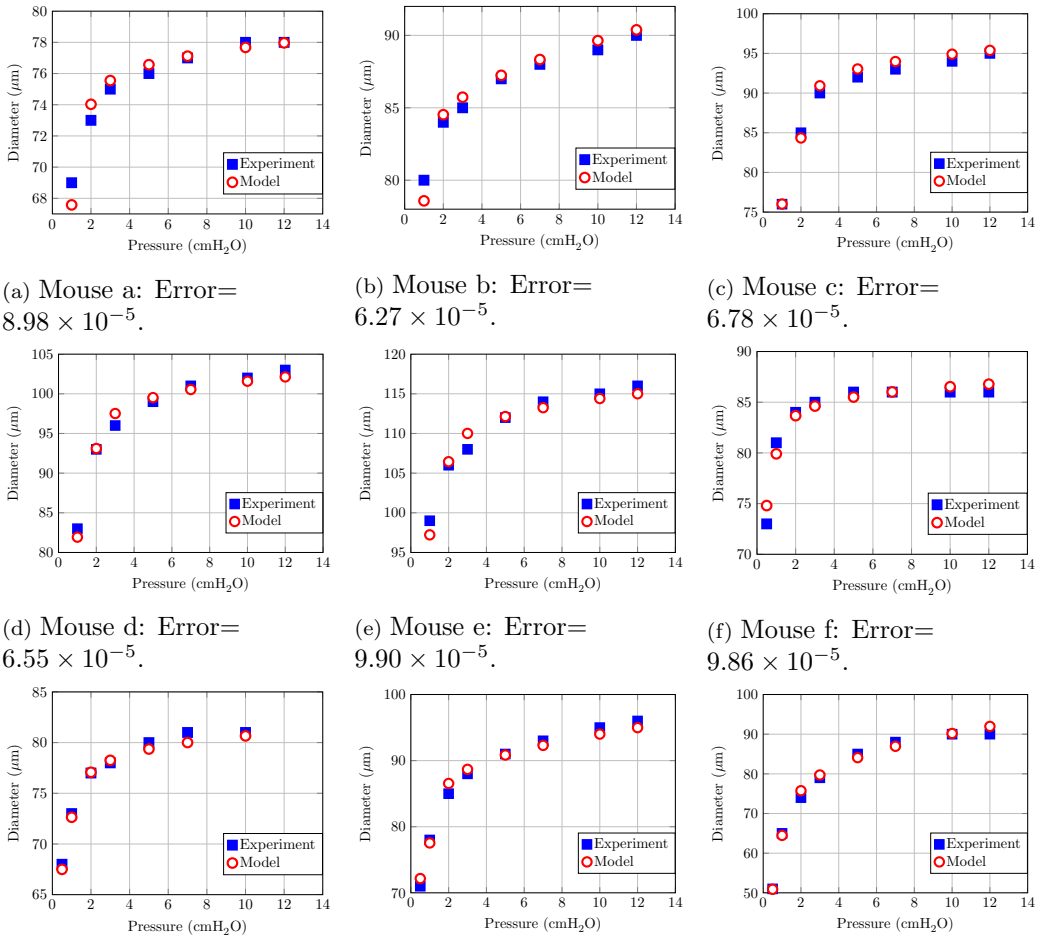

(a) Mouse a: Error= 8.98×10^{-5}.

(b) Mouse b: Error= 6.27×10^{-5}.

(c) Mouse c: Error= 6.78×10^{-5}.

(d) Mouse d: Error= 6.55×10^{-5}.

(e) Mouse e: Error= 9.90×10^{-5}.

(f) Mouse f: Error= 9.86×10^{-5}.

(g) Mouse g: Error= 4.26×10^{-5}.

(h) Mouse h: Error= 9.38×10^{-5}.

(i) Mouse i: Error= 1.49×10^{-4}.

Figure 2.14: Comparison of individual experiments and corresponding models for mouse lymphatics. Experimental data provided by Joshua Scallan.

2.3.3 Lymphatic Data with Variable Fibre Angle

Figure 2.16 shows that the fibre orientations for the variable fibre angle case are different at 0.5 cmH_2O and 12 cmH_2O. At the lower pressure the fibres run along the length of the vessel. At the higher pressure the fibres have turned and become more spread out.

The parameter values for the variable fibre angle are shown in table 2.10 and the result for each vessel in figures 2.17 and 2.18. Although some of the values for k_1 are two orders of magnitude and k_2 are one order of magnitude higher, in general the values of k_1 and k_2 for the variable fibre angle are more similar to the values found in the literature than the values for the constant fibre angle. The values found for the Young's modulus are within the range presented for lymphatic vessels in the literature.

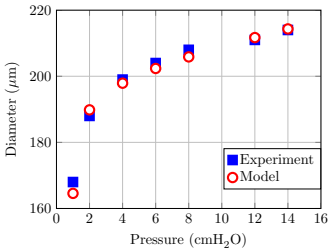

(a) Rat a: Error= 7.57×10^{-5}.

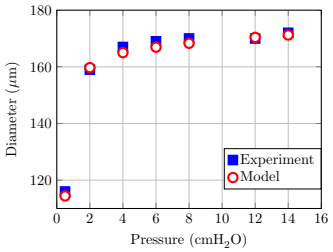

(b) Rat b: Error= 7.15×10^{-5}.

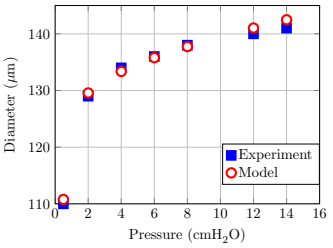

(c) Rat c: Error= 3.37×10^{-5}.

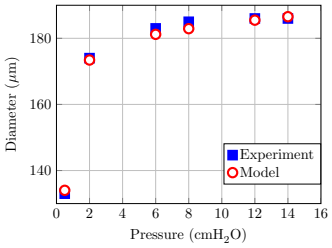

(d) Rat d: Error= 4.56×10^{-5}.

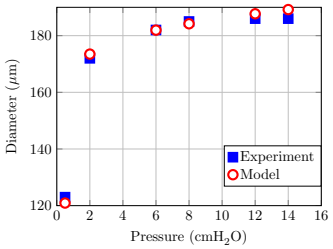

(e) Rat e: Error= 9.84×10^{-5}.

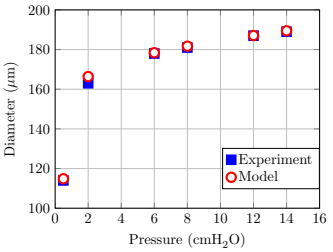

(f) Rat f: Error= 6.06×10^{-5}.

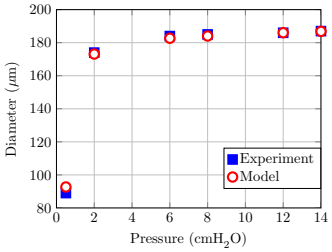

(g) Rat g: Error= 8.21×10^{-5}.

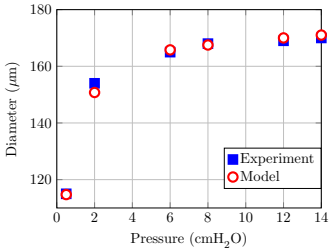

(h) Rat h: Error= 7.81×10^{-5}.

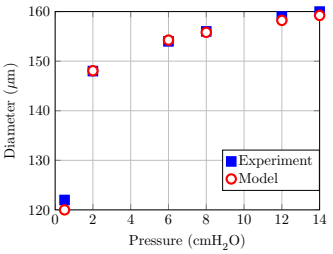

(i) Rat i: Error= 3.44×10^{-5}.

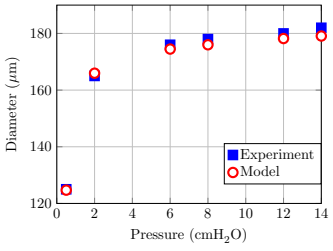

(j) Rat j: Error= 9.60×10^{-5}.

Figure 2.15: Comparison of individual experiments and corresponding models for rat lymphatics. Experimental data provided by Joshua Scallan.

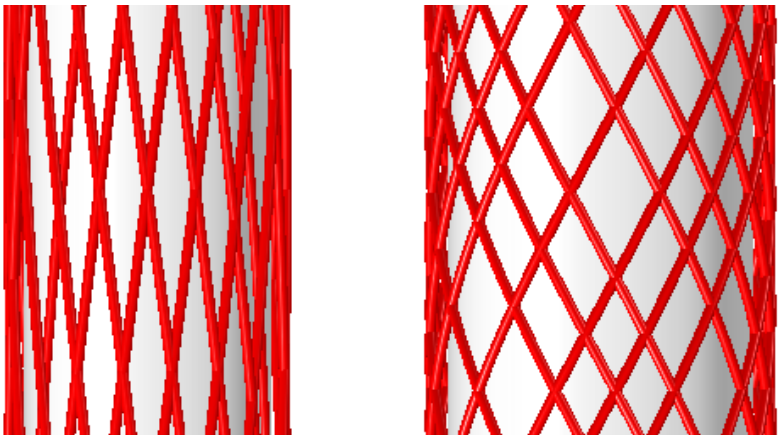

(a) Internal pressure 0.5 cmH_2O (b) Internal pressure 12 cmH_2O

Figure 2.16: Variable fibre angle at two different internal pressures.

	c (kPa)	k_1 (kPa)	k_2	E (kPa)	D_0 (μm)
Mean Mouse	0.5203	13.441	2.8248	17.799	88.837
Mouse a	0.5440	16.816	3.0744	17.800	79.954
Mouse b	0.4989	14.423	3.2445	18.912	93.036
Mouse c	0.4795	12.634	2.9109	17.772	90.399
Mouse d	0.4597	12.244	3.1852	17.016	97.723
Mouse e	0.5155	14.541	3.2613	16.252	108.89
Mouse f	0.5043	16.805	3.0222	17.645	91.291
Mouse g	0.5409	15.830	3.0748	17.571	81.931
Mouse h	0.4171	12.626	3.6093	15.366	88.488
Mouse i	0.1980	4.3253	2.2164	19.266	84.959
Mean Rat	0.2732	1180.4	62.237	7.8801	165.4
Rat a	0.5439	13.045	2.7387	18.536	195.0
Rat b	0.3969	11.526	2.8083	15.853	161.2
Rat c	0.4329	12.270	2.5701	17.864	140.0
Rat d	0.3796	11.879	3.2959	16.048	181.0
Rat e	0.2955	9.8824	3.6086	15.367	186.5
Rat f	0.2147	135.50	25.500	8.3020	174.7
Rat g	0.1658	289.88	34.125	7.6810	171.9
Rat h	0.3000	410.41	27.928	8.3172	160.0
Rat i	0.2544	249.07	25.051	10.544	188.0
Rat j	0.3548	33.394	2.9881	11.876	173.1

Table 2.10: Table of parameter values based on the data fitting using a variable fibre angle.

2.3.4 Summary

The results have shown that it is possible to use the strain energy function from Holzapfel et al. [2000] to create a model of a collecting lymphatic wall that has the same passive pressure-diameter behaviour as seen in experiments. The procedure described in section 2.2.5 was shown to be an effective method for finding optimised parameters. Optimising the model to the artery data from Zulliger et al. [2004] showed that the HGO SEF can also reproduce the pressure-force data. Some of the parameters found for the SEF were very different to those reported in the literature.

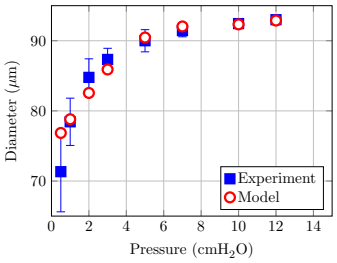

(a) Mean, Error=5.52×10^{-4}

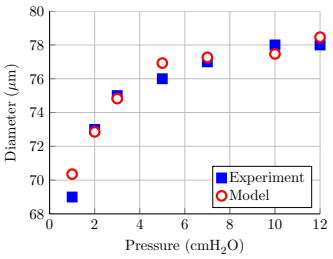

(b) Mouse a: Error=0.78×10^{-4}

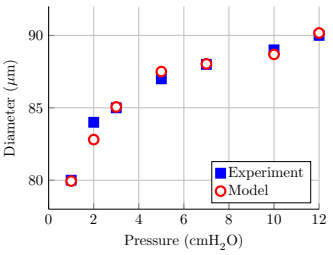

(c) Mouse b: Error=0.32×10^{-4}

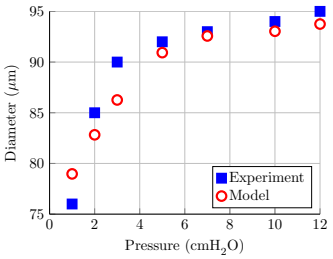

(d) Mouse c: Error=4.96×10^{-4}

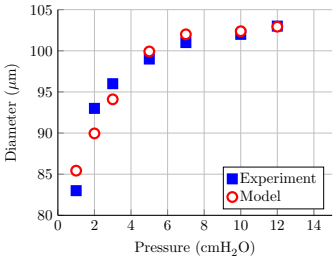

(e) Mouse d: Error=2.80×10^{-4}

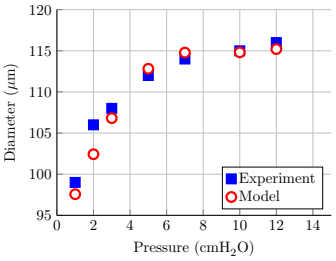

(f) Mouse e: Error=1.93×10^{-4}

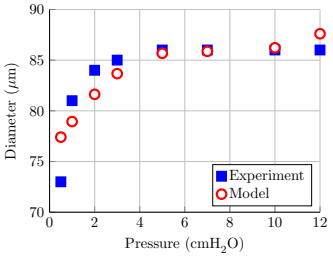

(g) Mouse f: Error=5.71×10^{-4}

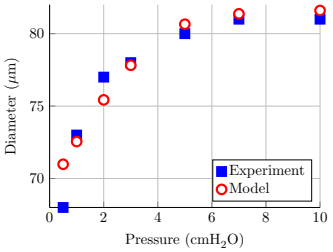

(h) Mouse g: Error=2.73×10^{-4}

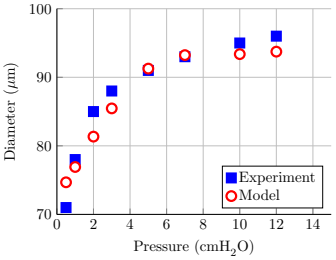

(i) Mouse h: Error=5.75×10^{-4}

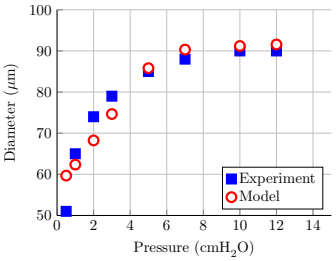

(j) Mouse i: Error=22.29×10^{-4}

Figure 2.17: Comparison of individual experiments and corresponding variable fibre models for mouse lymphatics. Experimental data provided by Joshua Scallan

2.4 Discussion

In this chapter a 2D finite element model was created in COMSOL Multiphysics. A Kriging algorithm was implemented in MATLAB and the COMSOL with MATLAB LiveLink application was utilised to use the Kriging algorithm to optimise the parameters for the HGO SEF so that the finite element model demonstrated the same

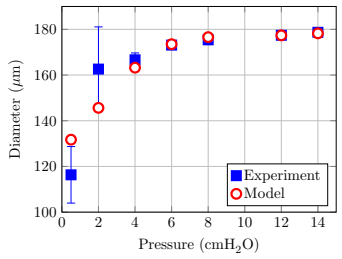

(a) Mean, Error=2.41×10^{-3}

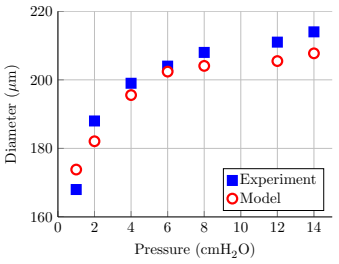

(b) Rat a: Error=0.53×10^{-3}

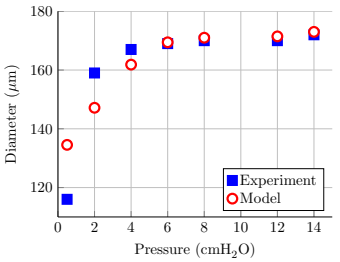

(c) Rat b: Error=2.49×10^{-3}

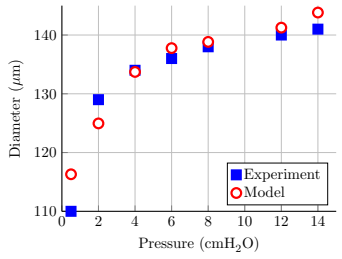

(d) Rat c: Error=0.50×10^{-3}

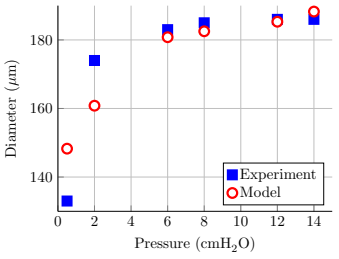

(e) Rat d: Error=2.04×10^{-3}

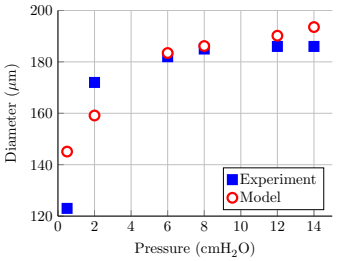

(f) Rat e: Error=2.13×10^{-3}

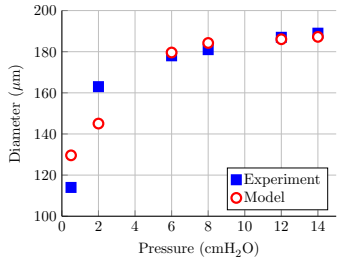

(g) Rat f: Error=2.72×10^{-3}

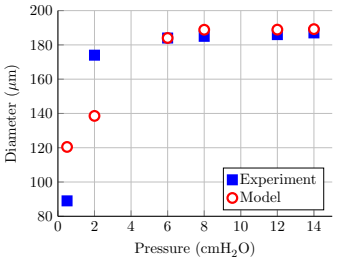

(h) Rat g: Error=10.83×10^{-3}

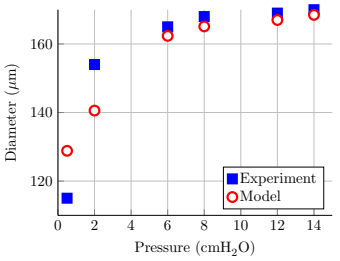

(i) Rat h: Error=2.27×10^{-3}

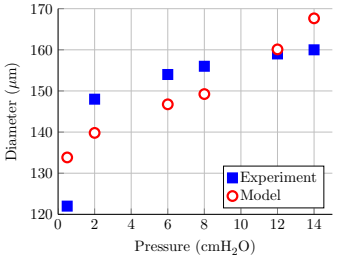

(j) Rat i: Error=2.38×10^{-3}

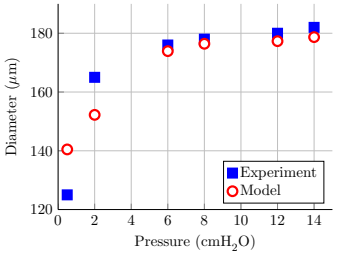

(k) Rat j: Error=2.15×10^{-3}

Figure 2.18: Comparison of individual experiments and corresponding variable fibre models for rat lymphatics. Experimental data provided by Joshua Scallan

behaviour as observed in experiments. Experimental data for rat arteries [Zulliger et al., 2004] and mouse and rat lymphatics was used.

The SEF from Holzapfel et al. [2000] was chosen as it has been widely used to model blood vessels, which exhibit similar behaviour to lymphatic vessels. It takes into account the structure of the vessel by including a term for the behaviour of the collagen fibres. This SEF was further extended by adding a term to model the compressibility of the vessel wall using a term from Doll and Schweizerhof [2000].

This SEF, equation (2.43), was parametrised using Kriging and was compared to the model fit that Zulliger et al. [2004] produced for rat arteries. It was found that they had similar values of c, but the value of k_1 was two orders of magnitude smaller and k_2 was an order of magnitude larger for the Kriging fit. The inclusion of a compressible term in the SEF lead to a better fit for the force data. The data from Zulliger et al. [2004] shows that the longitudinal tension applied to the vessel, in this case an artery, affects its pressure-diameter behaviour.

Assuming a constant fibre angle, the SEF was able to reproduce the pressure-diameter plateau like curves. The compressibility term effects the values of the parameters that are required to achieve a good match to experimental data. The parameter values found for the SEF for individual vessels show that the values vary between different lymphatic vessels as well as between different types of vessels.

Incorporating the variable fibre angle into the model made it more difficult to match the experimental data. There is clearly an important relation between the fibre angle and elastic parameters k_1 and k_2, as incorporating fibre angle in the fitting leads to values more similar to other investigations.

The values of the parameters found are compared to the values from the literature in table 2.9 and are plotted in figure 2.19. c is a stress-like material parameter, which would be equivalent to the shear modulus if consistent with linear elasticity. The values of c found for the mice and rats had the same order of magnitude as the values that Sokolis [2013] and Badel et al. [2013] found for veins. The values of c for the arteries had a higher order of magnitude. This is what we would expect since veins are more similar to collecting lymphatic vessels and arteries are more rigid than the other types of vessels.

The values of k_1 are 10 or more orders of magnitude smaller for the mouse and rat vessels than the values found in literature. This appears to have been caused by the inclusion of the compressibility term. When considering the effects of each individual parameter, it was found that k_1 dictates where the pressure-diameter curve begins to plateau and E controls the gradient of the plateau. Without E, k_1 and k_2 would be solely responsible for the plateau. This may explain why the values for the incompressible models from the literature have very different k_1 compared to the mice and rats. k_2 values for the mouse vessels are three to five times larger than the highest k_2 value found in the literature. The k_2 values for the rats are two to three times larger. This is probably in response to the much lower values of k_1 as k_1 and k_2 are closely coupled in the SEF.

The fibre rotations may be more important in lymphatics than in the arteries and veins because collecting lymphatics have thinner, more compliant walls. Due to the lower pressures within the collecting lymphatic vessels compared to the vascular system, the walls do not have to be able to support as high amounts of stress for long

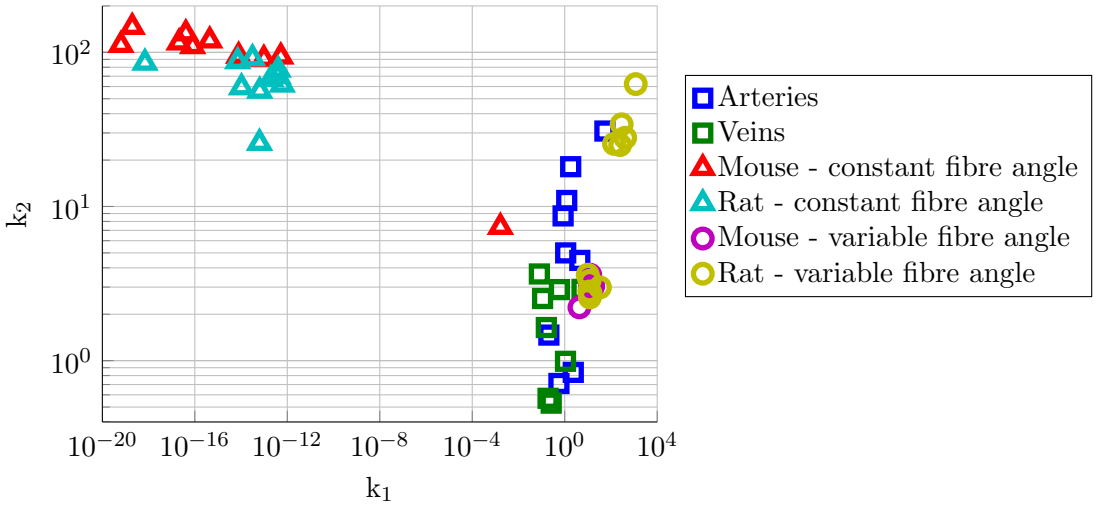

(a) k_1 vs. k_2

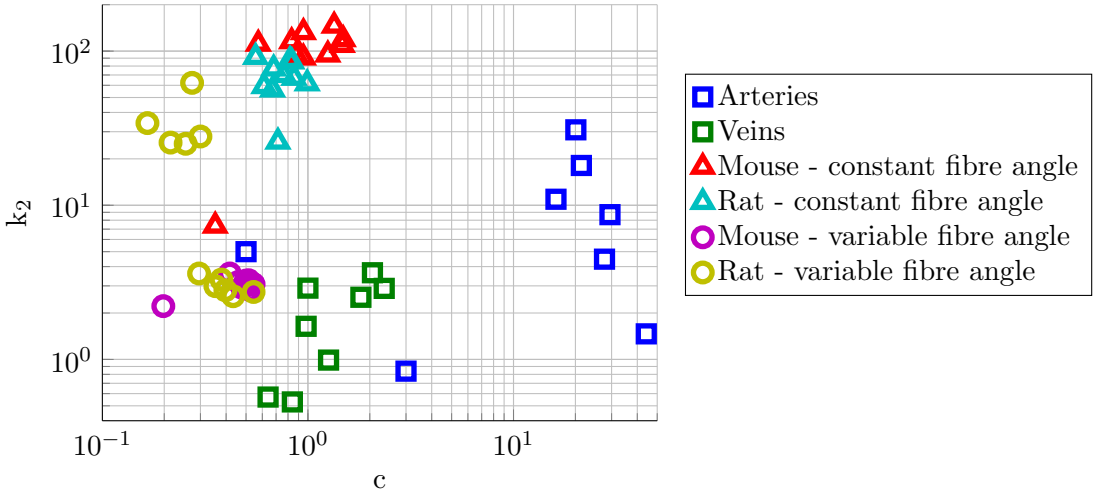

(b) c vs. k_2

Figure 2.19: Parameters found using the kriging algorithm for mouse and rat lymphatics are compared to the values presented in Holzapfel et al. [2000]; Auricchio et al. [2014]; Zulliger et al. [2004]; Cornejo et al. [2014]; Sunbuloglu et al. [2013] for arteries and in Badel et al. [2013]; Sokolis [2013] for veins.

periods of time. However, the collecting lymphatics must be able to react to increases in intraluminal pressure. The rotating fibre angles make this possible by reducing the compliance of the wall at high internal pressures. Figure 2.19a shows clearly that the values of k_1 and k_2 for the variable fibre case (circles) are much closer to the literature values (squares) than the constant fibre case (triangles). Figure 2.19b shows that the values for c for the lymphatics are more similar to veins (green squares) than arteries (blue squares).

Several authors, including Reddy et al. [1975]; Ohhashi et al. [1980] and Macdonald et al. [2008], have calculated values for the Young's modulus of the collecting lymphatic vessels, however the range of values spanned three orders of magnitude from 1200 Pa to 1.1×10^6 Pa.

From the nonlinear model developed, it is possible to determine values for Young's modulus by finding the linear limit of equation (2.24) it was found that,

$$2m = \lambda = \frac{E\nu}{(1+\nu)(1-2\nu)}. \tag{2.65}$$

Assuming $\nu = 0.2$ and a constant fibre angle of 60°, the values calculated for the Young's modulus ranged from 288 kPa to 36009 kPa. These values are too high to be biologically realistic. Assuming a fibre angle that was linearly dependent on the intraluminal pressure resulted in values for the Young's modulus of the collecting lymphatic walls between 7 kPa and 19 kPa. This range is comparatively small and is biologically realistic.

The experiments were carried out on isolated vessels, but the vessel behaviour is influenced by its surroundings, as discussed in section 2.1.3. This means that the behaviour observed in the experiments may not be an accurate representation of the behaviour *in vivo*. It is not known how much the lymphatic vessels were tensioned before the diameters were measured at the different pressures, in order to stop the vessel moving so the measurements could be more accurate. In the model of the lymphatic vessel, it is stretched by a fixed amount, i.e. 30%, as the amount the vessel was tensioned was unknown. The amount of axial stretch would change the behaviour of the values for the parameters as shown in Zulliger et al. [2004].

The parameter values found for the SEF for different vessels show that the values vary between vessels. The parameters of the SEF do not have a direct physical meaning. This means that we can use the equation to model the behaviour but we cannot use it to make any statements about the properties of the material. We have chosen to use the SEF from Holzapfel et al. [2000] as it has been widely used to model blood vessels but there maybe other SEFs that could be as successful is reproducing the behaviour from experiments. It would be useful to have more information about the directions of the fibres at different diameters, in order to incorporate this behaviour. The fibre angle affects the pliability of the lymphatic wall at higher pressures.

Using the Kriging method for the the parameter estimation technique made it possible to find parameter sets that when applied in the model reproduced the experimental behaviour. However, the method did not test the sensitivity or uniqueness of the parameters. Therefore it is possible that some parameters have very little impact of the final results or that different parameter sets could give the same results. It is possible to use sensitivity analysis to investigate the significance of each parameter. The one factor at a time method could be used, where a single parameter is changed and the others held at a baseline value. The advantages of this method is that it is obvious what effect each of the parameters have and if the model fails which parameter is responsible. However, it does not demonstate how the parameters interact when changed simultaneously. Therefore, it would be more suitable to use

a multivarite method such as the Monte Carlo method (MCM). In this method a matrix of possible parameters sets is created with repect to probability distributions, or perhaps a Latin hypercube, to ensure the whole input space is explored. The model is then run for all the parameters sets in the matrix and the output for each set recorded. A sensitivity value is calculated at the varience of the expected value of the output for all but one of the parameters. This will give the sensitivity of the output to that one parameter. A sensitivity value for multiple parameters can be calculated similarly by excluding two or more of the parameters in the calculation. This method requires the model to be run many times but takes into account the interaction between variables [Saltelli et al., 2002].

It should be noted that data from the lymphatics of different species were used to determine the geometry and boundary conditions of the model. The dimensions for the model are based on images from a mesenteric mouse lymphatic, but the pressures used are based on measurements from both excised mouse and rat mesenteric vessels. The fibre angle is based on measurements from bovine mesenteric lymphatic. It has been assumed that the relation of the fibre angles to the normalised pressure, i.e. pressure divided by the maximum pressure, is the same for all mammals.

Previous models of collecting lymphatic vessels had focus on modelling a network of lymphatics to understand the lymphatic system as a whole [Reddy et al., 1975, 1977] and short chains of lymphangions Bertram et al. [2011]. These models have shown the impact of the behaviour of the collecting lymphatic wall on the resulting fluid propulsion. This problem can be overcome by defining the movement of the lymphatic wall, but this does not allow for investigation of passive lymphatic vessels. The material model presented in chapter 2, accurately models the passive behaviour of the collecting lymphatic wall due to the intraluminal pressure. The determination of parameters for modelling vessels using a strain energy function has previously been done for arteries [Holzapfel et al., 2000; Zulliger et al., 2004; Sunbuloglu et al., 2013; Cornejo et al., 2014] and veins [Badel et al., 2013; Sokolis, 2013] but this is the first time that the parameters have been estimated for collecting lymphatics. This study differs from those for arteries and veins by allowing the vessel wall to be compressible. The material model was also extended by including a variable fibre angle, which had parameters more comparable to veins and were biologically realistic.

Future work that could be carried out to improve the model includes:

- Use sensitivity analysis to investigate the sensitivity and uniqueness of the parameters to identify which are most important for the proper functioning of lymphatic vessels.
- Gather more data to determine the relationship between the diameter of the collecting lymphatic vessels and the angle of the collagen fibres using experiments similar to those described by Arkill et al. [2010].

- Repeat the parameter optimisation for the nonlinear material model, incorporating the relationship observed.
- Consider if the parameter values are realistic and how well the behaviour of the passive collecting lymphatic wall is reproduced.
- Develop the wall model to include an active pumping phase in the wall behaviour. This should be time dependent and also dependent on fluid volume, wall shear stress and chemical transport.
- Investigate the parameter sensitivity of the pumping model.
- Compare the behaviour to pumping phases observed in experiments.

The techniques used to optimise the parameters to the data can be used for any tubular geometry with non-linear material behaviour. It could be applied to modelling the material of synthetic elastic tubing or other biological vessels. The Kriging procedure itself could be linked to any COMSOL model, not only axisymmetric models, to optimise parameters for other geometries. An application could be the investigation of materials used in micro-fluid devices to model the behaviour of small tubes under varying intraluminal pressures.

2.4.1 Summary

In this chapter, the structure and function of collecting lymphatic vessels have been reviewed. Using this information a computational 2D axisymmetric collecting lymphatic vessel wall model has been constructed with a nonlinear, compressible, material model that has been optimised to match experimental data. The optimised parameters have been compared to previous studies and potential future work has been outlined. In the next chapter 3, the collecting lymphatic valves are reviewed and a computational model of a collecting lymphatic vessel with valve is created.

Chapter 3

Modelling the Mechanical Behaviour of the Collecting Lymphatic Valve

It is now possible, from the model created and parametrised in the previous chapter 2, to replicate the behaviour of a collecting lymphatic vessel with a computational model. However, an important aspect has been ignored. The collecting lymphatic valves reduce the amount of back flow within the lymphatic system and are vital for the effective operation of the system. In this chapter, the structure and function of collecting lymphatic valves are reviewed as well as previous computational models of a variety of biological valves, i.e. heart, vein and lymphatic. The methods used for creating both 2D and 3D models of idealised collecting lymphatic valves are described. Finally, the results and conclusions drawn from these models are discussed.

3.1 Literature Review

The valves that separate the lymphangions allow stepwise pressure differences between them and reduce reverse flow [Schmid-Schönbein, 1990]. Valves with one to four leaflets have been observed in a variety of cases [Vajda and Tomcsik, 1971; Albertine et al., 1982; Gnepp and Green, 1980]. However, the bi-leaflet valve is observed most often [Lauweryns and Boussauw, 1973; Mazzoni et al., 1987; Schmid-Schönbein, 1990; Takada, 1971; Gnepp and Green, 1980; Albertine et al., 1982; Vajda and Tomcsik, 1971].

3.1.1 Structure

In this section the structure of bileaflet valves is reviewed. It is important that the construction of the idealised valve is based on the geometry observed in experiments. It is possible to infer how the valves function from the structure.

The valve leaflets are crescent shaped and attached to the wall along an arc at the base, the furthest upstream point of the valve, on opposite sides of the vessel [Vajda and Tomcsik, 1971; Mazzoni et al., 1987; Albertine et al., 1982], as shown in figure 3.1. At the downstream end of the valve the edges are free and appear wavy from end on. The leaflets are thicker at the base and thinner towards the free edge [Lauweryns and Boussauw, 1973; Albertine et al., 1982]. At either side of the vessel, the free edges of the valve leaflets meet together and join to the wall at a single point called a buttress [Gnepp and Green, 1980; Mazzoni et al., 1987; Albertine et al., 1982]. This connection to the wall makes it impossible for the valves to be reversed [Mazzoni et al., 1987; Albertine et al., 1982]. Sinuses are formed between the valve leaflets and the walls which can fill with fluid [Albertine et al., 1982; Mazzoni et al., 1987].

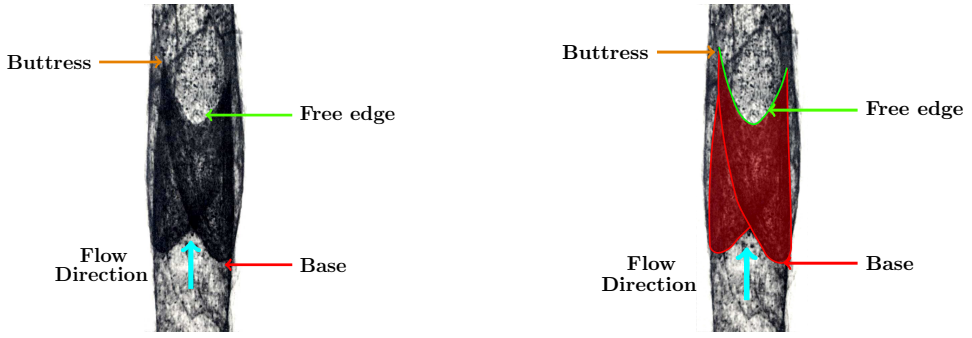

(a) Vessel with valve within.

(b) Valve leaflets highlighted with colour.

Figure 3.1: Image from Vajda and Tomcsik [1971]. Lymphatic valve showing curved base where valve connects to wall and buttresses with free edges in between. ©1971, Karger Publishers. Permission to use this figure granted by Karger Publishers.

Albertine et al. [1982] measured the distance between the buttress and base of valves in canine lymphatics. The distance of the free edge to the furthest point on the base was 400-600 μm, which was shorter than in the thoracic duct where they were about 500-1000 μm.

The leaflets consist of a layer of extracellular matrix between two single layers of endothelial cells, separated by a thin basement membrane [Lauweryns and Boussauw, 1973; Mazzoni et al., 1987; Schmid-Schönbein, 1990; Takada, 1971; Vajda and Tomcsik, 1971; Skalak et al., 1984]. Some studies have reported that the connective tissue in the valves contains mainly collagen fibres [Lauweryns and Boussauw, 1973; Takada, 1971], while others have observed elastin fibres with dense collagen fibres at the connections to the wall of the lymphatic [Vajda and Tomcsik, 1971; Rahbar

et al., 2012]. This may be due to the techniques used to image the valve leaflets or the species and location from which the lymphatic was taken [Rahbar et al., 2012]. Vajda and Tomcsik [1971] noted both collagen and elastin fibres in the leaflets of valves in larger vessels from cat mesentry, as did Rahbar et al. [2012] in rat mesenteric valves. In smaller vessels the connective tissue layer can be very thin, in some cases almost only the two endothelial layers. There is no smooth muscle in the valve leaflets [Gnepp and Green, 1980; Albertine et al., 1982; Takada, 1971].

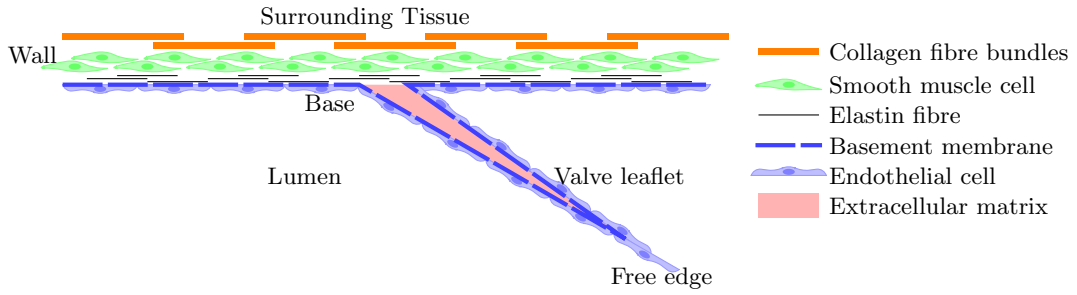

Figure 3.2: Sketch of wall and valve structure, not to scale

Lauweryns and Boussauw [1973] measured the valve leaflets in adult rabbit lungs. The thickness ranged from 0.5 μm to 6 μm. In the rabbit thoracic duct leaflets were 0.6 μm at the thinnest point and up to 7.5 μm in the thickest part. The thickness of the connective tissue layer was 0.1-5 μm. The endothelial layer had a variable thickness, near the nuclei it could be 3-4 μm thick, and in other areas about 0.3 μm thick. Cat mesenteric valve leaflets were found to have a thin endothelial layer, just 0.1 μm thick [Vajda and Tomcsik, 1971].

The structure of the collecting lymphatic valves depends on the species and their location. However, the basic shape of the most common bileaflet valves is the same, although the size can be different. It is important to construct a model geometry that is based on observations of real collecting lymphatic vessels and their valves in order for the model to yield results that can be related to vessels used in experiments. The information reviewed here is used when constructing the three-dimensional model. It is important to note that the valve itself does not contain any smooth muscles cells. This implies that the valve functions as a passive structure. This will be investigated further in the next section 3.1.2.

3.1.2 Function

From the structure of the valves, they contain no smooth muscle so must act passively, reacting to the hydrodynamic forces. When the valve is open, fluid flows between the free edges of the leaflet from one lymphangion to the next [Mazzoni et al., 1987]. Open valves should not resist forward flow [Albertine et al., 1982].

The valves operate due to pressure differences across the valve leaflets. When the pressure downstream of the valve is lower than the pressure upstream, the leaflets are open. If the pressure downstream increases and becomes higher than upstream, there is a pressure drop across the leaflets since the pressure in the sinuses is higher than the pressure between the leaflets. This causes the leaflets to move inwards until they are pushing together. This completely closes the valve and stops reverse flow. The valve opens again when the pressure drop reverses [Mazzoni et al., 1987; Schmid-Schönbein, 1990]. Mazzoni et al. [1987] also suggest that if tension is applied to the valve, possibly from the tissue around the vessel, this could also cause the valve to close. However, no literature was found where this hypothesis had been tested.

Davis et al. [2011] carried out an experiment to active study lymphatic valve behaviour during the contraction cycle. They put a lymphangion with a valve at either end between two pipettes and changed the pressure at each end, a sketch of the set up is shown in figure 3.3. They considered two cases; one where the pressure at the inlet was equal to the pressure at the outlet, 1cmH_2O, the second where the outlet pressure was increased so that it was higher than the inlet pressure.

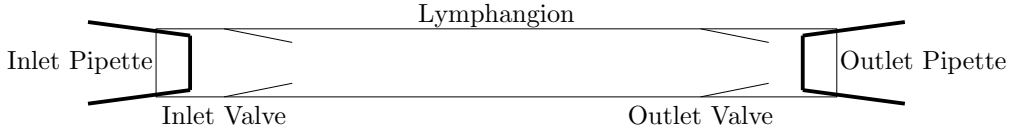

Figure 3.3: Sketch of experimental set up by Davis et al. [2011] used to investigate valve behaviour during the collecting lymphatic contraction cycle. The pressures in the pipettes were adjusted to investigate valve gating behaviour. Not to scale.

For the case with equal pressures, at the start of systole the inlet valve closed and the outlet valve remained open. The inlet valve reopened at the end of systole. The outlet valve closed as diastole began, then opened again once the pressure in the lymphangion was equal to the pressure of the pipettes [Davis et al., 2011]. Figure 3.4 shows a sketch of this process.

For the case where the outlet pressure was higher than the inlet pressure, the outlet valve was always closed and the inlet valve always open, except during systole when the outlet valve opened and the inlet valve closed [Davis et al., 2011]. This is sketched in figure 3.5. A graph showing the valve position, pressure and diameter for both cases can be seen in figure 3.6.

Davis et al. [2011] videoed a rat mesenteric lymphatic *in vivo*. The lymphocytes present in the flow made it possible to view the movement of the fluid. Frames from the video can be seen in figure 3.7. Back flow through the valve is observed at the end of diastole before the valve closes.

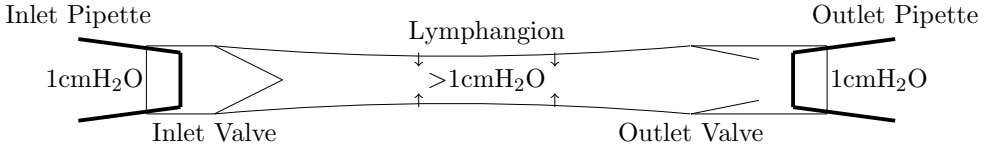

(a) During systole

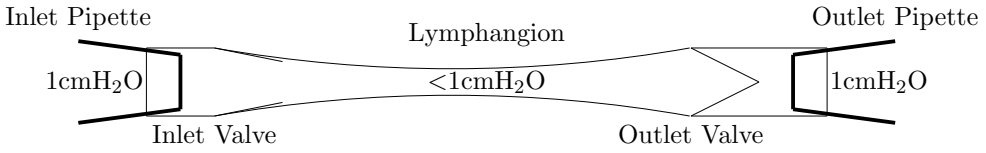

(b) End of systole, start of diastole

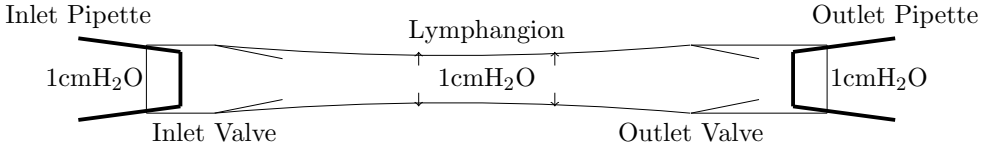

(c) Diastole when lymphangion pressure equal to pipette pressure

Figure 3.4: Sketch of valve positions during a collecting lymphatic contraction cycle for case one with inlet and outlet pressure set at 1 cmH_2O.

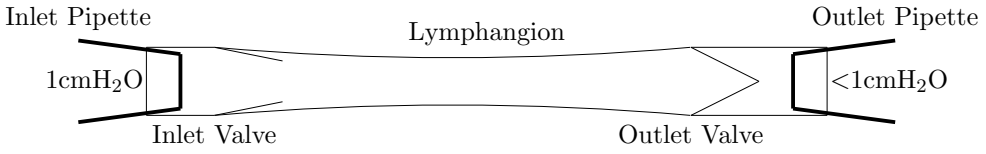

(a) At all times, except systole

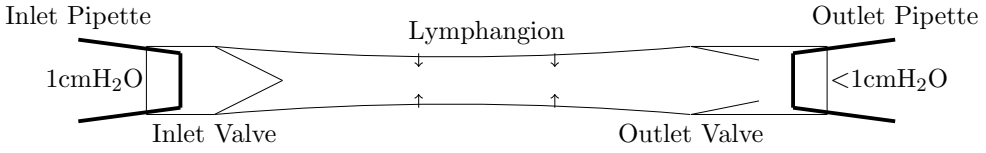

(b) During systole

Figure 3.5: Sketch of valve positions during a collecting lymphatic contraction cycle for case two with outlet pressure higher than inlet pressure.

Valves that are deformed can be ineffective at preventing reverse flow. Figure 1.5 compares deformed and healthy valves. The deformed leaflets are much shorter than the healthy ones. They are unable to press against one another in order to close the valve and, therefore, cannot resist reverse flow. This reduces how much fluid can be removed from the tissue and leads to lymphoedema [Bazigou et al., 2009].

There is very little information in the literature about the pressure at which collecting lymphatic valves close and open. The majority of the information we have about how valves act when the vessel is passive and active is from Davis et al. [2011]. This information is important for validating whether the valve in the model behaves in the same way as in experiments.

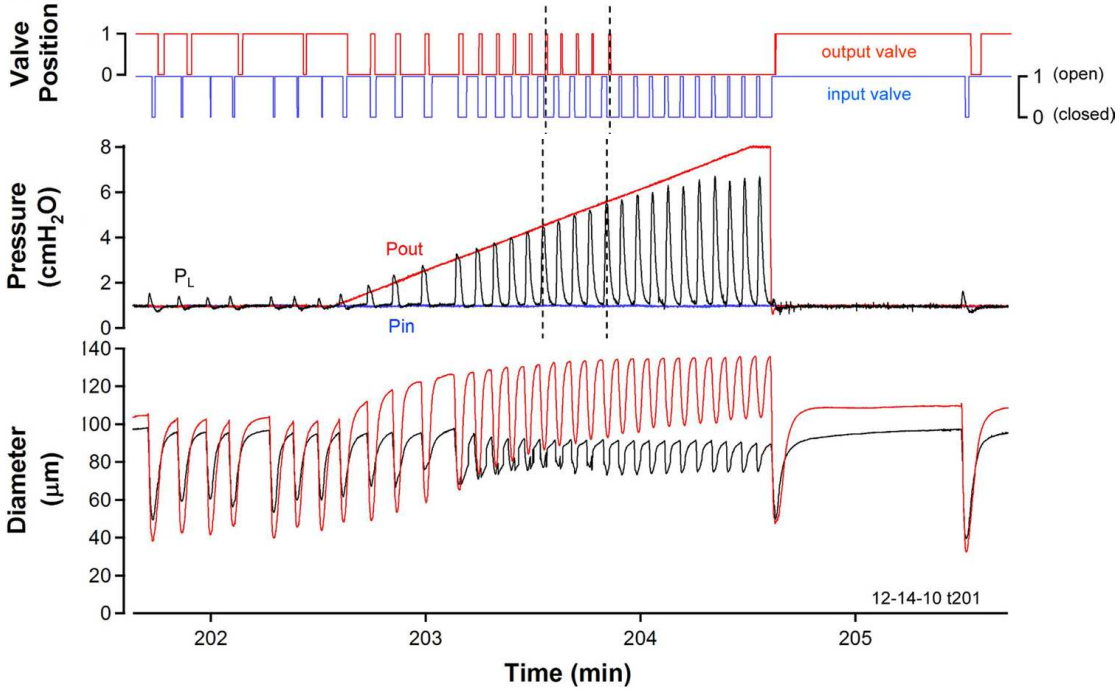

Figure 3.6: Graph showing valve position, pressure and diameter from Davis et al. [2011]. The first minute shows the behaviour when the inlet and outlet pressures are equal. For the next two minutes the outlet pressure is gradually increased. In the last minute the outlet pressure is lowered and the vessel is allowed to begin pumping again, this takes about a minute after the outlet pressure is lowered. In the diameter trace the red line is the inner diameter of the outlet segment and the black line is the inner diameter of the central lymphangion. Pin: inlet pipette pressure, Pout: outlet pipette pressure, P_L intraluminal pressure in lymphangion. ©2011, The American Physiological Society. Permission not required.

3.1.3 Summary

In the previous two sections, 3.1.1 and 3.1.2, the physiological structure and function of the collecting lymphatic valves have been reviewed. It is important to understand the structure of the collecting lymphatics and how this contributes to valve function. Experiments that investigated the behaviour of valves as part of the contractile cycle show that the valves and lymphatic walls work together to ensure the forward propulsion of fluid. Computational models are useful for investigating the collecting lymphatic vessels because they are physically small and delicate. In the next section 3.1.4, we review previous computational models of biological valves.

3.1.4 Computational Models of Biological Valves

The most commonly modelled biological valves in the literature are the aortic and mitral valves in the heart. This is because these valves are more susceptible to disease that the tricuspid and pulmonic valves of the heart [Sun et al., 2014]. The geometries

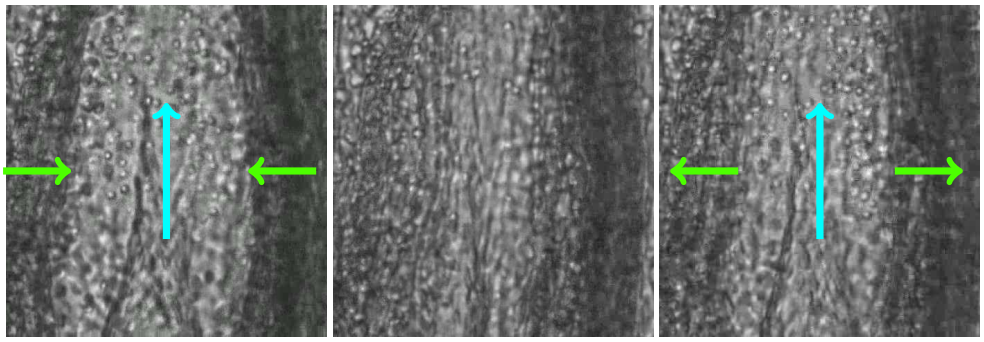

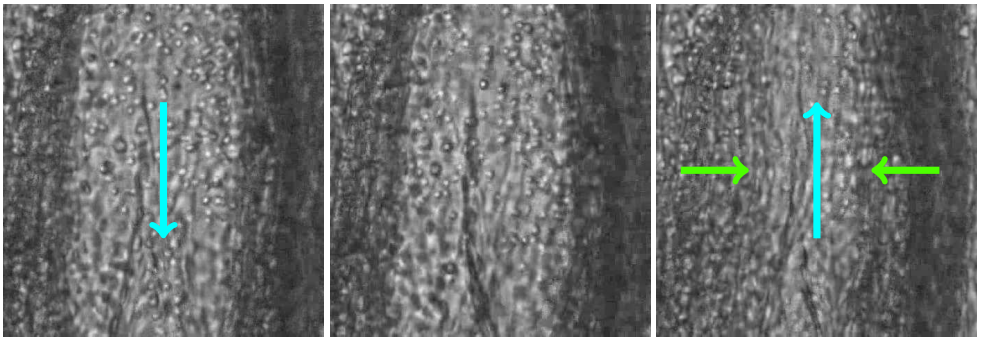

Figure 3.7: Frames captured from video from Davis et al. [2011] of *in vivo* rat mesenteric collecting lymphatic valve. The triangle shape on the centre of the image is the leaflets and buttress. Blue arrows show direction of fluid flow, green arrows show direction of wall motion. No arrows imply there is no movement. Those with no blue arrows have closed lymphatic valves. ©2011, The American Physiological Society. Permission not required.

of these valves are very different to lymphatic valves, but they are still thought to function due to passive mechanisms [Sun et al., 2014]. Venous valves have also been modelled, which have a similar geometry to collecting lymphatic valves, and probably function is a similar way. Both initial and collecting lymphatic valves have been modelled computationally.

3.1.4.1 Aortic Valve

The aortic valve has three leaflets, as shown in figure 3.8. The valve in open position is in quasi-steady state, see figure 3.9a. As the blood flow through the valve begins to slow, the valve leaflets begin to move inwards due to the pressure gradient created by the different velocities of the flow though the valve and the swirling in the sinus behind it, see figure 3.9b. The valve closes when the flow reverses and remains closed, preventing back flow [Bellhouse and Talbott, 1969].

The model by Peskin [1982] of a heart valve leaflet has a viscous incompressible fluid domain to represent the blood, within which there is a massless elastic boundary that

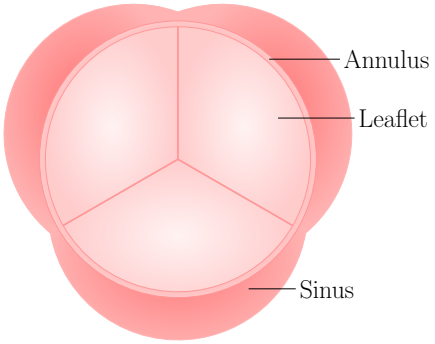

Figure 3.8: Illustration of aortic valve.

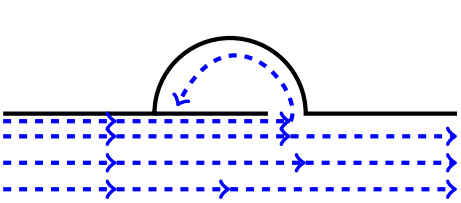

(a) Valve in open position.

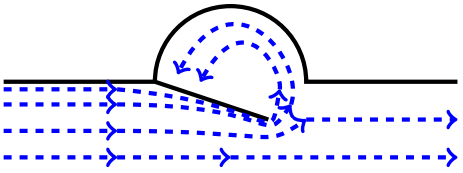

(b) Valve closing as fluid velocity through centre of valve decreases.

Figure 3.9: Aortic valve sketch. Black lines indicate valve leaflets and vessel walls, blue lines indicate flow direction. Sketched based on [Bellhouse and Talbott, 1969].

represents the valve leaflet. The Navier-Stokes equations are used to describe the fluid domain in Eulerian form, i.e.

$$\rho \frac{\partial \boldsymbol{u}}{\partial t} + \boldsymbol{u} \cdot \nabla \boldsymbol{u} = -\nabla p + \mu \Delta \boldsymbol{u} + \boldsymbol{F}, \tag{3.1}$$

$$\nabla \cdot \boldsymbol{u} = 0. \tag{3.2}$$

where ρ is the density of the fluid, $\boldsymbol{u}$ is the velocity of the fluid, t is time, μ is the viscosity of the fluid and $\boldsymbol{F}$ is an external force. In this case Peskin [1982] defines this to be the force applied to the fluid by the immersed boundary. The Lagrangian form used to describe the boundary configuration is $\boldsymbol{X}(s,t)$, where $s = (s_1, s_2)$ describes a material point. The boundary force is defined as,

$$\boldsymbol{F} = \int_B \boldsymbol{f} \delta \left[\boldsymbol{x} - \boldsymbol{X}(s,t)\right] ds, \tag{3.3}$$

where B is the immersed boundary, f is the density of the boundary force, δ represents the δ-function and $\boldsymbol{x}$ is the point in Eulerian form. This equation couples the solid to the fluid. A second equation is used to couple the fluid to the solid,

$$\frac{\partial \boldsymbol{X}}{\partial t}(s,t) = \int_\Omega \boldsymbol{u} \delta \left[\boldsymbol{x} - \boldsymbol{X}(s,t)\right] \, d\boldsymbol{x}. \tag{3.4}$$

This defines the movement of the immersed boundary to be at local fluid velocity. The

boundary force at any time was determined by the boundary configuration at that time [Peskin, 1982]. A finite-difference method was implemented that required for each time step:

1. Calculate boundary forces from boundary configuration,
2. Apply boundary forces to nearby fluid mesh points,
3. Update fluid velocity,
4. Update the boundary position by interpolating the local fluid velocity to the points on the boundary.

Griffith [2006] developed this two dimensional model to create a three dimensional model of the whole heart with adaptive meshing. They found that using adaptive meshing improved the boundary layer resolution. A gap between the valve leaflets had to be left in order for the valves to open. This is because the velocity field is assumed to be continuous. There must be a gap between the leaflets in order to allow the valves to open because the valve leaflets touched this would create two discrete fluid domains, and if two material points coexist at any one time, they must coexist for all time [Griffith, 2006]. The adaptive meshing method allowed for the size of this gap to be smaller than in the previous models.

Hart et al. [2000] used a fictitious domain approach. The velocity of a solid, $\boldsymbol{v}_s$, is related to its displacement, $\boldsymbol{u}_s$, with a first order approximation,

$$\boldsymbol{v}_s = \frac{\boldsymbol{u}_s}{\Delta t} \tag{3.5}$$

where Δt is one time step. The fluid velocity, $\boldsymbol{v}_f$, is coupled to the solid velocity on the boundary, Γ, by the condition

$$\boldsymbol{v}_s - \boldsymbol{v}_f = 0. \tag{3.6}$$

This condition means that the node points on the boundary must be the same for the fluid and solid domains. To overcome this, the condition is implemented weakly using Lagrange multiplies, λ,

$$\int_\Gamma \lambda \cdot (\boldsymbol{v}_s - \boldsymbol{v}_f) \ \mathrm{d}\Gamma = 0, \tag{3.7}$$

[Hart et al., 2000].

Hart et al. [2000] compared the model to experiments carried out using a rubber sheet to represent the valve leaflet. They found that for leaflet position and fluid flow the model produced similar results to the experiments during systole. The differences during diastole were larger and could be a result of neglecting buoyancy forces in the numerical model. Hart et al. [2003] expands the model to three dimensions. They

model a stented aortic valve by simulating half an aortic leaflet and introduce a contact surface for modelling closure. Hart et al. [2000, 2003] emphasise that they are describing the models and how they work but they do not compare the results with physiological data and so no conclusions can be drawn to their physiological relevance.

Spühler et al. [2015] used a continuum arbitrary Lagrangian Eulerian (ALE) finite element method to model an aortic valve, which is implemented in Unicorn, part of the FEniCS project[1]. The model used the incompressible unified continuum equations, which is expressed using Einstein summation convention as,

$$\rho\left(\frac{\partial u_i}{\partial t} + u_j\frac{\partial u_i}{\partial x_j}\right) = \frac{\partial}{\partial x_j}\left(\sigma_{ij}^D - p\delta_{ij}\right) + f_i, \tag{3.8}$$

$$\frac{\partial u_j}{\partial x_j} = 0, \tag{3.9}$$

$$\frac{\partial \theta}{\partial t} + u_j\frac{\partial \theta}{\partial x_j} = 0, \tag{3.10}$$

where ρ is density, u_i is velocity and the stress has been decomposed into deviatoric, σ_{ij}^D, and pressure, $p\delta_{ij}$, parts. The stress is described by a linear θ phase function, $\sigma = \theta\sigma^f + (1-\theta)\,\sigma^s$ that combines the solid stress, σ^s, and fluid stress, σ^f. The contact condition between the valve leaflets is modelled by switching the phase from fluid to solid depending on the distance between the two leaflets.

3.1.4.2 Mitral Valve

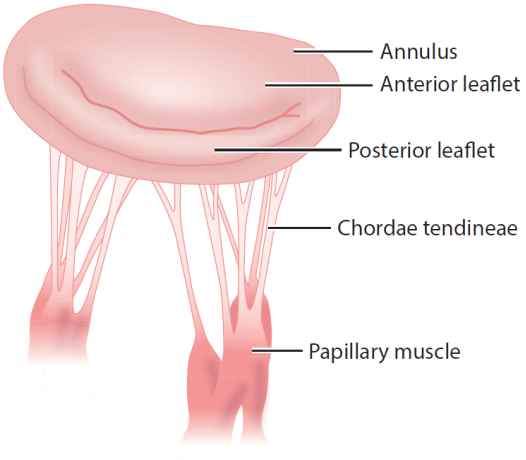

Figure 3.10: Illustration of mitral valve from Sun et al. [2014]. ©2014, Annual Reviews. Permission is not required.

The mitral valve has two leaflets, each of which are attached to the papillary muscle by chordae tendineae, see figure 3.10. These chords prevent the valve turning inside out. The mitral valve closes due to vortices forming behind the valve cusps. As the

[1] www.fenicsproject.org

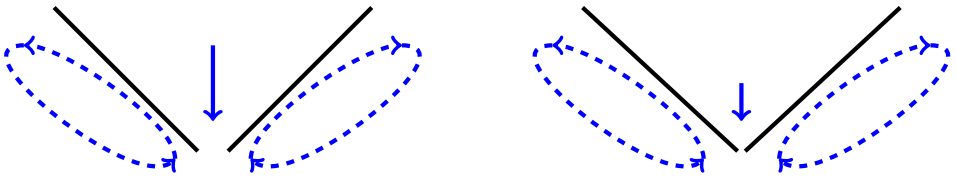

(a) Flow through valve and vortex regions results in equal pressure on both sides of the leaflets causing to valve to remain open.

(b) Slow flow, indicated by small central arrow, through valve and the same velocity in the vortex regions causing the valve to close.

Figure 3.11: Mitral valve sketch. Black lines indicate valve leaflets, blue lines indicate flow direction. The chordae have been neglected for clarity.

flow through the centre of the leaflets slows down, the swirling fluid behind the valve leaflets continues at the same velocity. This velocity difference causes the pressure between the leaflets to be lower than behind the leaflets, and the valve closes, see figure 3.11 [Caro et al., 2012].

The method by Peskin [1982] has been used to model the mitral valve by McQueen et al. [1982]. They modelled the valve and the left atrium and ventricle, see figure 3.12. The valve leaflets are modelled as elastic flexible membranes [McQueen et al., 1982]. The forces applied by the papillary muscles and chordae are modelled by tethering the ends of the leaflets, but this did not affect the flow. They also used a cross link to represent the support provided by the mitral annulus. A source term for the flow is located in the left atrium.

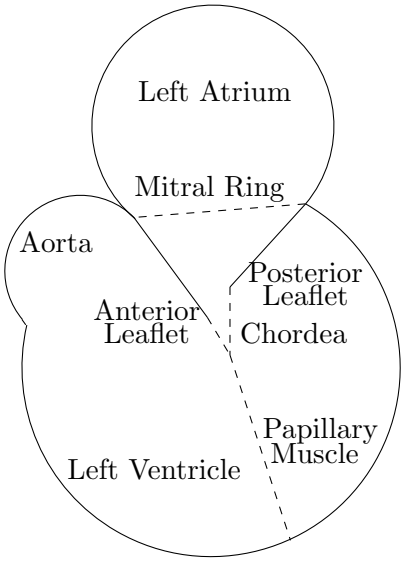

Figure 3.12: Sketch of two dimensional geometry used to model the mitral valve, left atrium and ventricle.

McQueen et al. [1982] found that the flow patterns created from their model were similar to those observed in experiments. They used the model to compare the closing behaviour of a healthy mitral valve with mitral prolapse syndrome, reducing the stiffness of the papillary muscle, a mitral valve with no chordae, the chordae and papillary muscle are removed, and three types of artificial valves, which will not be reviewed here. In the healthy valve, as the flow passes between the leaflets vortices are formed at the leaflet tips and the shedding of these vortices causes the valve to begin closing. As the gap between the leaflets narrows, back flow occurs in the mitral ring area, while forward flow occurs between the leaflet tips and the valve closes. For the mitral prolapse case, initially the closing behaviour is the same as the healthy valve, however as the gap between the leaflets narrows there is no forward flow between the leaflet tips causing the leaflets to fold back into the left atrium. The posterior leaflet prolapses suddenly causing regurgitation. For the valve with no chordae, the vortices initially form between the valve leaflets causing them to be forced wide open before returning to equilibrium position parallel to the flow passing through the leaflets. The valve does not close in this case [McQueen et al., 1982].

Kunzelman et al. [2007] created a fluid-structure interaction model of a mitral valve using LS-DYNA[2]. They modelled half the valve to save on computational resources. The leaflets are modelled as membranes and the chordae provided tension to the leaflets but did not affect the fluid flow. The blood is modelled as a compressible, Newtonian fluid. The fluid and solid were coupled by overlapping the fluid domain with the solid domain. The interaction between the Eulerian and Lagrangian domains is staggered by one time step:

1. Calculate the solid domain
2. Calculate the fluid behaviour using the boundary nodes from the solid domain as a boundary condition
3. Calculate the next time step for the solid domain using the velocities and pressures from the fluid domain as boundary conditions.

The authors used the model to investigate the amount of fluid regurgitated as the material properties of the mitral valve were changed. Varying the amount of collagen in the valve leaflets or the stiffness of the collagen did not greatly alter the behaviour of the valve. Kunzelman et al. [2007] found that decreasing the fibre alignment resulted in floppy valves that closed later and therefore there was more regurgitated flow. They also found that increasing the stiffness of the isotropic term used to simulate the matrix without the collagen fibres increased the amount of back flow. Therefore, Kunzelman et al. [2007] concluded that the anisotropy of the mitral valve material was important for the valve to function correctly.

[2]A commercial finite element software

3.1.4.3 Venous Valves

A three-dimensional model of a valve from a vein has been attempted by Buxton and Clarke [2006]. The vein valves have a similar structure to the lymphatics, i.e. they are formed of two valve leaflets which push together to close in order to stop reverse flow and are thought to close due to pressure gradients [Buxton and Clarke, 2006; Qui et al., 1995]. Buxton and Clarke [2006] modelled the vein wall and valve using the lattice spring model as curved elastic shells. The Poisson ratio of the wall and valve was $\frac{1}{3}$. The wall was 0.05 cm thick and had a Young's modulus of 1000 kNm^{-2}. The fluid dynamics was modelled using the lattice Boltzmann method. The blood had density 1060 kgm^{-3} and viscosity 0.0027 Nsm^{-2}. The authors used this model to look at the flow field around the valve, the opening area of the valve, and how the flow rate changed as the valve opened from closed position as the pressure difference across the valve changed [Buxton and Clarke, 2006].

Narracott et al. [2010] created a three dimensional model of a venous valve in LS-DYNA. Due to the symmetrical nature of the valve and surrounding wall, only a quarter of the vessel had to be modelled. The vessel was 1.19 cm in diameter and 200 cm long. The valve geometry was created by curving a rectangular surface and intersecting it with the vessel wall. The leaflet length was double the vessel diameter and the thickness was 0.05 mm. The authors chose to apply a parabolic velocity profile along the vessel length rather than apply a pressure condition and allowing the flow to develop in order to save computational time. The outlet pressure was set at zero. The ends of the vessel walls were fixed. Narracott et al. [2010] simulated the movement as a person moved from lying to standing position by applying a gravitational body force after an initial period of time. They used the model to analyse how changing the elastic modulus of the wall, which was assumed to be a linear material, altered the valve dynamics. The fluid was assumed to be compressible. Narracott et al. [2010] found that the leaflet displacement, deformation and local velocity field was similar, regardless of the elastic modulus of the wall for the initial boundary conditions. After the gravitational body force was imposed, the amount the valve closed was affected by the different elastic moduli of the wall. The model was developed further in Narracott et al. [2015], by modelling the whole valve with contact condition between the valve leaflets. The leaflets had a Youngs modulus of 50.7 MPa and the wall 0.507 MPa. They investigated the leaflet displacement for different Reynolds numbers. They found that for Reynolds number 272 the simulation compared well with the experimental data, however this required a much higher velocity magnitude that observed *in vivo*. This could be a result of the assumed material properties of the leaflets and wall and the initial position of the leaflets [Narracott et al., 2015].

3.1.4.4 Lymphatic Valves

Bertram et al. [2011] modelled a one dimensional series of segments separated by valves. The valves were modelled as having variable resistance to the flow depending on the pressure difference across the valve. They included pressure terms for when the valve would open, a small positive value, and when it would fail, a large negative value. Their model solved for the diameter and pressure at either end of each segment [Bertram et al., 2011].

A few years later the model was developed by incorporating realistic parameter values [Bertram et al., 2013b]. They considered vessels with diameter of the order of 200 μm. In order to model the valve behaviour, the valves were set as having a variable resistance. This was a smoothed step function, dependent on the difference in pressure across the valve and four parameters: a closing threshold, when the valve closes totally, an opening threshold, when the valve opens fully, a threshold pressure drop and the gradient from open to closed state. To calculate these parameter values realistically, experiments were carried out to measure the pressure drop across the valve, the flow-rate and the diameter of the vessel. The resistance was then calculated as the change of pressure across the valve differentiated by the flux. There is a large variation in the data, so a curve fitting was used in the model. The order of magnitude is considered to be correct even though the uncertainty is quite large [Bertram et al., 2013a].

Bertram et al. [2013a] found that incorporating the pressure differences for opening and closing the valve from Davis et al. [2011] resulted in inefficient pumping by the lymphangions. They suggest that the experiments conducted overestimate the pressure needed to close the valve, which may have occurred due to the resistance to the flow caused by the pipettes that cannulated the vessel. They estimated the error and using their 'corrected' value found the model produced more efficient pumping. To date there have been no experiments to test this theory. It was also found that increasing the opening threshold parameter for the valve resistance resulted in more powerful pumping, and they speculate on the reasons for this. Another reason their model was inefficient could be that the model is based on isolated vessels. The collecting lymphatics are effected by their surroundings and the experiments that the model is based on are carried out on isolated vessels. It may be that isolated vessels are not as effective at pumping as *in situ* vessels. They also assume that primary activity of the collecting lymphatics is efficient pumping but do not consider the amount of energy that would be required to achieve this. This one dimensional model does not give us any information about the deformation of the valve or its interaction with the fluid. It does attempt to quantify the amount of resistance that the valve causes to the flow.

Wilson et al. [2013] used confocal microscopy to create a 3D model of a valve and surrounding wall. It was used to model the nitric oxide (NO) transport around a rigid valve. There were two recirculation areas either side of the valve although the flow was so slow the velocity was almost zero. They found that the endothelial cells that experience the highest wall shear stress produced NO at the highest rate, but that the concentration of NO was highest in the sinuses around the valve as the NO was transported to this area by the fluid flow. The strength of this model is that the geometry is based on images of a real vessel. This was a rigid model and therefore provides no information about the mechanical behaviour of valve with the fluid.

Wilson et al. [2015a] created a two dimensional model of the collecting lymphatic valve and surrounding wall by capturing a series of images of an isolated pumping lymphatic vessel over time using confocal microscopy. From each image the lumen was segmented and meshed. The displacement between each image was discretised and imported into Star-CCM+ as an input condition for the model. The model was used to investigate the fluid velocity within the lymphatic vessel as the wall and valve deformed. The study covered a time period of 0.017 seconds and captures the expansion of the valve [Wilson et al., 2015a]

Wilson et al. [2015b] created a three dimensional collecting lymphatic valve model based on idealised geometry. The purpose of the model was to calculate the resistance of the valve and sinus to the lymphatic flow. To do this the modelling was conducted as follows:

1. Compute the steady state flow around an almost closed valve (valve leaflet edges 2 μm apart).
2. Evaluate the mean pressure across each valve leaflet.
3. Apply mean pressure to structural model of the valve to cause valve to open.
4. Export the open valve geometry.
5. Import open valve geometry into fluid domain.
6. Compute steady state flow around open geometry.
7. Evaluate the resistance of the valve.

For the fluid models the inlet velocity was 1.5 mm/s and the outlet pressure was a gauge pressure of 0. For the structural model a neo-Hookean material was used with a shear modulus of 45 kPa and the base of the leaflets were fixed in space.

Watson et al. [2015] modelled a closing collecting lymphatic valve. The valve geometry was created from segmented images and modelled in ANSYS as a solid mechanics model. The leaflets were modelled as an incompressible neo-Hookean material with

shear modulus 60 kPa. The base of the leaflets were fixed in space. The authors found that the maximum displacement occurred at the centre of the free edge of the valve.

In this section the literature of modelling biological valves has been reviewed. Many attempts with different techniques have been used to approach modelling problems. In particular the closure of valves is very challenging. It is important to be able to model biological valves because they are difficult to study experimentally, especially the fragile lymphatic and venous valves, and are very important for the correct function of their respective systems. In the next section, 3.2, four different approaches to modelling collecting lymphatic valves are presented along with the respective results.

3.2 Methods and Results

In this section the methods used to create the valve model are described. To begin, the methods of data collection to define the material properties and geometry dimensions are presented. This is followed by four models that increase in complexity. These models are used to investigate different aspects of the interaction between the lymphatic valve and the fluid around it. To begin this section, the methods for gathering the initial information for the model are described.

3.2.1 Young's Modulus for Leaflets

From the structure of the leaflets, it is expected that the Young's modulus of the leaflet would be larger than an endothelial cell which is about 1000 Pa [Ohashi and Sato, 2005; Ohashi et al., 2002]. Two equations are used to find an approximate value for the Young's modulus of the valve leaflets, the beam equation and equation (2.7).

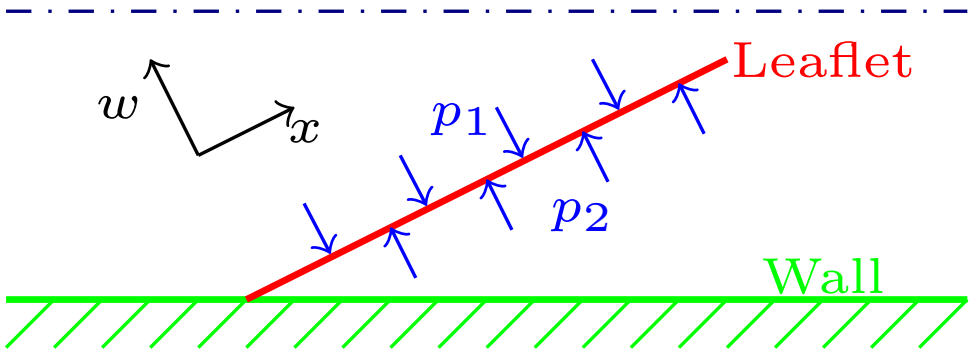

Figure 3.13: Diagram of valve leaflet modelled as a beam. w is the vertical displacement, x is the horizontal distance along the beam and p_1 and p_2 are the pressures either side of the valve leaflet.

The leaflet can be modelled in two dimensions using the beam equation, given in Howell et al. [2009] by

$$-EI\frac{\partial^4 w}{\partial x^4} + T_{\text{force}}\frac{\partial^2 w}{\partial x^2} - \rho g = \rho\frac{\partial^2 w}{\partial t^2} + F, \tag{3.11}$$

where EI is the bending stiffness, w is the vertical displacement, x is the horizontal distance along the beam, T_{force} is the tangential force component, ρ is the density, g is gravity and t is time. In this case the force, F, is from the difference in pressure across the valve leaflet, $P = p_1 - p_2$. If the valve is assumed to be a plate, the bending stiffness is,

$$EI = \frac{E_l h_l^3}{12(1-\sigma^2)}, \tag{3.12}$$

where E_l is the Young's modulus of the valve, h_l is the thickness of the valve leaflet, σ is the Poisson ratio [Howell et al., 2009]. It is assumed there is no longitudinal stretching displacement, gravity is neglected and only steady displacements are considered. Hence the beam equation reduces to

$$\frac{d^4 w}{dx^4} = \frac{P}{D_l h_l^3}, \tag{3.13}$$

where $D_l = \frac{E_l}{12(1-\sigma^2)}$. When the valve is closed it can be assumed that both ends of the beam are clamped which gives the following boundary conditions:

$$w(0) = 0,\ w(L_l) = 0,\ \left.\frac{dw}{dx}\right|_{x=0} = \alpha,\ \left.\frac{dw}{dx}\right|_{x=L_l} = \beta, \tag{3.14}$$

where L_l is the length of the leaflet, α is the gradient the beam is clamped at $x = 0$ and β is the gradient the beam is clamped at $x = L_l$. The beam equation is integrated four times to find,

$$w(x) = \frac{P}{24 D_l h_l^3}x^4 + C_3 x^3 + C_2 x^2 + C_1 x + C_0, \tag{3.15}$$

where $C_0,\ C_1,\ C_2,\ C_3$ are arbitrary coefficients to be found using the boundary conditions, i.e. for equations (3.14) and (3.15) these are given by

$$\begin{aligned}
C_0 &= 0,\\
C_1 &= \alpha,\\
C_2 &= -\frac{24\beta D_l h_l^3 - P L_l^3 + 48\alpha D_l h_l^3}{24 D_l h_l^3 L_l},\\
C_3 &= -\frac{2P L_l^3 - 24\beta D_l h_l^3 + 24\alpha D_l h_l^3}{24 D_l h_l^3 L_l^2}.
\end{aligned}$$

Thus the solution is

$$w(x) = \frac{P}{24D_l h_l^3}x^4 - \frac{2PL_l^3 - 24\beta D_l h_l^3 + 24\alpha D_l h_l^3}{24D_l h_l^3 L_l^2}x^3 - \frac{24\beta D_l h_l^3 - PL_l^3 + 48\alpha D_l h_l^3}{24D_l h_l^3 L_l}x^2 + \alpha x. \tag{3.16}$$

In order to calculate the displacement of the valve leaflet images of an open and closed valve from Davis et al. [2011] were used, see figure 3.14a. The images were edited so that Matlab could be used to measure the leaflet thickness and the displacement from open to closed state.

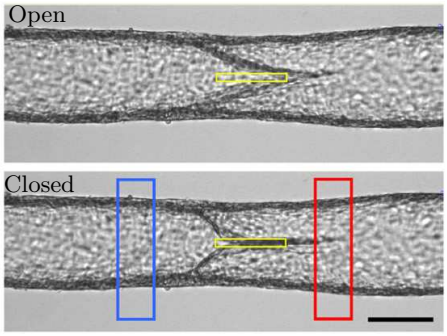

(a) Open and closed valve [Davis et al., 2011]. Scale bar=120 μm. Blue and red rectangles show approximate location where the diameter was measured as part of the experiment. Yellow rectangle shows where the densitometer measured the density of the image for analysis of whether valve was open or closed. ©2011, The American Physiological Society. Permission not required.

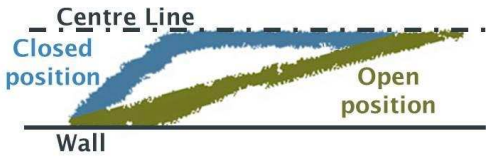

(b) Resulting edited image for measurements in Matlab. The colours emphasise the open and closed positions of the valve.

Figure 3.14: The image comparing an open and closed valve from Davis et al. [2011], a, was edited so that the leaflet thickness and displacement of the valve could be evaluated in MATLAB, b.

The image was edited using ImageJ. The image of the closed valve was overlaid onto the image of the open valve. The background details were removed and the result was rotated so that the open valve appeared horizontal. Edge detection was used before it was converted to a binary image. A smoothing function was then applied to compare the difference caused by the rough edges. The three final images used can be seen in figure 3.15.

The leaflets are approximately 2.2 μm thick, based on the measurements from images shown in figure 3.18, see section 3.2.2 for more details. In order to scale the images the last column before the two leaflets split (indicated by the green lines in figure 3.15) is assumed to be the total thickness of two leaflets. The number of pixels in

this column is assumed to be equivalent to 4.4 μm. This gives the ratio for scaling the images to the physiological leaflet size.

The mean of the thickness of the leaflets was calculated based on these images. For the initial image the thickness was 2.2 μm and for the outer and inner regions the leaflet thickness was 1.9 μm. The displacement of the leaflet from open to closed position was measured from the upper surface of the open leaflet to the upper surface of the closed leaflet. Only the displacement up to the maximum point is considered, as it is assumed that after this the two leaflets would be pressing against each other. The assumed pressure difference across the valve leaflets that caused the valve to close was 0.17 cmH_2O, indicated as the closing pressure for a valve for a low inlet pressure of 0.2 cmH_2O [Davis et al., 2011].

The value of D_l was calculated as the value which gave the minimum error when the calculated displacement was compared to the measured displacement. The plots from this comparison can be seen in figure 3.15. For the initial image $D_l = 4190$ Pa. For the outer image $D_l = 2270$ Pa. For the inner image $D_l = 9280$ Pa. If we assume incompressibility, this gives a Young's modulus between 252 and 1031 Pa. The larger value is similar to the Youngs modulus of an endothelial cell, which implies that these values are probably too low for the valve.

A supplementary video (video 3) from Davis et al. [2011] highlights that assuming the images used are a good enough approximation of the behaviour of the centre line of the valve is inaccurate when the valve is open. In the video it can be seen that the upper side of the valve is above the line which was considered previously as the centre. It can be seen fluttering and then disappearing as the valve closes. This is highlighted with the orange box in figure 3.16 but it is difficult to see. This would increase the displacement that the leaflet must move in order to close, which would reduce the values calculated for D_l.

The value of D_l was calculated using the equation (2.7) for the thick walled tube. This is the same equation that was used for the walls. ImageJ was used to take measurements from Davis et al. [2011], as presented in figure 3.17. The displacement of the valve leaflets was taken as the difference between the distance of the leaflet from centre line of the vessel in open and closed position. The black lines in figure 3.17 show where the measurements were taken, slightly upstream of where the two leaflets met, and the dashed line is the centre line of the vessel. The displacement was calculated as 29 μm. The thickness of the leaflets was measured as 11 μm. This gives $D_l = 1.804$ Pa. The value of E_l was calculated using equation (2.2), resulting in $E_l = 13.55$ Pa. These values are too small to be realistic when compared to the Young's modulus of an endothelial cell.

The methods used here do not appear to have provided a realistic set of values for the Young's modulus of the valve leaflets. Instead of using the values calculated, it will be

(a) Resulting image after editing.

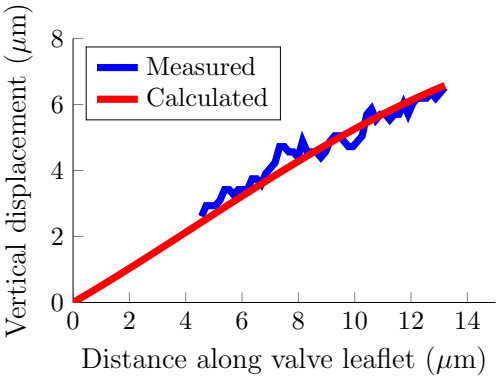

(b) Comparison of vertical displacement calculated using the initial image after editing, seen in figure 3.15a.

(c) Outer region after smoothing the resulting image in 3.15a.

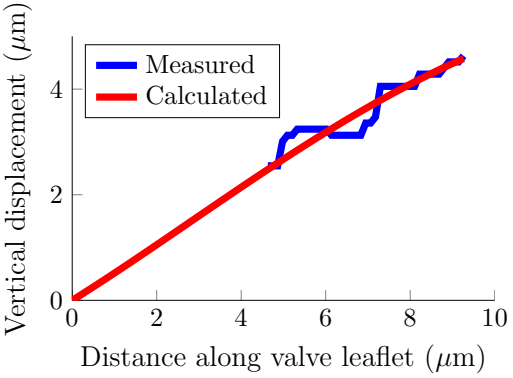

(d) Comparison of vertical displacement calculated using outer region after smoothing, seen in figure 3.15c.

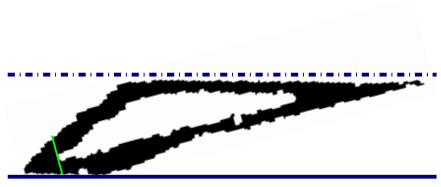

(e) Inner region after smoothing the resulting image in 3.15a.

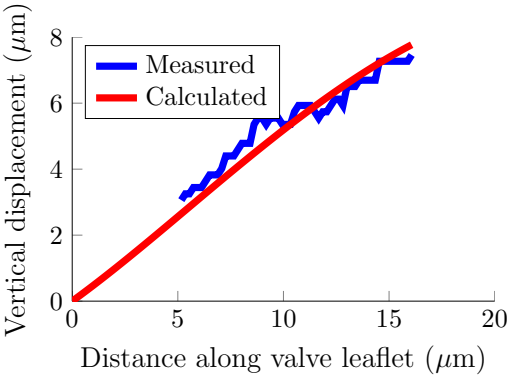

(f) Comparison of vertical displacement calculated using inner region after smoothing, seen in figure 3.15e.

Figure 3.15: a, c and e: Images used with Matlab to find the leaflet thickness and valve displacement from open to closed position. The green lines indicate the column of pixels which were scaled to 4.4 μm in order to interpret the measurements made into physiological values. The outer and inner images were used to find the error caused by the rough edges. b, d and f: Result of calculating the value of D_l such that the beam equation gives the minimum error when compared to the measured values from the edited images. The blue line is the displacement measured from the corresponding image, the red line is the displacement calculated by the beam equation using the value of D_l which gave the minimum error when compared to the measured values.

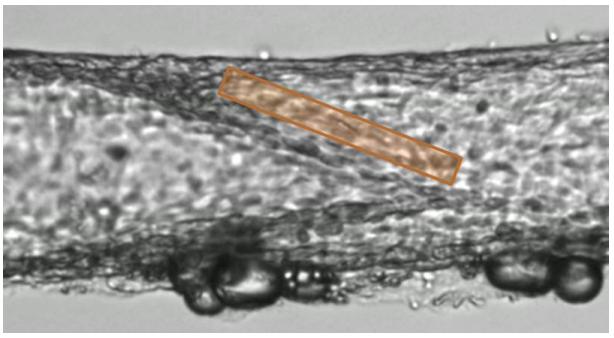

Figure 3.16: Frame from video 3 in the supplementary material from Davis et al. [2011]. The orange box highlights the upper side of the valve which flutters while the valve is open. The darker, thicker lines, which have been assumed to represent the behaviour of the valve leaflets, do not flutter as much, presumably because they are attached to the wall. The part highlighted in orange displaces more between opening and closing positions than the sides of the leaflets which were used in the calculations. This shows that the assumption of the darker lines indicating the displacement of the whole valve leaflet is untrue. ©2011, The American Physiological Society. Permission not required.

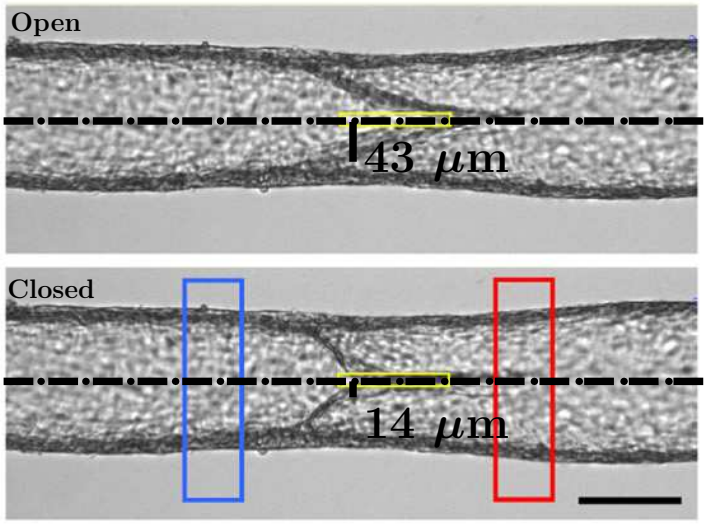

Figure 3.17: Images comparing an open and closed valve. The measurements were used with the equation (2.7), to calculate the value of D_l. The dashed lines indicate the centre line of the vessel. The thick lines show where the distance between the leaflet and the centre line was measured. Image adapted from Davis et al. [2011], scale bar=120 μm. ©2011, The American Physiological Society. Permission not required.

assumed that the Young's modulus of the valve is 15000 Pa, about half that calculated for the wall. The Young's modulus of the leaflets should be lower than the Young's modulus of the walls because the valves do not contain smooth muscle cells.

Having established the material properties, in the next section the methods used to determine the dimensions for the valve geometry will be presented. These values are compared to literature values for validation.

3.2.2 Valve Dimensions

The geometry of the valve models were based on the descriptions from literature, as presented in subsections 2.1.2 and 3.1.1. The same frames from videos 40_hires_3 and 40_hires_4 as used in chapter 2, were used to measure the geometry of mesenteric collecting lymphatic valve for a mouse. During the fixation process the lymphatic vessels become flattened. The images used can be seen in figure 3.18. The measurements taken from these images can be seen in table 3.1.

	Side							Front			
Figure	3.18a	3.18c	3.18b	3.18d	3.18e	3.18f	**Mean**	3.18g	3.18h	3.18i	**Mean**
Buttresses Width(μm)								75.2	79.5	63.8	**72.8**
Entrance width (μm)			33.8		35.2	32.4	**33.8**	57.6	59.7	49.4	**53.9**
Mid-line length (μm)	31.9		49.0		36.0	36.9	**38.4**	34.4	31.1	33.5	**33.3**
Side length (μm)	100.4		106		110.8	109.1	**106.6**	48.5	53.1	63.7	**55.1**
Thickness with valve (μm)		11.4		11.6			**11.5**				

Table 3.1: Measurements from images in figure 3.18. They form the basis for the geometry of the model of the collecting lymphatic valve and surrounding vessels. The mean values for the front and side measurements are also recorded. All measurements are accurate to one decimal place. The empty values could not be measured from the particular image.

Using the mid-line and side lengths of the valve measured from the images in figure 3.18 resulted in very thin sections leading to the buttress, that was difficult to mesh. Therefore, the valve length measured in subsection 3.2.1, 44 μm, was used instead. The measurements used for the model are shown in table 3.2. All measurements are assumed to be external. The internal dimensions are calculated by subtracting either the wall thickness or valve thickness.

Position	**μm**
Front upstream width	56
Front downstream width	88
Front valve entrance width	54
Side upstream width	35
Side downstream width	68
Side valve entrance width	34
Front width between valve tips	73
Valve mid-line length	33
Valve side length	44
Wall thickness	3.6
Leaflet thickness	2.2

Table 3.2: The measurements used for three-dimensional model based on measurements in tables 2.5 and 3.1.

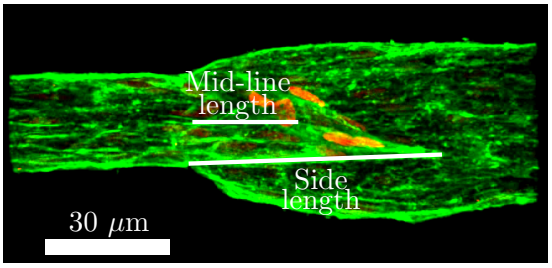

(a) 40_hires_3, frame 1

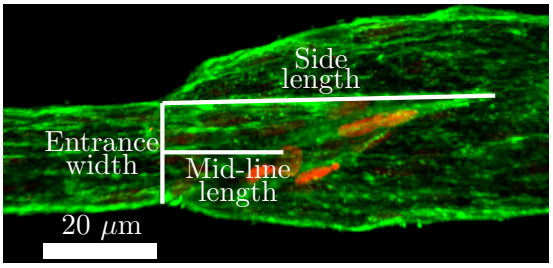

(b) 40_hires_3, frame 76

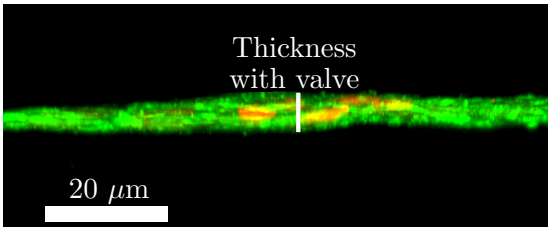

(c) 40_hires_3, frame 53

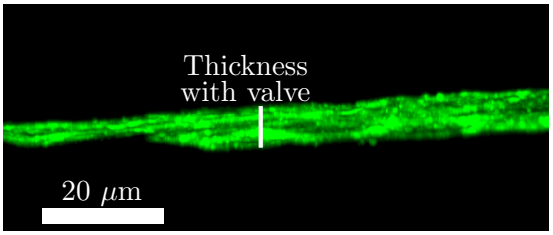

(d) 40_hires_3, frame 85

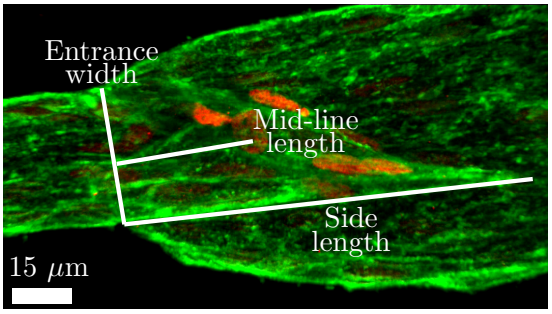

(e) 40_hires_3, frame 351

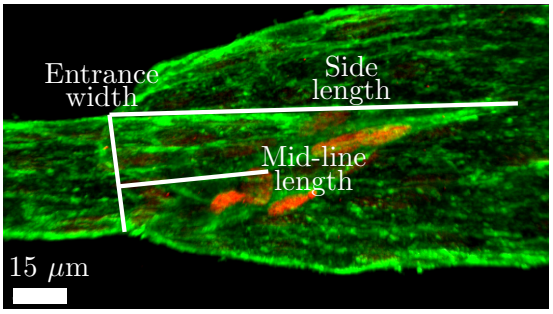

(f) 40_hires_3, frame 431

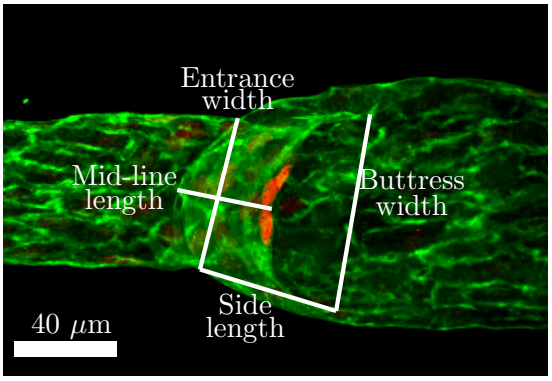

(g) 40_hires_4, frame 4

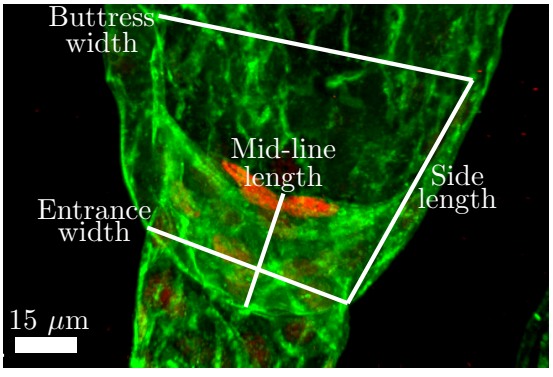

(h) 40_hires_4, frame 60

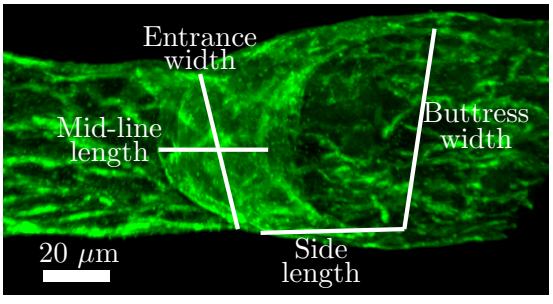

(i) 40_hires_4, frame 241

Figure 3.18: Frames from videos 40_hires_3 and 40_hires_4 by Taija Makinen and colleagues at Cancer Research UK of mouse lymphatic vessels. The white lines show the approximate position where the measurements were taken using ImageJ.

In order to verify that these measurements are realistic, they are compared to values from the literature. The diameters for mouse mesenteric lymphatic vessels in the literature were between 50 and 1170 μm, see table 2.1. Comparing the width measurements from table 3.2 most fall into this range near at the lower end, except for the side upstream width, which is less than 50 μm. This is not considered unrealistic as it is still the same order of magnitude. No data was found in the literature on the thickness of mouse mesenteric lymphatic walls and valves. However, compared to the rat data from Rahbar et al. [2012], the wall thickness is of the same order of magnitude although smaller for the mouse than for the rat, which is to be expected. The valve leaflet thickness lies in the same range as the leaflets from adult rabbit lung lymphatics measured by Lauweryns and Boussauw [1973], 0.5 to 6 μm. Therefore, the values measured appear to be suitable when compared to the values reported in the literature.

Having established the geometry and material properties of the model, the boundary conditions for realistic fluid behaviour are required for the model. In the next section the range of suitable boundary conditions used are presented.

3.2.3 Experimental data

For the fluid domain boundary conditions, the inlet and the outlet conditions need to be defined. The values used for the models are within the range of pressures presented by Davis et al. [2011] for the values at which the valves of a passive rat mesenteric valve would close, see figure 3.19. The data was read from the graph using DataThief. It is displayed in table 3.3.

Baseline pressure (cmH_2O)	Pressure difference (cmH_2O)	Outlet pressure (cmH_2O)
0.2	0.1	0.3
0.5	0.3	0.8
1.0	0.6	1.6
2.0	1.2	3.2
3.0	1.4	4.4
5.0	1.7	6.7
7.0	1.9	8.9
11.0	2.2	13.2
15.0	2.4	17.4
20.0	2.8	22.8

Table 3.3: Pressures required for valve closure read from figure 3.19 using DataThief.

3.2.4 Computational Models

In this section four models are presented: A 2D axisymmetric fluid model is used to investigate the affect of the Reynolds number of the recirculation area in the sinus

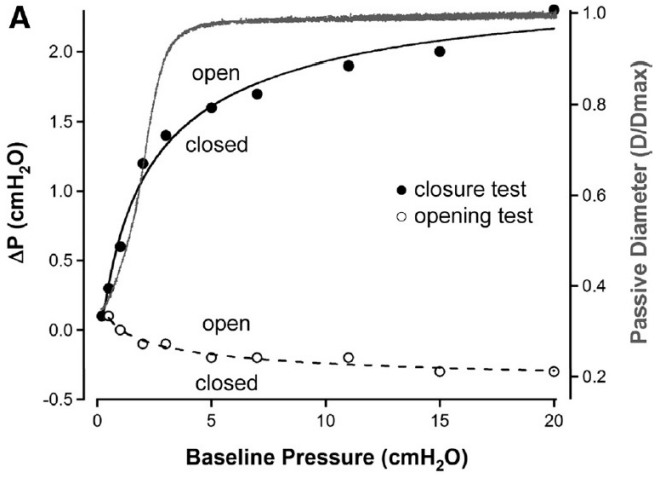

Figure 3.19: Graph showing pressures required for valve closure [Davis et al., 2011]. The black circles show the pressure where the valve closed, the white circles where the valve opened and the grey line is the pressure diameter curved caused by increasing baseline pressures. ©2011, The American Physiological Society. Permission not required.

of the valve; a 3D fluid structure interaction model using a linear material is used to explore if using a linear material model with the previously defined Young's moduli for the wall and the valve is a suitable approximation of the vessel behaviour; a 2D fluid structure interaction model of only the valve with the nonlinear material model from chapter 2 is used to investigate if the open area ratio of the original geometry affects the closing pressure of the valve; finally a 3D solid mechanics nonlinear material model is used to find the pressures required for valve closure for a particular geometry.

3.2.4.1 2D Axisymmetric Fluid Model Method

A 2D axisymmetric model of the laminar flow domain was created to investigate whether the Reynolds number of the flow affected the shape of the recirculation area. The geometry based on the measurements in table 3.2 were used to create a 2D axisymmetric geometry, shown in figure 3.20. The fluid behaviour in the domain Π was modelled using the Navier-Stokes equations for incompressible flow,

$$\rho\left(\boldsymbol{u}_{fluid}\cdot\nabla\right)\boldsymbol{u}_{fluid}=\nabla\cdot\left(-p\boldsymbol{I}+\mu\left(\nabla\boldsymbol{u}_{fluid}+\left(\nabla\boldsymbol{u}_{fluid}\right)^{T}\right)\right)+\boldsymbol{F}_{b},\quad\text{for } x\in\Pi \tag{3.17}$$

$$\rho\nabla\cdot\boldsymbol{u}_{fluid}=0,\quad\text{for } x\in\Pi \tag{3.18}$$

where $\boldsymbol{u}_{fluid}$ is the velocity vector, p is pressure, $\boldsymbol{I}$ is the identity matrix, $\boldsymbol{F}_b$ is body force vector, and x represents the mesh points.

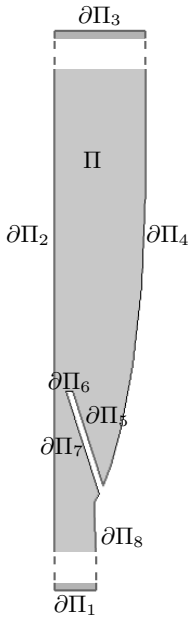

Figure 3.20: Geometry of 2D axisymmetric model with boundaries and fluid domain labelled.

The boundaries had no slip conditions applied to them, i.e.,

$$\boldsymbol{u}_{fluid} = 0, \quad \text{for } x \in \partial\Pi_i \text{ where } i = 4, 5, ..., 8. \tag{3.19}$$

The inlet and outlet pressures, p_{in} and p_{out} respectively, are assigned to either end of the domain,

$$p = p_{in}, \quad \text{for } x \in \partial\Pi_1 \tag{3.20}$$

$$\left(-p\boldsymbol{I} + \mu\left(\nabla\boldsymbol{u}_{fluid} + (\nabla\boldsymbol{u}_{fluid})^T\right)\right) \cdot \boldsymbol{n} = -p_{out}\boldsymbol{n}, \quad \text{for } x \in \partial\Pi_3 \tag{3.21}$$

where $\boldsymbol{n}$ is the normal vector to the boundary.

This was much quicker to solve than the 3D model, but because the model is rotated the valve is modelled as cone-shaped rather than having an elliptical shaped opening. This was considered a good enough approximation for comparing whether the Reynolds number of the flow affected the shape of the recirculation area.

3.2.4.2 2D Axisymmetic Fluid Model Results

Streamlines were plotted for different pressure differences. The colour bars show the velocity non-dimensionalised by the pressure difference. The velocity was non-dimensionalised as,

$$\frac{V\mu}{R\Delta P}, \tag{3.22}$$

where V is the velocity magnitude of the flow, μ is the viscosity, $R = 30.4$ μm is the radius of the outlet and $\Delta P = p_{in} - p_{out}$ is the pressure difference between the inlet and the outlet. The changes in pressure change the Reynolds number of the flow, however this did not seem to alter the shape of the recirculation area, within the biologically relevant range.

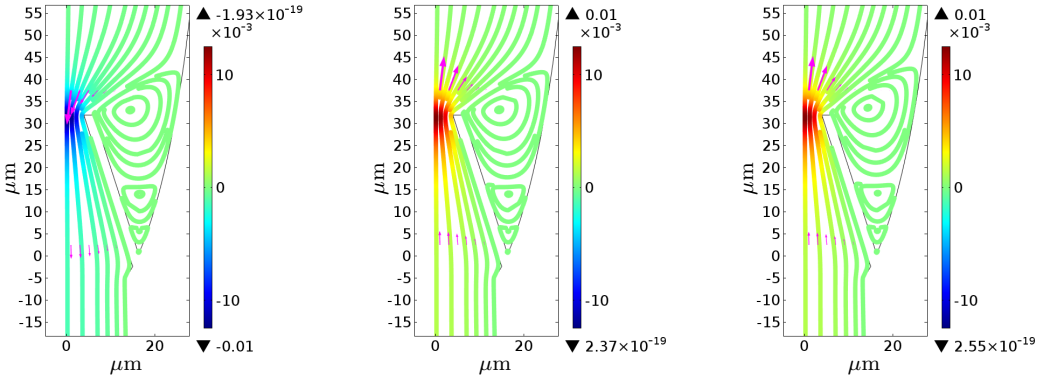

(a) Inlet 0.5 cmH_2O. Outlet 1 cmH_2O.

(b) Inlet 2 cmH_2O. Outlet 1 cmH_2O.

(c) Inlet 12 cmH_2O. Outlet 1 cmH_2O.

Figure 3.21: Streamlines with colour bars showing non-dimensionalised velocity. The magenta arrows show flow direction.

A video was provided by Michael Davis, Medical Pharmacology and Physiology, University of Missouri, of florescent beads in a lymphatic vessel. Some of the frames from the video were processed to give the impression of streamlines for comparison. The recirculation region can be seen, figure 3.22. This shows that the recirculation regions seen in figures 3.21 can also be observed experimentally.

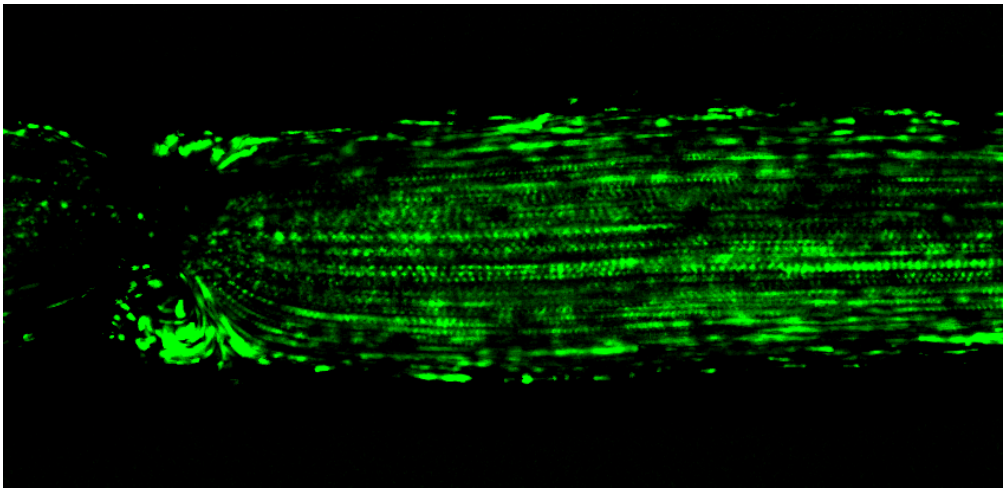

Figure 3.22: Overlaid frames from video by Michael Davis showing recirculation regions.

3.2.4.3 3D Fluid Structure Interaction Model with Linear Material Method

The initial model geometry is presented in figure 3.23. The literature described the valve leaflets as having a curved base and a buttress where the valve is attached to the wall. This has been reproduced in the model. The mesh was created using the COMSOL Multiphysics inbuilt meshing algorithm. A relatively course mesh was used with 143597 elements.

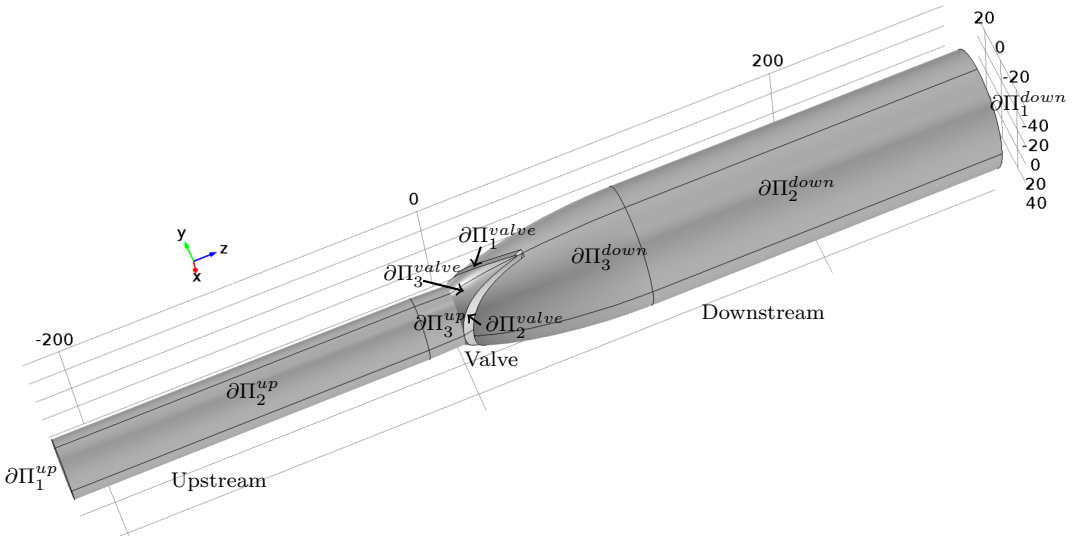

(a) Fluid domain with boundaries labelled.

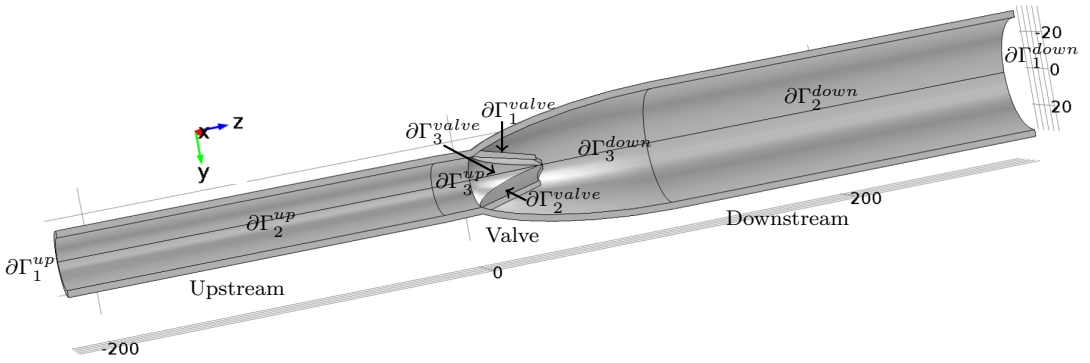

(b) Half the geometry for solid domain with boundaries labelled. The whole geometry was modelled, half is shown here to make the boundary labels clearer.

Figure 3.23: Geometry of the 3D fluid structure interaction model with a linear material model.

Some of the dimensions were difficult to achieve in the model due to the methods used to construct the geometry in COMSOL Multiphysics. The valve mid-line and upstream width were not exactly as shown in table 3.2. For example, the leaflet

thickness is exactly 2.2 μm at the free edge, but at the base where it connects to the wall it is slightly thicker, 2.75 μm.

The fluid domain, Π, was modelled using equations (3.17) and (3.18). For the solid domain, Γ, the behaviour was modelled by,

$$-\nabla \cdot \sigma = \boldsymbol{F}_v \text{ for } \boldsymbol{x} \in \Gamma \tag{3.23}$$

where σ is the stress tensor and $\boldsymbol{F}_v$ is the volume force vector. Both the wall and valve of the vessel had density 1500 kg/m^3 and a Poisson ratio of 0.24. The vessel wall had a Young's modulus of 33500 Pa and the valve had a Young's modulus of 15000 Pa.

In order to combine the behaviour of the fluid to the behaviour of the solid, the total force, $\boldsymbol{f}$, applied to the solid boundary by the fluid is calculated as,

$$\boldsymbol{f} = \boldsymbol{n} \cdot \left\{ -p\boldsymbol{I} + \mu \left(\nabla \boldsymbol{u}_{\text{fluid}} + (\nabla \boldsymbol{u}_{\text{fluid}})^T \right) \right\} \quad \text{on} \quad \boldsymbol{x} \in \partial\Pi_i^{up}, \partial\Pi_i^{down}, \partial\Pi_j^{valve} \quad \text{where } i = 2,3 \text{ and } j = 1,2,3, \tag{3.24}$$

where $\boldsymbol{n}$ is the normal vector pointing out of the fluid domain, p is the pressure and $\boldsymbol{I}$ is the identity matrix. However, in COMSOL Multiphysics, the Navier-Stokes equations are solved on the spatial frame, where as the solid equation, (3.23), is solved on the material frame. The transform from one to another is calculated as,

$$\boldsymbol{F} = \boldsymbol{f} \cdot \frac{dv}{dV} \quad \text{on} \quad \boldsymbol{x} \in \partial\Pi_i^{up}, \partial\Pi_i^{down}, \partial\Pi_j^{valve} \quad \text{where } i = 2,3 \text{ and } j = 1,2,3, \tag{3.25}$$

where $\boldsymbol{F}$ is the force in the material frame, $\boldsymbol{f}$ is the force in the spatial frame, dv is the mesh element scale factor for the spatial frame and dV is the mesh element scale factor for the material frame [COMSOL Multiphysics, 2013]. There is also a no slip condition applied to the fluid-solid interface in all other directions. This is given by the equation,

$$\boldsymbol{u}_{\text{fluid}} \cdot \boldsymbol{t} = 0 \quad \text{on} \quad \boldsymbol{x} \in \partial\Pi_i^{up}, \partial\Pi_i^{down}, \partial\Pi_j^{valve} \text{ where } i = 2,3 \text{ and } j = 1,2,3, \tag{3.26}$$

where $\boldsymbol{t}$ is the vector tangent to the solid domain.

The external boundary of the vessel, $\partial\Gamma_1$, has no constraints. Both ends of the vessel had a fixed constraint boundary condition

$$\boldsymbol{u}_{\text{solid}} = \boldsymbol{0} \quad \text{on} \quad \boldsymbol{x} \in \partial\Gamma_1^{up}, \partial\Gamma_1^{down}. \tag{3.27}$$

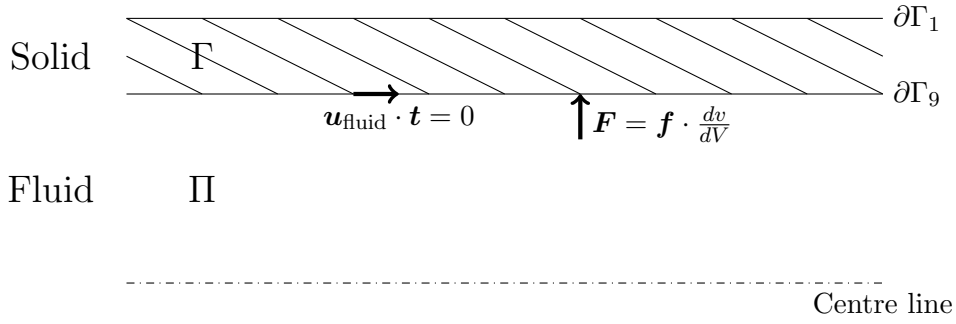

Figure 3.24: Summary of fluid-solid interface boundary conditions, not to scale.

An inlet condition was applied to the upstream end of the fluid domain. The inlet pressure, p_{in}, was defined,

$$p = p_{in} \quad \text{on} \quad \boldsymbol{x} \in \partial\Pi_1^{up}, \tag{3.28}$$

$$\left[\mu\left(\nabla \boldsymbol{u}_{\text{fluid}} + (\nabla \boldsymbol{u}_{\text{fluid}})^T\right)\right] \cdot \boldsymbol{n} = \boldsymbol{0} \quad \text{on} \quad \boldsymbol{x} \in \partial\Pi_1^{up}. \tag{3.29}$$

An outlet condition was applied to the downstream end of the fluid domain. The outlet pressure, p_{out}, was defined as,

$$\left[-p\boldsymbol{I} + \mu\left(\nabla \boldsymbol{u}_{\text{fluid}} + (\nabla \boldsymbol{u}_{\text{fluid}})^T\right)\right] \cdot \boldsymbol{n} = -p_{\text{out}}\boldsymbol{n} \quad \text{on} \quad \boldsymbol{x} \in \partial\Pi_3^{down}. \tag{3.30}$$

3.2.4.4 3D Fluid Structure Interaction Model with Linear Material Results

In the experiment, the change in the diameter of the vessel caused by increasing the internal pressure from 0.2 cmH_2O to 0.37 cmH_2O was 2.6%. A comparison is made to see if the finite element model exhibits the same behaviour as was seen in the experiment. The displacement is measured approximately 100 μm downstream of the valve.

The inlet pressure was set to 0.2 cmH_2O and the outlet pressure to 0.199 cmH_2O. The inlet and outlet pressure could not be equal as this would result in having no flow. This resulted in a diameter of 64.2 μm. The inlet pressure was then set to 0.37 cmH_2O and the outlet pressure to 0.369 cmH_2O. This resulted in a diameter of 66.1 μm. This gives a 2.9% diameter change. This is slightly larger than the diameter change seen in the experiments, so the value for the Young's modulus of the wall is perhaps too low.

The model was only able to converge for intraluminal pressures up to 14 cmH_2O. This could be a result of using a mouse vessel geometry with rat intraluminal pressures. In order to compare the model results with the data from Davis et al. [2011] and Rahbar et al. [2012] the diameters were normalised by dividing by the diameter at 14 cmH_2O. Figure 3.26, shows that the diameter change of the model does not have

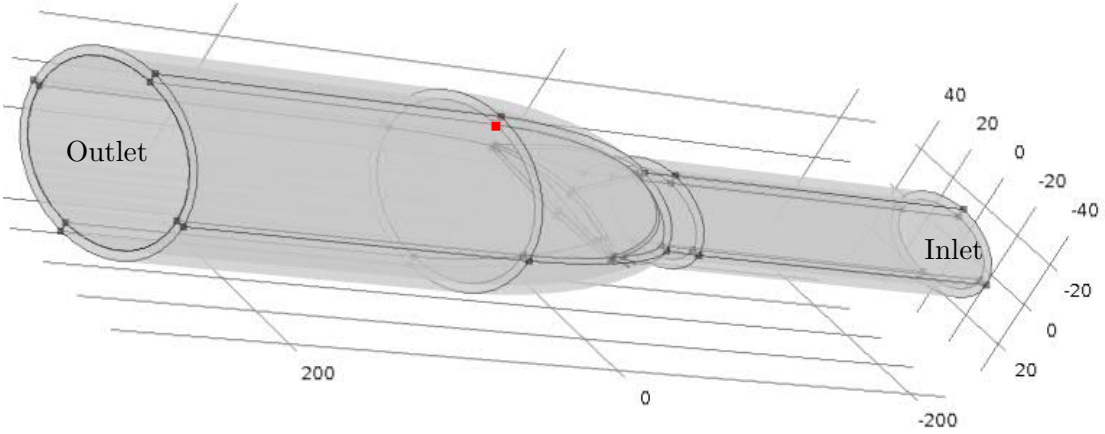

Figure 3.25: The displacement of the lymphatic wall in the model was measured at the red point shown on the internal boundary

the steep gradient followed by the sharp transition to a shallow gradient as seen in the experiments. The initial sharp increase between 0.2 cmH_2O and 0.5 cmH_2O is probably a result of the elliptical shape of the initial geometry configuration. As the pressure increases the vessel quickly forms a circular cross section and then expands. As the pressure increases from 1 cmH_2O to 14 cmH_2O the diameter increases linearly, as should be expected from a linear material model.

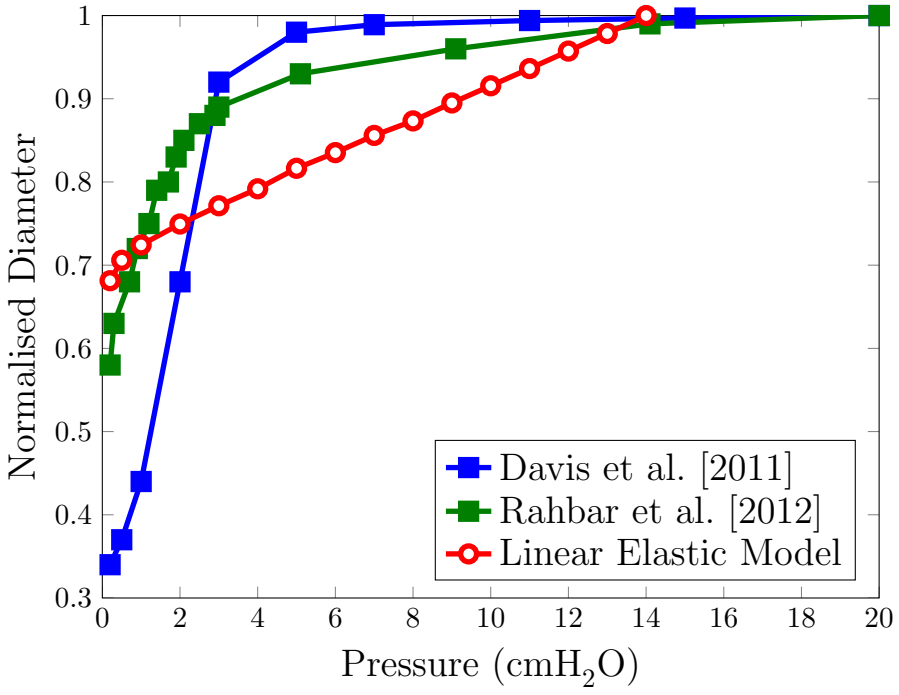

Figure 3.26: Pressure-diameter comparison to Davis et al. [2011]; Rahbar et al. [2012]. The diameter values in the literature was normalised by the diameter at 20 cmH_2O. The model data is normalised by the diameter at 14 cmH_2O.

The behaviour of the model was investigated for the case where the outlet pressure was fixed at 1 cmH_2O as the inlet pressure increased from 0.5 cmH_2O to 1.1 cmH_2O and 2 cmH_2O. The results are shown in figure 3.27. For inlet pressure 0.5 cmH_2O, see figures 3.27a and 3.27b, all the flow is backwards. At a smaller pressure difference than this the valve was shown to close in Davis et al. [2011]. The model valve does not close. This may be because the Young's modulus for the valve is too high or that the diameter of the surrounding walls is too large.

The inlet pressure 1.1 cmH_2O causes forward flow through the valve, as shown in figure 3.27c, but the inlet pressure was not high enough overcome the outlet pressure and make all the fluid flow forwards. A large recirculation region has formed downstream of the valve, see figure 3.27d. At about 100 μm downstream the forward flow through the valve meets the backward flow further downstream. The valve is open wider than for inlet pressure 0.5 cmH_2O.

When the inlet pressure is 2 cmH_2O the majority of the fluid flows downstream, figure 3.27e. There is a small amount of reverse flow around the valve as small recirculation areas are formed, as shown in figure 3.27f. These appear different to the regions in the axisymetric model due to the differences in the geometries used. The valve is wider than for inlet pressure 1.1 cmH_2O.

3.2.4.5 2D Fluid Structure Interaction model of Valve with Nonlinear Material Model Method

A simple two dimensional valve model was created in COMSOL of a beam in a channel to investigate the affect of the initial valve opening on the pressure required for valve closure. A diagram of the model can be seen in figure 3.28. The parameters used for the SEF with constant fibre angle were those calculated for the mean mouse vessel.

The height of the channel, H, was calculated by using Data thief to measure the value of D/D_{max} from Davis et al. [2011]. D_{max} was assumed to be 177 μm, taken from the maximum average rat diameter data used in chapter 2. The value for H was changed depending on the baseline pressure being investigated. The three baseline pressures used and their corresponding H values are shown in table 3.4. The thickness of the

Baseline Pressure (cmH_2O)	H (μm)
1	75
3	83
11	86.5

Table 3.4: The height of the channel was calculated from D/D_{max} from Davis et al. [2011] assuming that $D_{max} = 177$ μm.

leaflet (beam) was approximated as 6.6 μm by measuring the thickness of the valve tip

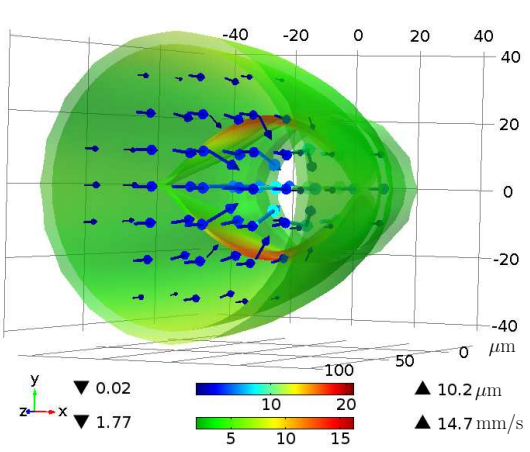

(a) Inlet 0.5 cmH_2O. Outlet 1 cmH_2O.

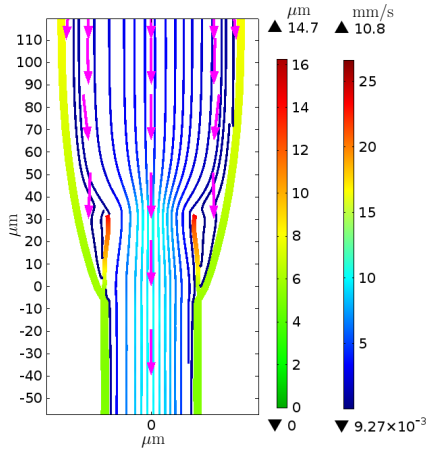

(b) Inlet 0.5 cmH_2O. Outlet 1 cmH_2O.

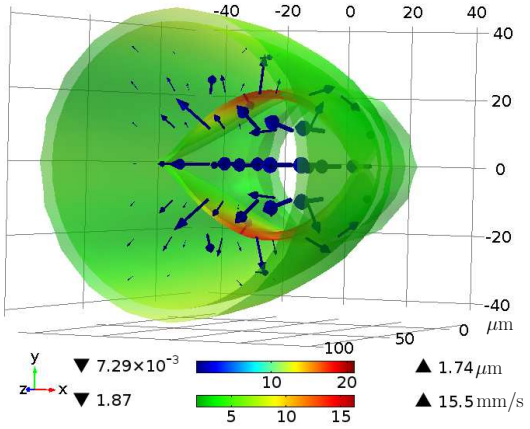

(c) Inlet 2 cmH_2O. Outlet 1 cmH_2O.

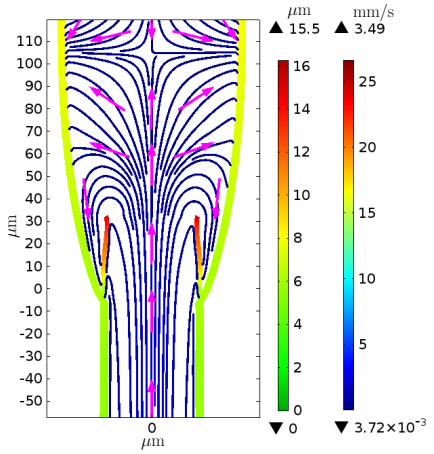

(d) Inlet 2 cmH_2O. Outlet 1 cmH_2O.

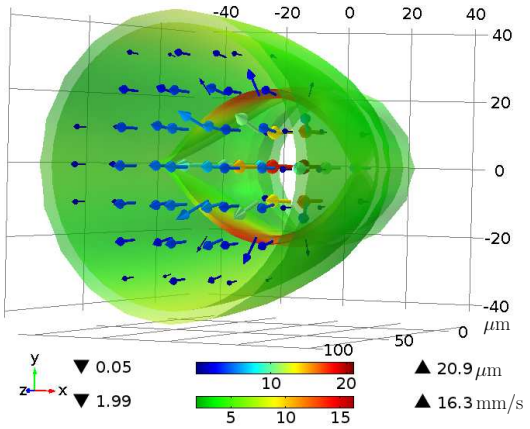

(e) Inlet 2 cmH_2O. Outlet 1 cmH_2O.

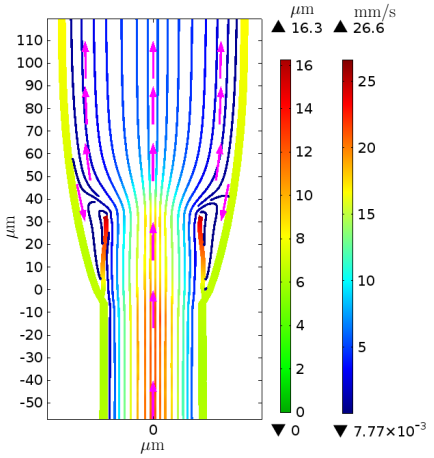

(f) Inlet 12 cmH_2O. Outlet 1 cmH_2O.

Figure 3.27: a,c and e: Wall and valve coloured to show displacement. Arrows coloured to show velocity magnitude. b,d and f: Wall and valve coloured to show displacement. Streamlines coloured to show velocity magnitude. Magenta arrows show flow direction.

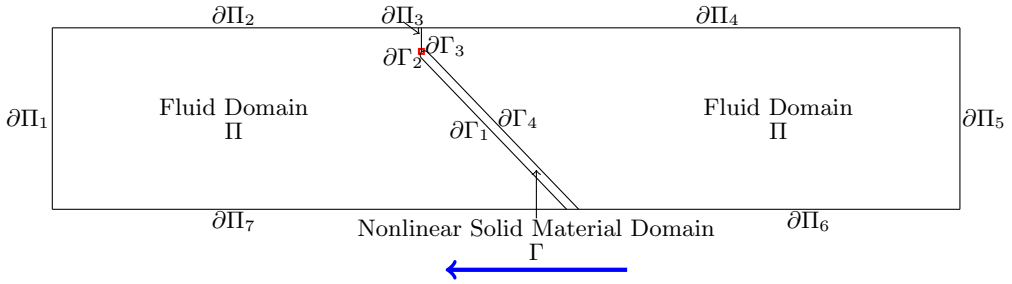

Figure 3.28: Diagram of 2D valve model. The blue arrow below indicates the direction of positive flow.

in the confocal image of the valve in Davis et al. [2011]. The valve length was equal to $2H$, so that it would always be long enough to close for the whole range of diameters. The angle of the valve was adjusted so that the initial ratio of vessel lumen to valve opening was 1:7 as reported in Davis et al. [2011] for each diameter.

As in section 3.2.4.3, the fluid domain is modelled using incompressible Navier-Stokes equations, (3.17) and (3.18). The solid domain is modelled as in section 3.2.4.3 with equation (3.23) using the material model developed in chapter 2. The solid and fluid domains are coupled together as described in section 3.2.4.3 on boundaries $\partial\Gamma_i$, where $i = 1, 2, 3, 4$.

The boundary conditions were prescribed as follows. The outlet condition defined on $\partial\Pi_1$ is given as,

$$\sigma \cdot \boldsymbol{n} = p_{out}\boldsymbol{n} \quad \text{on} \quad \boldsymbol{x} \in \partial\Pi_1 \tag{3.31}$$

At the opposite side of the rectangular fluid domain, the inlet condition is defined as,

$$\sigma \cdot \boldsymbol{n} = -p_{in}\boldsymbol{n} \quad \text{on} \quad \boldsymbol{x} \in \partial\Pi_5 \tag{3.32}$$

A symmetry condition is applied to the upper boundaries,

$$\boldsymbol{n} \cdot \boldsymbol{u}_{fluid} = \boldsymbol{0} \quad \text{on} \quad \boldsymbol{x} \in \partial\Pi_2, \partial\Pi_4 \tag{3.33}$$

and the mesh on these boundaries is allow to move in the x direction, but not in y.

$$d_x = 0 \tag{3.34}$$

$$d_y \text{ free} \tag{3.35}$$

A mesh displacement condition is defined on $\partial\Pi_3$, the boundary from the top of the flow domain to the top of the valve. This is present to maintain the mesh quality as the valve is displaced and does not effect the flow behaviour. The displacement

condition is defined as,

$$d_x = \int (X - x)\ du \tag{3.36}$$

$$d_y \text{ free} \tag{3.37}$$

where X is the coordinate of the point where the boundaries $\partial\Gamma_2$ and $\partial\Gamma_3$ meet in the original geometry and x is the coordinate of the same point after it has been deformed. Indicated by a red square on the valve sketch. This means that boundary $\partial\Pi_3$ remains vertical and moves horizontally as the tip of the valve moves. The bottom of the fluid domain is fixed,

$$d_x = 0 \tag{3.38}$$

$$d_y = 0 \tag{3.39}$$

and so is the base of the valve,

$$\sigma \cdot \boldsymbol{n} = \mathbf{0}. \tag{3.40}$$

A boundary load is applied to the tip of the valve, $\partial\Gamma_2$ and $\partial\Gamma_3$. The load is a Heaviside step function dependent on the maximum vertical non-dimensionalised position of the valve tip, $H(y/1\text{ m})$, that applies a large force to the tip as it nears the upper boundary of the channel.

$$\sigma \cdot \boldsymbol{n} = \begin{pmatrix} H(y/1\text{ m}) \times 10^6\text{ N/m}^2 \\ H(y/1\text{ m}) \times 10^6\text{ N/m}^2 \end{pmatrix} \tag{3.41}$$

This prevents the valve from leaving the channel and prevents the valve tip from contacting with the upper fluid boundary, which would cause numerical errors. It also means that when the valve is in 'closed' position there is a small gap that allows fluid through, however this gap is so small ($< 0.5\ \mu$m) and the fluid velocity so low that the valve is considered closed.

3.2.4.6 2D Fluid Structure Interaction model of Valve with Nonlinear Material Results

Three instances of the closing valve can be seen in figure 3.29. The valve remains straight until is reaches the mid-line of the vessel and then bends as the force is applied to the upper boundary to prevent the valve leaving the fluid domain. This bending of the valve is similar to the shape observed experimentally for a closed valve, see figure 3.14a.

A study was carried out to see how the initial valve opening ratio alters the closure pressure. The initial valve opening ratios were 1:7, 2:7 and 3:7 with respect to the

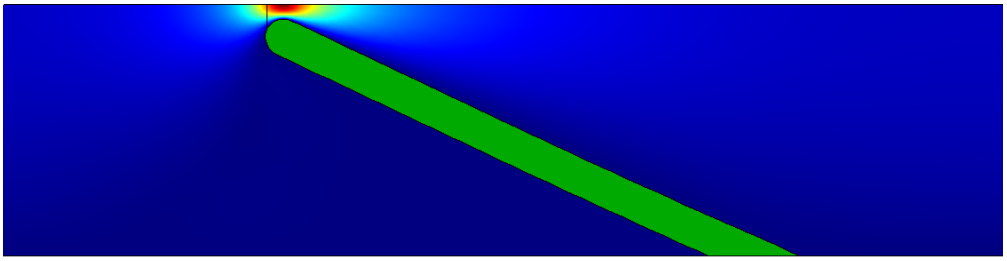

(a) Outlet pressure 1.0004 cmH_2O

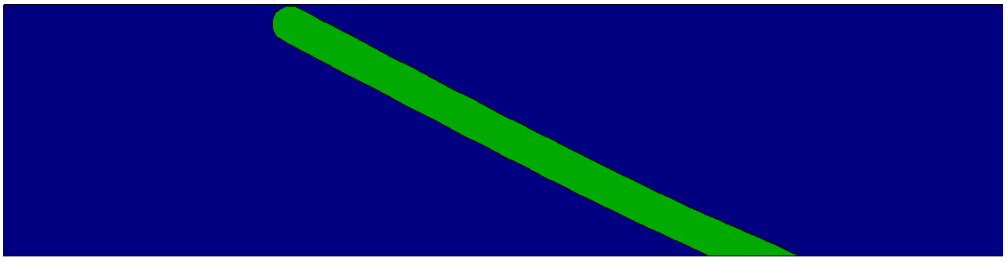

(b) Outlet pressure 1.0009 cmH_2O

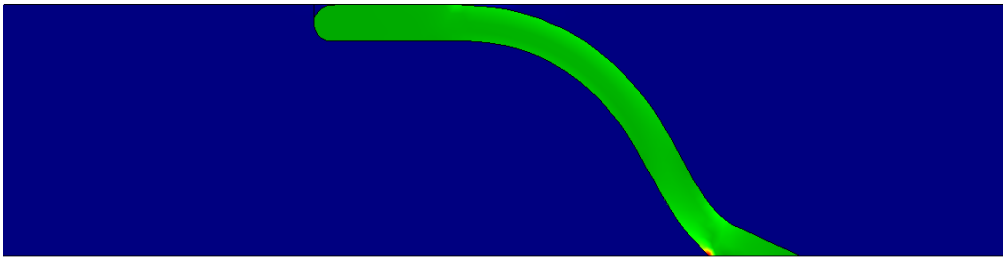

(c) Outlet pressure 1.3079 cmH_2O

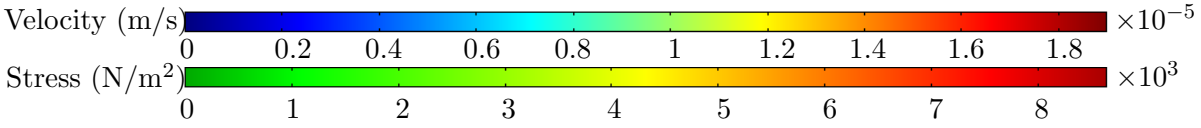

Figure 3.29: Inlet pressure 1 cmH_2O, opening ratio 1:7

diameter of the lumen. The ratios were each modelled at three different baseline pressures. The valve closure pressures are presented in figure 3.30

It can be seen in figure 3.30, that the pressure difference required for closure is five times larger for the 3:7 opening ratio than the 1:7 opening ratio. This shows that the original geometry of the model has a significant effect of the pressure difference for valve closure.

The pressure differences required are also three orders of magnitude smaller for the 2D model than the experiments. This is a result of simplifying the problem to two dimensions.

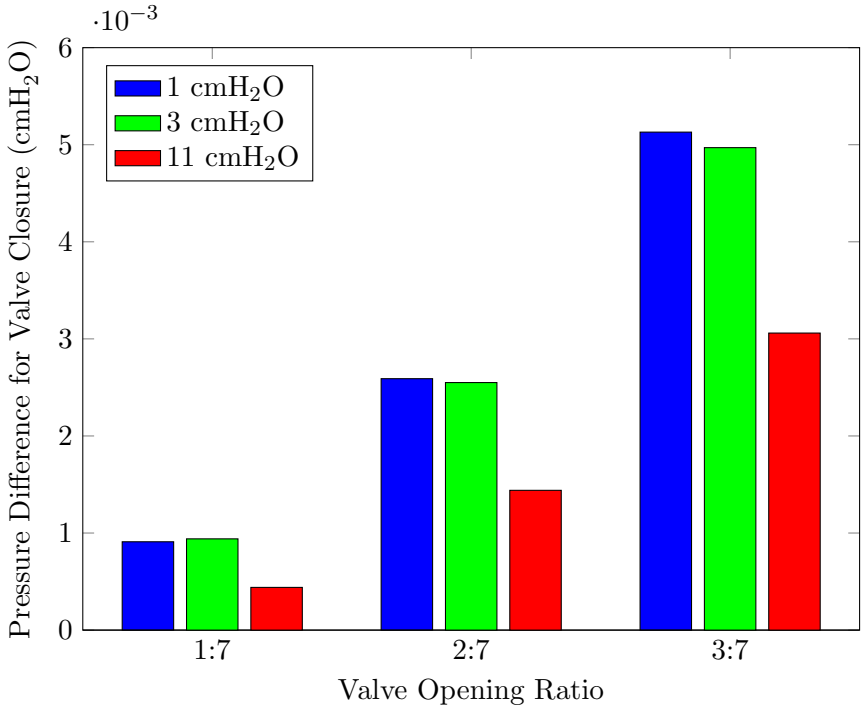

Figure 3.30: Summary of Valve Results. The different colours represent three different baseline pressures.

3.2.4.7 3D Solid Mechanics Nonlinear Material Model Method

The 3D geometry was simplified to include a valve within a cylindrical vessel. It was found during the development of the model that certain features of the valve geometry affected the closing behaviour. These are summarised in appendix A.2. Only a quarter of this geometry was modelled in order to reduce computational time and also to enforce four way symmetry of the problem. It was assumed that the material model was the same for the valve and the wall. The boundaries are defined as shown in figure 3.31.

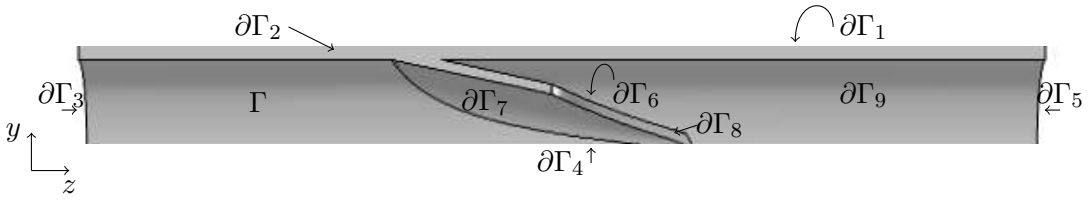

Figure 3.31: 3D model geometry of solid model, 90 degree segment of circular lymphatic vessel with valve. Boundaries are labelled.

A prescribed displacement is applied to the downstream end of the cylinder, to stretch the wall by a third,

$$\begin{aligned} u_x &= 0 \\ u_y &= 0 \qquad\qquad \text{on} \quad \boldsymbol{x} \in \partial\Gamma_5. \\ u_z &= \lambda_z Z \end{aligned} \tag{3.42}$$

where u_x, u_y and u_z are the components of the displacement vector $\boldsymbol{u}$. At the opposite end, the boundary is fixed,

$$\boldsymbol{u} = 0 \quad \text{on} \quad \boldsymbol{x} \in \partial\Gamma_3. \tag{3.43}$$

The boundary load was applied to the internal wall of the cylinder, both sides of the valve and the upper face of the valve,

$$\boldsymbol{\sigma} \cdot \boldsymbol{n} = -p\boldsymbol{n} \quad \text{on} \quad \boldsymbol{x} \in \partial\Gamma_6, \partial\Gamma_7, \partial\Gamma_8, \partial\Gamma_9. \tag{3.44}$$

In addition to these conditions, a symmetric boundary condition was applied to the faces that would be reflected in order to create the complete cylinder,

$$\boldsymbol{n} \cdot \boldsymbol{u} = \boldsymbol{0} \quad \text{on} \quad \boldsymbol{x} \in \partial\Gamma_2, \partial\Gamma_4 \tag{3.45}$$

This restricts movement in the direction normal to the boundary but allows movements in the other directions. The external boundary, $\partial\Gamma_1$, is free. A boundary load was applied to boundary $\partial\Gamma_7$, similarly to the valve tip in the 2D valve model that simulated the contact condition by applying a load as the boundary approached the centre line. The valve length was 115 μm.

A mesh refinement study was carried out that found a mesh with maximum element size equal to the wall thickness and a minimum element size equal to half the wall thickness was suitable. It was accurate to a finer mesh within 1 μm

3.2.4.8 3D Solid Mechanics Nonlinear Material Model Results

The valve closure pressure is defined as the first pressure at which there is a constant band of valve leaflet surface within 1 μm of the vessel central plane. This is evaluated by plotting the valve leaflet with blue representing the area more than 1 μm away from the central plane and red the area less than 1 μm away, see figure 3.32.

The three dimensional model of the collecting lymphatic valve closed at pressures lower than the experimental results, the values are compared in figure 3.33a to the experimental results from Davis et al. [2011]. The ratio of the inlet to outlet pressure at valve closure is also compared to the baseline pressure in figure 3.33b. The model

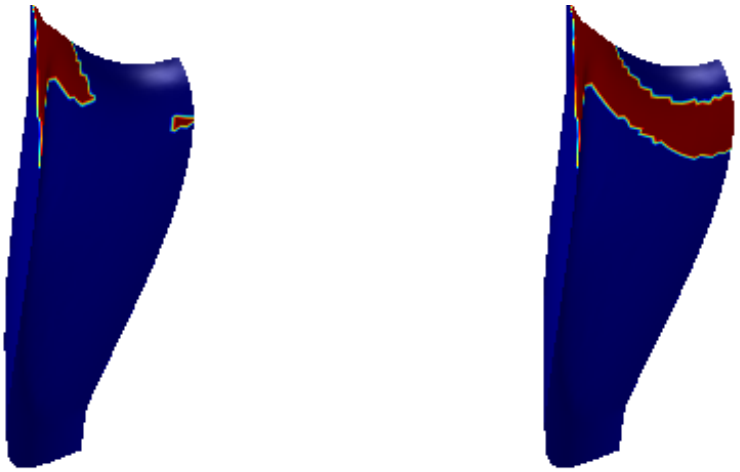

(a) Open: incomplete band of red

(b) Closed: complete band of red

Figure 3.32: Comparison of open and closed valve used for evalution of pressure difference required for valve closure.

results show that the ratio of inlet pressure to outlet pressure is constant for the model where as it decreases for the experimental data. Both the experimental data and the model results behaviour changes for baseline pressures less than or equal to 2 cmH_2O. However, for the experimental data the ratio plateaus between 1 cmH_2O and 2 cmH_2O, where as the model results show the ratio decreases.

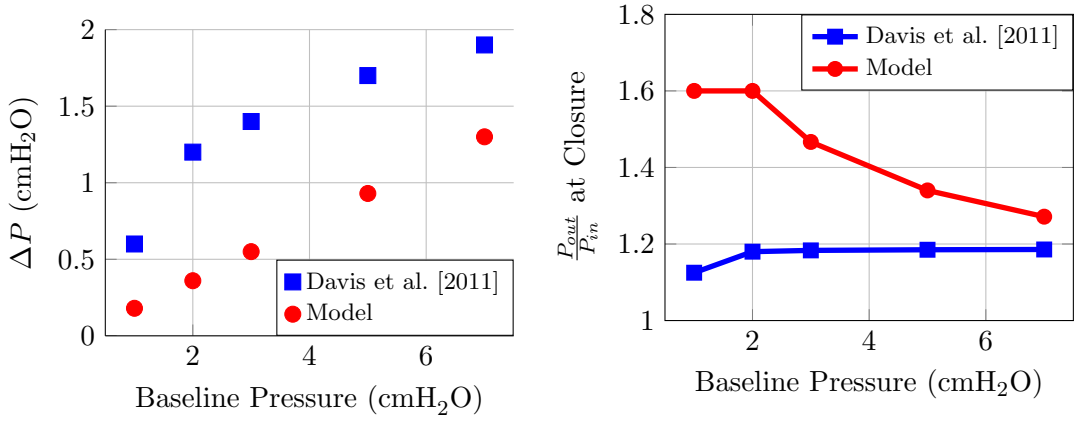

(a) Baseline pressure compared to pressure difference for valve closure

(b) Baseline pressure compared to ratio of baseline pressure to outlet pressure at valve closure

Figure 3.33: 3D model comparison with experimental results from Davis et al. [2011]

Figure 3.34 shows the lymphatic valve when the inlet and outlet pressures are equal, the pressure at which the valve closed, and the pressure that was reported for closure by Davis et al. [2011]. The tips of the valve leaflets curl back on themselves due to the buttresses being stretched by the vessel wall as it is stretched axially and as it expands due to increasing intraluminal pressure, see figures 3.34a and 3.34d. This means that the valve leaflet tips do not make contact first. A short distance along the

leaflets is the first point of closure, figure 3.34e. As the pressure is increased further, more of the valve leaflet surface comes into contact, figures 3.34c and 3.34f.

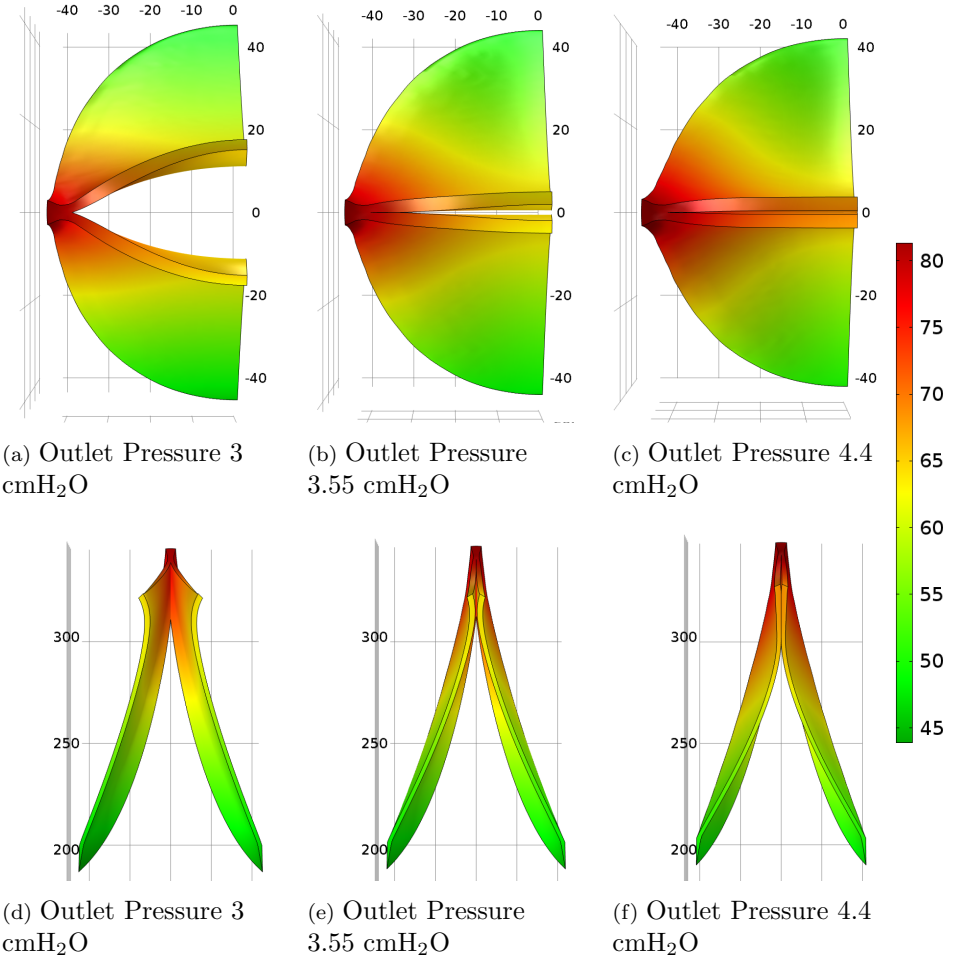

(a) Outlet Pressure 3 cmH_2O

(b) Outlet Pressure 3.55 cmH_2O

(c) Outlet Pressure 4.4 cmH_2O

(d) Outlet Pressure 3 cmH_2O

(e) Outlet Pressure 3.55 cmH_2O

(f) Outlet Pressure 4.4 cmH_2O

Figure 3.34: Valve results for baseline pressure 3 cmH_2O. Colour bar shows displacement in μm. Although not shown here, the lymphatic wall was also modelled.

3.2.4.9 Summary

In the previous sections, the methods and results of four models of the collecting lymphatic valve have been presented. In the next section the implications of these results are discussed.

3.3 Discussion

In this chapter the literature for collecting lymphatic valves and previous models have been reviewed. Four different models of the valve have been presented incorporating the behaviour of the wall.

A two dimensional axisymmetric fluid model was used to investigate the effect of changing the Reynolds number on the flow dynamics. The results showed that the shape of the recirculation region in the sinus of the valve did not change significantly for Reynolds numbers between 5.7×10^{-5} and 1.3×10^{-3}. The recirculation region was qualitatively compared to an image that had been obtained of the recirculation area by introducing fluorescent beads to the flow by Micheal Davis [personal communication including video].

A three dimensional fluid structure interaction model was used to investigate if using a linear elastic material model would be a suitable approximation for modelling the behaviour of the collecting lymphatic wall and valve over a range of physiologically relevant pressures. This model did not reproduce the behaviour of the wall when compared to the pressure-diameter curves in the literature. The initial sharp increase in the diameter at low pressures was hypothesised to be due to the elliptical vessel deforming to a more circular shape. The model was unable to converge for baseline pressures higher than 14 cmH_2O.

Coupling the fluid and solid behaviour together allows investigation into how the lymph, the wall of the vessel and the valve interact. Three pressure differences were considered. The outlet pressure is 1 cmH_2O and the inlet pressures are 0.5, 1.1 and 2 cmH_2O. The valve did not close for any of the pressure differences, but the gap widened for all of them. For an inlet pressure of 0.5 cmH_2O, it was shown in experiments that the valve closes for an outlet pressure of 0.8 cmH_2O [Davis et al., 2011]. Therefore, the valve should have closed for a pressure gradient of -0.5 cmH_2O. This implies that the Young's modulus for the model valve was too high. If the lymphatic vessels in the body behaved in this way, lymphoedema would probably develop as there is no way so stop the lymph flowing back towards the tissues. A small pressure gradient of 0.1 cmH_2O was not sufficient to cause all the lymph to flow in the same direction. This is caused by the widening of the vessel around the valve. It may be more appropriate to model a vessel with constant diameter as this flow interaction could be causing the widening of the wall downstream of the valve, whereas in the model the flow behaviour is a reaction to the geometry. The model presented estimated only the passive behaviour of the vessel. An active vessel could pump the lymph forwards, increasing the upstream pressure to overcome the downstream pressure. The positive pressure gradient of 1 cmH_2O was found to open the valve the widest. The majority of the lymph is flowing downstream, with the exception of the recirculation areas around the valve. An active vessel may decrease the frequency and amplitude of contractions in this case, as they are not necessary to ensure the fluid is drained away from the tissues.

The two dimensional fluid structure interaction model of the valve with a nonlinear material model was used to investigate the affect of the valve opening ratio on the

pressure required for valve closure. Increasing the opening ratio from 1:7 to 3:7 caused a five fold increase in the pressure required for valve closure.

Figure 3.30 showed that a smaller pressure difference is necessary for valve closure for higher baseline pressures. In contrast, the experimental results showed the opposite to be true [Davis et al., 2011]. The pressure differences required are also three orders of magnitude smaller for the 2D model than the experiments. The reasons for this may be a result of simplifying the problem to two dimensions, the assumptions made for the geometry and initial valve position and the densiometer method used to measure the closure pressure in the experiments.

The valve closes at much lower pressures than measured in Davis et al. [2011] - assuming it is closed when the valve tip is within 0.5 μm of the upper boundary. This finding agrees with Bertram et al. [2013a], who also predict that the closure pressure should be lower in order for the valves to be more efficient. However their predicted values are still much higher than the 2D model predicts. Bertram et al. [2013a] believe that the discrepancies between model and experimental are the result of resistance caused by the micropipettes cannulating the vessel. A reason for the discrepancies with the model presented above is that the closure pressure is measured when the tip of the valve reached an upper threshold. The densiometer in the experiments is measuring the closure pressure when the pressure is great enough to push the leaflets flat against each other. Another reason could be that due to the flexible material of the valve, too much of the structural strength is lost by modelling the valve in only two dimensions.

It was not possible to model the wall and valve in two dimensions because the non-linear material model had been developed as part of a two dimensional axisymmetric model, which has different boundary constraints to a 2D model. This resulted in the material model being much more flexible without the cylindrical support. It was assumed that the valve would be less sensitive to the change to symmetric from axisymmetric since the geometry of the valve is not axisymmetric. It was also assumed that the valve had the same material properties as the lymphatic wall. Assuming that the wall and valve have the same material properties implies that it is also assumed that the angle of the collegen fibres in the wall is the same as the angle of the collegen fibres in the valve. This is not the case. In reality, there may only be collegen fibres where the valve joins the wall [Vajda and Tomcsik, 1971; Rahbar et al., 2012] or the collegen fibres in the valve are aligned parallel to the face of the valve leaflet, extending from the buttresses towards the centre line of the leaflet [Lauweryns and Boussauw, 1973; Takada, 1971].

The three dimensional solid mechanics model of the collecting lymphatic wall and valve with a nonlinear material closed at pressure similar to those seen experimentally. However, during the development of the valve model, if was found that the geometry

of the valve and it's initial position could have a large affect on when the valve closed. The model valve closing at similar pressures to the experiment could imply that the final geometric arrangement is similar to a biological collecting lymphatic valve.

More recently, one dimensional models have highlighted the importance of effective valves to the efficient functioning of chains of lymphangions [Bertram et al., 2013a]. Of particular importance is how much resistance the valve causes to the flow and at what pressure difference the valve closes to prevent reverse flow [Bertram et al., 2013b]. A three dimensional mathematical model is a useful tool to investigate this phenomenon because it is difficult to make measurements experimentally without affecting the behaviour of the valve and surrounding wall. The finite element method has been used to model heart, venous and collecting lymphatic valves [Spühler et al., 2015; Kunzelman et al., 2007; Narracott et al., 2010; Wilson et al., 2015a,b] and Spühler et al. [2015]; Kunzelman et al. [2007] and Narracott et al. [2010] used the method to create two way coupled fluid structure interaction models of arterial, mitral and venous valves, respectively.

Using a linear approximation or even a simple nonlinear model such as the neo-Hookean model to a non linear material restricts the range of strains at which the model can be manipulated. Wilson et al. [2015b] used a nearly incompressible neo-Hookean material model with a shear modulus of 45 kPa to model the collecting lymphatic valve. The range used by Wilson et al. [2015b] was restricted to between 1 and 6 cmH_2O. The HGO strain energy function parametrised in chapter 2 allows for investigation in a range from 0.5 cmH_2O to 12 cmH_2O for mice and 14 cmH_2O for rats. The parameter c in the HGO SEF can be considered as the shear modulus of the material of the lymphatic vessel wall without the collagen fibres. Compared to the value used by Wilson et al. [2015b] for the valve leaflets the values for c are two orders of magnitude smaller, ranging from 0.35 to 1.48 kPa for the constant fibre angle model and 0.16 to 0.54 for the variable fibre angle model.

Wilson et al. [2015a] created an image based two dimensional model of flow around an opening lymphatic valve by using the images to define the deformation of the domain as the valve opened. The valve model created in section 3.2.4.5 similarly defines the height of the channel using experimental data, however the idealised valve leaflet is two way coupled to the fluid domain surrounding it allowing for investigation into the closing behaviour of the valve.

Bertram et al. [2013a] hypothesised that the closing pressures differences measured by Davis et al. [2011] overestimate the actual values. Bertram et al. [2013a] found that incorporating the valves from Davis et al. [2011] lead to inefficient pumping in their network model and that this could be remedied by decreasing the closing pressures and predict that the pressure difference for valve closure should never be higher than 0.5 cmH_2O. The nonlinear material model developed in chapter 2 implemented on a

three dimensional solid only model was used to investigate this claim. It was found that the solid model from section 3.2.4.7 estimated the pressure difference for valve closure to be lower than measured in experiments, but higher than predicted by Bertram et al. [2013a]. Bertram et al. [2013a] suggest the source of experimental error could be due to the resistance caused by the tip of the micro-pipette used by Davis et al. [2011] to calculate the vessel. An alternative reason for the difference could be the use of the densitometer to define whether the valve is open or closed. In the model from section 3.2.4.7 the pressure difference for closure is defined as the pressure at which the minimum distance of the inner surface of the valve leaflet is within 1 μm of the centre line of the vessel. The densitometer measured the mean pixel intensity to determine if the valve was closed. It may be that the two leaflets have to be in contact along a length of the leaflets before the densitometer registers that the valve has closed, therefore the pressure required for valve difference is higher than found using the model. This shows an advantage of using a computational model over experiments as it allows for observation of the valve position from all angles as there is no restriction due to visual obstructions as there are in the physical experiment.

In this chapter it has been shown that it is possible to create a fluid structure interaction model of a lymphatic valve and the surrounding wall. It has also been shown it is possible to model valve closure within finite element method if some assumptions are made, i.e. that valve is closed when it is within a micrometer of actual closure and the valve opening to lumen ratio is not too large. Finally, it has been presented that incorporating a non-linear material model produces more accurate solid behaviour, but increases the computational challenges. The initial geometry has been found to have a significant affect on the behaviour of the model valve.

3.4 Future Work

Modelling the closing behaviour of the collecting lymphatic valve has unearthed many necessary routes of investigation about the geometry of these valves. The shape is very important for the valve to function correctly. This has been highlighted previously by Bazigou et al. [2009]. It would be useful to image or measure a valve at a good resolution during and after it has been used for valve closure experiments, perhaps applying confocal microscopy techniques such as those used by Wilson et al. [2015a] and Watson et al. [2015]. Discovering which aspects of the valve geometry are important for proper functioning of the valve would be useful as effective valves could be manufactured for use in microfluidics. The variation in geometry could be a factor that leads to the wide variation of closure pressures seen by Bertram et al. [2013a].

- Using the geometry and material properties from the solid only three dimensional valve model created in chapter 3, include a fluid domain and create a fluid structure interaction model of a passive collecting lymphatic valve.
- Compare the results of the closing pressures required to experimental data from Davis et al. [2011].
- Perform a sensitivity analysis on the material parameters and geometry of the valve and surrounding wall.
- Increase and decrease the inlet and outlet pressure beyond healthy physiological values to investigate under what conditions the valve fails to prevent significant back flow.
- Calculate the resistance to forward flow caused by the valve at different pressures to compare how the resistance relates to changes in pressure. This information could be used as an input to the network model developed by Bertram et al. [2011, 2013b,a].
- Increase the stiffness of the wall to model the thickening of the lymphatic wall which develops during lymphoedema.
- Develop an image based model using techniques such as those presented in Wilson et al. [2015a] in order to capture the geometry of the valve as accurately as possible.
- Investigate materials that could be used to manufacture valves for micro-fluidic devices and apply the material properties to the model to evaluate if the material produces a valve that functions effectively.
- Use the model to investigate on how different fluid behaviours affect the behaviour of the pumping vessel and effective functioning of the valve.

Chapter 4

Selective Plane Illumination Microscopy Image Based Modelling of Lymph Nodes

4.1 Introduction

In this chapter an image based model of fluid flow through a lymph node is presented. The transport of cells and particles through the nodes is thought to be influenced by the fluid behaviour. In this chapter a literature review of lymph nodes is presented, followed by a description of the methods used to create an image based model of fluid flow through a lymph node and the results from this model.

4.2 Literature Review

The average human has about 650 lymph nodes [Földi et al., 2003]. They filter the lymphatic fluid, facilitate the migration and production of lymphocytes and regulate the lymph protein content. Many primary immune responses originate in lymph nodes [Gretz et al., 2000]. Depending on their location, nodes are between 0.1 and 3 cm in diameter. Lymph nodes can be different shapes, such as spherical, oval, or kidney-shaped [Földi et al., 2003]. Lymph nodes dissected from near the throat of 24 dogs were about $36 \times 12 \times 20$ mm. In some cases smaller nodes were found near by with approximate dimensions $4 \times 8 \times 3$ mm [Belz and Heath, 1995a]. Popliteal, from the back of the knee, nodes from mice were approximately $2 \times 1 \times 1$ mm [Kowala and Schoefl, 1986]. A generalised description of the structure of the lymph node is presented in the next subsection 4.2.1. There is variation among lymph nodes depending on location and species.

4.2.1 Structure

Each lymph node is contained within a capsule, which is made up of collagen, elastin and some smooth muscle cells. Collecting lymphatics feed into the lymph node through the capsule. One or two efferent lymph vessels lead out of the lymph node near to where an artery enters the node and a vein leaves the node. This area of the node is called the hilus.

Larger nodes may have more than one artery, vein and efferent lymphatic. Belz and Heath [1995a] observed up to 10 efferent vessels leaving the node in the hilar region of dog lymph nodes and vessels with diameter 30 μm or greater contained valves. Kowala and Schoefl [1986] found that for majority of mouse popliteal lymph nodes that they studied had the same number of afferent lymphatics as lobules, units within the node, although this was not always true. The number of efferent lymphatics varied, some having up to 5 per node [Kowala and Schoefl, 1986].

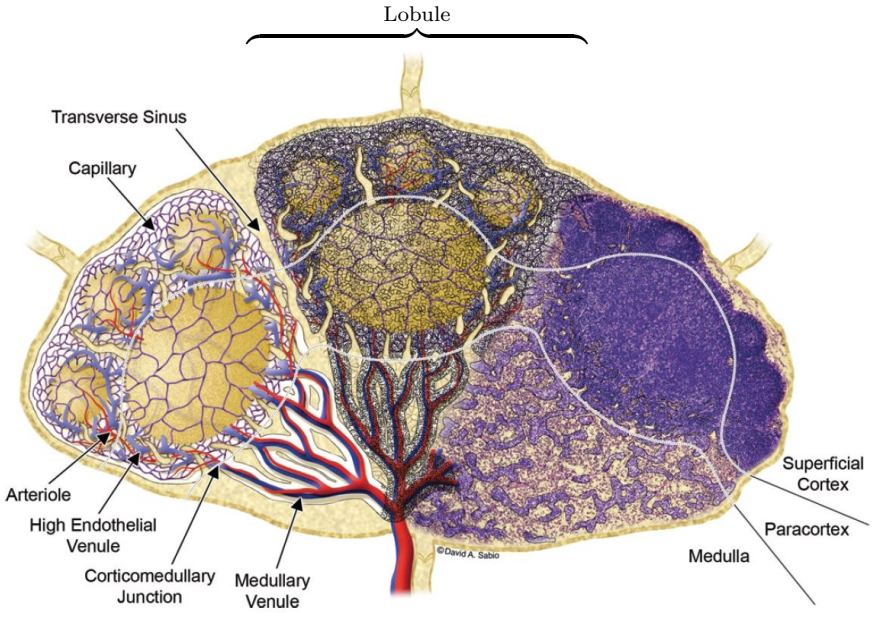

Figure 4.1: Sketch of lymph node from Willard-Mack [2006]. Three lobules are shown. The left lobule shows arteries (red), veins (blue) and capillary networks (purple), although the capillary networks are neglected from the cords. The lobule in the centre includes a representation of the reticular fibre network. The right lobule shows how a lobule appears in a histological section from a rat mesenteric node. ©2006, SAGE Publications. Permission to use this figure has been granted by SAGE Publications, Inc.

The main structures that make up a lymph node are:

- Trabeculae: Collagen structures that extend into the node from the capsule forming a skeleton for the node. Blood vessels and lymph vessels can run through the centre.

- Lobules: Individual units within the node, see figure 4.1.
- Superficial Cortex: Very dense lymphatic tissue near the node capsule. Also known as the cortex.
- Follices: Spherical sections of lymphatic tissue homed to by B lymphocytes (immune cells originating from the bone marrow, also known as B cells).
- Paracortex: Dense lymphatic tissue homed to by T lymphocytes (immune cells originating from the thymus, also called T cells). Also known as the deep cortex or inner cortex.
- Medulla: Less dense lymphatic tissue.
- Sinus: Cavity or channel through which the lymph flows.
  - Subcapsular Sinus: Afferent lymph vessels deliver the lymph into this sinus, which runs round the node just below the capsule. Also known as the marginal sinus.
  - Cortical sinus: Sinus which allows passage of fluid through the cortex. Also known as intermediate sinus.
  - Medullary sinus: Sinus through the medulla.

Within the antihilar side of the node, just beneath the capsule, lies the subcapsular sinus. Below this is the superficial cortex and then the paracortex. Between the superficial cortex and the subcapsular sinus there are occasional follices. Beneath the paracortex is the medulla and finally the hilus. These sinuses are the primary pathways for fluid flow through the node. In the rest of this chapter we discuss these structures in more detail and the pathways through the node for both blood and lymph.

The lymphatic tissue that makes up the internal structures of the lymph node is mainly formed of lymphocytes and reticular cells surrounded by reticular fibres. Reticular cells are a type of fibroblast. These are immature connective tissue cells that synthesize collagen and elastin [Földi et al., 2003]. The reticular cells form a network that is a frame work for the lymph node [Gretz et al., 2000]. This forms a extracellular space separate from the lymphocyte spaces [Gretz et al., 2000]. Fluid and solutes can flow through the reticular extracellular space, which may protect the lymphocytes from certain solutes [Gretz et al., 2000]. The fluid flow through lymph nodes has been shown to regulate the reticular cell network [Tomei et al., 2009]

Within a lymph node capsule there are one or more lobules, depending on the size of the node [Kowala and Schoefl, 1986; Willard-Mack, 2006]. The lobules appear bulbous near antihilar side of the node and narrow towards the hilus. The lobules are surrounded by sinuses, see figure 4.1. Frequently the number of afferent lymphatics

is equal to the number of lobules, but this is not always the case [Willard-Mack, 2006; Kowala and Schoefl, 1986]. It is possible that each of the lobules are exposed to different solutes and pathogens as the lymph could have come from different areas.

4.2.2 Lymph Pathways

It is possible for some of the lymph to bypass a node completely. This is facilitated by some afferent and efferent vessels that are connected together [Kowala and Schoefl, 1986; Földi et al., 2003]. The lymph that does enter the node through the afferent lymph vessels flows into the subcapsular sinus.

The sinuses are channels for the lymph fluid to move through the lymph node. They have an porous endothelial lining [Anderson and Anderson, 1975]. They exist throughout the node, having different names depending on their location. The sinuses in different regions of the node have different dimensions and structures.

The subcapsular sinus is traversed by reticular fibres, formed from collagen [Ohtani et al., 2003]. These fibres form a mesh to filter the lymph. The fluid can move freely through pores in the subcapsular sinus lining but larger particular matter cannot [Ohtani et al., 2003]. Belz and Heath [1995a] observed that the subcapsular sinus ran around the periphery of the node. It is assumed from the structure that lymph flows from the subcapsular sinus into the intermediate sinuses although the intermediary sinus is not always present [Ohtani et al., 2003]. Pores in the lining of the subcapsular sinus allows fluid to flow into the cortex [Ohtani et al., 2003]. Particles in the lymph that are larger than 0.05 μm do not pass from the cortical sinus into the cortical parenchyma [Gretz et al., 1997]. This may protect the lymphatic tissue from certain pathogens. The subcapsular sinus is also continuous with the medullary sinuses in the hilar region so some fluid follows this pathway [Ohtani et al., 2003].

The cortical sinus, or intermediary sinus, is a network of sinuses that connect the subcapsular sinus to the medullary sinus. Belz and Heath [1995a] saw two forms of cortical sinuses in dog lymph nodes. Mainly in the superficial cortex around the base of follicles they saw gaps 10 to 45 μm across with few reticular cell processes. In the deep cortex near to high endothelial venules (HEVs), which will be discussed further in section 4.2.3, they were 20 to 115 μm across and crossed with many processes. The walls had holes 2 to 3.5 μm across through which cells appear to pass. Kowala and Schoefl [1986] saw that some of the cortical sinuses in the mouse popliteal lymph node were filled with so many lymphocytes that they resembled lymphatic tissue.

The paracortical sinuses are also known as lymphatic labyrinths and lie beneath the follicles in rat mesenteric lymph nodes. They are a network of lymphatic vessels with diameters less than 100 μm in rat lymph nodes that connect to the medullary sinuses [Ohtani et al., 2003]. The paracortical sinuses contain many lymphocytes, but are not

criss-crossed with reticular fibres and the lymphocytes can pass through the walls [Ohtani et al., 2003]. HEVs are often located less than 10 μm away and the space between is full of lymphocytes [Ohtani et al., 2003; Willard-Mack, 2006]. In rat lymph nodes the sinuses formed networks around HEVs [Anderson and Anderson, 1975].

The medullary sinuses surround the medullary cords and are criss-crossed with reticular fibres [Belz and Heath, 1995a; Ohtani et al., 2003]. The medullary sinuses are formed of branching, tortuous channels and in the rat lymph node were large and connected to the subcapsular sinus at the hilus [Anderson and Anderson, 1975; Ohtani et al., 2003]. Efferent lymph vessels drained fluid from the medullary sinuses and the subcapsular sinus near by [Belz and Heath, 1995a; Ohtani et al., 2003; Kowala and Schoefl, 1986]. These vessels were initially 20 to 50 μm across, formed by interlinking cell processes, 2.5 to 7.5 μm diameter [Belz and Heath, 1995a]. Closer to the trabeculae the efferent vessel walls were more complete with holes 10 to 30 μm diameter.

Apart from the sinuses there are other pathways for the lymph to flow through, cords, perivenular channels, corridors, conduits and ducts. However, this a comparatively small compared to the feature discussed above and therefore will not be included in this review. A review of these features can be found in appendix A.3.

4.2.3 Blood Vessels

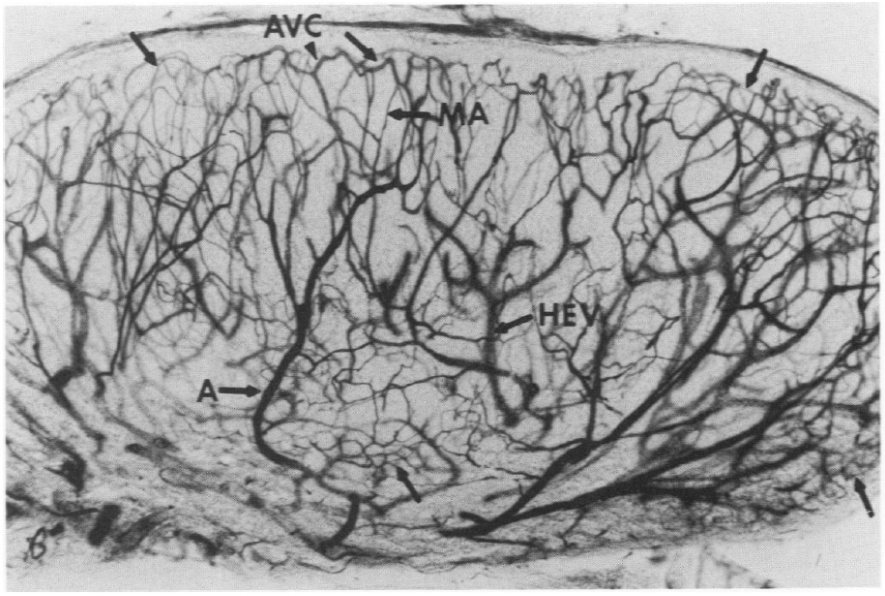

Figure 4.2: Blood vessels of a rat lymph node. A: arteries, AVC: arteriovenous communication, MA: metarterioles, HEV: high endothelial venules, arrows: cortical and medullary capillary arcades (×47). This image was published in Anderson and Anderson [1975] Copyright 1975, American Society for invesitagtive pathology; Published by Elsevier Inc; All rights reserved.

Blood vessels in the lymph nodes form a complex network. As the arteries extend from the hilus to the superficial cortex of dog lymph nodes they branched off and in the cortical parenchyma joined capillary networks mainly next to the subcapsular sinus, next to the trabecular sinuses and around secondary nodules [Belz and Heath, 1995b]. Other arteries also fed into these networks. The networks drained into venules that were further from the sinuses or the nodules than the capillaries [Belz and Heath, 1995b]. These venules in turn drained into larger venules, into HEVs and finally into a few larger HEVs that merged together, passing through trabeculae, so that only 2 or 3 veins left the node [Belz and Heath, 1995b]. Crivellato and Mallardi [1997] studied lymph nodes from mice. They saw that blood vessels were surrounded by reticular cells. More details about the blood vessels in lymph nodes can be found in the appendix A.3

Within lymph nodes there are both high endothelial venules (HEVs) and low endothelial venules (LEVs). HEVs appear to be the most common site for lymphocytes to leave the blood stream. In mouse popliteal lymph nodes HEVs arise near the subcapsular sinus and widen abruptly [Kowala and Schoefl, 1986]. Anderson and Anderson [1975] observed a similar effect in rat lymph nodes as can be seen in figure 4.3. LEVs and small HEVs (< 20 μm) contained few lymphocytes, large HEVs had many lymphocytes in the walls [Kowala and Schoefl, 1986].

4.2.4 Fluid Flow through Lymph Nodes

Adair et al. [1982] and Adair and Guyton [1983, 1985] investigated the flow though lymph nodes in dogs and found that the node acts as a fluid exchange chamber. For each lymph node they cannulated an efferent and an afferent lymphatic, ligating other afferent and efferent lymphatic vessels. In each experiment the change in the protein concentration of the fluid was assessed with respect to changing different inputs. The concentration of proteins is important because it affects the amount of fluid transfer into and out of the blood vasculature.

Adair et al. [1982] increased and decreased the afferent flow to investigate how this affected the protein concentration. They found that increasing the perfusion rate, increased the amount of flow crossing the wall of the blood vessels and that the protein concentration of the lymph leaving the node was higher than the concentration entering the node. The authors hypothesised that 98% of the increase in protein concentration was due to the transfer of fluid into the blood vessels.

Adair and Guyton [1983] investigated the affect of increasing the venous blood pressure in the node. They found increased blood pressure caused an increase in the amount of efferent flow out of the node and a decrease in the efferent protein

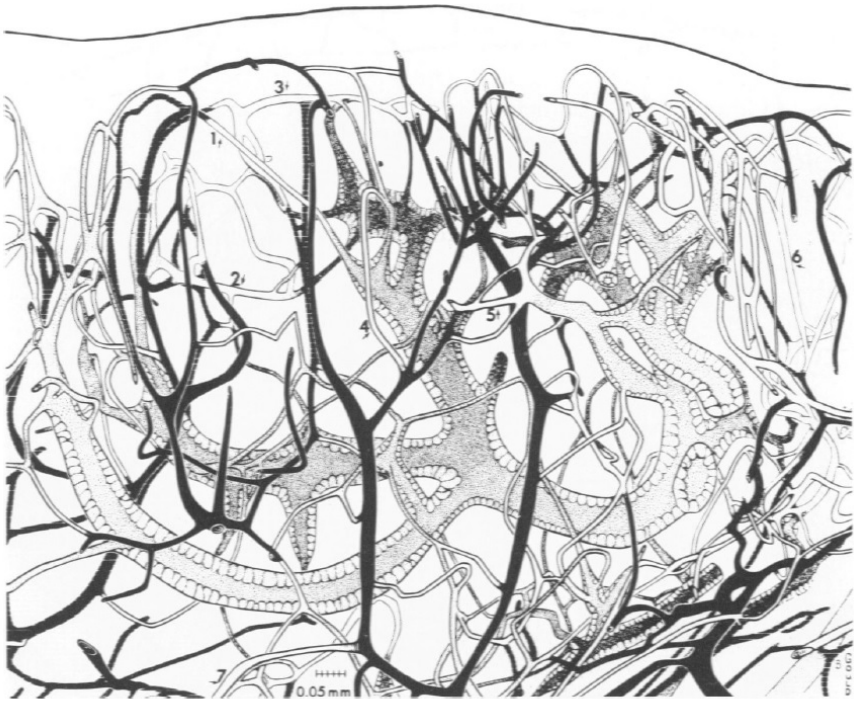

Figure 4.3: Structure of blood supply to cortex in rat lymph node. Arteries are black and high endothelial venules are stippled. The numbers indicate arteriovenous communications. This is a tracing of a projected image of lymph node vasculature. This image was published in Anderson and Anderson [1975] Copyright 1975, American Society for invesitagtive pathology; Published by Elsevier Inc; All rights reserved.

concentration. This supported deductions made in Adair et al. [1982] that fluid transfer across the blood vessel walls caused the change to the protein concentration.

Adair and Guyton [1985] increased the pressure of the efferent flow. At efferent pressures up to 8 mmHg the protein concentration increased. However, for efferent pressures higher than 8 mmHg the protein concentration decreased. This implies that under extreme conditions, such as a patient with lymphoedema, when the pressures in the lymphatic system are much higher than under normal conditions the function of the lymph node is impaired.

Nagai et al. [2008] carried out an experiment to investigate lymph node perfusion properties and how these were effected when the lymph node was inflamed. Using a set up similar to Adair et al. [1982] and Adair and Guyton [1983, 1985], they found that increases in afferent pressure or decreases in efferent pressure caused the efferent flow rate to increase, and that these relationships were linear, which agrees with the findings of Adair and Guyton [1985]. To model an inflamed lymph node, the lymph node was perfused with artificial lymph within which formyl-Met-Leu-Phe-OH was dissolved. This produced acute inflammation in the node. As a result of this, the

efferent outflow rate decreased, implying the inflammation caused more resistance to flow across the blood vessel wall [Nagai et al., 2008].

These experiments are useful for deducing how the afferent and efferent flow properties may affect fluid exchange within the node. However, they do not give empirical information on what is occurring within the node. Other authors have attempted to investigate this by tracing particle movement.

4.2.5 Flow of Particulate Matter through Lymph Nodes

Ikomi et al. [2012] investigated how micro-spheres travelled though a popliteal node from a rabbit. They state that particles of 2 mm or greater rarely passed through the node. As the particle size decreased, the amount of particles passing through the node increased hyperbolically [Ikomi et al., 2012]. Gretz et al. [2000] showed that two molecules with similar molecular weights, but different radii took different pathways within the node. Gretz et al. [2000] concluded that it depends on the radius of the molecule whether it can make it's way into the cortex along the fibres, rather than the molecular weight.

Ohtani et al. [2003] discuss the possibility that the lymph node may have a macromolecule concentrating mechanism. If the interstitial fluid in the node is absorbed into other vessels this would cause fluid in the subcapsular sinus to be sucked through the pores into interstitial space along with molecules in the fluid [Ohtani et al., 2003]. Guyton and Adair [1985] discuss how water can move between blood and lymph in nodes, possibly by Starling's hypothesis, which is discussed section 4.2.7.

Most of the information about how fluid moves through the lymph node is inferred from the movement of particles within the node. Particles can be used to trace the pathways of fluid flow though lymph nodes. However, this may be biased because lymph nodes filter the lymph and hence are able to capture particles and retain them.

4.2.6 Three Dimensional Lymph Node Imaging

Deep tissue imaging is possible through techniques such as computed tomography, selective plane illumination microscopy (SPIM) and optical projection tomography (OPT). Due to the small size and transparent tissue of the lymph node, it is possible to use these techniques to image the whole organ. Computational tomography will be covered in detail in chapter 5; here SPIM and OPT are described.

For SPIM, a cylinder of agarose gel, within which the sample to be imaged is embedded, is immersed in fluid. The lens of the microscope objective is also in

the fluid. A laser sheet is projected through the sample through a glass window, orthogonal to the microscope lens [Huisken et al., 2004]. This method enables the sample to be optically sectioned without needing to physically cut up the sample. The laser excites the florescence in the sample and the microscope collects this florescence. Since different florescence can be excited by changing the laser wavelength, different stains can be used to stain various aspects within the sample. This technique has been used by Mayer et al. [2012] to image lymph nodes, see figure 4.4. They used two stains to highlight the high endothelial venules and dendritic cells to investigate the relation between them.

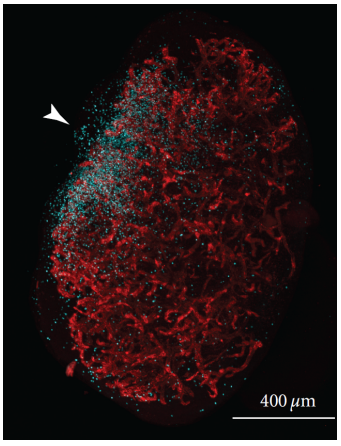

Figure 4.4: SPIM image from Mayer et al. [2012] of high endothelial venules in red and dendritic cells in blue. Arrow indicates approximate position of afferent lymphatic vessel. ©2012 Jürgen Mayer et al. Permission not required.

For OPT the sample is also within a cylinder of agarose gel. The light transmitted from the sample is collect onto a camera imaging chip. A plane through the cylinder corresponds to a line of pixels on the detector. The projections must then be reconstructed to create the 3D image stack. This technique has been used to image lymph nodes by Pfeiffer et al. [2008] staining the high endothelial venules and medullary sinuses to show that the venules did not cross the sinuses, see figure 4.5.

4.2.7 Computational Models of Porous Media

Fluid flow in porous media is modelled using Darcy's law and conservation of mass,

$$\boldsymbol{u} = \frac{\boldsymbol{\kappa}}{\mu}\boldsymbol{\nabla} p, \tag{4.1}$$

$$\nabla \cdot \boldsymbol{u} = 0 \tag{4.2}$$

where $\boldsymbol{u}$ is the Darcy velocity, the average fluid velocity per unit of total volume of the material, $\boldsymbol{\kappa}$ is the permeability dependent on the pore size and geometry, and p is

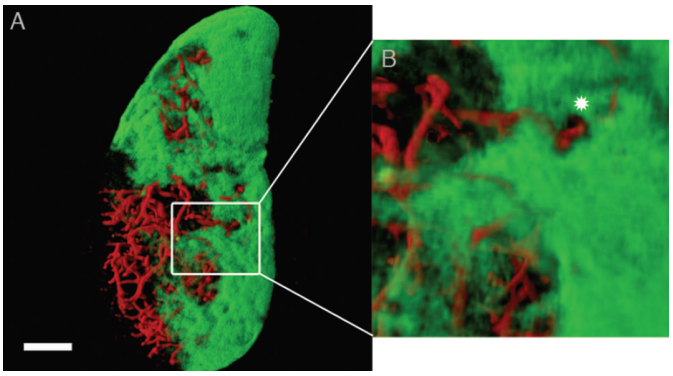

Figure 4.5: OPT image of lymph node from Pfeiffer et al. [2008]. The high endothelial cells are stained red and the medullary sinuses are stained green. Scale bar = 200 μm.

the average pore pressure. Darcy's Law is based on the assumption that the flow in the pore spaces is at low Reynolds number so the forces are linear and instantaneous.

Biological tissue can be modelled using Darcy's law as interstitial tissue is made up of cells within a matrix of collagen fibres [Swartz and Fleury, 2007]. Interstitial flow passes through the spaces between the collagen fibres and around the cells delivering nutrients and removing waste. Some examples of biological tissues that have been modelled using Darcy's law include the brain [El-Bouri and Payne, 2015], tumours [Shipley and Chapman, 2010] and bone [Li, 2013].

An important aspect of modelling fluid flow in biological tissue is that the mass of the fluid is not necessarily conserved due to the presence of blood and lymphatic vessels. The fluid is able to pass through the walls of the vessels depending on the hydrostatic or colloid osmotic pressure. Starling's equation is used to model this behaviour,

$$J_v = L_p S \left[(p_c - p_i) - \sigma \left(\pi_c - \pi_i \right) \right] \tag{4.3}$$

where J_v is the volume filtered per unit time, L_p is the hydraulic conductivity of the blood vessel wall, S is the surface area of the blood vessel, p_c is the pressure in the blood vessel, p_i is the pressure in the interstitium, σ is the osmotic reflection coefficient, π_c is the colloid osmotic pressure in the blood vessel and π_i is the colloid osmotic pressure in the interstitium. The transfer between blood and interstitial fluid has been modelled either by defining phase equations, a blood phase and a tissue phase [Causin and Malgaroli, 2015], or by explicitly defining the location of the blood vessels [He et al., 2008].

In order to define the location of the blood vessels within a tissue, imaging techniques are often used. Two examples are magnetic resonance imaging (MRI) [He et al., 2008] and computational tomography [Deng et al., 2012; Li, 2013]. In theory any imaging technique that can visualise the blood vessels can be used. In this chapter, the idea of

using images to define the geometry of a model is extended. The images are also used to determine the material properties of tissue by relating the grey scale of the image to the permeability of the tissue.

Finite element [He et al., 2008], finite difference [Deng et al., 2012] and collocation [Li, 2013] methods have been used to model fluid flow through biological tissues. In this chapter finite element modelling is used. This is because there is software available to create a finite element mesh from images, e.g. ScanIP, a commerical software from Simpleware[1], and so that it is possible to link the lymph node with the valve model created in chapter 3 in COMSOL Multiphysics.

Computational models of lymph nodes relate to the movement of cells within lymph nodes. Models including the 3D Cellular Potts Model [Beltman et al., 2007], Ornstein-Uhlenbeck process [Bogle and Dunbar, 2008], hybrid phantom [Lee et al., 2013], random walk [Figge et al., 2008], ordinary differential equations [Chan et al., 2013] and diffusion [Andrews and Timmis, 2006] have been implemented to model the dynamics of the cells. No examples were found in the literature of modelling the fluid flow through lymph nodes.

4.2.8 Summary

Lymph nodes have a complex structure. The blood vessels and lymphatic vessels do not join directly, but lymphocytes and fluid can move between the two. The nodes play an important role in immunity. Modelling the flow through the node could lead to insights into the transport of material through the node that cannot easily be investigated experimentally. For the image based model of the lymph node, COMSOL multiphysics will be used to implement the finite element model for a geometry based on light sheet microscope images. The permeability of the model will be determined from the greyscale values of the images.

4.3 Method

4.3.1 Data used in this study

In the 1980's experiments were carried out on lymph nodes to find out how the composition of the lymph changed as it passed through the node. Adair et al. [1982] and Adair and Guyton [1983, 1985] isolated popliteal lymph nodes from dogs and cannulated an efferent and an afferent lymphatic to assess the flow; other afferent and efferent lymphatics vessels were ligated. The lymph nodes were then perfused

[1] https://simpleware.com/software/scanip/

at physiological flow rates through the afferent lymphatic and the efferent lymphatic was maintained at a hydrostatic pressure 0 mmHg, considering atmospheric pressure as gauge pressure. A branch of the lateral saphenous vein was cannulated for the measurement and control of venous pressure.

Adair and Guyton [1985] varied the efferent lymphatic pressure to see how this affected the protein concentration of the efferent lymph fluid. The authors also recorded the changes in the efferent flow rate in response to changes in fluid pressure. These results were used as inputs for the lymph node model.

For the first four nodes in the experiments presented in Adair and Guyton [1985], the efferent lymphatic pressure was increased in 6 steps from 0 to approximately 2170 Pa. The mean values were calculated for the afferent lymphatic pressure and flow rate, efferent lymphatic pressure and venous pressure. The mean efferent pressure, afferent flow rate and venous pressure were used as inputs in the model. The afferent pressure and efferent flow rate were used to estimate the unknown parameter values that represented the permeability of the internal lymph node material, the hydraulic conductivity of the blood vessel walls and the colloid osmotic pressure difference across the blood vessel walls.

4.3.2 Image Processing

Images were obtained from Jürgen Mayer of mouse popliteal lymph nodes imaged using selective plane illumination microscopy (SPIM); for more information see Mayer et al. [2012]. In this work, two nodes, one from a wild type mouse (WT) and one from a plt/plt mouse (PLT), a mutant mouse that lacks certain proteins in the T-cell zone, resulting in a decreased accumulation of dendritic cells in this zone, were imaged. Alexa594-coupled MECA-79 mAB was injected into the mouse to visualise the HEVs [Mayer et al., 2012]. The images of the lymph nodes had a voxel size of 1.29 $\times$ 1.29 $\times$ 5 μm and were received in 16 bit grayscale tiff format.

To create a computational mesh for finite element modelling of fluid flow through a lymph node, the raw image data had to be segmented and smoothed. This was achieved in the following manner: The images were processed to enable segmentation by Avizo Fire[2] and analysed as follows. The first stage of image processing was carried out using Fiji[3] [Schindelin et al., 2012] to convert the stack to 8 bit greyscale. A mean filter with a 4 pixel radius was applied to remove noise from the images. The brightness and contrast adjustment tool in Fiji was used in automatic model so that the features of the node were clearer; in particular the HEVs were bright white. The results of these processes are compared to the original image, figure 4.6a, in figure

[2]a commercial 3D image analysis software http://www.fei.com/software/avizo3d/
[3]a free, open source image processing package: http://fiji.sc/Fiji

4.6. The end slices were removed from the stack so that the final stack only contained images of the node.

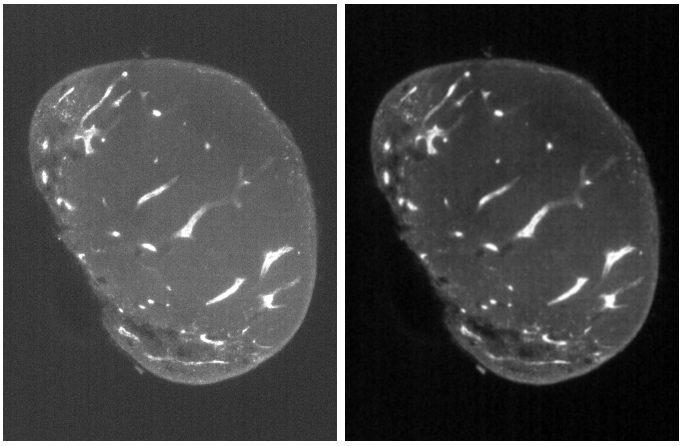

(a) Original 16 bit image

(b) Filtered 8 bit image with auto adjusted brightness and contrast

Figure 4.6: Comparison of original image to filtered image. The filtered image results in more distinguishable features.

Semi-manual segmentation was carried out in Avizo Fire using the magnetic lasso tool. The outline of the node was segmented every 20 slices, except where there were features that required more frequent selections. The selections were then interpolated so that the node was selected. Views from other planes were checked to confirm the selection. This segmentation was then used to create a mask that formed the outline of the node, see figure 4.7a. The mask stack and the filtered image stack were imported into Fiji. Two new image stacks were created: one of the node on a black background, by subtracting the inverted mask from the image stack; and one of the node on a white background, by adding the inverted mask to the image stack, see figure 4.7b.

The image stack of the node with the black background was opened in Fiji. By selecting a line that crossed a single HEV, it was possible to plot the grey scale profile, see figure 4.8b. From this, the approximate threshold could be found to segment out the HEVs (140 in this case). The brightness and contrast of the image stack were adjusted so that everything above 140 was white and everything below was black. This resulted in another stack of images, which only showed the HEVs. The fill holes tool was applied and then the remove outliers tool for radius 4 pixels. The erosion tool was applied 4 times and after the dilate tool 4 times. This simplified the HEVs structure and removed small features that would make computational mesh generation difficult. This resulted in a mask of white HEVs on a black background. In order for the meshing software to create a boundary between the lymph node tissue and the HEVs, thresholding would be used. Therefore, to make the HEVs have a different grey

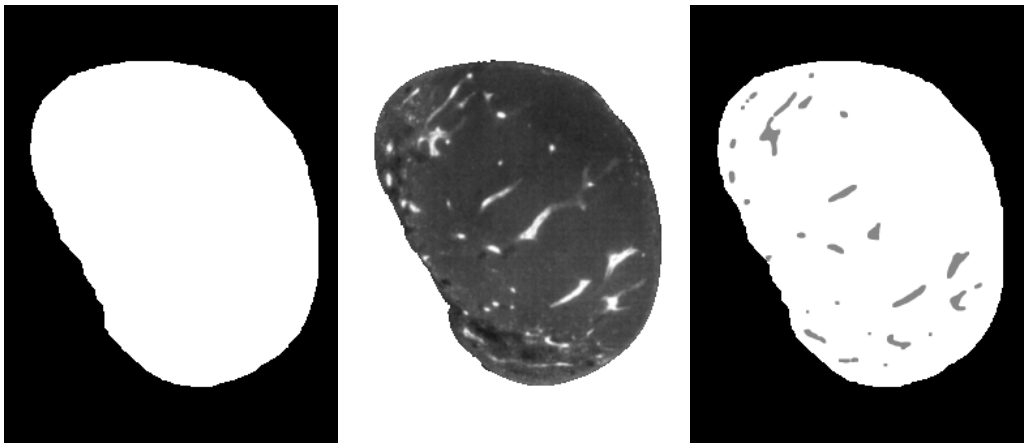

(a) Node mask (b) Node with white background (c) Node mask with HEVs

Figure 4.7: Node mask, the mask with HEVs and the node with white background stacks were all reduced in size by a quarter in the x and y directions.

value to the white node mask, the value of the HEVs was divided by a number, here 4 was used, to lower the value.

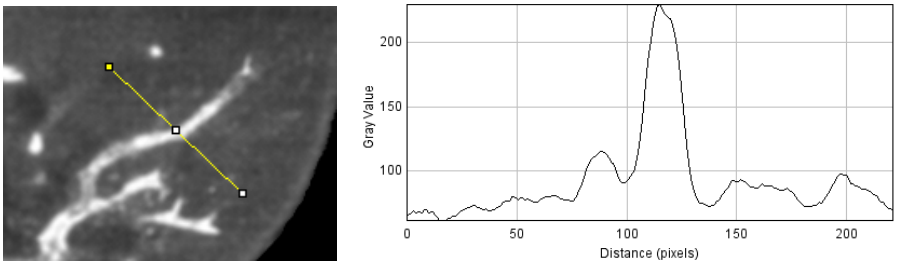

(a) Line across HEV (b) Grey scale profile

Figure 4.8: Greyscale profile along line over HEV.

The node mask, the node with a white background, and the mask with HEVs, figure stacks were all reduced in size by a quarter in the x and y directions, see figure 4.7. This resulted in the final voxel size of the images being 5.16 x 5.16 x 5 μm. The stack of the node with a white background was saved as an image sequence of jpeg images for use in COMSOL Multiphysics, which would be used to model the fluid flow.

In order to create surfaces that would act as the afferent and efferent vessel connections with the node, grey areas 1 pixel thick were created. This was done by opening the node mask in Fiji and rotating the stack 90 degrees using the TransformJ turn tool. This stack was duplicated and the duplicate stack was eroded by 1 pixel. The eroded stack was subtracted from the turned stack leaving a 1 pixel outline of the node. Two circles were selected, approximately 80 μm in diameter, and everything outside these circles was made black. The position of these circles were chosen to be close to places where the afferent and efferent lymphatic may have entered and exited

the node based on the original images. White pixels within the circles appear in two sets of slices. For one circle, the set of white pixels was removed from near the top of the stack. For the other, the set of white pixels was removed from near the bottom of the stack. A macro was used to divide the grey scale value by half and then the TransformJ turn tool was used to rotate the stack back to its original perspective. This stack was then subtracted from the node mask with HEVs, creating a mask with HEVs and thin grey areas on either side of the node. This process is summarised in figure 4.9.

ScanIP was used to create a mesh from the edited white and grey image stack. Using the threshold tool, three masks were created. The first selected only the pale grey pixels that represent the HEVs, the second only the white voxels, and the third only selected the grey voxels that represent the afferent and efferent lymphatic boundaries. The afferent and efferent lymphatic surfaces was dilated by 1 voxel in all directions. This creates surfaces that represent the afferent and efferent lymph vessels. The three masks that resulted from this were then added to the model. The model was configured to create a COMSOL mesh file using +FE Free volume meshing. The advanced parameters, such as mesh size, target error and rate of change of element size, were modified. Three mesh sizes were used for the mesh refinement study. For all the meshes the target minimum edge length was set to 8.8 μm (= $\sqrt{5.16^2 + 5.16^2 + 5^2}$ μm, the longest length between voxels). The maximum length was 8.8, 17.6 or 35.2 μm for the three different meshes. The target maximum error was set to 4.4 μm, half the minimum edge length. The size of the mesh elements on the surface was allowed to change rapidly (set to 75 in ScanIP), because the manual segmentation of the node outline meant a high level of detail was not appropriate. The volume elements within the node changed more slowly (set to 30). All other settings were left as default.

4.3.3 Model Implementation

The fluid flow is modelled as an incompressible fluid with dynamic viscosity, μ, 1.5 cP and density, ρ, 1000 kg/m^3 using Darcy's law, i.e. equation (4.1) in the domain Ω.

The permeability, $\boldsymbol{\kappa}$, was defined based on the images. A linear relation was used to relate the grey scale of the image to the permeability, e.g. the darker the image, the less dense the material and therefore the more permeable it is. This was implemented in COMSOL using the Matlab Livelink application. A script was written to read in the jpeg images for the node on the white background into the COMSOL Model. The images were imported as functions, called im$i$ where i was the number of the image in

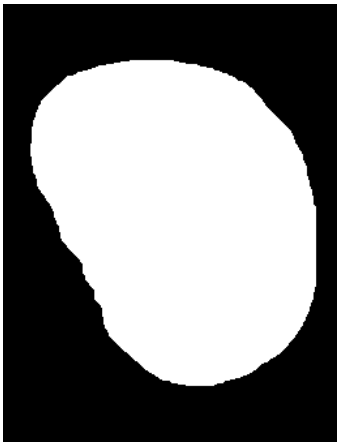

(a) Original mask

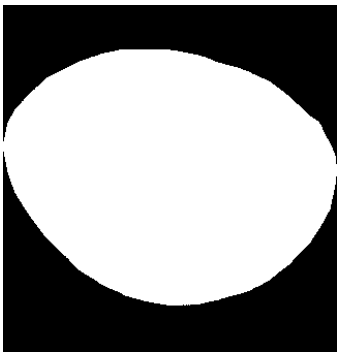

(b) Rotate 90 degrees

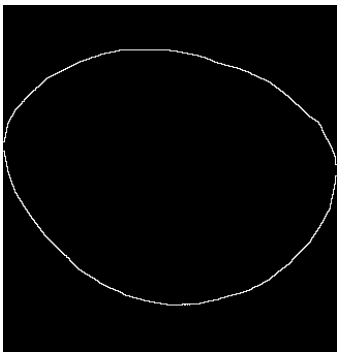

(c) Duplicate and erode by 1 pixel, then subtract the two masks

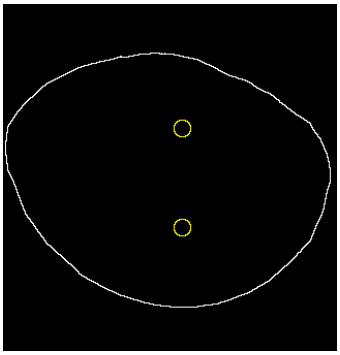

(d) Create circle approximately 80 μm in diameter

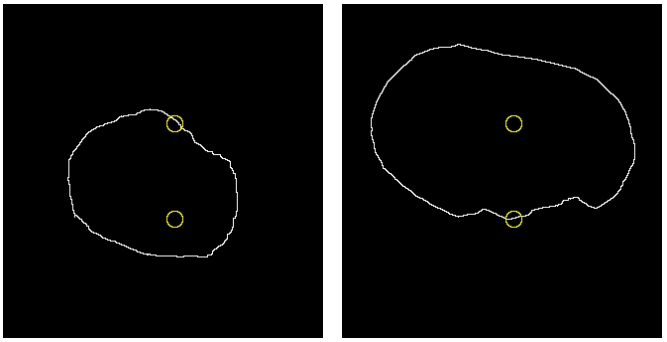

(e) Find where circles intersect mask edge and on which slices

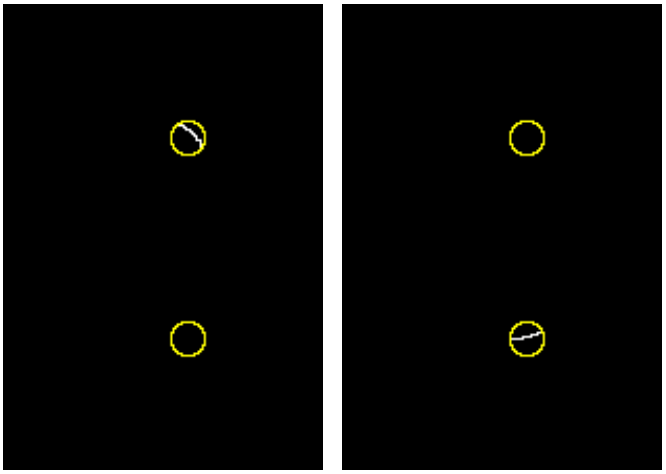

(f) Delete every thing outside of the circles and on other slices

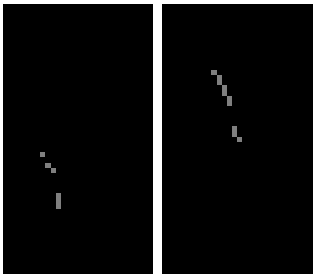

(g) Rotate 270 degrees to return to original plane

Figure 4.9: Images showing process for creating faces as afferent and efferent boundaries.

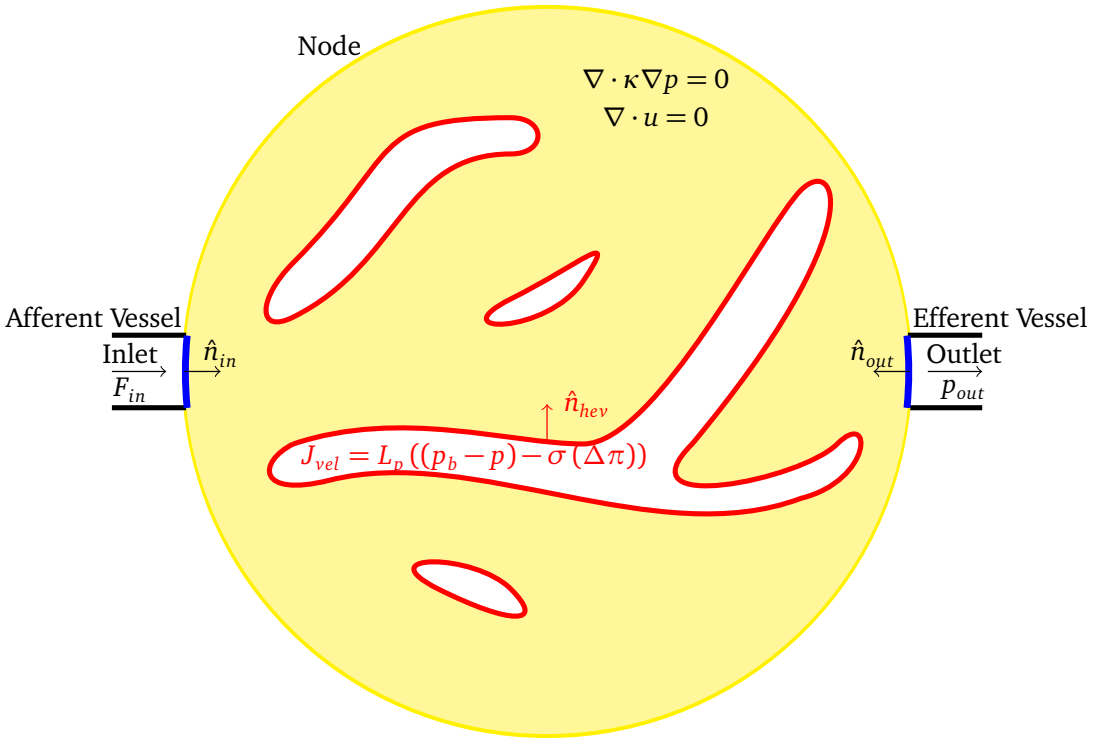

Figure 4.10: Sketch of lymph node model. Red lines indicate HEV boundaries, Γ_{hev}, yellow shows the interstitium of the node, Ω, the blue lines show the afferent and efferent lymphatic boundaries, Γ_{in} and Γ_{out} respectively, and the black lines show where the afferent and efferent vessels would be, although these are not modelled. The arrows labelled with $\hat{n}$ show the positive normal vectors to the boundary they are on.

the stack. This linear relation has the general form,

$$\begin{aligned}(-k_0\mathrm{im1}(x,y)+k_1)\times(z<5\ \mu\mathrm{m})\\ +(-k_0\mathrm{im2}(x,y)+k_1)\times(z\geq 5\ \mu\mathrm{m})\times(z<10\ \mu\mathrm{m})+\\ \cdots+(-k_0\mathrm{im}n(x,y)+k_1)\times(z\geq 5(n-1)\ \mu\mathrm{m}),\qquad X\in\Omega\end{aligned} \tag{4.4}$$

where k_0 and k_1 are constants that define the linear relation between the grey scale of the image and the permeability[4], x and y are the coordinates of the point in the image which is to be evaluated, z is the distance along the vertical axis and n is the total number of images. Each image is defined on a 5 μm thickness using a logical expression, e.g. $(z \geq 5\ \mu\mathrm{m}) \times (z < 10\ \mu\mathrm{m})$. Due to file type the image stack required vertical flipping to correlate with the mesh stack.

The afferent flow rate, F_{in}, was given in units of μL/min in Adair and Guyton [1985]. Thus it was divided by 6×10^7 (kg·min/μL·s) (= 60 min/s $\times 10^6$ kg/μL) to change units to kg/s, assuming the fluid density is 1000 kg/m^3. The efferent pressure was set to 0 mmHg. Starling's principle, equation (4.3) was used for the boundary condition

[4]an extrinsic value that is a property of the porous media, independent of the fluid

on the HEVs. Thus, the boundary condition is given by,

$$\hat{\boldsymbol{n}}_{hev} \cdot \rho \boldsymbol{u} = J_{vel} = \frac{J_v}{S} = L_p \left[(p_v - p) - \sigma \left(\Delta \pi \right) \right], \quad X \in \Gamma_{hev} \tag{4.5}$$

where $\hat{\boldsymbol{n}}_{hev}$ is the vector normal to the surface of the HEVs pointing into the node, J_{vel} (m/s) is the velocity of the fluid across the boundary, L_p (m/sPa) is the hydraulic conductivity of the HEV wall, S is the surface area of the HEVs, p_v (Pa) is the venous pressure, p (Pa) is the pressure in the node, σ (no units) is the osmotic reflection coefficient and $\Delta\pi = \pi_v - \pi_n$ (Pa) where π_v (Pa) is the plasma colloid osmotic pressure in the HEVs, and π_n (Pa) is the node colloid osmotic pressure. σ is set to be equal to 0.9 based on Levick [2009].

The condition on the afferent lymphatic boundary is given by,

$$\hat{\boldsymbol{n}}_{in} \cdot \rho \boldsymbol{u} = \frac{F_{in}}{A_{in}}, \quad X \in \Gamma_{in} \tag{4.6}$$

where $\hat{\boldsymbol{n}}_{in}$ is the vector normal to the afferent lymphatic boundary pointing into the node, F_{in} is the afferent flow rate and A_{in} is the area of the afferent boundary. The pressure was defined on the efferent boundary,

$$p = p_{out}, \quad X \in \Gamma_{out} \tag{4.7}$$

A no flux boundary condition was applied to all other boundaries, $\partial\Omega$. The boundary conditions are summarised in figure 4.10. A summary of the parameters used in the model and their approximate values from the literature are shown in table 4.1.

4.3.4 Mesh Refinement Study

A mesh refinement study was carried out to optimise the accuracy of the results verses the computational cost, such as time and computer memory usage. A coarser mesh, a mesh with fewer elements, produces less accurate results when compared to a fine mesh, which has more elements, however the coarser mesh requires less computational resources.

For the mesh refinement study, the afferent flow rate was defined as 7.58×10^{-7} kg/s, the efferent pressure was set to 0 Pa and the blood pressure was 1067 Pa. These values were taken from the experimental data for one node from Adair and Guyton [1985]. The hydraulic permeability of the HEVs was 3.42×10^{-10} m/(Pa·s) [Renkin and Michel, 1984] and the colloid osmotic pressure difference was 267 Pa. The experimental data was measured to an accuracy of 0.1 μL/min, which is equivalent to 1.67×10^{-9} kg/s [Adair and Guyton, 1985].

Parameter	Symbol	Unit	Value	Source
Afferent lymph flow rate	F_{in}	kg/s	7.596×10^{-7}	Mean from experimental data Adair and Guyton [1985]
Efferent lymph pressure	p_{out}	Pa	0, 270, 697, 1103, 1653, 2170	Mean from experimental data Adair and Guyton [1985]
Blood pressure	p_v	Pa	973	Mean from experimental data Adair and Guyton [1985]
Average Permeability	κ_a	m^2	10^{-14} to 10^{-8}	Range from Swartz and Fleury [2007]
Varying Permeability	k_0, k_2	m^2		No values in literature
Fluid density	ρ	kg/s^{-3}	1000	From literature Macdonald et al. [2008]
Dynamic viscosity	μ	Pa·s	0.0015	From literature Dixon et al. [2006]
Hydraulic permeability of blood vessels	L_p	m/(Pa·s)	1.02×10^{-11} to 6.7×10^{-10}	Range from Renkin and Michel [1984] for capillaries
Osmotic reflection coefficient	σ	no units	0.8 to 0.95, fixed at 0.9	From literature Levick [2009]
Colloid osmotic pressure difference	$\Delta\pi$	Pa	2080	Mean from experimental data Adair and Guyton [1985], calculated using Navar equation and protein concentrations of plasma, afferent and efferent lymph

Table 4.1: Parameters for lymph node model.

Figures 4.11a and 4.11c show that the efferent flow rates between the course and fine meshes were smaller than one standard deviation from the mean of the experimental data. Figures 4.11b and 4.11d show a comparison between the pressures calculated at the afferent boundary for each mesh size. The experimental data was accurate to 0.1 mmHg, equivalent to 13 Pa. The differences between the pressures for the three meshes is always below 10 Pa, which also suggests that the coarsest mesh was sufficient to capture the relevant information within the accuracy of the experimental measurements. Therefore, it was concluded that the results obtained from the coarse mesh were suitable for all further analyses. Adopting the coarse mesh will enabled calculations over a wider range of parameters within a reasonable period of time without compromising on accuracy within the context of experimental data available.

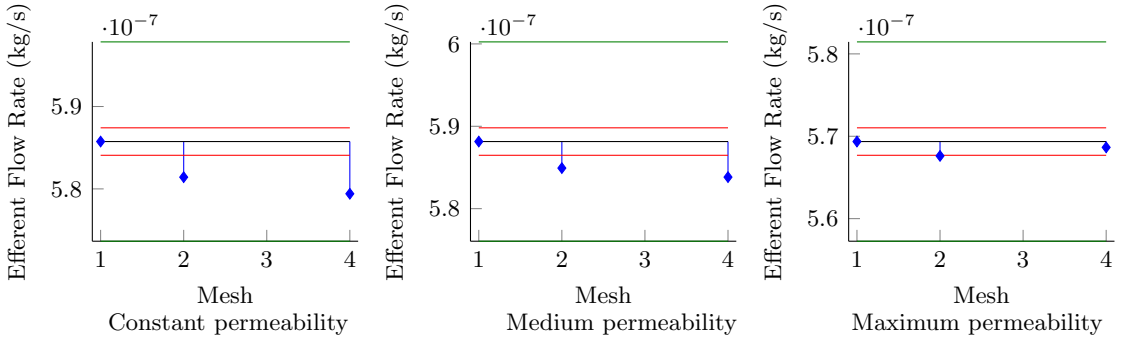

(a) WT comparison of efferent lymphatic flow for three meshes.

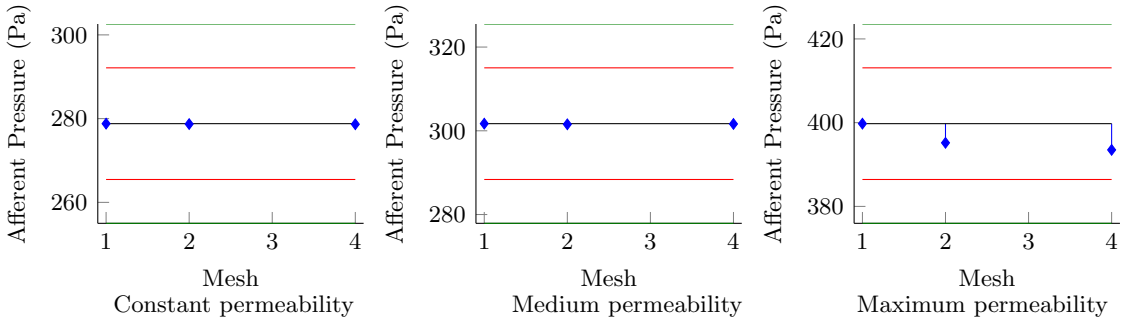

(b) WT comparison of afferent lymphatic pressure for three meshes.

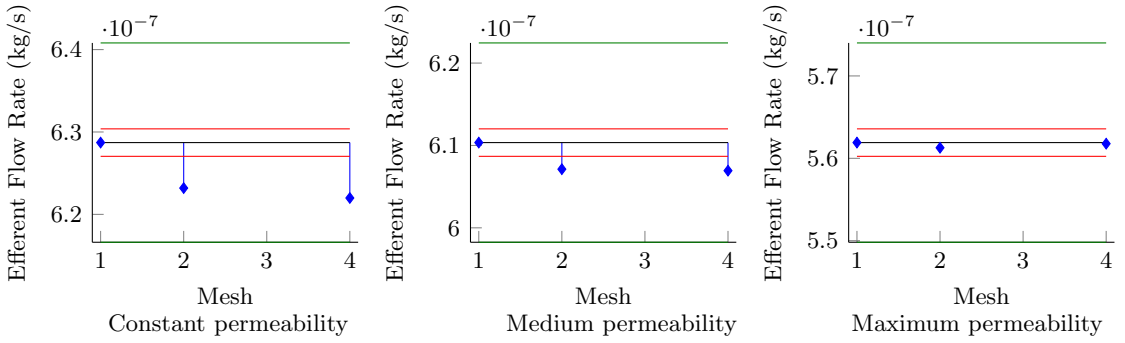

(c) PLT comparison of efferent lymphatic flow for three meshes.

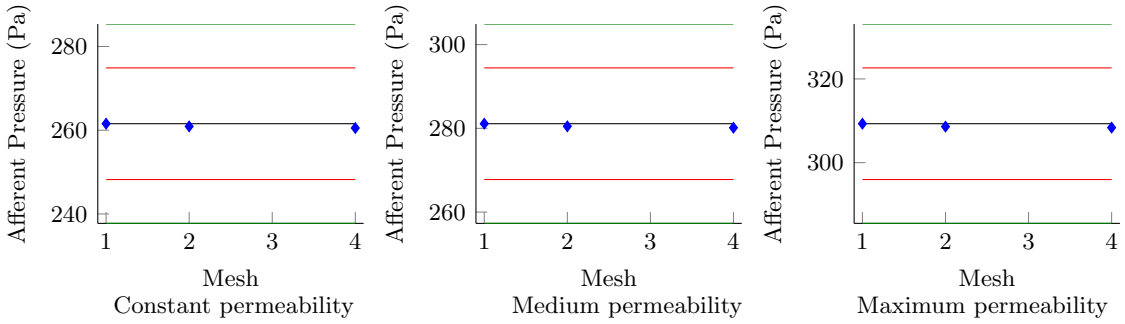

(d) PLT comparison of afferent lymphatic pressure for three meshes.

Figure 4.11: Results of mesh refinement study. The finest mesh is 1, the coarsest mesh is 4. The red lines shows the experimental measurement accuracy and the green lines show ± 1 standard deviation, based on the experimental data from four nodes with efferent lymphatic pressure 0 Pa from Adair and Guyton [1985].

4.3.5 Parameter Optimisation

In order to estimate the values that best fit the data of Adair and Guyton [1985] for the average permeability, κ_a, hydraulic conductivity, L_p, and colloid osmotic pressure difference, $\Delta\pi$, a Kriging algorithm was used. Kriging is an iterative method that interpolates known function values to estimate an optimal parameter set [Krige, 1951]. This Kriging was implemented in Matlab [Forrester et al., 2008] and was run using the COMSOL with Matlab LiveLink application. Initially arbitrary values for the parameters were tested in order to approximate appropriate bounds used within the Kriging algorithm. Three values were chosen based on these initial tests for each of the parameters, κ_a, L_p and $\Delta\pi$. From these, 27 sample points (27 sets of three parameter values) were estimated in COMSOL and they provided the initial known function values for the objective function in the Kriging algorithm. The error/objective function, E, used two least squares terms; one for the afferent pressure and the other for the efferent flow rate. Thus, E, was calculated as,

$$E = \sum_{j=1}^{6} \frac{(p_{in}^{j} - \widetilde{p_{in}^{j}})^2}{\left(s_p^j\right)^2} + \sum_{j=1}^{6} \frac{(F_{out}^{j} - \widetilde{F_{out}^{j}})^2}{10\left(s_f^j\right)^2} \tag{4.8}$$

where p_{in}^{j} is the experimental mean afferent pressure at the j^{th} efferent pressure, $\widetilde{p_{in}^{j}}$ is the afferent pressure calculated by the model for the same efferent lymphatic pressure, s_p^j is the experimental standard deviation afferent pressure at the j^{th} efferent pressure, F_{in}^{j} is the experimental mean efferent flow rate for the j^{th} efferent pressure, $\widetilde{F_{in}^{j}}$ is the efferent flow rate calculated by the model at the same efferent lymphatic pressure, and s_f^j is the experimental standard deviation for the efferent flow rate at the j^{th} efferent lymphatic pressure. The aim of the Kriging algorithm was to minimise the objective function over a range of values of L_p, $\Delta\pi$ and κ_a, thus minimising the difference between the experimental data and the model results. Both the afferent pressure and the efferent flow rate were used because the hydraulic permeability of the blood vessels, L_p, and the colloid osmotic pressure difference, σ, had only a small affect on the afferent pressure but a large affect on efferent flow rate. However, the average permeability, κ_a, had a large affect in the afferent pressure and a small affect on the efferent flow rate.

Two optimisation methods within the Kriging algorithm were used to estimate the minimum function value for E. Initially, a predicted function was interpolated from the known function values. The first method (local optimisation) found the minimum point of the predicted function. The second method (global optimisation) found the point at which the predicted function had the maximum estimated error. These two new points were estimated by the COMSOL model and then the new function values were interpolated with all of the existing points to update the predicted function (one iteration). The number of iterations for the Kriging algorithm was fixed due to the

computational time required. Each iteration required approximately 30 minutes run time and the computational time for the entire process was approximately 40 hours. This allowed 81 total sample points to be estimated. The value of E was found to converge within the number of iterations.

Adair et al. [1982] hypothesised that the increase in protein concentration in the interstitium of the lymph node is 98% due to fluid transfer. If we assume that 100% is due to fluid transfer, this implies that the blood vessels within the node must absorb fluid, in order to increase the concentration of protein in the lymph node interstitium. This hypothesis required $J_{vel} < 0$ for which, a further assumption that colloid osmotic pressure difference should be greater than the mean venous pressure is required. The venous pressure was assumed to be 973 Pa, the mean venous pressure measured by Adair and Guyton [1985]. In order for $J_{vel} < 0$, it can be seen from Starlings equation (4.3), that $(p_v - p) - \sigma(\Delta\pi) \leq 0$, and therefore $(p_v - p) \leq \sigma(\Delta\pi)$. Considering the limit where $p = 0$ and $\sigma = 1$, $p_v \leq \Delta\pi$. Therefore, $\Delta\pi \leq 973$ Pa. In Adair et al. [1982], the mean equilibrium colloid osmotic pressure difference (when there was no flow across the blood vessel walls) from eight dog lymph nodes was calculated as 1187 ± 279, which showed this to be a reasonable assumption.

4.3.6 Varying Lymph Node Tissue Permeability

The grey scale variations in the images contained information about the density of the material within the lymph node. Therefore, these variations can be used as a indicator of permeability, i.e. the lighter the grey scale the denser the material, the lower the permeability. This was integrated into the model by relating the grey scale to permeability, $\boldsymbol{\kappa}$, with a linear relation, equation (4.4).

	WT		PLT	
	k_0	k_1	k_0	k_1
Maximum	6.2086×10^{-11}	6.2096×10^{-11}	6.8988×10^{-11}	6.8998×10^{-11}
Medium	3.1043×10^{-11}	4.9960×10^{-11}	3.4494×10^{-11}	5.1756×10^{-11}
Constant	0	3.7825×10^{-11}	0	3.4515×10^{-11}

Table 4.2: Parameters for varying permeability for nodes.

The average grey scale of the lymph node images, G (no units), was found using Matlab. After finding the average permeability using Kriging, κ_a (m^2), the grey scale was related to the permeability by a linear relation that passed through the points (G, κ_a) and $\left(1, 10^{-14}\mathrm{m}^2\right)$. This was the maximum gradient. The medium gradient was a linear relation that passed though (G, κ_a) and $\left(1, \left(\kappa_a + 10^{-14}\mathrm{m}^2\right)/2\right)$. The parameters used are shown in table 4.2 and the relations are shown in figure 4.12. With this implementation, it was now possible to examine the flow through the

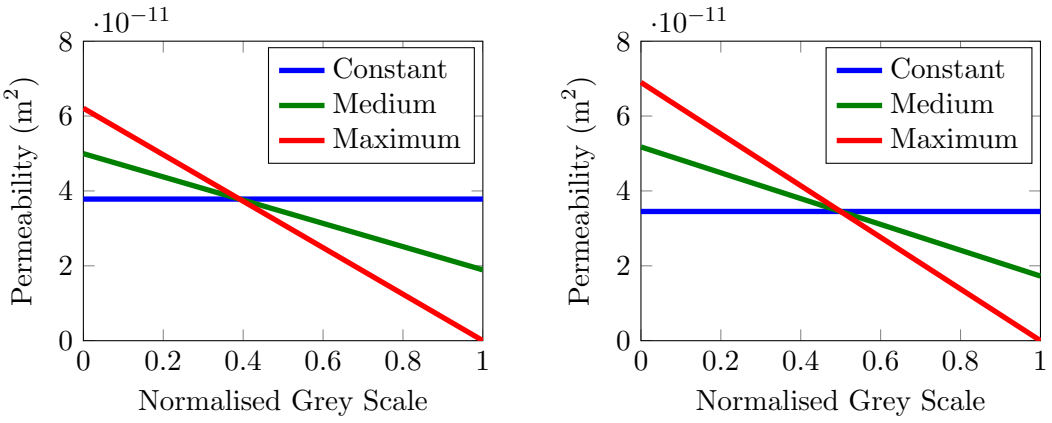

(a) WT (b) PLT

Figure 4.12: Graphs showing permeability to grey scale relations.

lymph nodes for two different distributions of the permeability and yet ensure that the average permeability was consistent with the results obtained using the kriging procedure (and therefore the experimental data).

4.4 Results and Discussion

For the parameter estimation using the Kriging algorithm, the error value, E, was used to evaluate the goodness of fit between the experimental data and the model results. The parameter set which resulted in the lowest error value, E_{min}, was selected as the optimal parameter set for the data. From the Kriging algorithm with the assumption $\Delta\pi \geq 973$ Pa, it was found that the best fit resulted when $\Delta\pi = 973$ Pa with $E = 15.8$. The results for the WT node in 4.13 show that although there is good agreement for the afferent pressure, the efferent flow has a much shallower gradient than is observed in the experiments.

Therefore assumption that $\Delta\pi \geq 973$ Pa was relaxed to $\Delta\pi \geq 0$, i.e. the osmotic pressure difference had to be positive. With this relaxed condition, the model produced results that are similar to the experiments, see figure 4.14. This shows that the results from the model at low efferent pressures and the experimental data are not consistent with the hypothesis in Adair et al. [1982], because extravasation is occurring across the walls of the HEVs in the model, not absorption. The optimal value of $\Delta\pi = 341$ was found by the model, with an error value is $E_{min} = 9$. The gradient of the efferent pressure to efferent flow rate was more similar to the experimental data. The average permeability of the lymph node tissue, $\kappa_a = 3.8 \times 10^{-11}$, was 5.2% higher than the $\Delta\pi \geq 973$ Pa limited case and the hydraulic conductivity of the HEVs was 149% higher but the same order of magnitude, 5.1×10^{-8} m/Pa·s compared to 2×10^{-8} m/Pa·s.

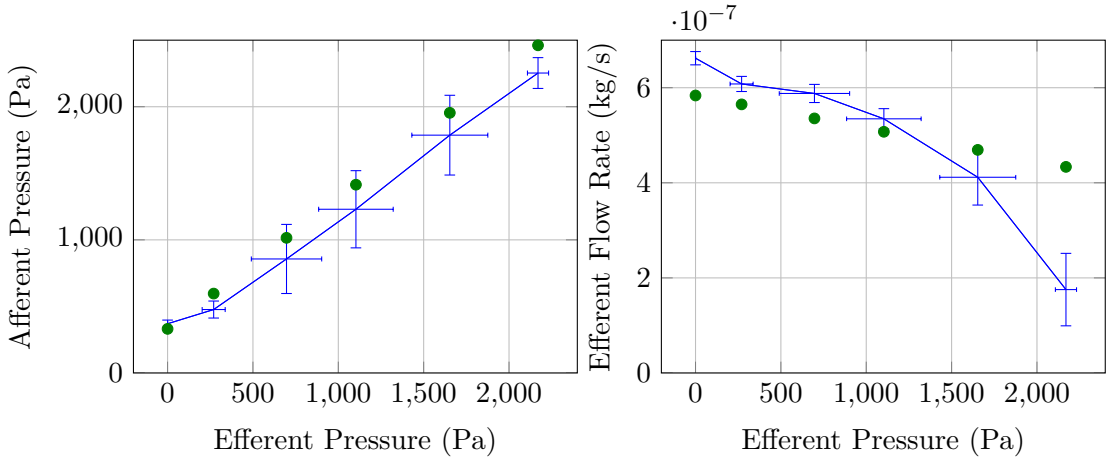

Figure 4.13: Blue line shows mean values from experiments on four nodes. Error bars show one standard deviation. Green dots show model results for case where $\Delta\pi > 973$ Pa. $E_{min} = 15.867$ (no units), $\kappa_a = 3.5959 \times 10^{-11}$ m^2, $L_p = 2.0473 \times 10^{-8}$ m/Pa·s, $\Delta\pi = 973$ Pa

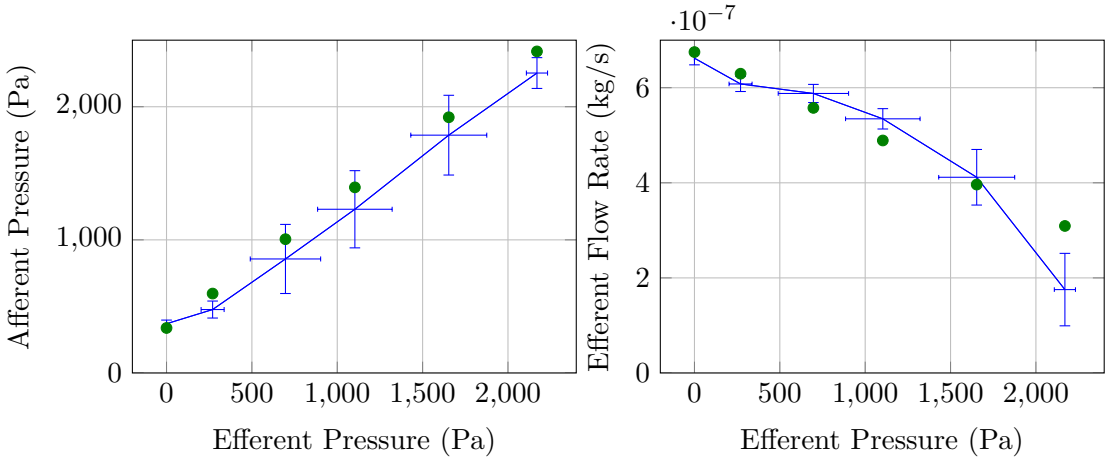

Figure 4.14: WT node. $E_{min} = 8.9876$ (no units), $\kappa_a = 3.7825 \times 10^{-11}$ m^2, $L_p = 5.1113 \times 10^{-8}$ m/Pa·s, $\Delta\pi = 341$ Pa. Blue line shows mean values from experiments on four nodes. Error bars show one standard deviation. Green dots show model results for limited case.

For the PLT node, the Kriging algorithm was also used for $\Delta\pi \geq 0$, with $E_{min} = 9$, the result can be seen in figure 4.15. The values for κ_a and L_p were similar to the WT node, the value of $\Delta\pi$, 553 Pa, is about 200 Pa higher. The results are shown in figure 4.15.

Fluid flow stream tubes are plotted in figure 4.16 to show the flux through the node for efferent lymphatic pressure, 0 Pa. Stream tubes are curves that the velocity vectors are tangential to and have an area which was define, in this case, as proportional to the fluid flux. For the highest efferent lymphatic pressure, 2170 Pa, there are fewer stream tubes at the efferent lymphatic than the node for the lowest efferent lymphatic pressure, 0 Pa. The value of J_{vel} changed for the different

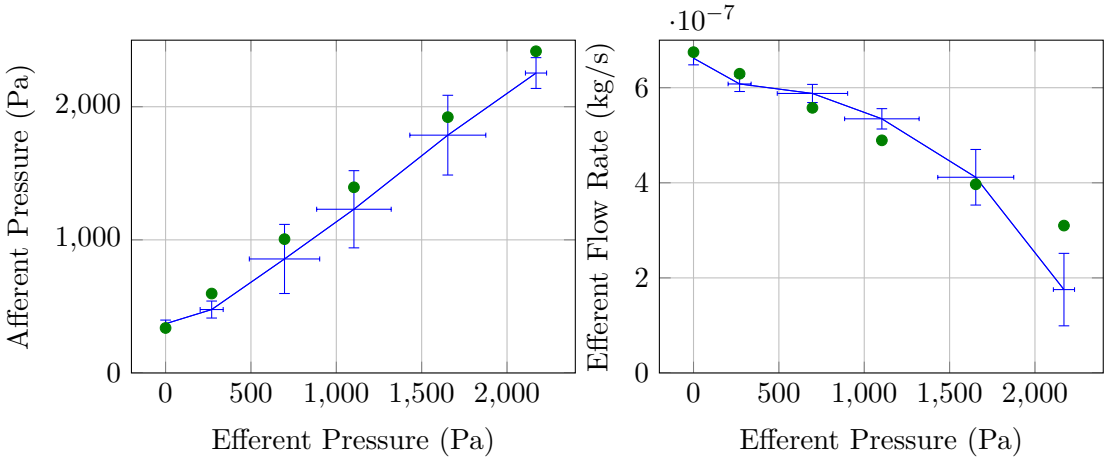

Figure 4.15: PLT node. $E_{min} = 9.0295$ (no units), $\kappa_a = 3.4515 \times 10^{-11}$ m^2, $L_p = 4.3304 \times 10^{-8}$ m/Pa·s, $\Delta\pi = 553$ Pa. Blue line shows mean values from experiments on four nodes. Error bars show one standard deviation. Green dots show model results for limited case.

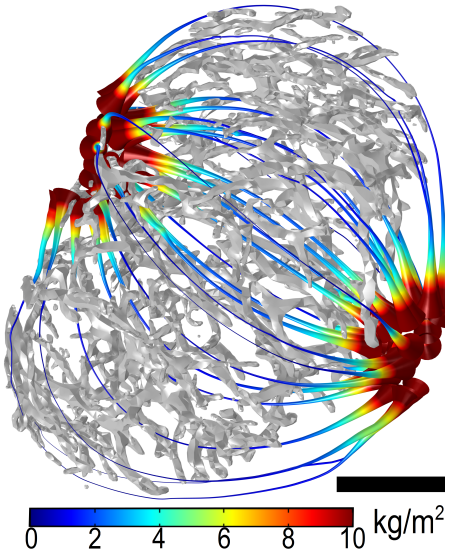

Figure 4.16: Stream tubes for WT node. Efferent pressure = 0 Pa. Scale bars = 250 μm.

efferent lymphatic pressures. For the two lowest pressures, the flow direction was out of the HEVs. For the other four pressures, the flow was into the vessels. This implied that for some efferent lymphatic pressures 270 Pa$<$ p_{out} $<$697 Pa some flow would be absorbed by the HEVs and some will be extravasated. It can be shown that this occurs for all the efferent lymphatic pressures used in this study, see figure 4.17. The red HEVs surfaces show where fluid is leaving the blood vessel and entering the lymph node, whereas the blue surfaces show where fluid is entering the blood vessels from the interstitium. For efferent lymphatic low pressures, figures 4.17a and 4.17b, the majority of the HEVs have fluid extravasation into the node. For higher efferent lymphatic pressures figures 4.17c to 4.17f, the majority of the HEVs have fluid

entering the vessels from the node.

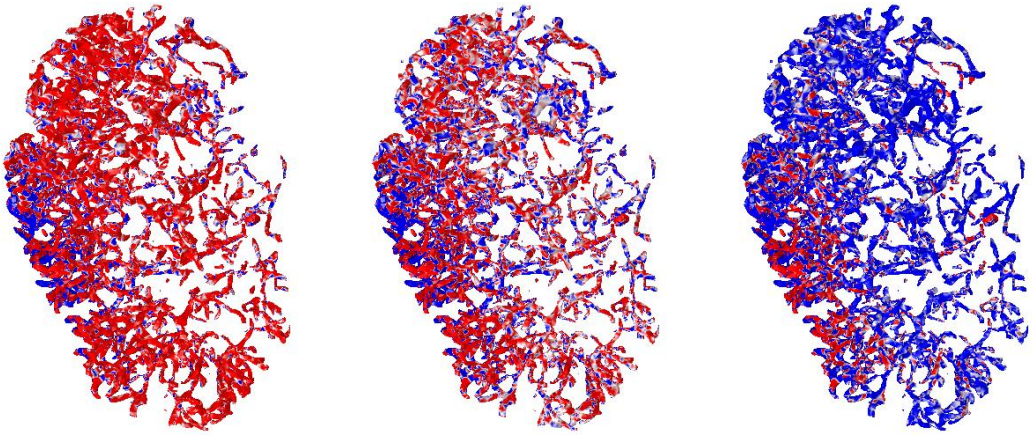

(a) Efferent pressure = 0 Pa

(b) Efferent pressure = 270 Pa

(c) Efferent pressure = 697 Pa

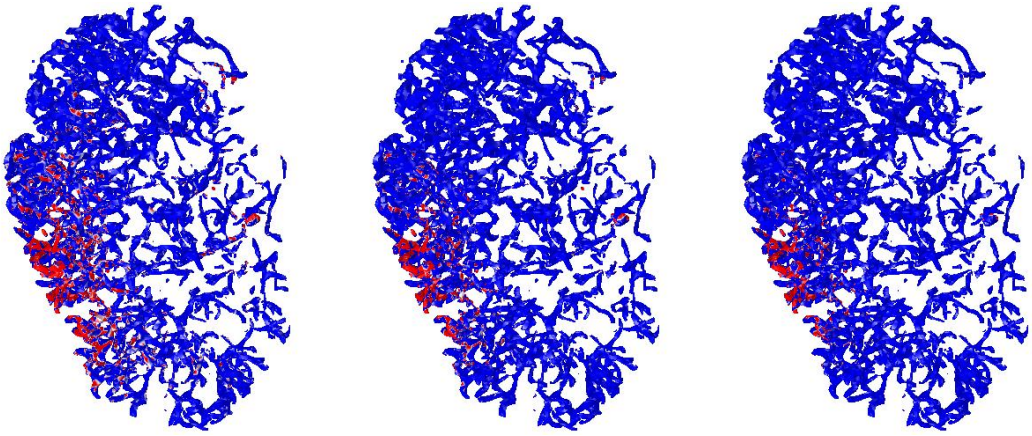

(d) Efferent pressure = 1103 Pa

(e) Efferent pressure = 1653 Pa

(f) Efferent pressure = 2170 Pa

Figure 4.17: Flow entering and leaving HEVs for PLT node. Red shows where fluid is leaving the blood vessels and entering the node. Blue shows where fluid is leaving the node and entering the blood vessels. As the efferent lymphatic pressure increases more of the fluid is absorbed by the HEVs.

Two varying permeability cases were modelled and compared to the constant case. The results show that the inclusion of a gradient for the permeability caused more flow through the centre of the node and less round the outside, as seen in figure 4.18. The varying permeability cases slightly lowered the flow rate for each efferent lymphatic pressure. This implies that the HEVs are absorbing more fluid. This is a result of the higher permeability values for the node tissue, as shown in figure 4.19.

The average permeability of the interstitium was estimated as 10^{-11} m^2 by optimising the image based model of a mouse lymph node to the experimental data from canine lymph nodes [Adair and Guyton, 1985]. This permeability was comparable to that of mouse tail skin, blood clot and mesentery [Swartz and Fleury, 2007]. Relating the permeability linearly to the grey scale resulted in more flow through the centre

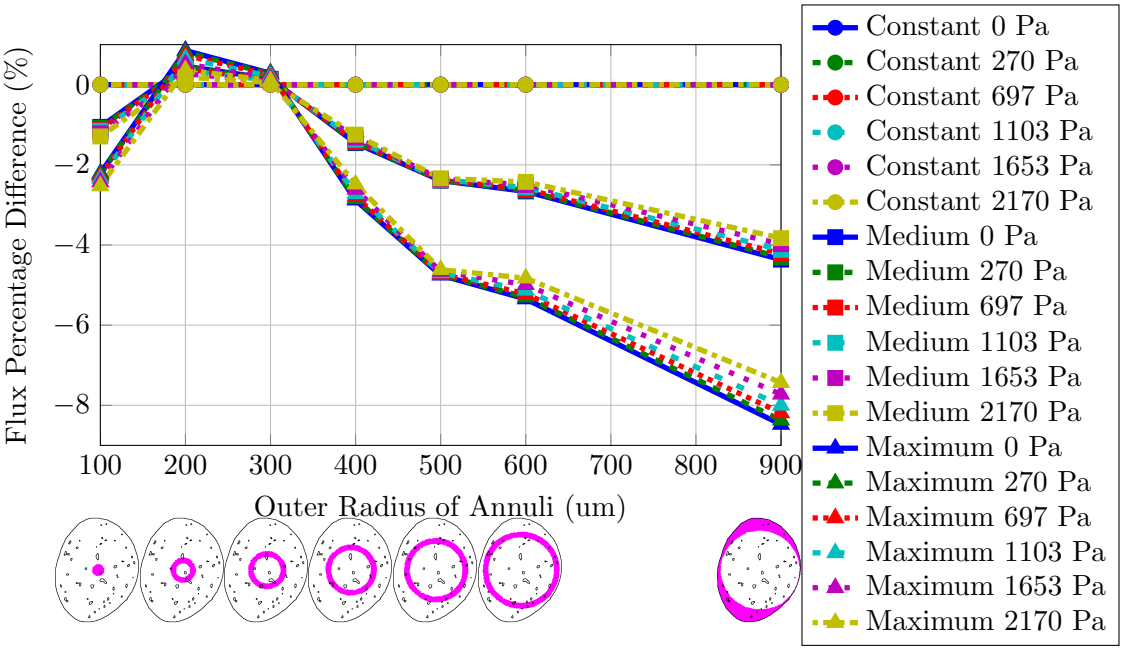

(a) WT node

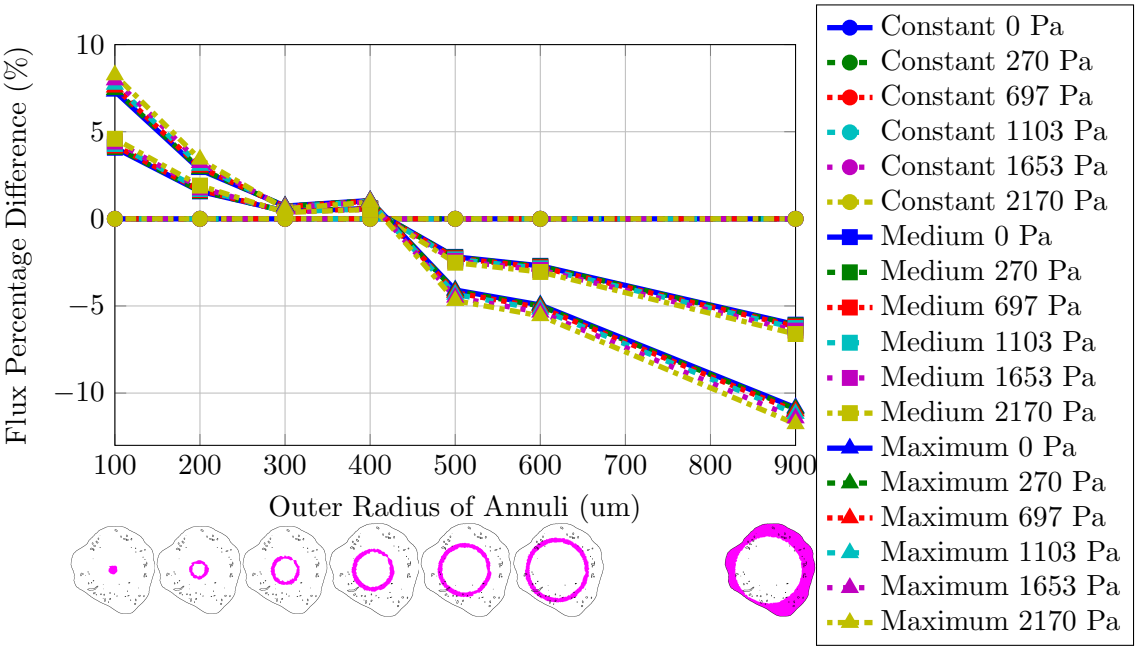

(b) PLT node

Figure 4.18: Comparison of the flux percentage difference though different annuli (shown in images in pink) through central 2D plane of lymph node. Values are normalised to constant results for comparison, hence all constant values are 0.

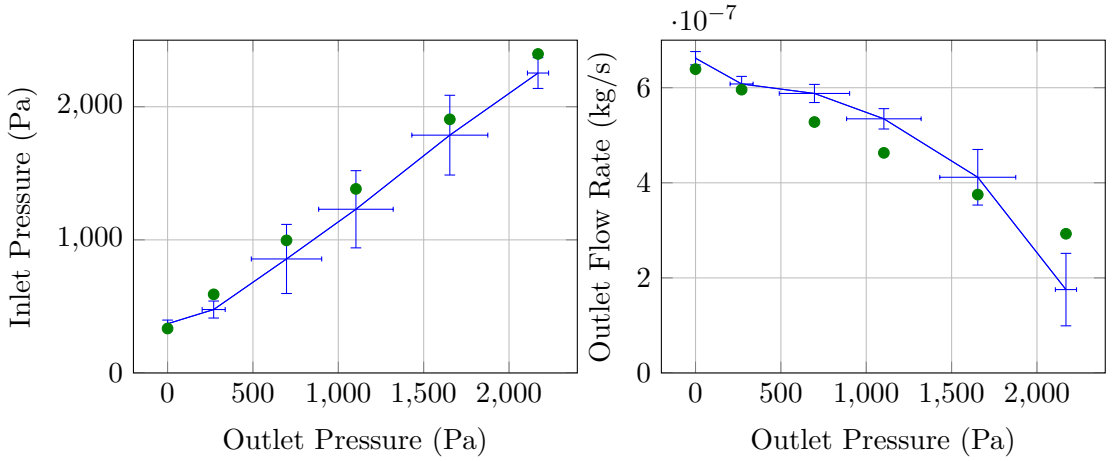

Figure 4.19: WT Max Permeability. Error=9.8684

of the node than the constant permeability case. The images used to create the model did not clearly show some of the structural detail that has been described in the literature. Within the lymph node, beneath the capsule is the subcapsular sinus [Ohtani and Ohtani, 2008]. This is thought to be an area of low resistance to the flow, however it was not clearly shown in the images used for this study. To resolve this issue a follow up study using high resolution micro computed tomography images, which show more structural detail, is required.

The values of L_p found as part of the parameter optimisation were three orders of magnitude higher than the values for capillaries found in Renkin and Michel [1984]. Since only the HEVs were modelled, the value of L_p had to be higher, the vessels must allow more fluid to cross the wall, so that the same amount of flow across the blood vessel wall in the experiment, which will have many more blood vessels, could be achieved by the model.

Initially it was assumed that the increase in protein concentration was caused by the fluid being absorbed into the HEVs, and therefore the value $J_{vel} < 0$. However, it was possible to get a much better fit, $E_{min} = 9$ compared to $E_{min} = 15$, for the model to experimental data by removing this limitation. Hence, the original assumption was inaccurate. However, the parameter fitting had been able to account for the behaviour of the efferent flow rate as the efferent pressure increase, however it was not able to reproduce the curve of the efferent pressure verses efferent flow rate. This implies that the fluid flow dominates this behaviour. The model can be extended in the future by including a convection-diffusion expression for the proteins. This may cause the model to exhibit the nonlinear behaviour as in the experimental data. The model can be developed to include a convection/diffusion model for the protein transport. This will allow investigation of the colloid osmotic pressure which it was not possible to capture in the current model. This will also introduce a time-dependent variable to the model, which will allow investigation of transient effects. The model does capture

the main profiles of the afferent to efferent pressure relations and the efferent flow rate to efferent pressure. This shows that the fluid flow is the dominant behaviour which agrees with the hypothesis in Adair et al. [1982].

Considering the grouping $L_p\sigma\Delta\pi$ (m/s) and taking the largest value of $L_p = 6.7 \times 10^{-10}$ m/(Pa·s) from Renkin and Michel [1984] and $\sigma = 0.9$ from Levick [2009], the value for the grouping is $L_p\sigma\Delta\pi = 1.3 \times 10^{-6}$ m/s. For the WT node, using the values for the optimised model, this value is $L_p\sigma\Delta\pi = 1.57 \times 10^{-5}$ m/s and for the PLT node, $L_p\sigma\Delta\pi = 2.16 \times 10^{-5}$ m/s. These values found for the optimised models are an order of magnitude larger than calculated using the values from Renkin and Michel [1984] and Levick [2009]. In order to make the model values the same order of magnitude as the literature, the value of σ would need to be less than 0.57 for the WT node or 0.42 for the PLT node. This implies that the HEVs are more leaky than capillaries. If a lower value of σ were used, a higher values of $\Delta\pi$ would be required to achieve the same fit to experimental data as was achieved from the Kriging algorithm. This would mean that the model values of $\Delta\pi$ could be more similar to the value estimated from Adair and Guyton [1985], 2080 Pa.

The HEVs hydrostatic pressure was fixed at 973 Pa, as calculated as the mean of the venous pressure from the experiments from Adair and Guyton (1985). The lymph node contains arteries, capillaries and veins, so it is expected that the hydrostatic pressure of the blood vessels should vary throughout the node. The pressure in the veins is lower than the pressure in the arteries, therefore, if the average blood pressure was found within the node it is likely to be higher than the venous pressure measured. The optimised value of L_p found by Kriging is two orders of magnitude higher than the values recorded in literature. If the value of L_p from literature was used, the HEVs hydrostatic pressure, p_v, would need to be increased by two orders of magnitude is order to produce the same J_{vel} currently implemented in the model.

4.4.1 Summary

This chapter describes an image based computational model of fluid flow through a lymph node. The model has related the grey scale values of the images to the permeability of the lymph node tissue with two different linear relations and these were compared to a case where the permeability in the node interstitium was constant.

In the next chapter 5, similar methods will be applied to computed tomography images of lymph nodes created using synchrotron radiation. These images show more detail of the lymph node parenchyma and this will affect the fluid flow pathways.

Chapter 5

Micro-Computed Tomography Image Based Modelling of Lymph Nodes

In this chapter a computational model of a fluid flow through a lymph node based on computed tomographic images will be described. To begin, computed tomography will be described and literature about the imaging of soft tissue using this technique will be reviewed. Techniques for creating artificial blood vessel networks will also be investigated. The methods used to create the model will be described and the results presented. Finally, the results will be discussed.

5.1 Literature Review

5.1.1 Computed Tomography

Computed tomography (CT) is an imaging method that enables the user to construct a three dimensional image stack of a sample. There are different CT systems, however here the focus will be placed on synchrotron radiation computed tomography (SRCT). Some applications of SRCT will be reviewed, but first SRCT will be described in more detail and image reconstruction will be described.

A generalised SRCT set up can be seen in figure 5.1. The source emits a monochromatic beam of x-rays, which are attenuated as they pass through the sample and then measured by the detector. The detector is made up of two parts: a scintillator, which converts the x-rays into visible light, and a photo detector, which creates projections of the visible light. The sample rotates and the detector outputs a projection for each angle. These projections are reconstructed to produce image

stacks, a series of 2D images that represent the 3D image, where the grey scale of each pixel represents the x-ray absorption of the corresponding point in the sample [Landis and Keane, 2010].

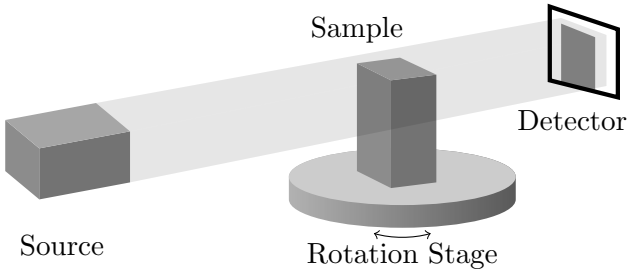

Figure 5.1: Sketch of CT set up.

Different reconstruction algorithms have been developed to convert the projections to image stacks. Here, the concept of Filtered Back Projection (FBP) will be explained using a simple example. Consider a sample made up of two cylinders within a third cylinder and a detector with only one row of pixels. Two projections are made, with the sample rotated by 90 degrees for the second projection, see figure 5.2. These projections are projected back along the length of the beam, see figure 5.3. The projections could then be summed together to calculate the intensities, as in figure 5.4. However, although the mathematics for this is relatively simple, it is expensive in terms of computational time and memory. Therefore, the FBP algorithm uses a Fourier transformation [Hsieh, 2009].

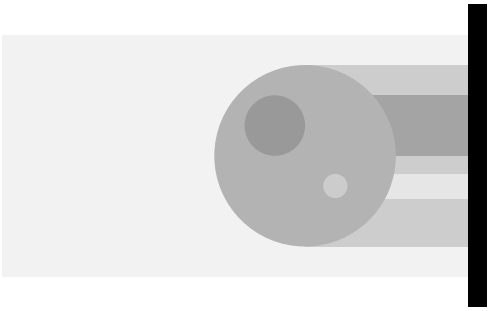

(a) Projection 1

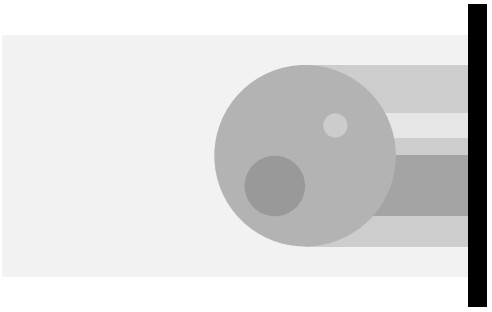

(b) Projection 2

Figure 5.2: Two projections

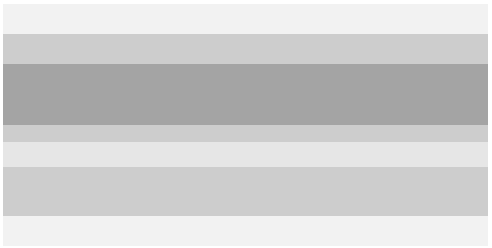

(a) Projection 1

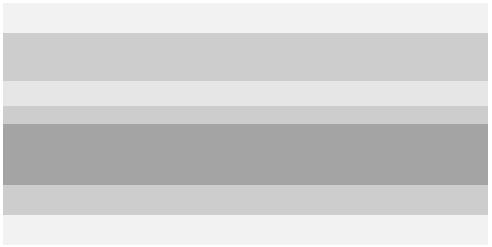

(b) Projection 2

Figure 5.3: Back projections

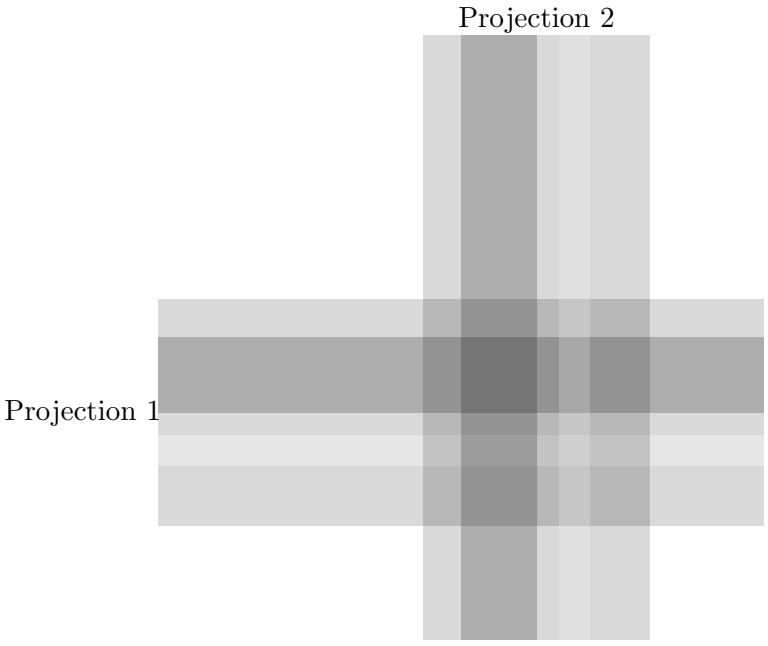

Figure 5.4: Back projections summed together

In an ideal world, performing a Fourier transformation on a projection would result in a line. However, this would require infinitely many scans. Therefore, when the discrete scans are transformed into Fourier space, the scan is stretched resulting in a strip in Fourier space. Each of these strips is weighted by a function, ω, that lowers the intensity in the centre and increases it at the outer edge, i.e. the energy is equalised. Once all the strips have been assembled in Fourier space, the inverse transform of the projections in Fourier space results in the reconstruction described in figure 5.4. The transformation to Fourier space means that at the outer edges the projections

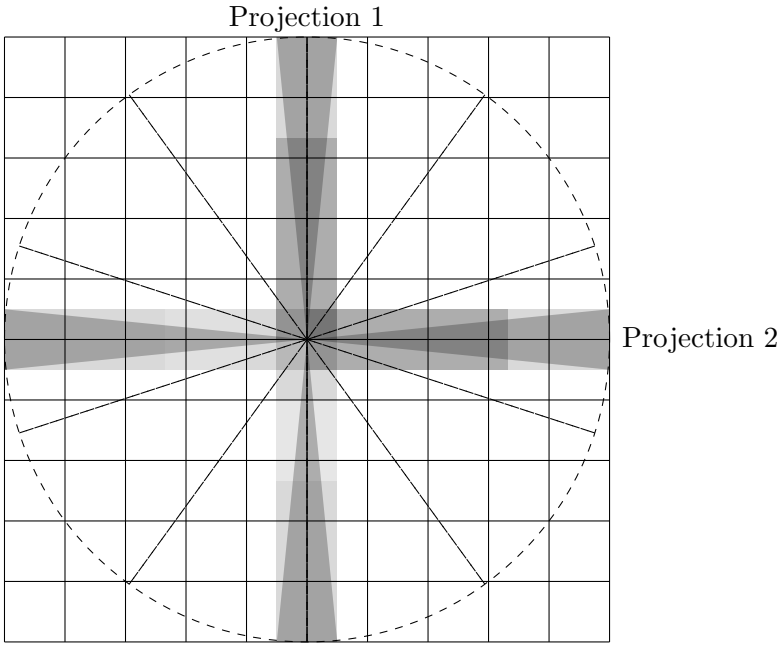

Figure 5.5: Transform of projections into Fourier space with weight function.

are spaced further apart, they are stretched further, and this causes more errors. Therefore, many projections must be made to reduce this source of error [Hsieh, 2009].

Producing good scans of soft tissue samples with CT is difficult due to the low x-ray contrast of the samples. Therefore phase contrast is utilised by moving the detector further away from the sample. As the x-rays pass through an object they are refracted, see figure 5.6. This increases the intensity.

The phase must be retrieved before the projections are reconstructed. Several methods have been developed for this, although they follow a similar procedure as described by Burvall et al. [2011]:

1. Take the intensity, $I(\boldsymbol{r})$, as a function of position, $\boldsymbol{r}$, on the detector
2. Calculate a function, $g\left(I(\boldsymbol{r})\right)$, which varies depending on which method is being used
3. Calculate the Fourier transform, $\mathcal{F}$, of $g(I)$ giving $\mathcal{F}\left(g(I)\right)$

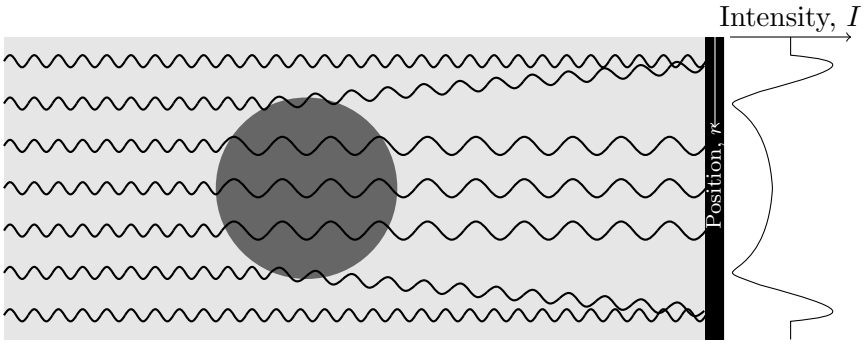

Figure 5.6: Phase created by the refraction of x-rays at the edges of the object. Based on figure from Burvall et al. [2011]

4. Multiply by a method dependent filter, $H(\boldsymbol{w})$, where $\boldsymbol{w}$ is the spatial frequency
5. Calculate the inverse Fourier transform resulting in $g_F(\boldsymbol{r})$
6. Calculate function $f(g_F)$ to get the phase distribution $\phi(\boldsymbol{r})$
7. Calculate the Fourier transform of $\phi(\boldsymbol{r})$
8. Multiply by the function, ω
9. Calculate the inverse Fourier transform

This results in filtered back projection utilising the phase from the image. Here the method developed by Paganin et al. [2002] is used.

SRCT has been used to visualise various biological tissues. Chugh et al. [2009] imaged the brains of mice to investigate the cerebral blood volume. They perfused the blood vessels with Microfil so that they contrasted with the surrounding brain tissue. Tschanz et al. [2014] imaged the development of post natal rat lungs. They noted that due to the embedding process the samples shrunk by an average of 63.2%. The authors used images to measure the alveoli size at 4, 10, 21 and 60 days, applying a correction term to account for the shrinkage. Fratini et al. [2015] used SRCT with phase contrast to image the murine spinal cord. They were able to visualise the grey and white matter of the spinal cord and the vascular network. Bonanno et al. [2015] similarly used SRCT with phase contrast to image a whole mouse heart. They were able to image the whole heart at high resolution, allowing for the identification of structures as small as 20 μm. The authors measured the diameter and all thickness of the coronary arteries.

5.1.2 Computational Creation of Blood Vessel Networks

In the CT scans of the lymph nodes it is not possible to trace the blood vessels through the node. The blood vessels are an important site of fluid transfer into and

out of the lymph node. Some methods of creating artificial blood vessel networks have been created.

Murray [1926b] assumed that the vascular system was a series of pipes that minimised the total work, E, required for a section of artery. The work required was assumed to be the sum of power lost due to friction and the energy required to maintain a certain volume of blood,

$$E = \underbrace{\frac{f^2 l 8\eta}{\pi r^4}}_{\text{friction}} + \underbrace{bl\pi r^2}_{\text{maintainance}}, \tag{5.1}$$

where f is the rate of blood flow, l and r are the length and radius of the blood vessel respectively, η is the viscosity of blood and b is the cost of blood maintenance. Finding the minimum of this equation results in the relation,

$$b = \frac{2f^2 8\eta}{\pi^2 r^6} \tag{5.2}$$

From this, the author determined that in order for the work to be minimised the flow must be proportional to the radius, $f = kr^3$ where $k = \sqrt{\frac{\pi^2 b}{16eta}}$.

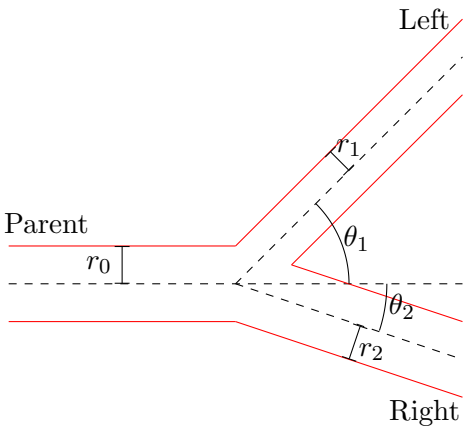

Figure 5.7: Sketch of blood vessel bifurcation

Consider a arterial tree of three branches, as shown in figure 5.7. The flow in the left and right branches must be equal to the flow in the parent branch, i.e.

$$f_0 = f_1 + f_2. \tag{5.3}$$

It follow from this that the relationship between the radii of the branches is,

$$r_0^3 = r_1^3 + r_2^3. \tag{5.4}$$

By rearranging equation (5.2) for f and substituting it into (5.1), Murray [1926a] was able to show that,

$$KE = lr^2, \tag{5.5}$$

where $K = \frac{3}{2}\pi b$.

If the length of the parent branch is extended by a short distance, δl_0, the amount of work for the parent branch increases, $KE_0 = l_0 r_0^2 + \delta l_0 r_0^2$. The amount of work for the left and right branches decreases, $KE_1 = l_1 r_1^2 - \delta l_0 r_1^2 cos\theta_1$ and $KE_2 = l_2 r_2^2 - \delta l_0 r_2^2 cos\theta_2$, respectively. Applying a similar argument to extending the left and right branches by δl_1 and δl_2 respectively, and using the principle of virtual work[1], three equations are obtained,

$$\delta l_0 r_0^2 = \delta l_0 r_1^2 \cos\theta_1 + \delta l_0 r_2^2 \cos\theta_2, \tag{5.6}$$

$$\delta l_1 r_1^2 = -\delta l_1 r_2^2 \cos(\theta_1 + \theta_2) + \delta l_1 r_0^2 \cos\theta_1, \tag{5.7}$$

$$\delta l_2 r_2^2 = -\delta l_2 r_1^2 \cos(\theta_1 + \theta_2) + \delta l_2 r_0^2 \cos\theta_2, \tag{5.8}$$

which when equation (5.6) is divided by δl_0, equation (5.7) is divided by δl_1, and equation (5.8) is divided by δl_2, gives

$$r_0^2 = r_1^2 \cos\theta_1 + r_2^2 \cos\theta_2, \tag{5.9}$$

$$r_1^2 = -r_2^2 \cos(\theta_1 + \theta_2) + r_0^2 \cos\theta_1, \tag{5.10}$$

$$r_2^2 = -r_1^2 \cos(\theta_1 + \theta_2) + r_0^2 \cos\theta_2. \tag{5.11}$$

These equations are rearranged to find,

$$r_0^2 = r_1^2 \cos\theta_1 + r_2^2 \cos\theta_2, \tag{5.12}$$

$$\cos\theta_1 = \frac{r_1^2 + r_2^2 \cos(\theta_1 + \theta_2)}{r_0^2}, \tag{5.13}$$

$$r_1^2 \cos(\theta_1 + \theta_2) = r_0^2 \cos\theta_2 - r_2^2. \tag{5.14}$$

Substituting equation (5.13) and (5.14) into (5.12) gives,

$$r_0^4 = r_1^4 + r_1^2 r_2^2 \cos(\theta_1 + \theta_2) + r_0^2 r_2^2 \cos\theta_2, \tag{5.15}$$

$$r_0^4 = r_1^4 + r_2^2 r_0^2 \cos\theta_2 - r_2^4 + r_0^2 r_2^2 \cos\theta_2, \tag{5.16}$$

$$2r_2^2 r_0^2 \cos\theta_2 = r_0^4 - r_1^4 + r_2^4, \tag{5.17}$$

$$\cos\theta_2 = \frac{r_0^4 - r_1^4 + r_2^4}{2r_2^2 r_0^2}. \tag{5.18}$$

[1] when the total work is at a minimum then a virtual change in the system does not change the total work Murray [1926a]

Substituting equation (5.18) into (5.14) gives,

$$r_1^2 \cos(\theta_1 + \theta_2) = r_0^2 \left(\frac{r_0^4 - r_1^4 + r_2^4}{2r_2^2 r_0^2} \right) - r_2^2, \tag{5.19}$$

$$r_1^2 \cos(\theta_1 + \theta_2) = \frac{r_0^4 - r_1^4 + r_2^4}{2r_2^2} - r_2^2, \tag{5.20}$$

$$\cos(\theta_1 + \theta_2) = \frac{r_0^4 - r_1^4 + r_2^4 - 2r_2^4}{2r_1^2 r_2^2}, \tag{5.21}$$

$$\cos(\theta_1 + \theta_2) = \frac{r_0^4 - r_1^4 - r_2^4}{2r_1^2 r_2^2}, \tag{5.22}$$

and substituting equation (5.22) into (5.13) gives,

$$\cos\theta_1 = \frac{r_1^2 + r_2^2 \cos(\theta_1 + \theta_2)}{r_0^2}, \tag{5.23}$$

$$\cos\theta_1 = \frac{r_1^2}{r_0^2} + \frac{r_0^4 - r_1^4 - r_2^4}{2r_0^2 r_1^2}, \tag{5.24}$$

$$\cos\theta_1 = \frac{2r_1^4 + r_0^4 - r_1^4 - r_2^4}{2r_0^2 r_1^2}, \tag{5.25}$$

$$\cos\theta_1 = \frac{r_0^4 + r_1^4 - r_2^4}{2r_0^2 r_1^2}. \tag{5.26}$$

This shows that the branching angles can be calculated from the radii of the branches [Murray, 1926a].

Schreiner and Buxbaum [1993] create a two dimensional network of blood vessels. The area of tissue to be perfused is defined as a circle with area A_{perf} and radius r_{perf}. They state that the total perfusion flow, Q_{perf} should be evenly distributed over the whole area. The authors ensure this by splitting A_{perf} into N_{term} equally size 'subareas' which represent micro-circulatory black boxes and design the network to supply equal flow, Q_{term}, at equal pressure, p_{term} [Schreiner and Buxbaum, 1993]. In order to optimise the vessel network, Schreiner and Buxbaum [1993] minimise the total blood volume within the tree.

Schreiner and Buxbaum [1993] define the bifurcation rule to be,

$$r^\gamma(i) = (r(L_i))^\gamma + (r(R_i))^\gamma \tag{5.27}$$

where $r(i)$ is the radius of branch i, γ is a constant parameter, L_i and R_i are the left and right daughter branches, respectively. If $\gamma = 3$ this is the same rule as defined by Murray [1926b], however Schreiner and Buxbaum [1993] allow different values for this parameter, as long as it is constant for the whole tree.

The algorithm of Schreiner and Buxbaum [1993] proceeds as follows:

1. Scale the perfusion area down so that the area is equal to one micro-circulatory black box, i.e. A_{perf}/N_{term}.

2. Select a point on the boundary of the perfusion area. This will be the proximal end of the first branch.

3. Generate a random point within the circle, which becomes the distal end of the first branch.

4. Calculate the radius of the first branch, using Poisuille's Law so that the flow is equal to Q_{term}.

5. For $i = 2$ to N_{term}

   (a) Increase the perfusion area so it is equal to i micro-circulatory black boxes, i.e. iA_{perf}/N_{term}, scaling the first branch, both the length and the radius, accordingly.

   (b) While $d < d_{thresh}$ and $iter < 10$.

      i. Generate a random point within the perfusion area.

      ii. Set $iter = iter + 1$

      iii. Calculate the minimum distance from previous segments, d.

      iv. If $iter = 10$, calculate $d_{thresh} = 0.9d_{thresh}$ and reset $iter = 1$.

   (c) For $j = 1$ to $i - 1$

      i. Select branch j and split it in half. Name the parent of the split branch, i_{old}, the half still connected to the parent branch i_{bif} and the other half i_{conn}, see figure 5.8.

      ii. Connect the new point to the point at which branch j was split and call this new branch i_{new}.

      iii. Calculate $r^{\gamma}(i_{bif}) = r^{\gamma}(i_{conn}) + r^{\gamma}(i_{new})$ and the bifucation ratio $\beta^{l}(i_{bif}) = r(i_{conn})/r(i_{bif})$.

      iv. For $k = j - 1$ to 1

         A. Calculate bifurcation ratio $\beta^{l}(k)$, known as 'scaling the tree'.

      v. Optimise the location of the new bifurcation, 'scaling the tree' each iteration, to minimise the volume.

      vi. Record the optimised volume and remove the new branch.

   (d) Select the branch that connects to the new point and results in the smallest volume without intersecting any previous branches as the new branch.

   (e) 'Scale the tree'

Schreiner and Buxbaum [1993] use the model to create the vascular bed of the left anterior descending coronary artery in humans. They repeated each model run ten

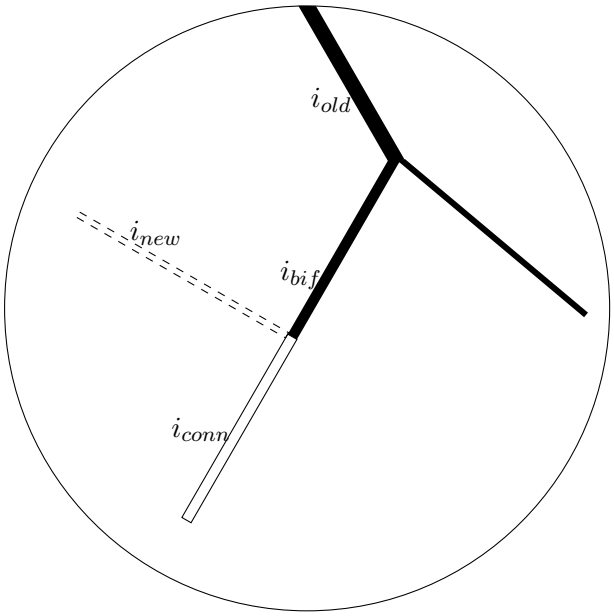

Figure 5.8: Sketch to illustrate algorithm for adding a new branch, corresponds to step 5(c)i.

times using different random numbers. They found good correlation between the mean model diameters and diameters measured from corrosion cast for the initial branch, the branches resulting from only 1 bifircation and the branches results from more than 10 bifurcations. However, those from between 3 and 10 bifurcations were found to have diameters smaller than the measured values [Schreiner and Buxbaum, 1993]. They also used the algorithm to create the vascular bed of the left anterior descending coronary artery in cats and used this to compare the pressures within the vessels to experimental data. The authors found that adjusting the value of γ to 2.55 caused the pressure profile at the distal ends of the branches to be similar to experimental data.

Karch et al. [1999] developed the algorithm for three dimensions and allowed different terminal pressures. The mean diameters of the vessels resulting from 1 to 3 and more than 7 bifurcations showed good correlation to the experimental data, however the branches resulting from 4 to 7 still underestimate the diameters [Karch et al., 1999].

Zamir [2001] took a different approach using a fractal Lindenmayer system (L-system). An L-system has a collection of symbols that are combined to make strings and a group of production rules that rewrite a symbol with a string. Before describing the L-system designed by Zamir [2001], the parameters used are presented.

Zamir [2001] authors define a bifurcation index as,

$$\alpha = \frac{r_2}{r_1}. \tag{5.28}$$

When $\alpha = 1$ the diameters of the left and right branches are equal. Zamir [2001] used equation (5.4) to define diameter ratios in terms of α,

$$\lambda_1 = \frac{r_1}{r_0} = \frac{1}{(1+\alpha^3)^{\frac{1}{3}}} \tag{5.29}$$

$$\lambda_2 = \frac{r_2}{r_0} = \frac{\alpha}{(1+\alpha^3)^{\frac{1}{3}}}. \tag{5.30}$$

The equations for the angles θ_1 and θ_2, (5.26) and (5.18) can also be expressed in terms of α,

$$\cos\theta_1 = \frac{\left(1+\alpha^3\right)^{\frac{4}{3}} + 1 - \alpha^4}{2\left(1+\alpha^3\right)^{\frac{2}{3}}} \tag{5.31}$$

$$\cos\theta_2 = \frac{\left(1+\alpha^3\right)^{\frac{4}{3}} - 1 + \alpha^4}{2\alpha^2\left(1+\alpha^3\right)^{\frac{2}{3}}}. \tag{5.32}$$

The L-system created by Zamir [2001] requires the parameters: L, the length of the branch; W, the width of the branch; and θ_1 and θ_2, the angle of rotation in the clockwise and anticlockwise directions respectively. The L-system is formed of an initial axiom, ω, and a production rule, $\mathfrak{p}$,

$$\omega: \quad X\left(L_0, W_0\right) \tag{5.33}$$

$$\mathfrak{p}: \quad X\left(L,W\right) \mapsto F\left(L,W\right)\left[-\left(\theta_1\right)X\left(\lambda_1 L, \lambda_1 W\right)\right]\left[-\left(\theta_2\right)X\left(\lambda_2 L, \lambda_2 W\right)\right] \tag{5.34}$$

where X has no graphical interpretation, it acts as a place holder, L_0 and W_0 are the length and width of the first branch, respectively, which must be stored, F creates a horizontal line of unit length, [stores the current branching point and] returns to the previous branching point, + rotates the direction clockwise by the angle θ_1 and $-$ rotates the direction anticlockwise by the angle θ_2. Since λ_1, λ_2, θ_1 and θ_2 are all functions of α, changing the value assigned to α results in different tree structures.

Galarreta-Valverde et al. [2013] extended the method from Zamir [2001] by including two extra symbols. $*$ and / that rotates the direction clockwise and anticlockwise, respectively in the plane orthogonal to the plane in which + and $-$ operate. The author's also included a boundary within which the network could develop by including a verification step to ensure each newly created vessel was contained within the boundary. Galarreta-Valverde et al. [2013] used their algorithm to create synthetic MRI scans within a liver and a thigh.

5.1.3 Summary

In this section SRCT and two methods of reconstruction have been reviewed. Different methods of constructing artificial blood vessels have also been reviewed. In the next section, the methods using for imaging the lymph nodes using SRCT and constructing blood vessel networks are described.

5.2 Methods and Results

5.2.1 Lymph Node Imaging

As preliminary work for the imaging of the lymph nodes, several scans of different nodes were made. The nodes have been prepared in three different ways, perfused, stained and unstained; to find the best method that would lead to a good quality scan. The nodes were prepared by Geraldine Clough and the scans made with Berit Plumhoff. The details of these initial scans can be found in the appendix A.4. The unstained lymph nodes were chosen as the best option for CT scanning. Mesenteric nodes were dissected from mice. They were fixed in formalin, dehydrated in methylated spirit and embedded in wax. The scans were made at the SLS. Three unstained mesenteric nodes were scanned. They had a resolution of 0.69 μm and were imaged on the TOMCAT beamline with a propagation distance of 60 mm. The exposure was 15 ms and 1501 projections were made for a 180°. One of the nodes was imaged using a 360° scan with 3001 projections as it was difficult to locate the node within the wax block. The nodes were reconstructed using FBP and using Paganin phase retrieval [Paganin et al., 2002] and then FBP. A comparison of the two results can be seen in figure 5.9. The FBP only reconstruction shows small length features within the node, which could possibly be the lymphocytes that make up the tissue of the node. The higher contrast of the Paganin and FBP reconstruction shows larger length scale features. It is possible to pick out structures that appear to be B cell follicles, lymphatic channels, the dense cortex and less dense paracortex. It would be necessary to preform histology on the sample to confirm these observations. It is equally difficult in both scans to identify the blood vessels within the node, hence the need to construct the vessels computationally.

5.2.2 Image Processing

One of the node scans was selected for image processing and modelling. The brightness and contrast of both the absorption, reconstructed using FBP without phase information, and phase, reconstructed using FBP with phase information obtained using the algorithm by Paganin et al. [2002], scans were automatically

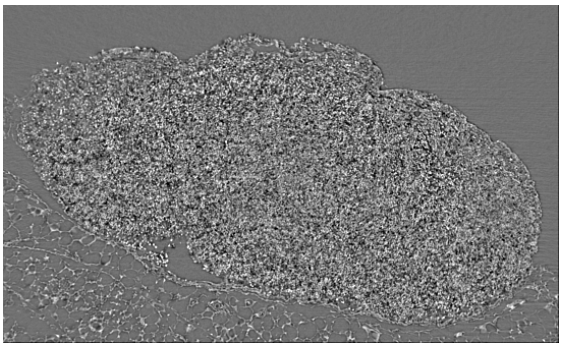

(a) FBP only

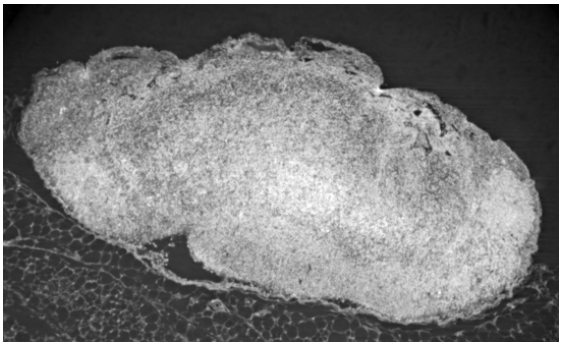

(b) Paganin and FBP

Figure 5.9: Comparison of FBP and Paganin and FBP reconstructions of the lymph node.

adjusted using the ImageJ tool. The whole lymph node was segmented using the phase reconstructions using thresholding. Any additional material selected was removed by cropping and manually removing the excess. A mask was created of the segmented node and this was used to remove everything outside of the node from the absorptions image stack, so that the node was on a white background. Each slice from the absorption image stack was then saved as .png files for use in COMSOL.

During this scanning session it was found that the scintillator was bent. This caused the lower half of the scan to be out of focus, which effected the grey scale values, see figure 5.10. A test was carried out on the processed images to see if this would have an affect on the final model. Results from this test are described below.

5.2.3 Scintillator Test

5.2.3.1 Method

Two cubes of 50 voxels^3 were taken from the middle of the node, CC2LN, one from within the section affected by bent scintillator and one from outside of this section, see figure 5.11.

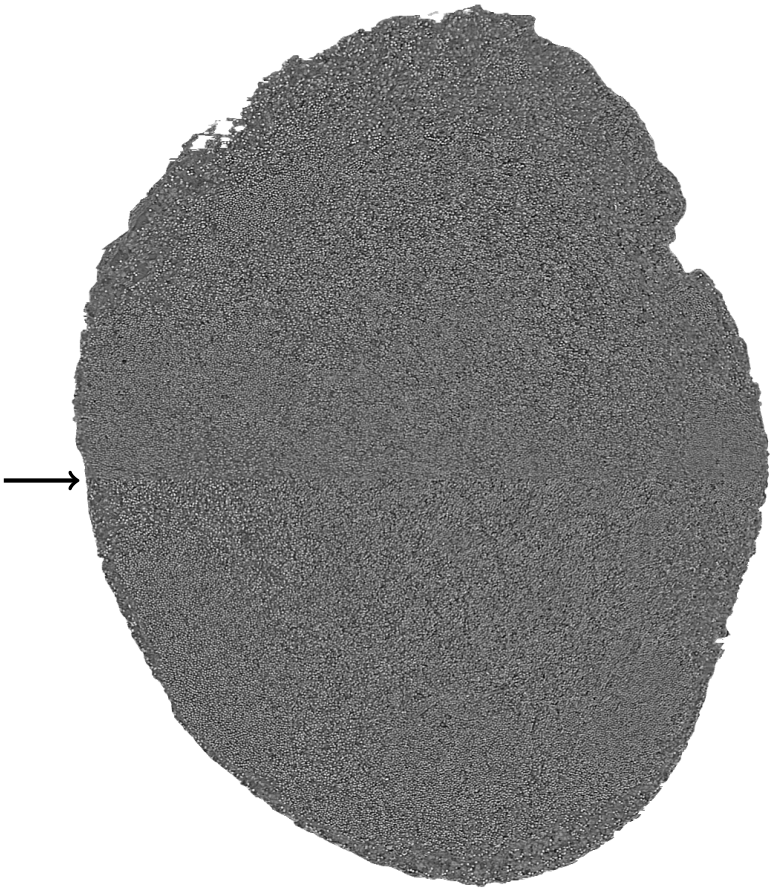

Figure 5.10: Slice through node showing area where region is affected by the bent scintillator. The background has been made white for clarity. Arrow indicated where change occurs.

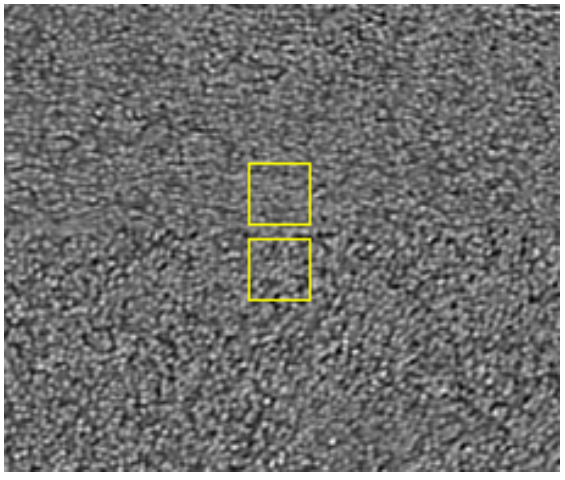

Figure 5.11: Regions used in scintillator test

A cube of 34.5 μm^3 (equivalent to 50 voxels^3) was constructed in COMSOL, see figure 5.12. The cube was meshed with quadratic elements with edge length 0.69 μm. An inlet flow rate of 5 μL/min was assigned to the top boundary and an outlet pressure of 0 Pa was set on the base. The image stack was used to relate the grey scale to the permeability using the values of k_0 and k_1 found for the PLT node in chapter 4, table 4.2.

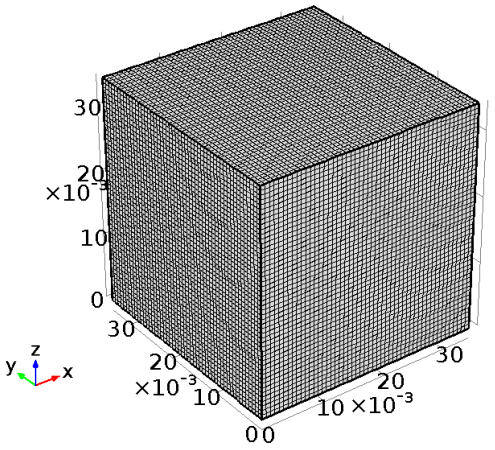

Figure 5.12: Mesh used for scintillator test.

5.2.3.2 Results

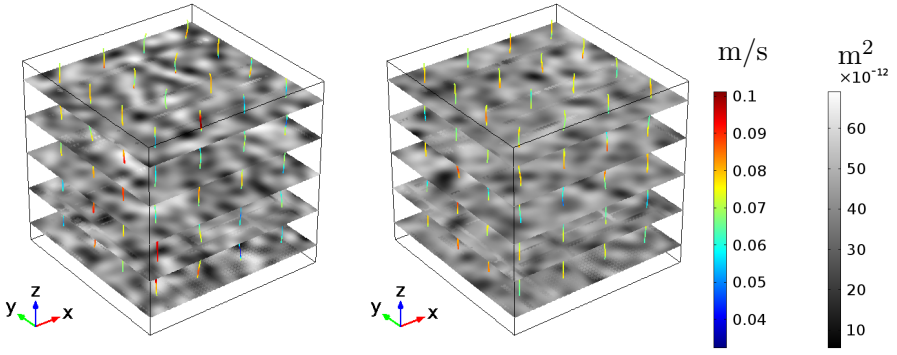

(a) Straight (b) Bent

Figure 5.13: Results for comparison of straight and bent scintillator regions. Grey colour bar shows permeability, colours show velocity magnitude.

The results from the two cubes can be seen in figure 5.13, where stream lines have been coloured with the magnitude velocity and slices through the cubes show the permeability. Comparing the two figures 5.13a and 5.13b, it can be seen that the straight result spans a wider range of values than the bent results, i.e. there are darker colours in the straight result compared to the bent. A few values were

chosen to compare the results from the straight area and the bent area: average velocity, average permeability, maximum velocity and outlet flow rate. The results are presented in table 5.1. It was found that all the values varied less than 0.5%. Therefore, the affect of the bent scintillator was considered negligible.

	Average Velocity (m/s $\times 10^{-2}$)	Average Permeability (m^2 $\times 10^{-11}$)	Maximum Velocity (m/s $\times 10^{-2}$)	Outlet Flow Rate (kg/s $\times 10^{-8}$)
Straight	7.03	3.99	13.6	8.33
Bent	7.02	4.00	13.7	8.33
Percentage Difference with Respect to Straight	0.14	0.24	0.46	9.53 $\times 10^{-13}$

Table 5.1: Comparison of results for cube from in focus area of node (Straight) and out of focus area (Bent) caused by bent scintillator.

5.2.4 Resolution Study

5.2.4.1 Method

There are some variations as to how the model could be set up, size of the mesh elements, resolution of the images and the histogram of the grey scales of the images. To explore the error resulting from these differences, a representative cube was selected as a subsection of the whole node. This cube was selected so that it contained one branch of a blood vessel and was 138 μm $\times$ 138 μm $\times$ 138 μm. Using a subsection of the volume reduced the amount of computational resources required. An inlet flow rate of 5.09619 $\times$ 10^4 m/s was applied to the upper face of the cube and an outlet pressure of 204 Pa was defined on the lower face. These values were evaluated from the two planes 138 μm apart through the WT node model in chapter 4. These boundary conditions are illustrated in figure 5.14.

Here, the maximum size of the mesh elements, Δx, and resolution of the images, Δy, is defined as a single parameter, $\frac{\Delta x}{\Delta y}$. The minimum element edge length was set to 2.39 μm. Mesh sizes were used with $\frac{\Delta x}{\Delta y} = 32$, 16, 8, 4, 2 and 1.

Three different grey scales were used. One created by the automatic adjustment from the ImageJ Brightness/Contrast tool to be known as 'Auto', figure 5.15a, another created by cropping the histogram so that all the channels within the node appear black, and will therefore be assigned maximum permeability, to be known as 'Black', figure 5.15b, and a third, where the grey scales of the image were adjusted so that the histogram was similar to a representative block from the wild type node

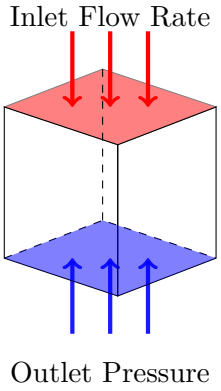

Figure 5.14: Boundary conditions for cube model. All boundaries have no flow condition except those labelled.

modelled in chapter 4, to be known as 'WT', figure 5.15c. Representative slices and the corresponding histograms of the stacks are shown in figure 5.15.

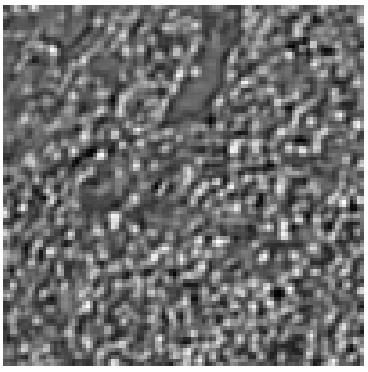

(a) Automatic brightness and contrast

(b) Histogram cropped so that channel is black

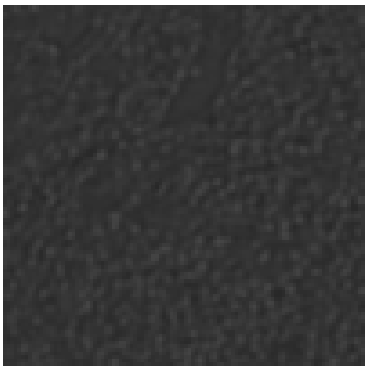

(c) Adjusted so mean and standard deviation similar to a block from the WT node.

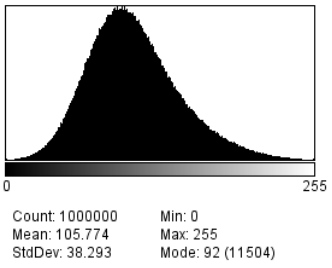

(d) Histogram for automatic brightness and contrast

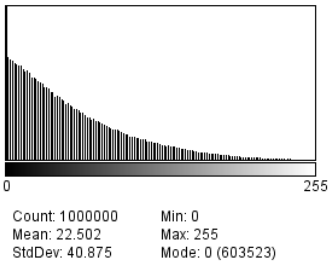

(e) Cropped histogram

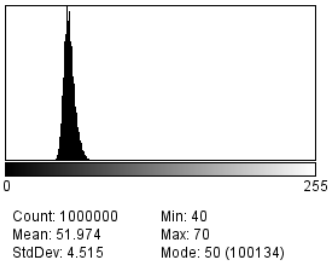

(f) Histogram similar to WT node

Figure 5.15: Different greyscales used to evaluate the affect of different histograms on the same image set on the flow pathways in the model

5.2.4.2 Results

The results of the mesh refinement and using the three different grey scales from figure 5.15 are shown in figure 5.16. The resolution ratio of the mesh to the images, $\Delta x/\Delta y$, did not have a significant effect on the inlet pressure or outlet flow results. However the midplane flow, figure 5.16d, is effected. The mesh with resolution $\Delta x/\Delta y$=4 is chosen as a suitable resolution as it is the coarsest mesh to have a difference of less than 1%. Therefore it is suitable to use the coarser resolution $\Delta x/\Delta y = 4$ for all further models. Using the different grey scale values also had little effect on the results, particularly for finer resolutions. This is due to the fact that the average permeability for all three is equal. This means that as long as the average permeability is correct, it is not relevant how the grey scale range has been defined.

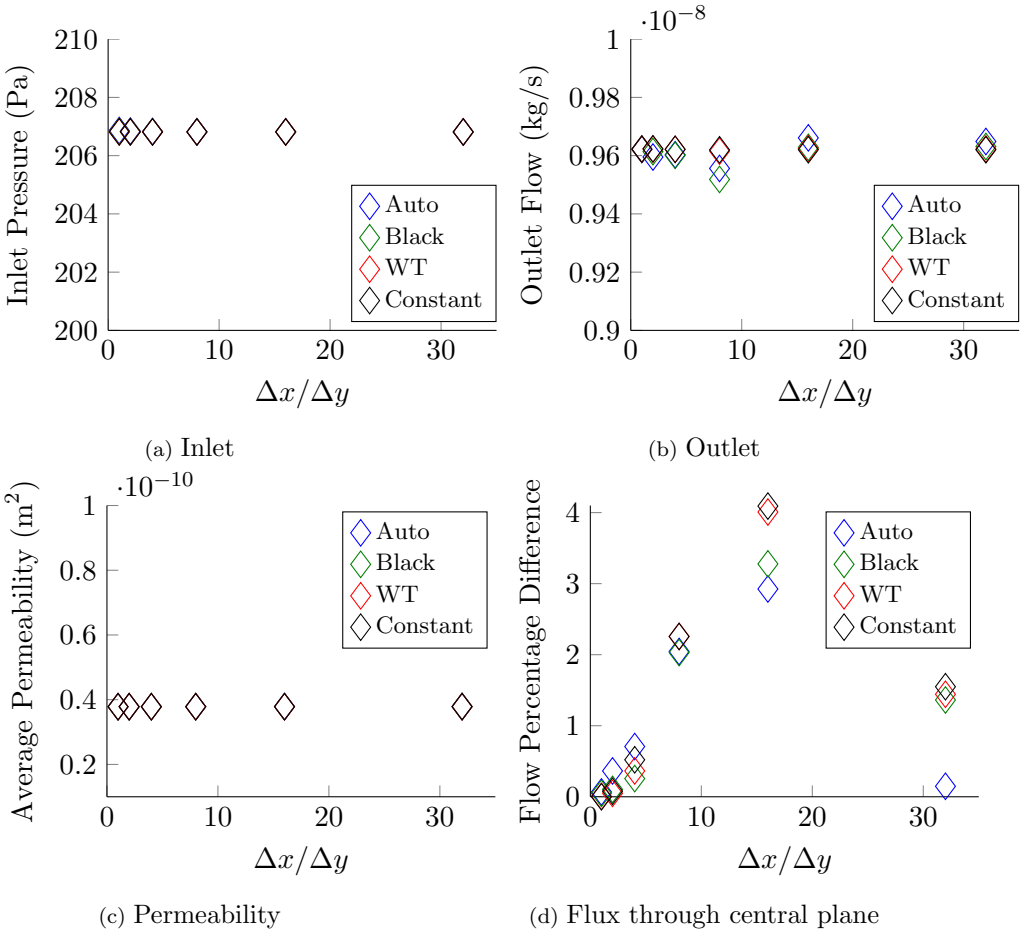

(a) Inlet

(b) Outlet

(c) Permeability

(d) Flux through central plane

Figure 5.16: Results of different mesh resolutions and image stack histograms.

5.2.5 Region Study

5.2.5.1 Method

A further study was conducted to investigate the effect of different textures within the node. Three different regions were used. The regions are highlighted figures 5.17a and 5.18a. The first was from a region containing channels, i.e. area not packed with lymphocytes, to be known as 'Channels', figure 5.17b, the second from a densely packed area, known as 'Dense', figure 5.17c, and the third a representative area from the centre of the node, to be called 'Medium', figure 5.17d. Representative slices and the corresponding histograms of the stacks are shown in figure 5.17. The same areas were selected from the Paganin stack, see figure 5.18.

5.2.5.2 Results

Taking stacks from different areas of the absorption images of the node did not result in much variation for the inlet pressure, figure 5.19a, outlet pressure, figure 5.19b, or average permeability, figure 5.19c. It did have an effect on the difference through the central cut plane, as can be seen in figure 5.19d, however it did not have the expected effect. It was expected that the channels image stack would allow more flow through than the medium and dense, but the results show more flow through the medium stack. This is probably a results of the very similar histograms for the image stacks, figures 5.17e, 5.17f and 5.17g. The grey scale of the channels does not distinguish them as different features.

Taking stacks from different areas of the Paganin images of the node resulted in comparatively more variation for the inlet pressure, figure 5.20a, outlet pressure, figure 5.20b, and average permeability, figure 5.20c. It affected the flow precentage difference through the central cut plane as was expected, see figure 5.20d, with the most flow though the channels image stack. The histogram for the paganin channels image stack, figure 5.18e, clearly shows two peaks, one which represents the grey scale of the channels, and the other the greyscale of the surrounding lymphatic tissue.

5.2.6 Blood Vessel Surface Area

5.2.6.1 Method

A fractal L-system was used to create blood vessels within the node. This was necessary because it was not possible to see many the blood vessels in the CT scans. The vessels that could be segmented out were used as inputs to the fractal L-system. The fractal L-system method described here is based on the methods created by

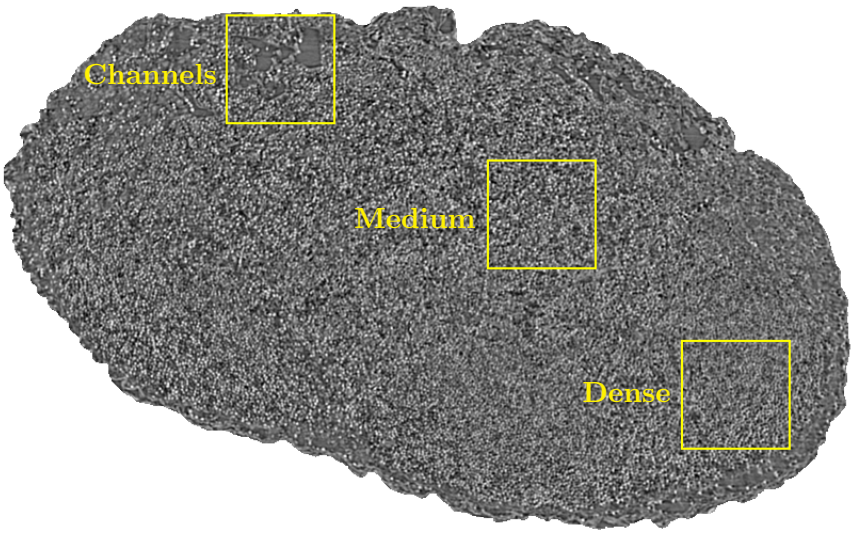

(a) Regions shown on absorption image stack

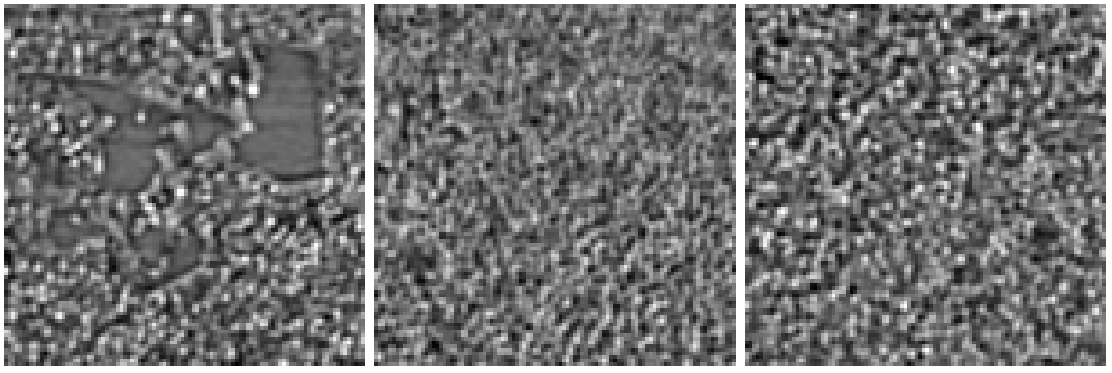

(b) Channels (c) Dense (d) Medium

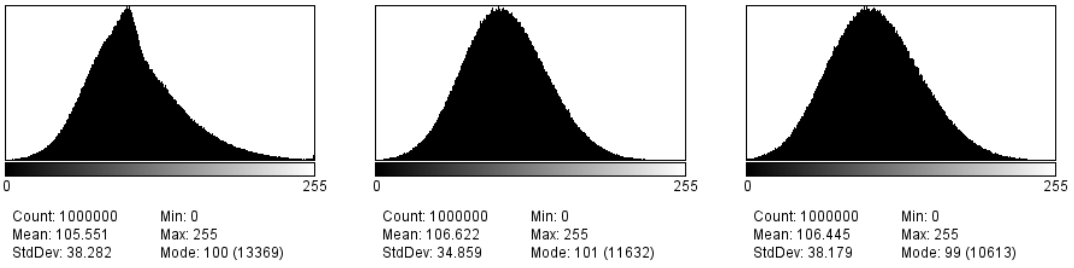

(e) Histogram of channels (f) Histogram of dense (g) Histogram of medium

Figure 5.17: Different regions used to evaluate the effect of areas of the node on the flow pathways in the model.

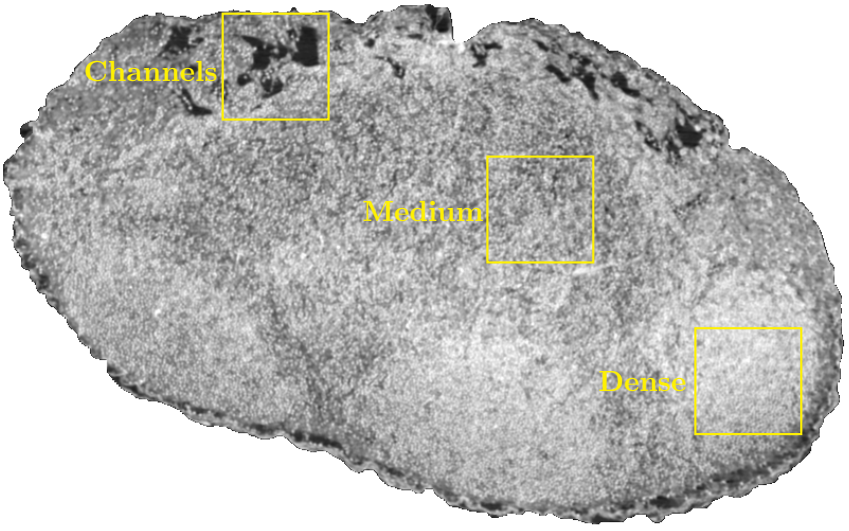

(a) Regions shown on Paganin image stack

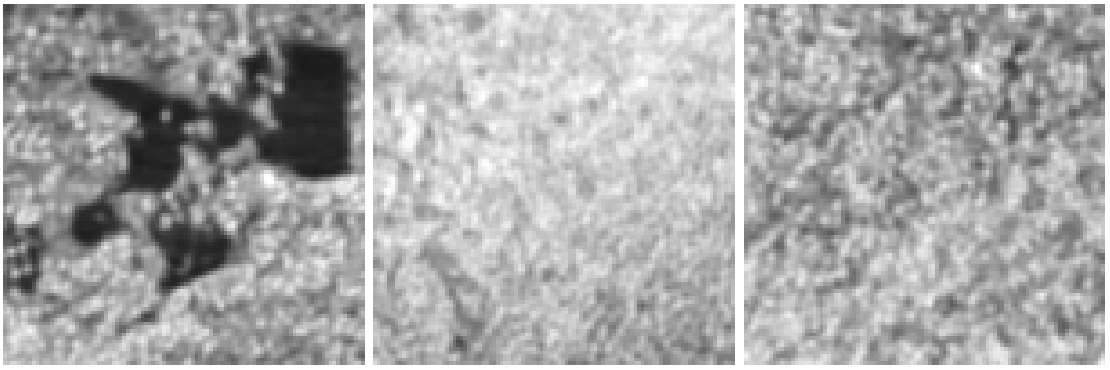

(b) Channels (c) Dense (d) medium

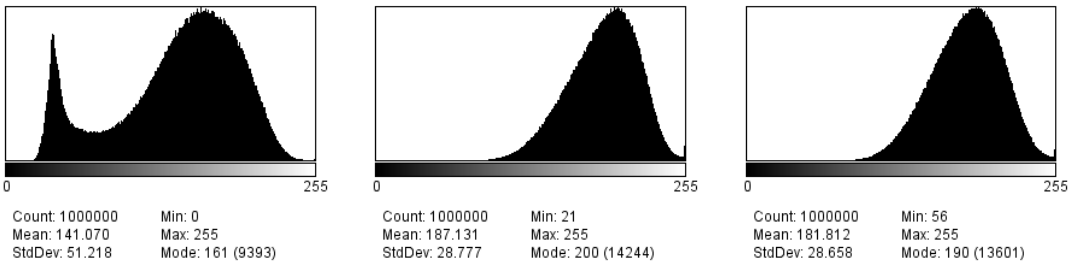

(e) Histogram of channels (f) Histogram of dense (g) Histogram of medium

Figure 5.18: Different regions used to evaluate the effect of areas of the node on the flow pathways in the model.

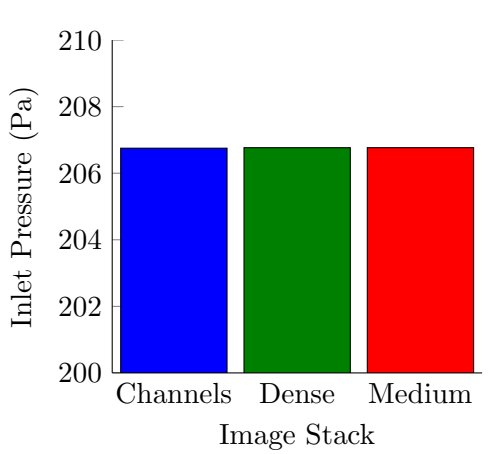

(a) Inlet

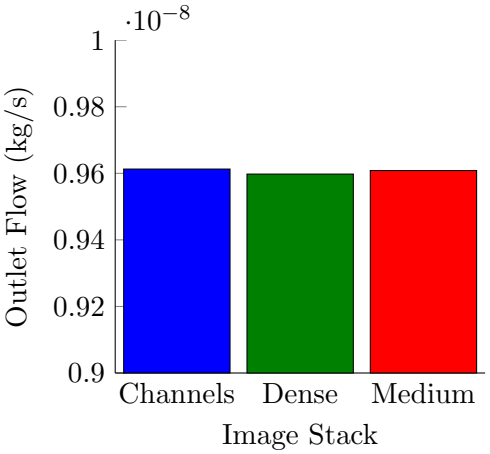

(b) Outlet

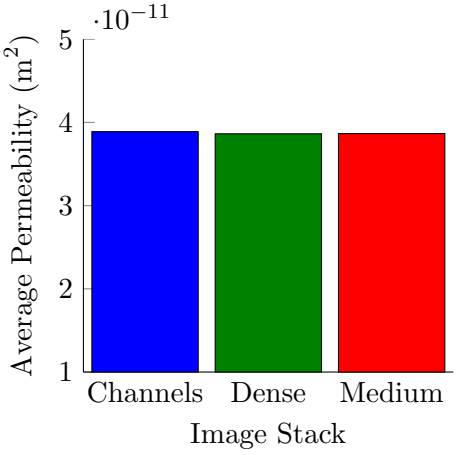

(c) Permeability

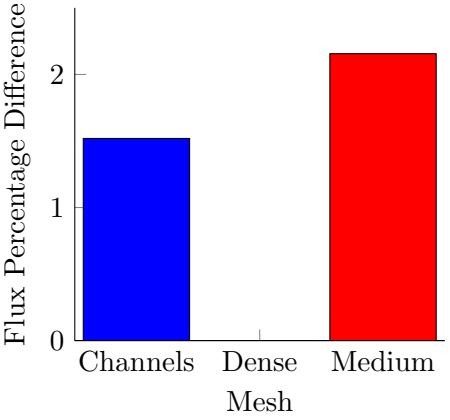

(d) Percentage difference of flux through central plane with respect to dense image stack results, hence dense results is zero.

Figure 5.19: Graphs show how using the image stacks from different regions of the node from the absorption images to define the permeability affected the flow in a subsection of the node. The inlet, outlet and average permeability are not affected, but the flux percentage difference is.

Zamir [2001] and Galarreta-Valverde et al. [2013]. It was implemented as a MATLAB script, which was adapted from `https://courses.cit.cornell.edu/bionb441/LSystem/Lsystem3Dtube.m`.

For a fractal L-system rules are created to define the branching structure. Each character represents an instruction. Two rules are used to describe the blood vessel structure,

$$X \mapsto F[-Y][+Y] \tag{5.35}$$

$$Y \mapsto F[/X][*X] \tag{5.36}$$

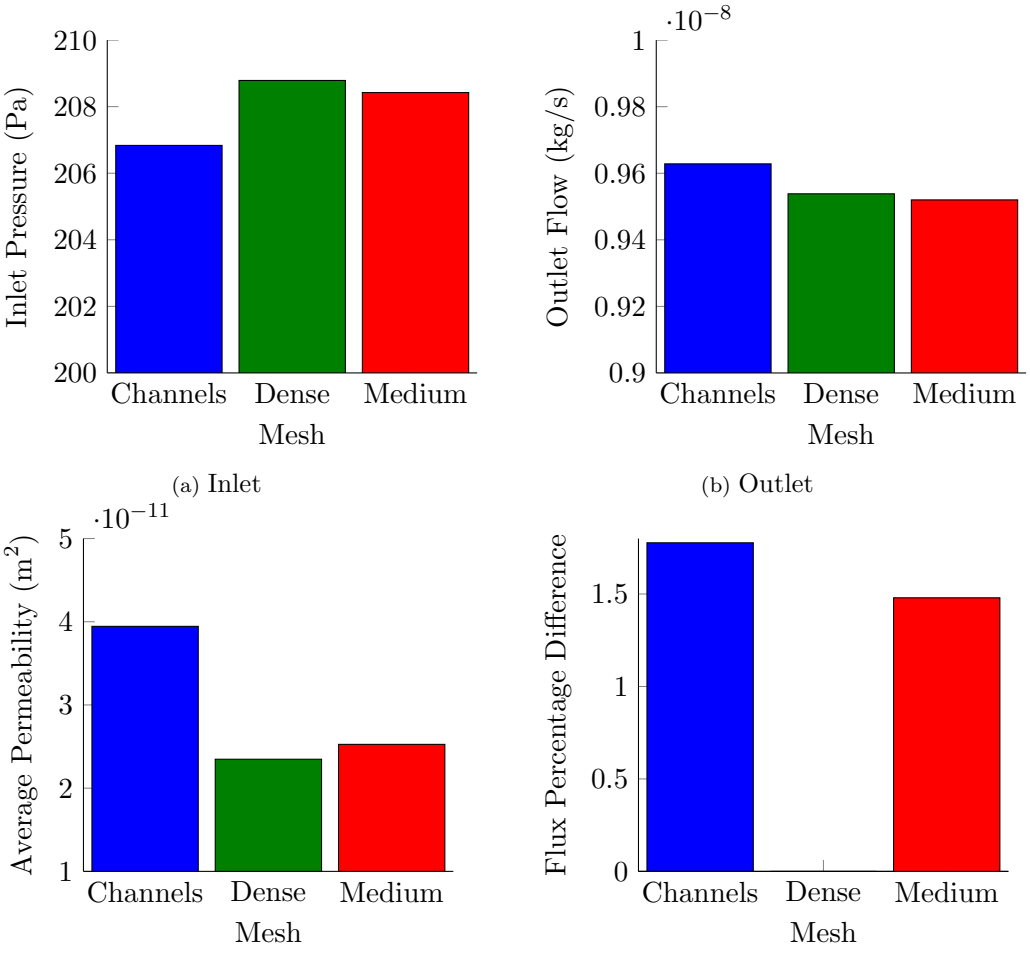

(a) Inlet

(b) Outlet

(c) Permeability

(d) Percentage difference of flux through central plane with respect to dense image stack results, hence dense results is zero.

Figure 5.20: Graphs show how using the image stacks from different regions of the node from the Paganin images to define the permeability affected the flow in a subsection of the node. The inlet, outlet, average permeability and flux percentage difference are all affected.

where the characters represent the following instructions: X and Y act a place holders, i.e. nothing happens for these characters, F mean move forward one step, [means save the current position, $-$ and $+$ mean rotate by θ degrees clockwise or anticlockwise, respectively, in the initial plane, / and $*$ mean rotate by θ degrees clockwise or anticlockwise, respectively, in the plane perpendicular to the initial plane and] means return to the previous position. θ is defined as

$$\theta = \arccos\left(\frac{\left(\left(1+\alpha^3\right)^{4/3}+1-\alpha^4\right)}{\left(2\left(1+\alpha^3\right)^{2/3}\right)}\right) \tag{5.37}$$

where $\alpha = 1$. The points of the segmented vessels ends are used as the start points for

growing the blood vessels trees. Another point was found approximately 10 μm back along the vessel length and the unit vector corresponding to the vector between these two points was defined as the heading vector.

The number of times these rules are used depends on the required number of branch bifurcations. An example of the rules used for different branch bifurcations are shown in table 5.2.

Bifurcations	Rule
1	$F[-Y][+Y]$
2	$F[-F[/X][*X]][+F[/X][*X]]$
3	$F[-F[/F[-Y][+Y]][*F[-Y][+Y]]][+F[/F[-Y][+Y]][*F[-Y][+Y]]]$

Table 5.2: Rules used to create blood vessel trees for different numbers of bifurcations

Using an image from Anderson and Anderson [1975], the vessel length of the first branch within in the node was estimated. Two initial branches were followed to find the branches after the bifurcation. These were segmented out, skeletonised and measured to calculate the length. The image was scaled into micrometers by assuming the arteriovenous connection was 10.5 μm in diameter. The branches were calculated to have a mean range of 328 μm. However the standard deviation is large, 288 μm.

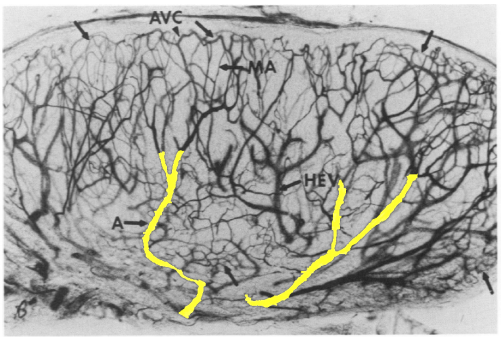

(a) Yellow areas show vessels that were segmented

(b) Skeleton of segmented vessels that were measured

Figure 5.21: Image of rat lymph node was segmented and skeletonised to measure the length of the vessels after the first branching point. AVC, arteriovenous connection, HEV, high endothelial venule, A, artery and MA, metarterioles. Unlabelled arrows point to cortical and medullary arteriole arcades. These images were published in Publication title, Vol number, Author(s), Title of article, Page Nos, Copyright ©1975, American society for investigative pathology; Published by Elsevier Inc; All rights reserved.

Before a new branch is created, the algorithm checks whether a new end point is inside the node by checking if the new point has the value of 1 (white) in the image stack. The algorithm also checks to see if the new branch intersects with any other

branches of the same tree by solving the simultaneous equations,

$$\boldsymbol{x}_{start} + a\boldsymbol{x}_{end} = \boldsymbol{p} \tag{5.38}$$

$$\boldsymbol{x}^i_{start} + b\boldsymbol{x}^i_{end} = \boldsymbol{p} \tag{5.39}$$

where $\boldsymbol{x}_{start}$ and $\boldsymbol{x}_{end}$ are the start and end points of the new branch, respectively, a is an unknown parameter, and p is the point of intersection, $\boldsymbol{x}_{start}$ and $\boldsymbol{x}_{end}$ are the start and end points of branch i and b is another unknown parameter. If the new branch and branch i intersect, then $\boldsymbol{p}$ is the point of intersection and a and b are the parameters that calculate that point. If the branches do not intersect then $\boldsymbol{p}$, a and b are returned as empty values.

If the branches are found to intersect it is further checked to see if this intersection occurs at the end of branch i. If it does, then the new branch is saved and the next iteration begins. If the new branch intersects with the beginning of branch i, another check is made to ensure that the new branch will not be the third branch initiated at that point, since the tree should only develop bifurcations not more. If all of these checks are passed, the final check is to find out if the intersection occurs within the length of the branch. The dot product of the vector between the start and end points of branch i and between the intersection point and the start of branch i is found, i.e.,

$$c_1 = \left(\boldsymbol{x}^i_{start} - \boldsymbol{x}^i_{end}\right) \cdot \left(\boldsymbol{p} - \boldsymbol{x}^i_{start}\right). \tag{5.40}$$

If c_1 is less than zero, the intersection occurs before the start point and the new branch can be saved. However, if it is greater than zero, the dot product between the start and end points of branch i and between the intersection point and the end of branch i must also be found, i.e.,

$$c_2 = \left(\boldsymbol{x}^i_{start} - \boldsymbol{x}^i_{end}\right) \cdot \left(\boldsymbol{p} - \boldsymbol{x}^i_{end}\right). \tag{5.41}$$

If c_1 is greater than c_2, the intersection occurs after the end point and the new branch can be saved. However, if not the intersection occurs within the length of the branch. If the new branch fails this, or any of the previous checks the new branch is discarded and the next new branch is initiated.

A new tree was initiated at the end points of each segmented branch. After all the trees were segmented the start and end points of each branch were imported into an ImageJ macro that created an image stack of the same dimensions as the image stack of the lymph node. The 3D line tool from the 3D tools plugin was used to draw white lines of a fixed radius on a stack of black images. The macro could then be run in ImageJ to create an image stack of the computationally created blood vessels that was then combined with the masks for the surfaces representing the lymphatic vessel connections and the mask for the outline of the lymph node. Three trees were

created of 4, 5 and 6 branches. Three other trees were created by defining start points and heading vectors randomly. Two of these trees were created with 14 and 28 start points, respectively, and 6 branches. The third tree was the 28 start point tree where the diameter of the vessels were increased by 11 μm. The value of L_p for each model was calculated from the value of $L_p \times S$, where S is the blood vessel surface area, for the WT node from chapter 4 by dividing by the surface area for the created blood vessel trees. The models with different branching structures were modelled with a constant permeability for the lymph node interstitium.

5.2.6.2 Results

The whole node model was calculated using a constant value for the permeability, for six nodes with the same external geometry, but with different geometries of blood vessels with different surface areas. The value of L_p for each node is shown in figure 5.22. The value of L_p for the WT node from chapter 4 has been included for comparison.

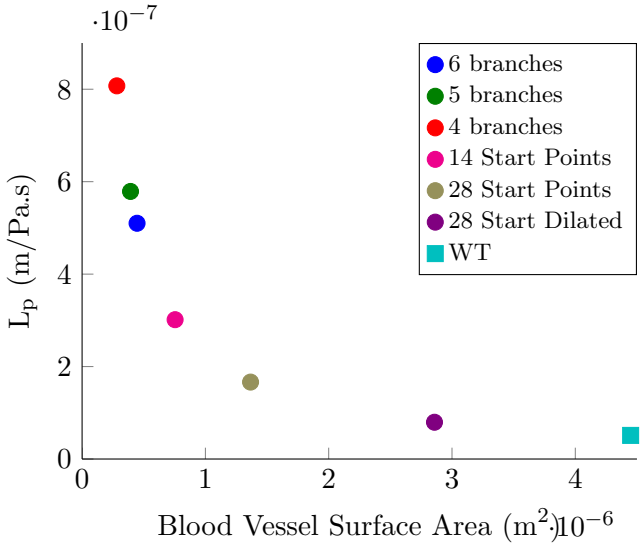

Figure 5.22: Relationship of blood vessel surface area to the value of L_p, where the value of L_pS from chapter 4 has been assumed.

Figure 5.23a, shows how that inlet pressure increased as the surface area of the blood vessels increased. This is likely to be due to more fluid being extravastated across blood vessels with larger surface area, requiring a higher pressure to push the lymph node interstitial flow towards the outlet or because more blood vessels are closer to the inlet. In figure 5.23b, it can be seen that the outlet flow rate is similar for all the blood vessel surface areas. This means that as long as the global value for L_p is chosen correctly, it is possible to produce the same outlet flow rate regardless of how much of the blood vessel surface area has been captured.

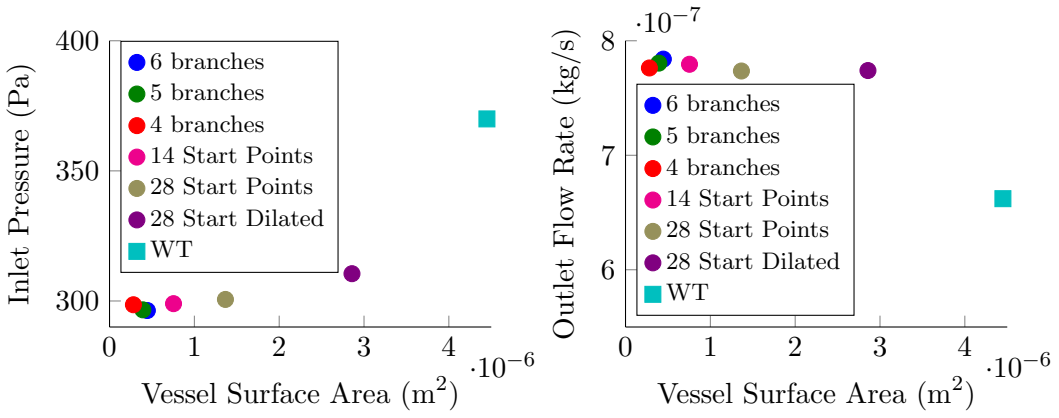

(a) Inlet Pressure

(b) Outlet Flow Rate

Figure 5.23: Results showing how the surface area of the blood vessels affects the inlet and outlet flow conditions.

It is interesting to note that for the blood vessels with different geometries, i.e. the 4, 5, 6 branch trees and the tree with 14 start points, that the difference is outlet flow rate is larger than the difference in outlet flow rate between the 28 start point tree and the 28 start point tree that has been dilated. This may imply that not only is the surface area of the blood vessels an important factor in fluid transport through the node, but also the geometry and position of the vessels. This requires further investigation.

5.2.7 Comparing Image Based Permeability to Constant Permeability

5.2.7.1 Method

The model with image defined start points and 6 branches was used to compare how using the Paganin images affected the flow pathways in the lymph node. The same mesh was used for both models, as well as the same parameter values. The only difference was using a constant permeability in one model and including the images to determine the permeability in the other model.

The computational model boundary conditions and material properties were defined as in chapter 4 for the case where the outlet pressure was equal to atmospheric pressure, i.e. 0 Pa.

5.2.7.2 Results

The streamtubes in figure 5.24 show that including the image based permeability causes the velocity to be more variable through the node. Some streamtubes take a

longer path, note the streamtube on the right of the images, which is due the flow taking a less resistant path.

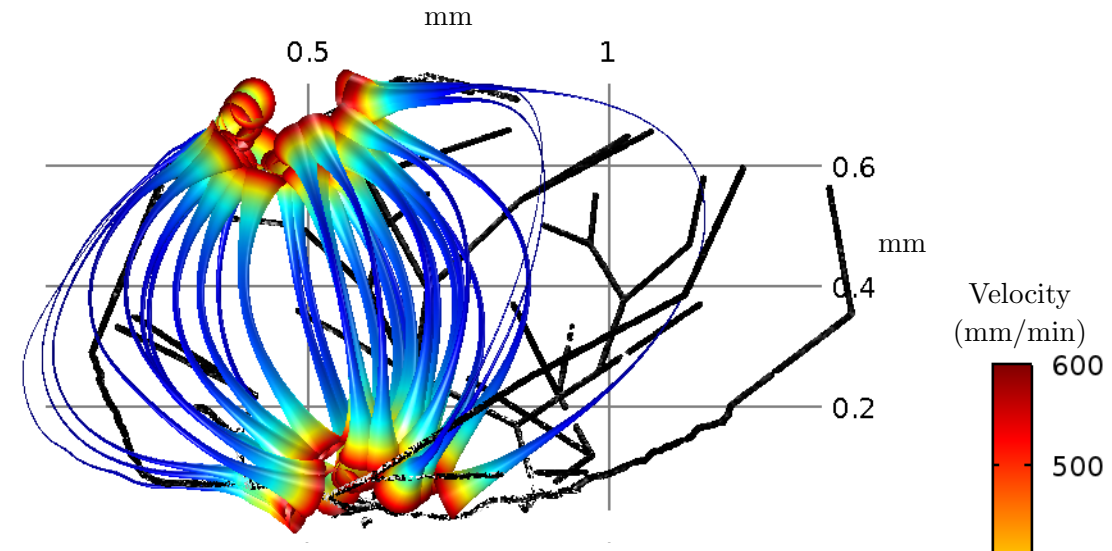

(a) Constant Permeability

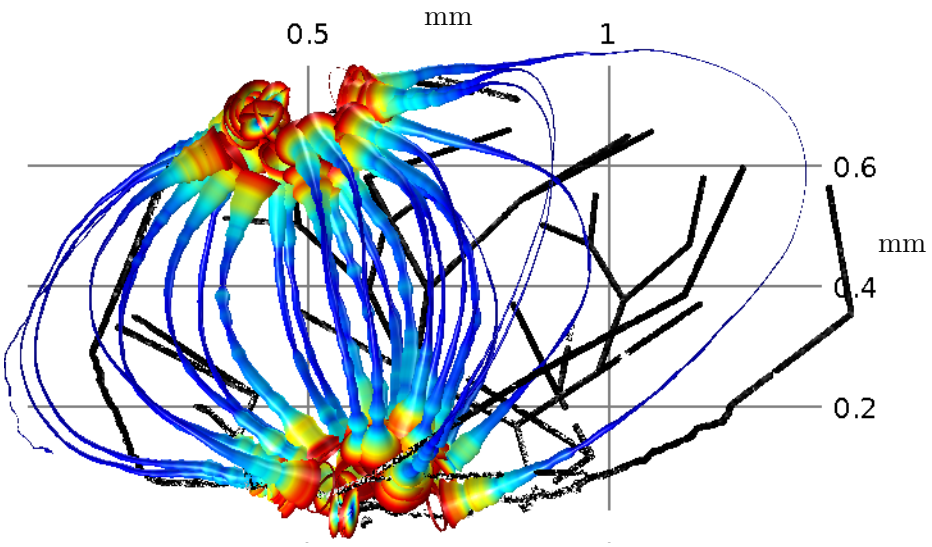

(b) Image Based Permeability

Figure 5.24: Comparing streamtubes for constant permeability and image based permeability. The colour and diameter of the streamtubes show the velocity (mm/min). The blood vessels are coloured white if fluid is being absorbed in the blood vessel or black if fluid is being extravasated across the walls into the lymph node interstitium.

To compare these differences quantitatively, the flux through a plane equidistant between the inlet and outlet, shown in figure 5.25, was evaluated. The results are shown in figure 5.26. Figure 5.26a shows that the model which used the image based

permeability causes more flow around the outer sections of the node than the constant permeability. The high density material in the middle of the node is causing the flow to take less resistant paths further out. Figure 5.26b shows the percentage of the total flux through the plane that passes through each annuli. This shows that the annuli with the highest percentage of flux is the middle annuli with outer radius 414 μm. These results mean that incorporating the image based permeability into the model does not cause the majority of the flow to pass around the outer edge of the node, which would be expected if the subcapsular sinus is considered as the path of least resistance.

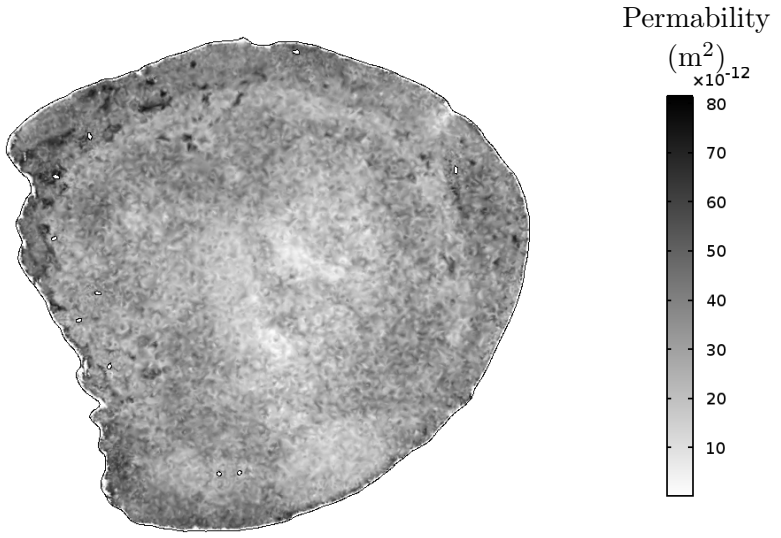

Figure 5.25: Image based permeability of slice through node used for comparing flux to constant permeability node.

The pressure distribution is similar between the two models, see figure 5.27. The pressure in the image based permeability model around the outlet is lower than the constant permeability.

Figures 5.28, 5.29 and 5.30 compare the flow velocity within the node between the two models. All three figures show that the direction of the flow is similar but that the velocity of the flow is different. Figure 5.28 is a vertical plane close to the inlet and outlet. The effect of the inlet and outlet can clearly be see in the flow velocity in the image from the constant permeability model. The fastest flow takes a direct path from the inlet to the outlet. The image based model similarly shows the majority of the fast flow taking a direct path but there is more variability in the flow velocity as certain areas provide more or less resistance.

Figures 5.29 and 5.30 compare the flow velocity in planes parallel to the plane used in figure 5.28, but further from the inlet and outlet. The flow in these planes is slower and it is possible to see in figure 5.29b, from the image based permeability model, that

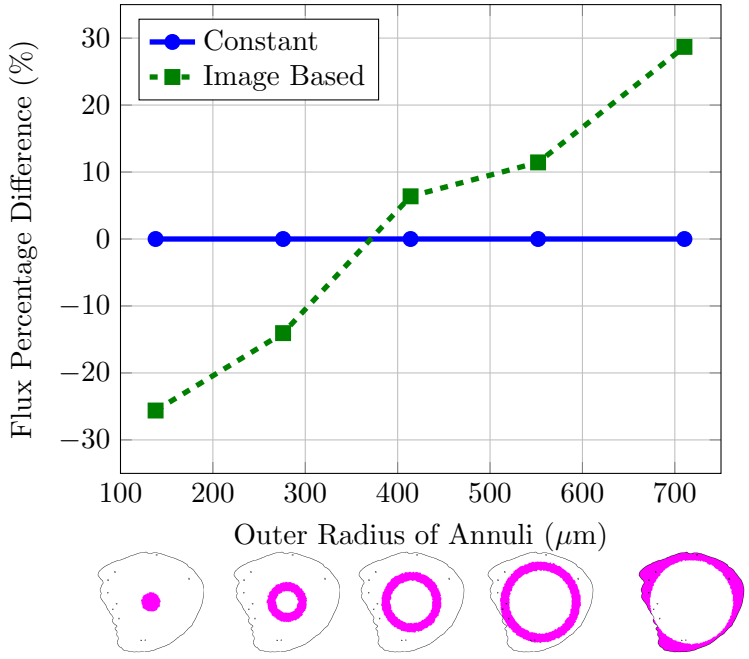

(a) Flux percentage difference through annuli. Values normalised to constant permeability results for comparison, thus all constant values are 0.

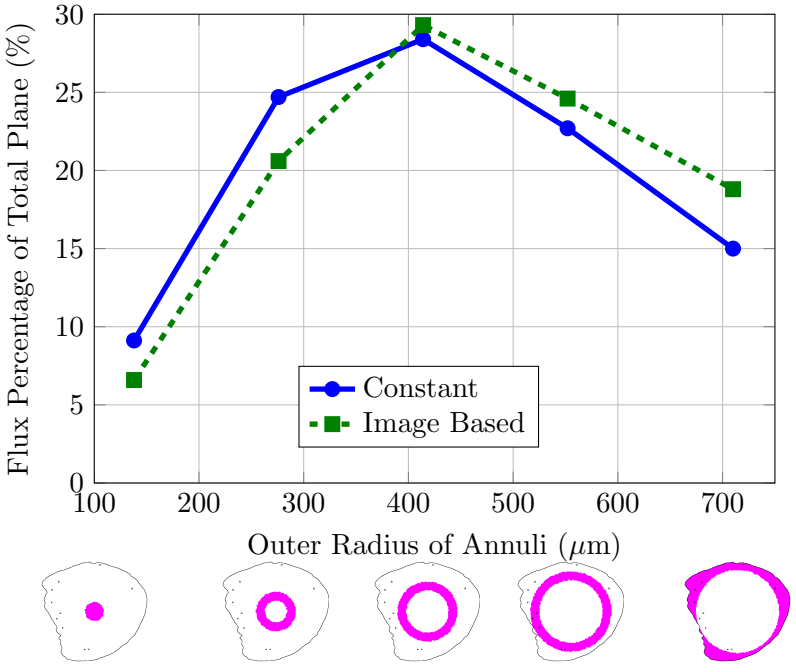

(b) Percentage of the total flux through the plane that passes through each annuli.

Figure 5.26: Comparing flux through different annuli (shown in images below graph) through 2D plane equidistant between the inlet and outlet.

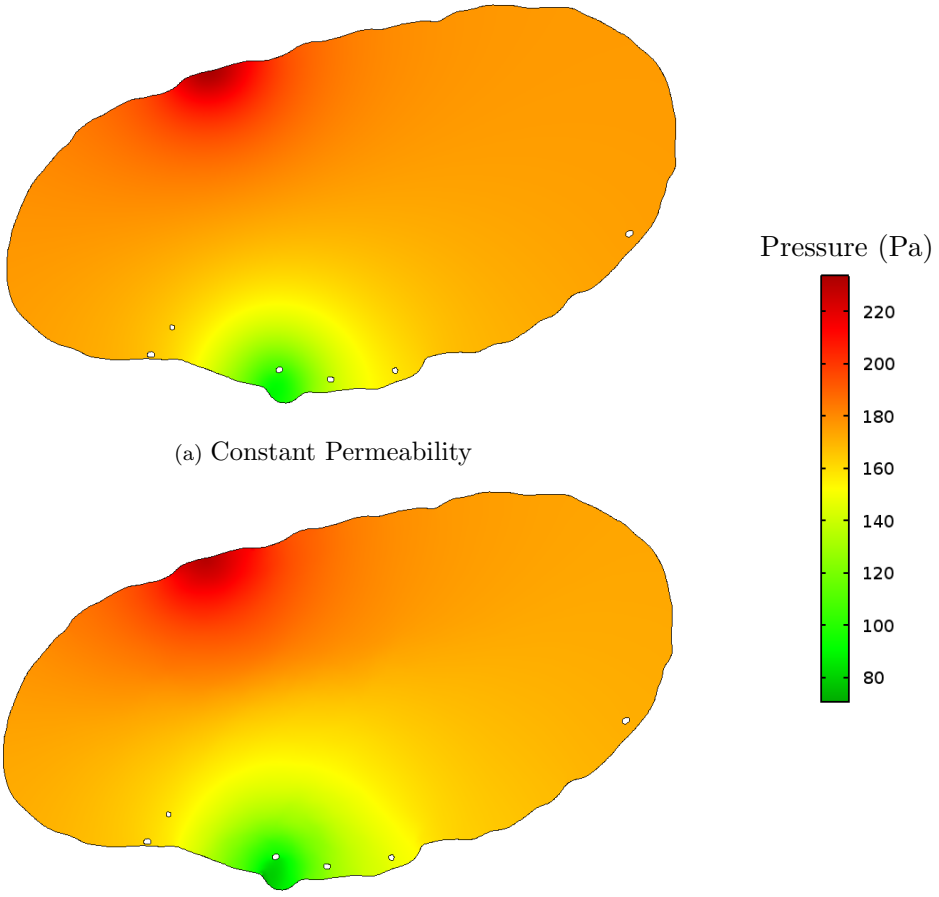

(a) Constant Permeability

(b) Image Based Permeability

Figure 5.27: Pressure distribution through a plane in the lymph node model. The high pressure, red, indicates the location of the position where the afferent lymphatic connects to the lymph node and the low pressure, green, indicates where the efferent lymphatic would leave the node.

near the upper surface, where there are dark areas, that the flow is faster than in the same area in 5.29a, from the constant permeability model. From descriptions in the literature, this area could be the subcapsular sinus and figure 5.29b shows that, if the subcapsular sinus is visualised, using the methods described above the effect can be captured by the model.

A similar phenomenon can be observed in figure 5.30b. The flow in the lower quarter of the image has a higher velocity than the flow in the equivalent area of figure 5.30a. In this area of the node, the presence of medullary sinuses is expected. Figure 5.30b shows that if the features are visualised in the images, these can have an effect on the flow using the methods described.

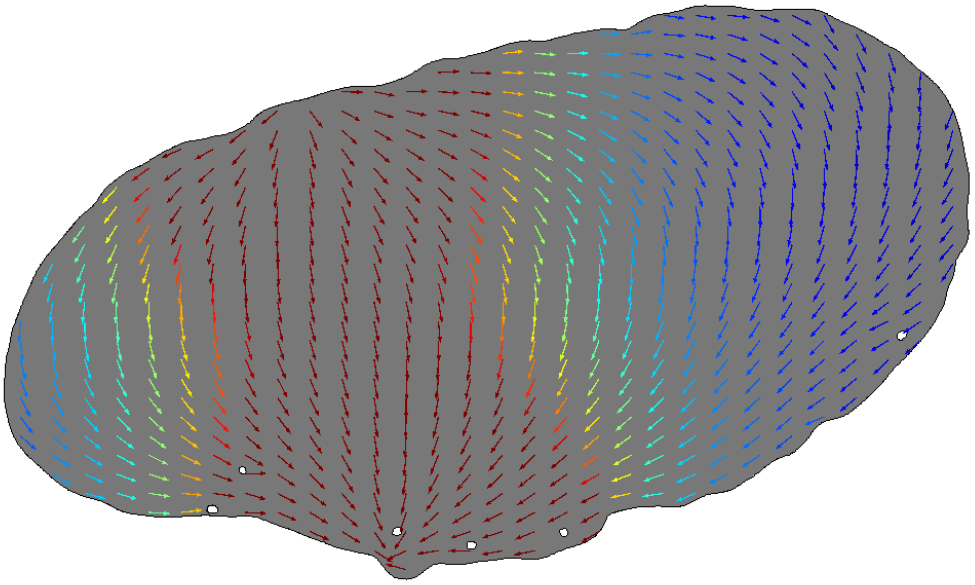

(a) Constant Permeability

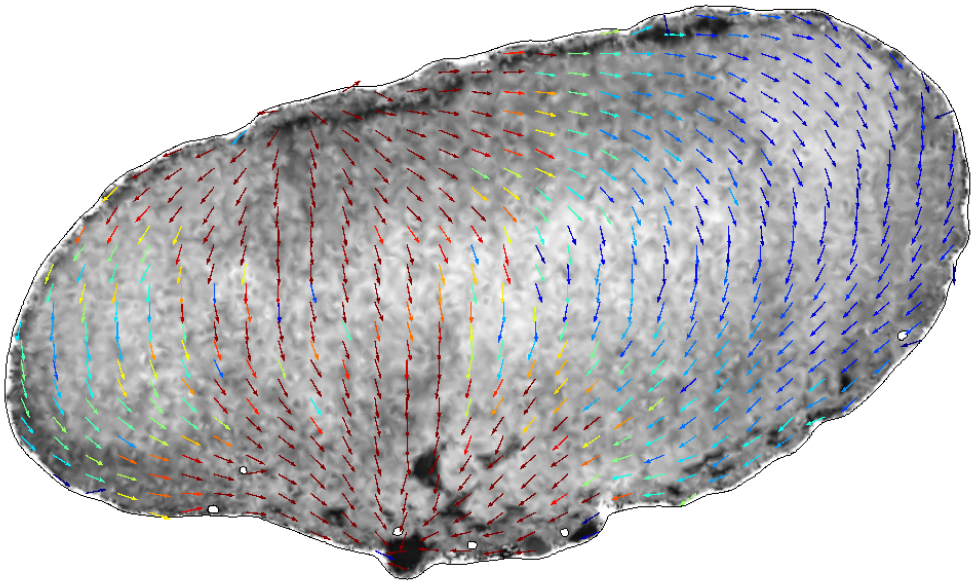

(b) Image Based Permeability

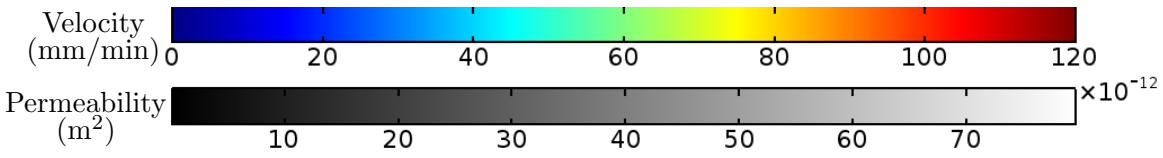

Figure 5.28: Plane close to inlet and outlet. Comparison of constant permeability and image based permeability models showing flow velocity in colour of arrows which indicate the direction of the flow overlaid on the permeability of the plane.

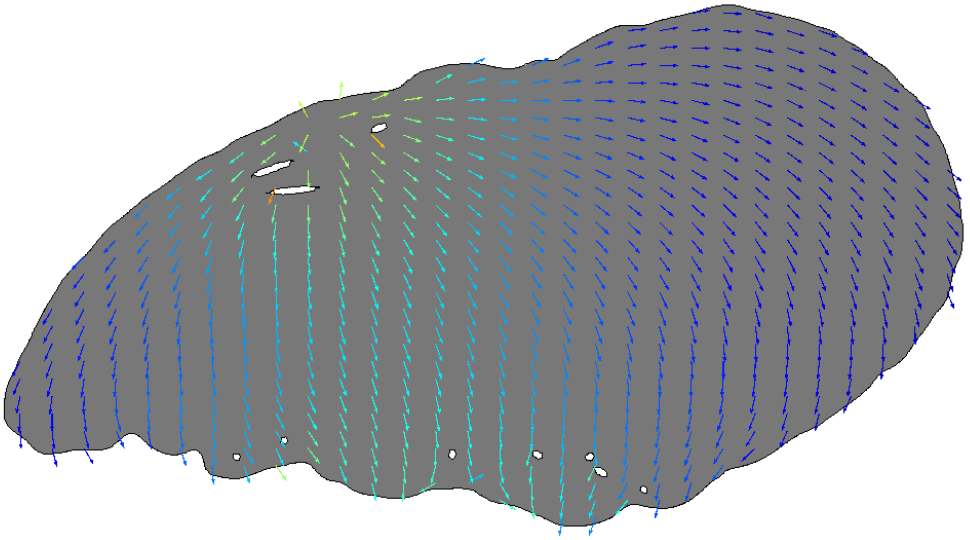

(a) Constant Permeability

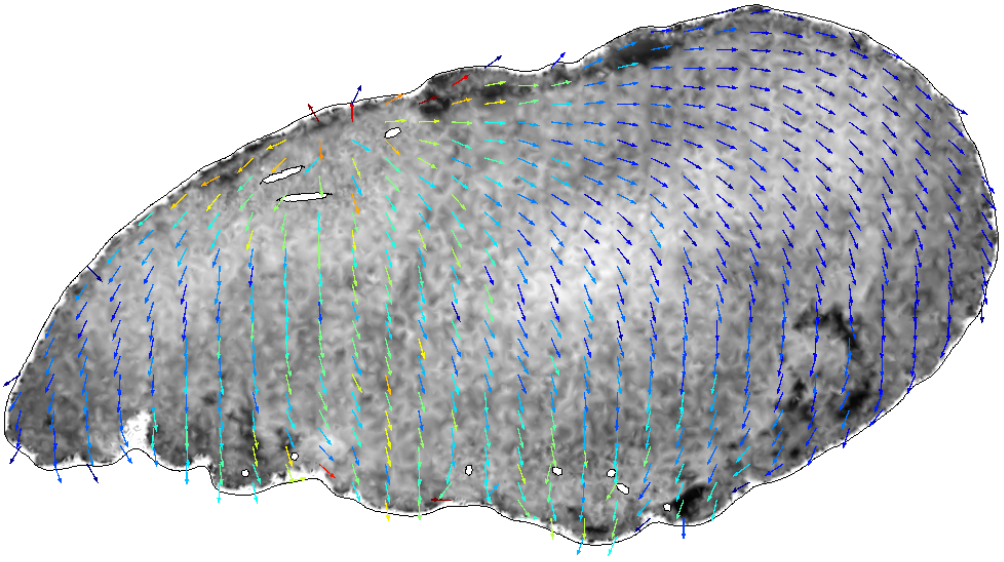

(b) Image Based Permeability

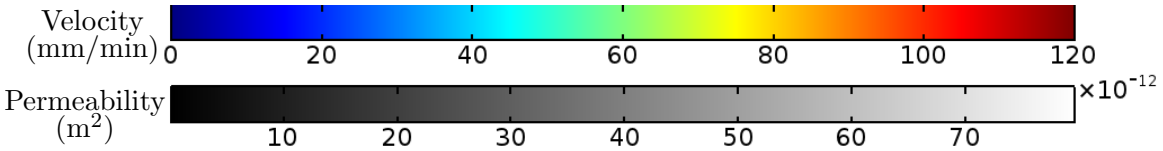

Figure 5.29: Plane parallel to plane in figure 5.28. Comparison of constant permeability and image based permeability models showing flow velocity in colour of arrows which indicate the direction of the flow overlaid on the permeability of the plane.

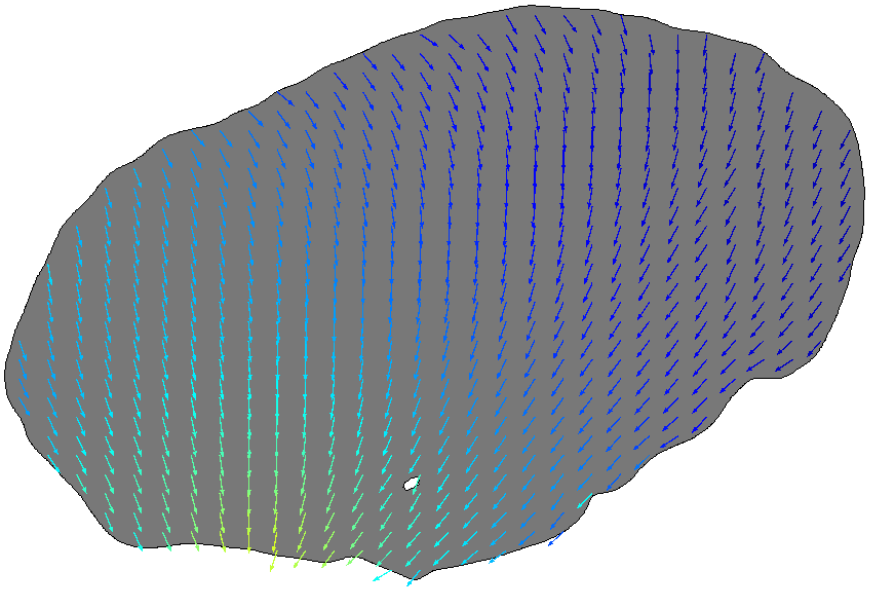

(a) Constant Permeability

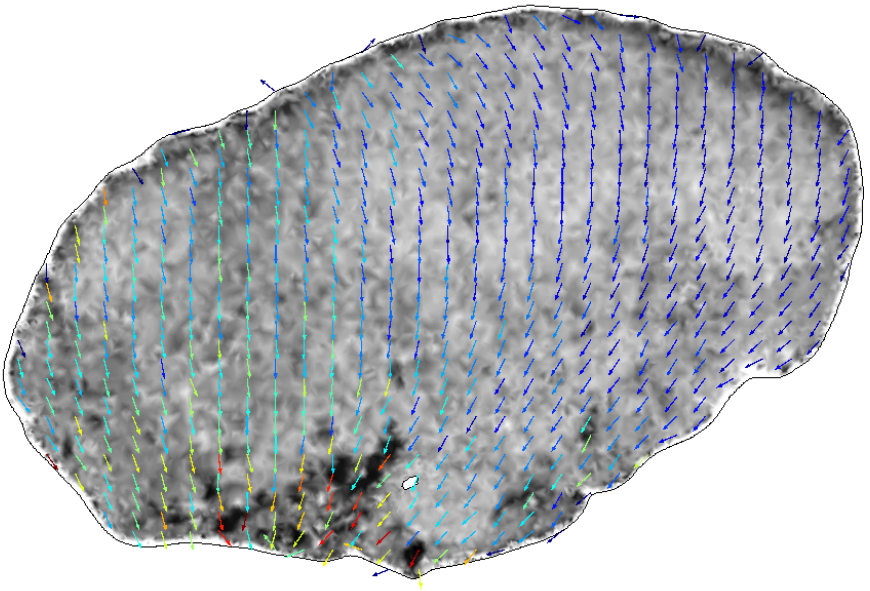

(b) Image Based Permeability

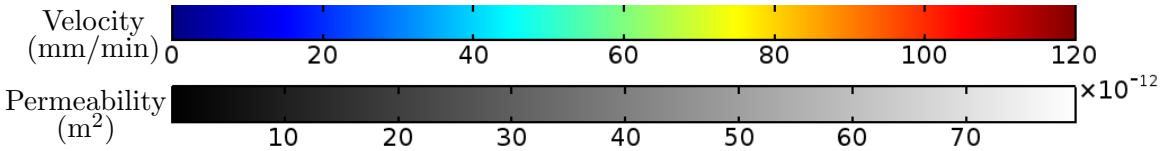

Figure 5.30: Plane parallel to plane in figure 5.28. Comparison of constant permeability and image based permeability models showing flow velocity in colour of arrows which indicate the direction of the flow overlaid on the permeability of the plane

5.3 Discussion

In this chapter a model of a lymph node has been created using images to define the geometry and material properties. A resolution study has been carried out, from which is can be concluded that in order to model the effect of the image based permeability on the flow it is necessary to have a mesh resolution of 5.5 μm. This implies that it is not necessary to scan the sample at a voxel size smaller than this, unless there are smaller features to be identified. It has been shown that Paganin reconstruction produces an image stack that predicts realistic looking fluid flow profiles. The number and position of the blood vessels does not significantly effect the inlet and outlet conditions of the flow as long as L_pS is consistent. However, it is not clear how the position of blood vessels affects the flow direction and it is important to investigate this further. The image based permeability resulted in more flow around the outer sections of the node. The direction of the flow is similar in the constant and image based permeability models however the varying permeability affects the velocity of the flow at small scales.

Compared to the results in chapter 4, which showed the SPIM image based model resulted in more flow through the centre of the node, the model based on CT images shows that the structure of the node causes more flow through the outer section of the node. In the CT images a lot more of the structure is visible compared to the SPIM images, where only the stained areas have been visualised. Thus, the more detailed structure from the CT scans is likely to lead to more realistic results.

After the work on this project had been completed a computational model of a lymph node was in the final stages of being published. Jafarnejad et al. [2015] used an idealised three dimensional geometry of a lymph node with one afferent and one efferent lymphatic vessel. The vessels and subcapsular sinus were modelled as laminar flow regions and the cortex, follicles and medulla were modelled as porous media using Darcy's law with Brinkman's term. Jafarnejad et al. [2015] used Starling's equation to model the flow across the blood vessel boundaries by adapting the conservation of mass. This was only applied to the T cell cortex area of the model. Jafarnejad et al. [2015] used the model to investigate the sensitivity of the model parameters. They found L_pS, the hydraulic conductivity of the blood vessel wall and surface area, increasing the value of L_pS sixteen times resulted in 52.6% more fluid being transferred across the blood vessel walls and into the blood stream. Lowering the medulla hydraulic conductivity increased the resistance of the node to fluid flow. For a high blood pressure of 10.5 mmHg, Jafarnejad et al. [2015] found that extravasation occurred across the blood vessels walls. The authors found that increasing the outlet pressure by an order of magnitude, increased the amount of flux entering the blood vessels.

Jafarnejad et al. [2015] make assumptions about the geometry and fluid behaviour in the regions created in their model, i.e. they used images to inform them to create an idealised geometry, they did not use the images directly. In the models presented in this thesis, such assumptions are not made as the geometry and material properties of the node are based on 3D image stacks.

The limitations of the study presented in this chapter, are that it was not possible to visualise the blood vessels using CT scanning at this time. Another limitation is the processing required for meshing the node results in the mesh not having exactly the geometry of the node. Here, the solution has been to place the images on a white background, so that any background within the meshed node presents a high resistance to the flow. The model does not include a model for protein concentration within the node, which would have an effect on the fluid exchange across the blood vessel walls.

The impact of the position of the blood vessels on the flow pathways requires further investigation. However, it was possible to visualise the blood vessels using SPIM imaging techniques [Mayer et al., 2012]. Lymph nodes could be prepared so that the blood vessels are stained and imaged using SPIM and then CT scanned to obtain the structure of the node interstitium and reconstructed using the algorithm from Paganin et al. [2002]. The two image stacks could then be combined to create a model with realistic blood vessel geometry and variable interstitium permeability. Another option would be to use confocal microscopy to obtain the blood vessel geometry and confirm the locations of B cell regions [Woodruff et al., 2013]. Having obtained this more detailed geometry, it would be possible to incorporate equations for the protein concentration within the lymph node interstitium and investigate the effect on the fluid crossing the blood vessels walls, and therefore on the pathways of fluid through the lymph node.

Comparing the results in this chapter, where the model has been based on x-ray CT images, to the results in the chapter 4, where the model was based on SPIM images, highlights limitations of relating the permeability of the structure to the grey scale of the images. If the lymph node is stained, as it was in the SPIM images, the amount of staining and the areas that the stain highlights can bias the flow pathways. It was assumed in both models that the relationship between the grey scale and the permeability of the tissue was linear. This had to be assumed as no data was found in the literature where the permeability of the lymph node had been measured. Neither was data found relating x-ray CT grey levels with lymph node permeability. A non-linear relation could create a bigger difference between the velocity of the flow through the sinuses and the lymphatic tissue

The permeability of a tissue is dependent on pore size, tissue composition and geometry. If the tissue is deformed, for example by hydrostatic and osmotic pressure,

tension in the extracellular matrix or smooth muscle cells contracting, this will also change the permeability [Swartz and Skobe, 2001]. It is difficult to experimentally measure all of these factors and relate them to the effect on permeability. Often the permeability is estimated assuming some ideal physical and geometry conditions, which means that the value of permeability found is only appropriate on the macroscale [Swartz and Skobe, 2001]. Without specific measurements for different areas of the node it is difficult to identify an appropriate grey scale to permeability relation or even if the flow should be modelled using Stoke's flow rather than Darcy's law in the sinuses.

This chapter has shown that two methods of imaging need to be utilised in order to gain a complete picture of the internal lymph node geometry. The necessary voxel size for the CT images is $\sim$5 μm^3 - using a higher resolution did not yield significantly improved results. The resolution of SPIM or confocal microscopy imaging need to be high enough to capture the smallest blood vessels, capillaries, which are approximate 5-10 μm in diameter. Therefore, if it is possible to visualise the capillaries it will be necessary to have a minimum mesh element size that can capture this geometry and a maximum element size equivalent to the voxel size of the CT images. This information will be useful for planning further imaging and modelling work.

It can be concluded from the modelling study that the structure of the lymph node does affect the fluid flow pathways. This has important implications for antigen, protein and cell transport within the node. The faster flow through the centre of the node suggests how particles in the lymphatic fluid can be passed into the T cell cortex of the node. In the case of antigens, this would trigger an immune response within the node.

The methods developed in the chapter are not restricted to lymph nodes. The method can be applied to any saturated porous material that can be imaged using CT. This could be other biological tissues, e.g. lung tissue, capillary beds; soil, rock, wood, cement or zeolites. In soil the methods could be used to model fluid uptake by plant roots, i.e. the plant roots would replace the blood vessels and the soil would replace the interstitial tissue. This method would remove the need to segment out individual soil grains, a time consuming and difficult process. It could be used in geology by petroleum companies drilling in ocean beds to investigate the affect of drawing oil out of rock beds or the sea water entering the space left once the oil have been removed.

5.4 Future Work

In order to capture more of the geometry of the node, SPIM and CT imaging can be combined. This would allow for the modelling of individual nodes, using the

techniques described in chapters 4 and 5. It would then be possible to investigate the differences between nodes. A possible work flow could be:

- Prepare sample lymph nodes by staining the blood vessels as described in Mayer et al. [2012] but for all blood vessels not just high endothelial venules. Image the samples using selective plane illumination microscopy and computational tomography. Reconstruct the CT scans using the algorithm by Paganin et al. [2002].
- Use the SPIM images to create a mask that represents the blood vessels and use the CT images to create a mask of the geometry of the node. Align the two masks, so that they are both orientated in the same way. Use these overlaid masks to create a mesh.
- Create the model of the lymph node.
- Compare results of different nodes.

It would be useful to obtain more experimental data, such as measured values for the permeability of the lymph node tissue and the hydraulic conductivity of the blood vessel walls. These could be used to validate the values used for the model.

The addition of a convection-diffusion expression to model the protein concentration within the lymph node would affect the fluid exchanges. It would be interesting to investigate the local effect of different protein concentrations on the fluid dynamics within the lymph node.

Chapter 6

Conclusions and Future Work

This thesis set out to create a computational model of a lymph node with pumping afferent and efferent collecting lymphatic vessels using experimental data published in the literature to investigate the fluid flow through lymph nodes and how changes in the fluid dynamics would affect the behaviour of the system. From the outset, it was obvious that this was a challenging problem due to the lack of information about the material properties and behaviour of the collecting lymphatic vessels and lymph nodes. The problem was approached by separating the model into three components, the collecting lymphatic vessel wall, collecting lymphatic valve and the lymph node. The chapters in this thesis discuss the methodologies and findings of these individual components.

The three dimensional models created in this thesis can be used to investigate the functionality of collecting lymphatic vessels and lymph nodes. The lymphatic system is composed of initial lymphatics, collecting lympahtics, the largest of which are called ducts, and lymph nodes. Therefore, from these models it is possible to draw conclusions about two of the three components of the system. However, it is not computationally viable to model an entire network of collecting lymphatic vessels with lymph nodes. Therefore, in order to understand the overall system level function it would be necessary to use the results from the 3D models to inform exisiting network models. Bertram et al. [2013a] have developed such a network model and identified that the resistance to the flow caused by the valve is an important aspect of pumping efficiency in the network. Measuring this resistance proved to be difficult and resulted in a wide range of values. The 3D model of the lymphatic valve with surrounding wall presented in this thesis could be used to investigate why there is such variability between valves. This could be related to the geometry, material properties, wall behaviour or vessel tension, all of which can be investigate with the 3D model. It would also be possible to introduce lymph nodes into the network model, again as causing resistance to the flow. The resistance can be predicted by the permeability values approximated here.

In chapter 2, the first material model for the collecting lympahtic wall was developed that reproduced the experimentally observed passive behaviour. This was achieved by combining an optimisation algorithm with a static structural finite element model in order to optimise the parameters of a strain energy function to the experimental data. The optimisation was carried out twice, once assuming a constant fibre angle and a second time assuming a fibre angle that varied linearly with increasing pressure. From this process, it was found that the varying fibre angle resulted in more realistic parameter valves, however the constant fibre angle produced a better fit with the experimental data. For the first time, this emphasises the importance of the fibre behaviour and the necessity to investigate further the relationship between the changes in diameter and fibre angle in lymphatic vessels. The technique used to find the appropriate parameters can be applied to other problems where the behaviour of a material is known (and nonlinear), but the material properties are not.

In chapter 3, three models of the collecting lymphatic valve were created. The first was three dimensional, assumed linear material properties, for simplification, and modelled the fluid structure interaction of flow though a lymphatic valve. The model showed the fluid behaviour observed experimentally, but the solid behaviour was incorrect, as expected due to the over simplification of the material model. The second model was two dimensional, again to simplify the computation, and only the valve and surrounding fluid domain were modelled. The valve was assumed to have the same material properties as found for the wall using a constant fibre angle in chapter 2. The aim was to use the model to evaluate how similar the behaviour of the valve was to experimental data to assess the validity of the material properties assumption and test the hypothesis of Bertram et al. [2013a] that the experiments from Davis et al. [2011] overestimated the pressure difference required for valve closure. The model required pressure differences two orders of magnitude smaller than observed experimentally and this was thought to be a result of the two dimensional assumption and neglecting the collecting lymphatic wall. Therefore, a third model was created, that was three dimensional and neglected the fluid domain, only modelling the static mechanics of the valve and surrounding wall. This is the first time that a 3D model of a collecting lymphatic vessel and valve have been modelled together using a material model that has been shown to reproduce experimental data. The results from this model predicted that the valve closed at pressure differences lower than observed experimentally, however these pressures were either of the same magnitude or one order of magnitude smaller, and were considered to be more biologically realistic. The results from the model agree with the hypothesis in Bertram et al. [2013a], but as this could be a result of using different geometry or different material properties, it is not possible to confirm if the hypothesis is true. However, the model does support the idea that assuming the same properties for the wall and the valve is a suitable first approximation. Unlike previous one and two dimensional models, the three

dimensional model allows for the investigation of the affects of both geometry and material properties on fluid transport.

Chapter 4 presents the first image based model of fluid flow through a lymph node based on images created using selective plane illumination microscopy. Only a small amount of information was found in the literature about the material properties of the lymph node interstitium, hydraulic conductivity of the high endothelial vessels and colloid osmotic pressure difference in lymph nodes. The model was used to estimate these properties by optimising the parameters that defined them to experimental data. This demonstrated an alternative use for the techniques developed in chapter 2. The values of the parameters found were compared to those found from literature for different tissues and were within biologically realistic values. The model was used to investigate the fluid flow pathways through the lymph nodes. It was found that using the grey scales from the images caused more flow through the centre of the lymph node, which was not what was expected from the descriptions of the structure in literature.

The work described in chapter 5 aimed to improve on the novel lymph node model in chapter 4 by using higher resolution images, with a voxel size of 1.38 μm^3, created using x-ray computed tomography. This was the first time lymph nodes have been imaged at high resolution. Depending on the reconstruction technique different structures could be visualised in the three dimensional image stack. The parameters found in chapter 4 were used and a small area of the node was modelled to assess the sensitivity of the model to the image grey scale values, contrast, the reconstruction techniques and mesh resolution. The important finding from this process was that is was necessary to use the images created from Paganin et al. [2002] reconstruction algorithm for the assumption to hold that the grey scales related to the permeability such that dark areas were more permeable than light areas. It was also found that a mesh resolution of 5 μm was sufficient to capture the flow pathways indicating that for further studies the node only need be imaged at this resolution. The results from the model show the expected result that the structure of the lymph node interstitium directed flow around the outer sections. It was interesting to note that the majority of the flow took a path that was neither around the outer sections or inner sections. This could be an effect of this particular node geometry and further studies would need to be conducted to investigate this further. The methods in this section could be used to model flow through any porous media that have been imaged using computational tomography images.

In summary the novel work presented in this thesis is as follows:

- A non-linear phenomenological material model has been parameterised to reproduce the pressure-diameter behaviour of colleting lymphatic vessels as observed in experiments. This means that the model can be used for estimate

the reaction of the collecting lymphatic vessel wall to different intraluminal pressures.

- The non-linear material model was adapted to model the rotation of the collagen fibres as the pressure increased. This was the first time that the experimental data for the behaviour of collagen fibres on the microscale has been linked to the pressure-diameter data on the macroscale for collecting lymphatic vessel behaviour. This highlights the importance of the fibre movement.

- A model that implemented the non-linear material model in a three dimensional computational model of a colleting lymphatic valve and surrounding wall. This is the first time that the material properties of the wall and valve, geometry of the valve and pressure-diameter behaviour of the wall have all been brought together within the same model. This allows for all these aspects of the model to be investigated within the context of the others for the first time.

- Image based models of fluid flow through a lymph node have been created for the first time. With these models it is possible to investigate the fluid flow pathways and estimate the velocity and pressure of the flow within a realistic geometry using only the afferent and efferent flow properties as inputs.

- The permeability of lymph nodes has been estimated based on experimental data of the afferent and efferent fluid flow and blood pressure. Measuring the permeability of lymph nodes is extremely challenging due to their size, the variability of the tissue porosity and the deformations caused by hydrostatic and osmotic pressures and the movement of immune cells. The method presented here enables the estimation of permeability without the need to measure it within the lymph node.

- SPIM imaging has been used for the first time to model the fluid flow through lymph nodes. The methods presented here show how the imaging and modelling can be combined to predict the flow pathways through the node.

- This is the first time that lymph nodes have been modelled relating the grey scale of the images to permeability to model the variability of the tissue within the node and how this affects the flow pathways. Linking the grey scale with the permeability emphasised the important of the imaging technique and image reconstruction technique on the model resutls. Using SPIM images showed that staining can biases the flow pathways to be through the centre of the node. Comparing FBP and phase retrieval reconsturction techniques for x-ray CT imaging showed that it was necessary to use phase retrieval to get enough contrast between the lymphatic channels and surrounding tissue in order that the highest velocity flow and the majority of the fluid passed through the lymphatic channels as expected.

As has been demostrated throughout this thesis, computational modelling can be utilised to bring together experimental data measured from different samples and species and using different techniques. This highlights how valuable having a computational model is for drawing together all the available information, predicting unavailable data and understanding underlying function. It is cheaper, and in many cases faster, than conducting practical experiments and does has the advantage of not requiring a living specimen. An important aspect of computational modelling that has been particularly difficult in this project is the lack of experimental data for model validation. Without validation it is difficult to prove that the model is accurate and the conclusion drawn from it correct. It has also been necessary to make assumptions and use parameter estimation to create material models that produce the same behaviour as the experments. This was essential due to the lack of experimental data available. This emphasises the areas in which further experimentation would be useful. In the following paragraphs experiments are discussed that could fill in some of these gaps in the current knowledge.

To approximate a material model of the collecting lymphatic vessel wall a phenomenological was used to reproduce the pressure-diameter data measured in experiments. The assumption that the vessels was stretched by a third before being pressurised had to be made as there was no record as to how much tension had been applied to the vessel. The force should be measured before, during and after the pressurisation experiment, as in Zulliger et al. [2004] so that the effect of the tension can be taken into account in the model or it must be consistent for all experiments regardless of vessel size. It would also be advantageous to measure the fibre angle position at the same time at every pressure to really understand how important fibre orientation is to vessel behaviour.

In the valve model the material model was assumed to be the same as the wall. This is not correct as the composition of the wall and valve is different. Therefore, to achieve a better informed model the matieral properties of the valve need to be measured. It would be useful if the valve properties were measured independently of the wall and when it is connected to the wall at different pressures. When combined in the model, this will extend the knowledge of how the valve behaves and how this behaviour depends on the wall.

For the lymph node models it would be advantageous to have experimental data to compare the flow pathways to. This would make it possible to validate the model and could lead to a better understanding of how the structure of the node affects the pathways as well as how the grey scales in the images relate to permeability. A potential problem of tracking fluid movement is that the lymph node filters particles from the fluid, therefore whatever method is used if particles are used to track the flow they must have a molecular size smaller than the node can filter. This size as not been identified in the literature. Magnetic resonance imaging (MRI) could potentially

be useful here as the technique works by exciting water molecules. Therefore any water in the lymph node would show up very clearly. Unfortunately, cells also contain water and therefore the contrast between water and cells may not be big enough to identify the pathways of flow. It may be necessary to combine several different imaging techniques in order to create a complete picture of fluid movement through lymph nodes.

The work presented in this thesis makes significant steps to achieve the ultimate aim of a biologically realistic computational model of a lymph node with afferent and efferent collecting vessels. Considering the work that has been undertaken during the project it is possible to consider the future work to be undertaken to realise this aim.

6.1 Future Work

In this section the future work to achieve the full model of a lymph node with afferent and efferent lymphatics using the models developed in this thesis. Finally, ideas of how to adapt the techniques used within this thesis to other research problems are considered.

The following bullet points describe possible stages in the development of a lymph node with afferent and efferent collecting vessels modelled using finite element analysis:

- Using the geometry and material properties from the solid only three dimensional valve model created in chapter 3, include a fluid domain and create a fluid structure interaction model of a passive collecting lymphatic valve.
- Develop the wall model surrounding the valve to include an active pumping phase in the wall behaviour. This should be dependent on time and also on fluid volume and wall shear stress.
- Link together two lymphatic vessels including valves with a lymph node in between by using the outlet flow rate of the first vessel as the inlet condition of the lymph node, the pressure at the inlet of the node would be the outlet condition for the first vessel, the outlet flow rate of the lymph node as the inlet condition on the second vessel, and the pressure at the inlet of the second vessel would be the outlet condition for the lymph node. This could be done a one large finite element model, a mesh could be created of the node with afferent and efferent vessels, which could each be assigned different properties and COMSOL could integrate the different physics. An iterative solver would be used to solve all the physics. An alternative would be three individual models where each model is given the required inlet/outlet condition after each solver iteration, i.e.:

1. Compute one iteration for first vessel with defined inlet condition and an estimated pressure outlet condition (e.g. half the pressure of the second vessel outlet condition). Evaluate the convergence criteria and export the calculated outlet flow rate.
2. Using a direct solver, calculate the flow through the lymph node using the outlet flow rate from step 1 as a inlet condition. Estimate the pressure at the outlet of the node (e.g. the pressure of the second vessel outlet). Export the calculated outlet flow rate.
3. Compute one iteration for the flow though the second vessel using the outlet flow rate from step 2 as an inlet condition and the defined outlet condition. Export the inlet pressure.
4. Calculate the flow through the lymph node again, using the outlet flow rate from step 1 as an inlet condition and the inlet pressure from step 3 as an outlet pressure. Evaluate the convergence criteria and export the inlet pressure.
5. Compute a second iteration for the first vessel using the inlet pressure from step 4 and the defined inlet condition. Evaluate the convergence criteria and export the calculated outlet flow rate.
6. Repeat steps 2 to 5 until both the vessels achieve convergence.

This process would be very time consuming. The lymph node requires a minimum of 20 minutes to solve for a constant permeability and has to be solved twice each iteration. It would require approximately 70 GBs of RAM. However, there is no guarantee that using the iterative solver for all the components, as would occur to modelling the whole as one model, would be any quicker as solving the lymph node model iteratively takes much longer than using the direct solver.

These steps would enable to fluid flow to be modelled through the afferent vessel, lymph node and efferent vessel. The inlet condition for the afferent vessel and outlet condition for the efferent vessel could be adjusted to investigate the effect this has on the flow through the model as a whole.

The techniques developed are also applicable to other areas of research such as soil science, materials and micro-fluidics. Similar techniques could be used to model other systems containing a porous media filtration or fluid exchange devices such as pond filters, dialysis machines or micro-fluidic devices.

Appendix A

Appendix

A.1 Blatz-Ko Strain Energy Function

For compressible porous rubbery materials, a SEF was developed by Blatz and Ko [1962],

$$W_{BK}\left(I_1, I_2, I_3\right) = \frac{Gf}{2}\left(I_1 - 3 - \frac{2}{q}\left(I_3^{\frac{q}{2}} - 1\right)\right) + \frac{G\left(1-f\right)}{2}\left(\frac{I_2}{I_3} - 3 - \frac{2}{q}\left(I_3^{\frac{-q}{2}} - 1\right)\right), \tag{A.1}$$

The I terms are invariants of a modified right Cauchy-Green tensor $\overline{\boldsymbol{C}} = J^{2/3}\boldsymbol{C}$ where $\boldsymbol{C}$ is the right Cauchy-Green tensor and J is the determinant of the deformation gradient. The invariants to the Cauchy strain tensor are,

$$I_1 = \mathrm{tr}\overline{\boldsymbol{C}}, \tag{A.2}$$

$$I_2 = \frac{1}{2}\left[\mathrm{tr}\left(\overline{C}\right)^2 - \mathrm{tr}\left(\overline{C}^2\right)\right], \tag{A.3}$$

$$I_3 = \lambda_x^2\lambda_y^2\lambda_z^2, \tag{A.4}$$

and λ_x, λ_y, λ_z are stretch ratios. G is the shear modulus, $f \in [0,1]$ and $q < 0$ are parameters. This has been used to model tumour growth and residual stress development [Ambrosi and Mollica, 2002; MacLaurin et al., 2012].

A.1.0.3 Linear Limit of Blatz-Ko Strain Energy Function

Begin by substituting the invariants into Blatz-Ko SEF,

$$W_{BK} = \frac{Gf}{2}\left(I_1 - 3 - \frac{2}{q}\left(I_3^{\frac{q}{2}} - 1\right)\right) + \frac{G(1-f)}{2}\left(\frac{I_2}{I_3} - 3 - \frac{2}{q}\left(I_3^{\frac{-q}{2}} - 1\right)\right), \tag{A.5}$$

$$= \frac{Gf}{2}\left(\left(\lambda_x^2 + \lambda_y^2 + \lambda_z^2\right) - 3 - \frac{2}{q}\left(\left(\lambda_x^2\lambda_y^2\lambda_z^2\right)^{\frac{q}{2}} - 1\right)\right) \tag{A.6}$$

$$+ \frac{G(1-f)}{2}\left(\frac{\frac{1}{2}\left(\left(\lambda_x^2 + \lambda_y^2 + \lambda_z^2\right)^2 - \left(\lambda_x^4 + \lambda_y^4 + \lambda_z^4\right)\right)}{\left(\lambda_x^2\lambda_y^2\lambda_z^2\right)} - 3 - \frac{2}{q}\left(\left(\lambda_x^2\lambda_y^2\lambda_z^2\right)^{\frac{-q}{2}} - 1\right)\right).$$

Substituting the Green's strains, into the SEF gives,

$$\begin{aligned} W_{BK} = {} & \frac{Gf}{2}\left(2E_x + 2E_y + 2E_z - \frac{2}{q}\left(\left(\left(2E_x+1\right)\left(2E_y+1\right)\left(2E_z+1\right)\right)^{\frac{q}{2}} - 1\right)\right) \\ & + \frac{G(1-f)}{2}\left(\frac{\frac{1}{2}\left(\left(2E_x+1\right) + \left(2E_y+1\right) + \left(2E_z+1\right)\right)^2}{\left(2E_x+1\right)\left(2E_y+1\right)\left(2E_z+1\right)}\right. \\ & - \frac{\frac{1}{2}\left(\left(2E_x+1\right)^4 + \left(2E_y+1\right)^4 + \left(2E_z+1\right)^4\right)}{\left(2E_x+1\right)\left(2E_y+1\right)\left(2E_z+1\right)} - 3 \\ & \left. - \frac{2}{q}\left(\left(\left(2E_x+1\right)^2\left(2E_y+1\right)^2\left(2E_z+1\right)^2\right)^{\frac{-q}{2}} - 1\right)\right). \end{aligned} \tag{A.7}$$

Differentiating by strains, we get

$$\begin{aligned}\sigma_{xx} = \frac{\partial W_{BK}}{\partial E_x} = \frac{Gf}{2}\left(2 - 2\frac{\left(\left(2E_x+1\right)\left(2E_y+1\right)\left(2E_z+1\right)\right)^{\frac{q}{2}}}{2E_x+1}\right) \\ + \frac{G\left(1-f\right)}{2}\left(\frac{4+4E_y+4E_z}{\left(2E_x+1\right)\left(2E_y+1\right)\left(2E_z+1\right)}\right. \\ - \frac{\left(2E_x+2E_y+2E_z+3\right)^2-\left(2E_x+1\right)^2-\left(2E_y+1\right)^2-\left(2E_z+1\right)^2}{\left(2E_x+1\right)^2\left(2E_y+1\right)\left(2E_z+1\right)} \\ \left. + 2\frac{\left(\left(2E_x+1\right)\left(2E_y+1\right)\left(2E_z+1\right)\right)^{\frac{-q}{2}}}{2E_x+1}\right),\end{aligned} \tag{A.8}$$

$$\begin{aligned}\sigma_{yy} = \frac{\partial W_{BK}}{\partial E_y} = \frac{Gf}{2}\left(2 - 2\frac{\left(\left(2E_x+1\right)\left(2E_y+1\right)\left(2E_z+1\right)\right)^{\frac{q}{2}}}{2E_y+1}\right) \\ + \frac{G\left(1-f\right)}{2}\left(\frac{4E_x+4+4E_z}{\left(2E_x+1\right)\left(2E_y+1\right)\left(2E_z+1\right)}\right. \\ - \frac{\left(2E_x+2E_y+2E_z+3\right)^2-\left(2E_x+1\right)^2-\left(2E_y+1\right)^2-\left(2E_z+1\right)^2}{\left(2E_x+1\right)\left(2E_y+1\right)^2\left(2E_z+1\right)} \\ \left. + 2\frac{\left(\left(2E_x+1\right)\left(2E_y+1\right)\left(2E_z+1\right)\right)^{\frac{-q}{2}}}{2E_y+1}\right),\end{aligned} \tag{A.9}$$

$$\begin{aligned}\sigma_{zz} = \frac{\partial W_{BK}}{\partial E_z} = \frac{Gf}{2}\left(2 - 2\frac{\left(\left(2E_x+1\right)\left(2E_y+1\right)\left(2E_z+1\right)\right)^{\frac{q}{2}}}{2E_z+1}\right) \\ + \frac{G\left(1-f\right)}{2}\left(\frac{4+4E_y+4E_z}{\left(2E_x+1\right)\left(2E_y+1\right)\left(2E_z+1\right)}\right. \\ - \frac{\left(2E_x+2E_y+2E_z+3\right)^2-\left(2E_x+1\right)^2-\left(2E_y+1\right)^2-\left(2E_z+1\right)^2}{\left(2E_x+1\right)\left(2E_y+1\right)\left(2E_z+1\right)^2} \\ \left. + 2\frac{\left(\left(2E_x+1\right)\left(2E_y+1\right)\left(2E_z+1\right)\right)^{\frac{-q}{2}}}{2E_z+1}\right).\end{aligned} \tag{A.10}$$

Expanding equations (A.8)-(A.10) as Taylor series, taking only the first two terms, and then setting this equal to Hooke's law for an isotropic material leads to,

$$\begin{aligned}\sigma_{xx}: \left(\frac{Gf}{2}\left(-2q+4\right) + \frac{G\left(1-f\right)}{2}\left(-2q+4\right)\right)E_x + \left(-Gfq - G\left(1-f\right)q\right)E_y \\ + \left(-Gfq - G\left(1-f\right)q\right)E_z = \lambda(E_x+E_y+E_z) + 2GE_x,\end{aligned} \tag{A.11}$$

$$\begin{aligned}\sigma_{yy}: \left(-Gfq - G\left(1-f\right)q\right)E_x + \left(\frac{Gf}{2}\left(-2q+4\right) + \frac{G\left(1-f\right)}{2}\left(-2q+4\right)\right)E_y + \\ \left(-Gfq - G\left(1-f\right)q\right)E_z = \lambda(E_x+E_y+E_z) + 2GE_y,\end{aligned} \tag{A.12}$$

$$\begin{aligned}\sigma_{zz}: \left(-Gfq - G\left(1-f\right)q\right)E_x + \left(-Gfq - G\left(1-f\right)q\right)E_y + \\ \left(\frac{Gf}{2}\left(-2q+4\right) + \frac{G\left(1-f\right)}{2}\left(-2q+4\right)\right)E_z = \lambda(E_x+E_y+E_z) + 2GE_z.\end{aligned} \tag{A.13}$$

This implies,

$$\frac{Gf}{2}(-2q+4)+\frac{G(1-f)}{2}(-2q+4)=\lambda+2G, \tag{A.14}$$

$$(-Gfq-G(1-f)q)=\lambda. \tag{A.15}$$

Rearranging this gives,

$$-Gq+2G=\lambda+2G, \tag{A.16}$$

$$-Gq=\lambda. \tag{A.17}$$

Therefore λ can be written as $\frac{2G\nu}{1-2\nu}$, this implies that $q=-\frac{2\nu}{1-2\nu}$ and so $0>q>-\frac{1}{3}$ in the linear limit.

A.1.0.4 Applications of Blatz-Ko Strain Energy Function

Ambrosi and Mollica [2002] implemented the Blatz-Ko SEF to model a growing tumour tissue. This allowed for the possibility of modelling how a growing tumour interacts with the surrounding tissue.

MacLaurin et al. [2012] used the Blatz-Ko SEF to model a tumour in order to investigate the buckling of capillaries within the tumour. The capillaries were treated as 'tunnels in gel' rather than as tube so the capillary wall was neglected. MacLaurin did model the wall of the capillary as well, but found that the effects were not significant in his case [MacLaurin, 2011]. Essentially this means the Blatz-Ko SEF modelled the behaviour of the capillary wall and surrounding tissue. The authors found that the capillaries buckled due to anisotropic growth.

A.1.1 Results of Parameter Optimisation for Blatz-Ko Strain Energy Function

It was not possible to find parameters for the Blatz and Ko [1962] SEF that adequately modelled the behaviour of the lymphatic vessel wall. It was possible to find parameters that resulted in a slow increase in diameter for low pressures followed by a sharp increase at high pressures, but no parameters were found that resulted in a sharp increase in diameter followed by a plateau. The best fit achieved can be seen in figure A.1. For these parameters, the material model is effectively linear. The parameters that result in this behaviour are $G=5460$ Pa, $f=0.492$, $q=-1.32$ and $D_{int}=101$ μm. The error given by equation (2.63) is 5.365.

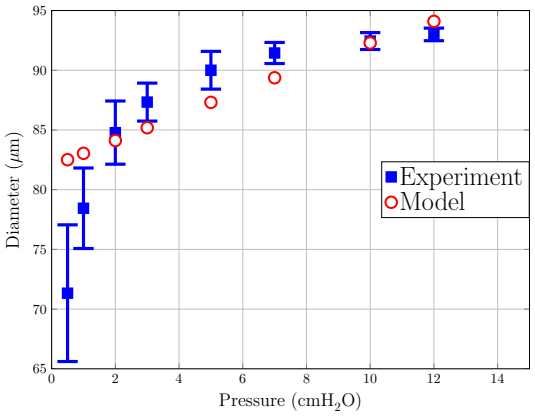

Figure A.1: Comparison of model to mean difference experiments using Blatz and Ko [1962] SEF.

A.1.1.1 Changing Parameters

In order to identify how each parameter altered the pressure-diameter results in the model, once appropriate parameters for the mean vessel had been found, the values were each adjusted individually by an order of magnitude to see how the behaviour would change. The results can be seen in figure A.2. c changes the initial flexibility of the vessel at low pressures. It appears to do this by 'moving' the pressure axis. As c increases the x-axis is shifted to the left. K dictates at what pressure the plateau will begin. Changing K by an order of magnitude does not seem to have much effect. This may be because K is so small that increasing the magnitude by one still results in a very small value for K. Changing K by an order of magnitude has very little effect, therefore it must be changed by at least an order of magnitude for it to influence the Kriging procedure. k changes the elasticity of the vessel just before the plateau. Increasing k by an order of magnitude caused the model to fail. This could be because the vessel become too rigid at low pressures. The parameter m alters the gradient of the plateau.

A.2 Valve Geometry Development

An initial run of the solid model found that the idealised geometry was preventing the valve from opening. The design of the buttress attaching the valve to the wall was keeping the edge of the valve open, see figure A.3. The buttress geometry was changed and the valve would be able to close, the new geometry is compared to the old geometry in figure A.4. The new geometry corresponds to the valve buttress described in Kampmeier [1969], where the valve leaflets intersect before connecting to the wall. The inner edge of the valve leaflet was also filleted so that a contact condition could be implemented.

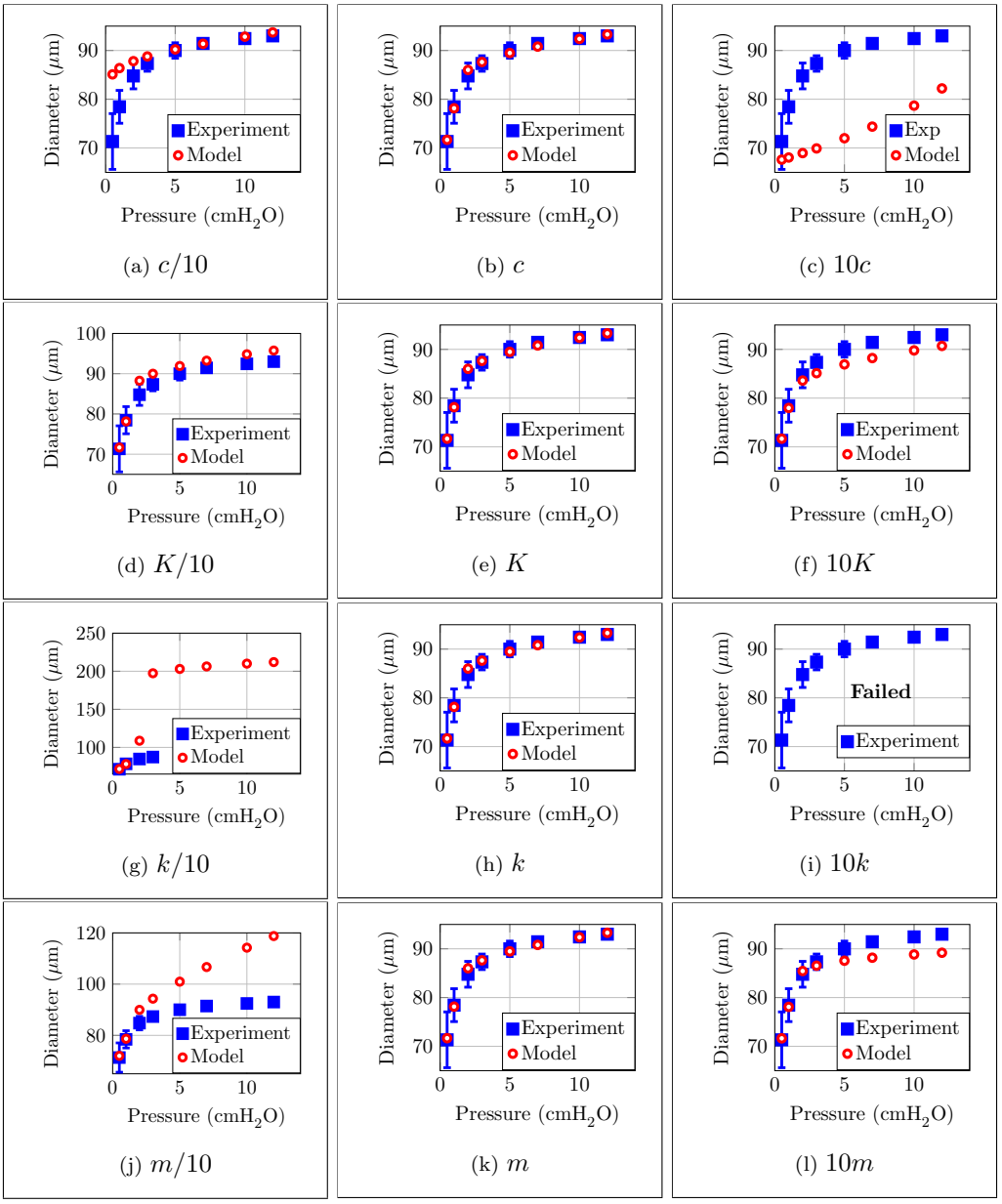

Figure A.2: Changing the parameters c, K, k and m by one order of magnitude emphasises the behaviour that each parameter controls and to what extent.

The new geometry was modelled as 180 degree section with a contact condition between the valve leaflets. The geometry is shown in figure A.5. The contact condition is applied on boundaries $\partial\Gamma_7$ and $\partial\Gamma_9$, which are shown in blue.

The contact was modelled using a penalty factor,

$$10^8 \text{ Pa}/Dst_{min} \tag{A.18}$$

where Dst_{min} is the minimum distance between the two boundaries. This condition essentially inserts a spring stiffness between the two boundaries. This prevents them from intersecting.

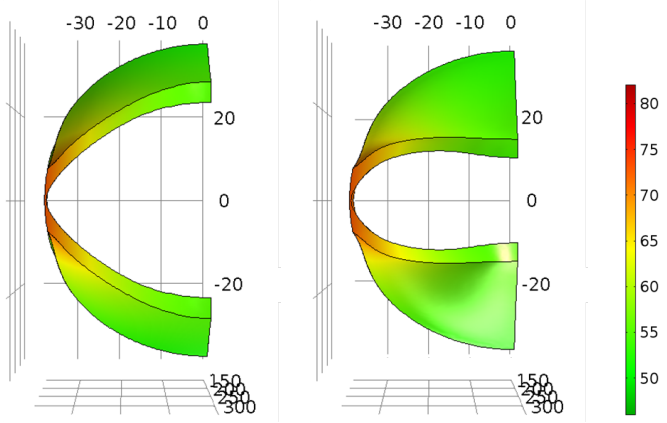

(a) Outlet pressure 0.5 cmH_2O

(b) Outlet pressure 0.8 cmH_2O

Figure A.3: End on view of solid only model, inlet pressure 0.5 cmH_2O. Colour bar shows displacement for solid in μm.

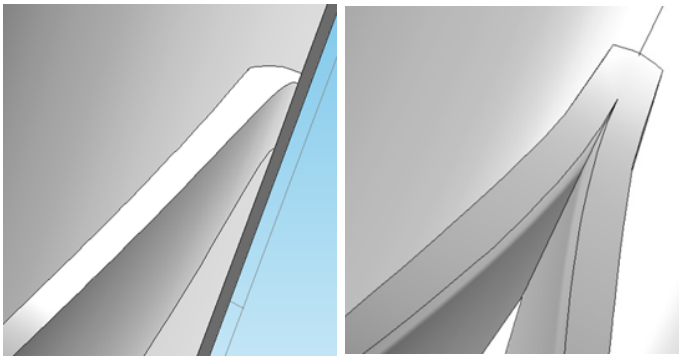

(a) Original geometry

(b) New geometry

Figure A.4: Comparison of different geometries used for valve buttress.

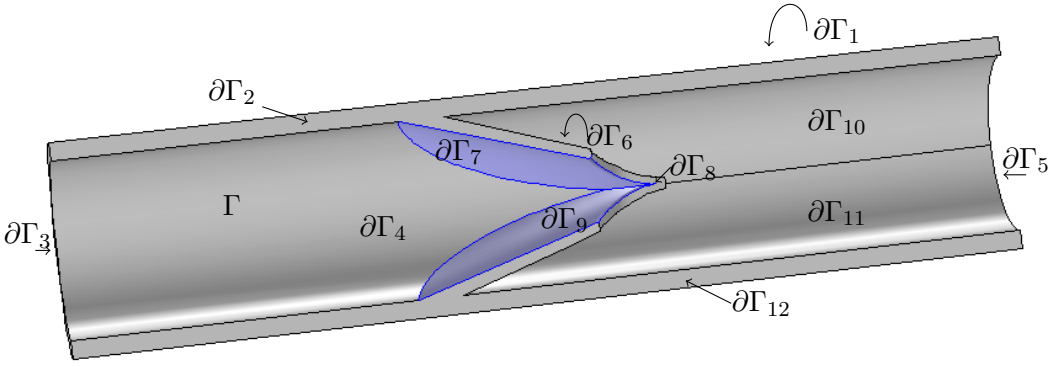

Figure A.5: Geometry of 180 degree vessel and valve section with boundaries labelled. The blue boundaries show where the contact condition was applied.

As a result of this change, the valve is able to close, see figure A.6. However, the pressure required for closure must be higher than reported in Davis et al. [2011]. It can be seen in figure A.6c that the valve is almost fully closed at outlet pressure 1.7 cmH_2O. The computational model is unable to converge for higher pressures. This is probably due to the contact condition between the two leaflets.

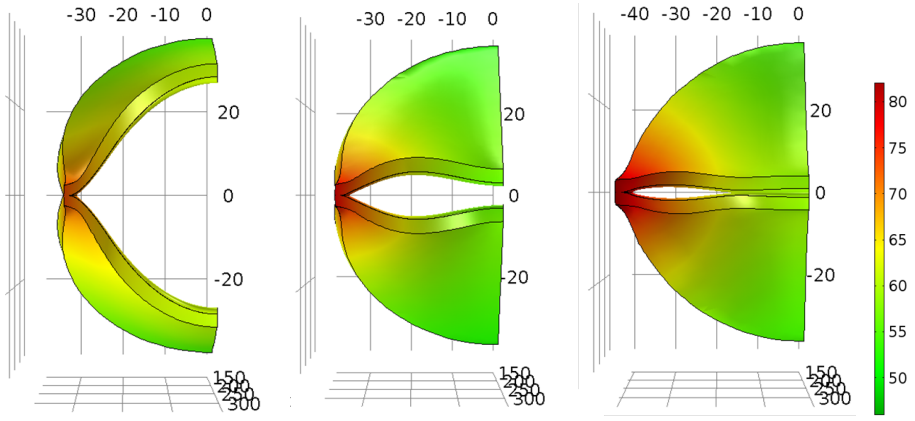

(a) Outlet Pressure 0.5 cmH_2O

(b) Outlet Pressure 0.8 cmH_2O

(c) Outlet Pressure 1.7 cmH_2O

Figure A.6: Solid only model with new buttress geometry showing position of valve. Colour bar shows displacement in μm. Although not shown here, the lymphatic wall was also modelled.

The valve was also extended to a length of 115 μm, after preliminary tests found that 93 μm (the diameter of the vessel at 12 cmH_2O) was not long enough for the valve to close at higher pressures.

A.3 Extension to Lymph Node Literature Review

A.3.1 Pathways for Fluid

Cords are blood vessels, either a single HEV or an arteriole and venule together [Willard-Mack, 2006], surrounded by a spiralling reticular cell networks (RCN), which are surrounded by a cortical sinus [Gretz et al., 1997]. Lymphocytes are contained within the chords and the diameter can change, depending on how many lymphocytes are within the cord [Anderson and Anderson, 1975; Gretz et al., 1997]. The RCNs surrounding the blood vessels are also referred to as reticular sheaths. The cords are surrounded by a network of capillaries [Anderson and Anderson, 1975; Kowala and Schoefl, 1986; Willard-Mack, 2006]. The paracortical cords, 100-200 μm diameter and 800-1500 μm in length, are part of the main structure of the rat lymph node cortex [Gretz et al., 1997]. Generally they run from the base of follicles of the subcapsular sinus to the medullary cords [Gretz et al., 1997]. In mouse nodes small venules ($<$ 20

μm) had a thin perivascular cord, large venules had a much more substantial cord [Kowala and Schoefl, 1986].

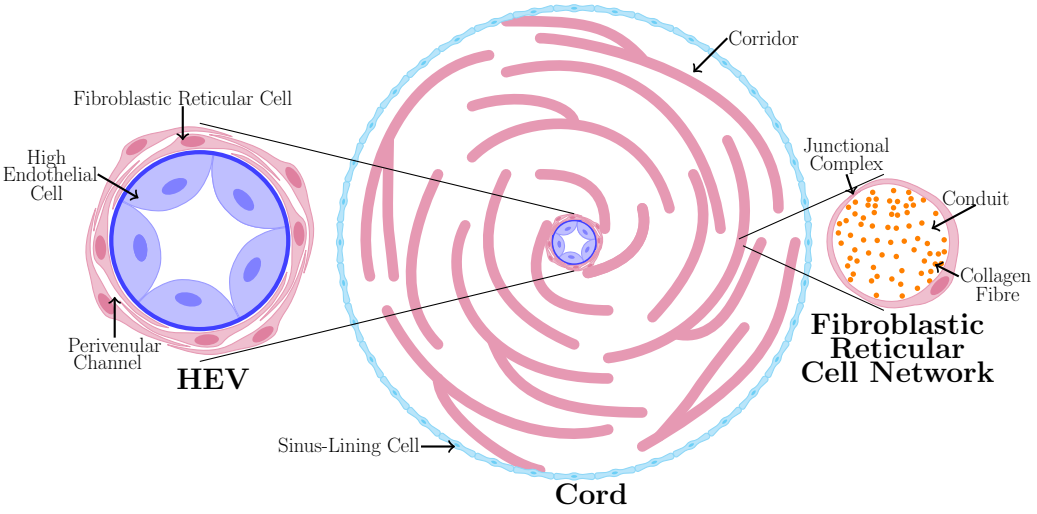

Figure A.7: Sketch of a cord centred around a HEV, not to scale. The blood vessel in the centre of a cord is not always a HEV. Fluid can flow in the corridor, channel and conduit. Based on figure from Gretz et al. [1997].

The perivenular channel is part of the HEV. It is a potential space that lies between the endothelium and the reticular cells that surround the HEV [Gretz et al., 1997]. The majority of lymphocytes leave the blood through the walls of HEVs and move along this space to corridors [Gretz et al., 1997; Girard et al., 2012].

The corridors are spaces between the FRCNs. They are distinct from the sinus [Gretz et al., 1997]. They are approximately 10 to 25 μm in diameter, which is wide enough for 2 lymphocytes to be contained next to each other [Gretz et al., 1997]. The lymphocytes are thought to move by actively pushing themselves along the walls, FRCNs, of the corridors rather than swimming through the fluid [Gretz et al., 1997].

The conduits are collagen fibre bundles encased by reticular cells [Gretz et al., 1997; Roozendaal et al., 2009]. Fluid and molecules are transported through the conduits. From the conduits moves towards and into the lumen of the HEV that the RCN surround [Gretz et al., 1997]. Cytokines, chemokines and small protein antigens are transported to the T and B cell areas of the node through the conduits [Gonzalez et al., 2010]. The conduits have a diameter of 1 to 2 μm. They are criss-crossed with collagen fibres, which only allows a spacing within of 4 to 8 nm [Gonzalez et al., 2010; Roozendaal et al., 2009].

Reticular cells express molecules that affect how the immune cells behave and the structure of the network that they form directs the movement of lymphocytes [Crivellato and Mallardi, 1997]. Crivellato and Mallardi [1997] saw small ducts in the cytoplasm of reticular cells that had openings on the surface of the cells, so they were

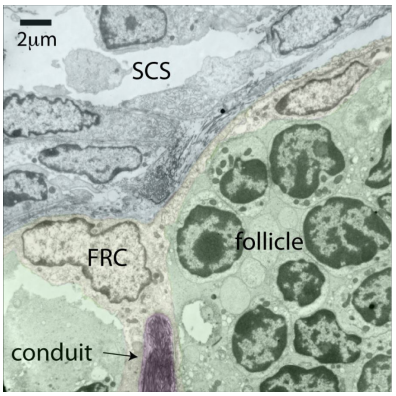

(a) Image from Gonzalez et al. [2010]. Conduit near follicle. SCS: Subcapsular sinus, FRC: Reticular cell. ©2010, The American Association of Immunologists, Inc.

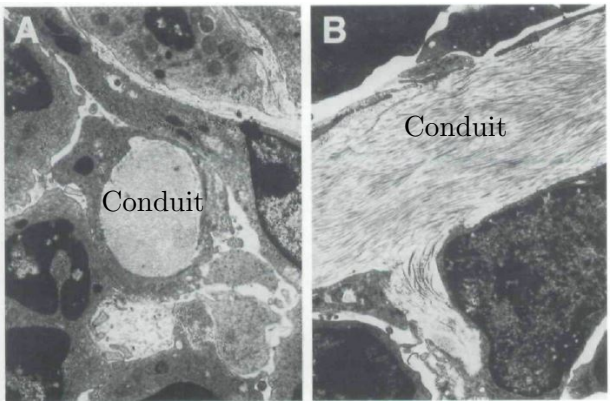

(b) Image from Gretz et al. [1997]. Conduits in the cortex of a rat lymph node transversely and longitudinally. ©2006, John Wiley and Sons. Permission granted by John Wiley and Sons.

Figure A.8: Conduits in lymph nodes.

connected to the extracellular space. This would allow fluid in the extracellular space to access the small ducts in the reticular cells.

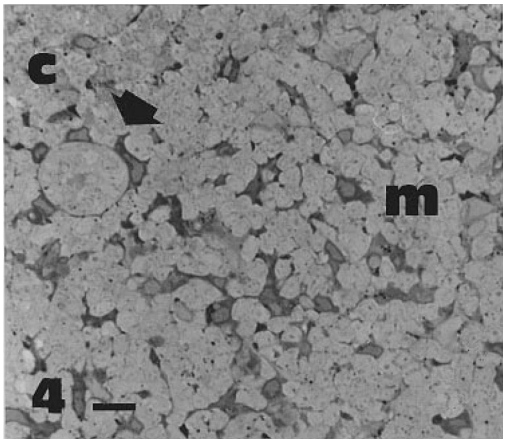

(a) Dark areas show network of reticular cells. The HEV is surrounded by reticular cells. Arrow: HEV, C: cortex, M: medulla. Scale bar = 15 μm.

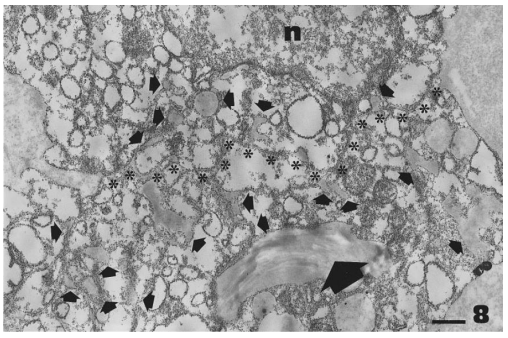

(b) The small arrows indicate the small ducts that run through the cytoplasm of the reticular cells. Small arrows: small ducts, Large arrow: intra-cytoplasmic reticulum, asterisks: meeting of two reticular cells. n: nucleus for reticular cell. Scale bar = 0.5 μm.

Figure A.9: From Crivellato and Mallardi [1997]. Images showing connections between reticular cells. ©1997, Anatomical Society of Great Britain and Ireland. Permission for use of this figure granted by John Wiley and Sons.

A.3.2 Flow of Particulate Matter through Lymph Nodes

Gretz et al. [2000] injected rat and mouse lymph nodes with various soluble molecules and tracked their progress through the nodes. Subcapsular and medullary sinuses were filled with fluorophore-labelled molecules. Most of the molecules did not enter

the cortical parenchyma. The molecules were separated into sections of the T cell-dependent areas [Gretz et al., 2000]. Molecules with molecular radius as small as 5.5 nm did not pass into the cortex [Gretz et al., 2000]. Gretz et al. [2000] used MHC class I antibodies as some lymphocytes express class I molecules. However the antibody was not present in the cortex. Gretz et al. [2000] states that this may imply there is a barrier that can limit proteins and polysaccharides from filtering through the lymph node.

Gretz et al. [2000] showed with lectins that the lymph left the subcapsular sinus and was transported through the node directly from the subcapsular sinus to the medullary sinus or via the reticular fibres and HEVs. There appeared to be no flow in the direction away from the medullary sinus along the reticular fibres.

The low molecular mass molecules were transported through the reticular network from the subcapsular sinus to the HEVs Gretz et al. [2000]. Gretz et al. [2000] used both 70 kD dextran and 68 kD bovine serum albumin (BSA). The two molecules had similar molecular weights, however the molecular radii were 5.5 nm and 3.6 nm respectively. They found that molecules with a diameter greater than 7.2 to 10.7 nm were not able to access the reticular fibre network. The dextran was constrained to the subcapsular sinus and medullary sinuses, but the BSA was seen along the reticular fibres and HEVs. Hence, Gretz et al. [2000] concluded that it depends on the radius of the molecule whether it can make it's way into the cortex along the fibres, rather than the molecular weight. Gretz et al. [2000] saw tracers fill reticular fibres. They claim to have seen small molecules (302 daltons) throughout the cortex.

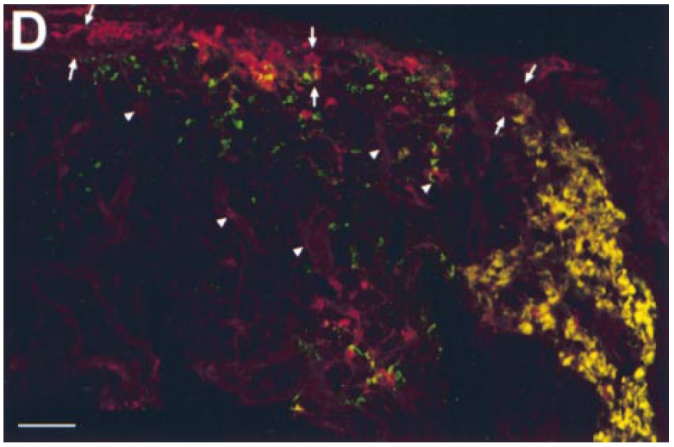

Figure A.10: Overlay of high molecular weight dextran after 4 hours (green) and low molecular weight dextran (red) after 10 minutes. Both are seen in the medullary sinus (yellow area). Arrows: subcapsular sinus, Arrowheads: HEVs. Scale bar = 50 μm. ©2000 Gretz et al. Journal of Experimental Medicine. 192:1425-1440. doi:10.1084/jem.192.10.1425.

Figure A.10 shows that the high molecular weight molecules do collect in the cortex, but in different locations than the low molecular weight molecules. This happens on

different time scales, the high molecular weight molecules taking 4 hours to collect and the low molecular weight molecules taking only 10 mins to reach their location. Both high and low molecular weight molecules are seen in the medullary sinus. Gretz et al. [2000] suggest that the high molecular weight molecules collect in the cortex through a different path, possibly taken up by cells.

A.3.3 Blood Vessels

Anderson and Anderson [1975] observed that rat lymph nodes had one or two arteries entering the node with diameter 50 to 70 μm. These repeatedly branched within the node. For dog lymph nodes some branches of the major arteries supplying the node entered at the hilus, although others entered elsewhere [Belz and Heath, 1995b]. Most nodes had an area that could be described as a hilus where one or more arteries entered the node and efferent lymphatics and veins left. Belz and Heath [1995b] occasionally saw up to 50 arteries entering a node. Some nodes had no hilus area and the arteries entered at various points on the surface of the capsule [Belz and Heath, 1995b]. Some of the arteries that did not enter at the hilus went through the trabeculae and others crossed the subcapsular sinus.

For dog lymph nodes, the majority of arteries were covered with connective tissue and entered the node into the medulla Belz and Heath [1995b]. Anderson and Anderson [1975] observed blood vessels on the external surface of the lymph node. These were not linked to the internal circulation. The vessels wiggles across the surface following indents in the capsule, that occurred above points away from which the trabeculae extended internally. Capillaries formed a network over the external surface of the node [Anderson and Anderson, 1975].

For rat lymph nodes, some arteries were seen to enter the base of the lobules and connected to capillary networks that surrounded germinal centres [Anderson and Anderson, 1975]. Occasionally, capillaries and arterioles passed through germinal centres, but lymphatic vessels were never seen in germinal centres. [Anderson and Anderson, 1975; Belz and Heath, 1995b; Kowala and Schoefl, 1986]. The arteries that passed through the centre formed junctions with AVCs reaching over the upper surface of the germinal centres. They had diameters between 3 and 5 μm and were surrounded by reticular fibres and processes [Anderson and Anderson, 1975].

Kowala and Schoefl [1986] saw most arterioles, 15-25 μm, in the hilar region and medullary cords. Any arterioles under 15 μm were called metarterioles Kowala and Schoefl [1986]. In the medulla of dog lymph nodes, there were networks of arterioles along medullary chords [Belz and Heath, 1995b].

Anderson and Anderson [1975] observed that many arterioles in rat lymph nodes looped under the subcapsular sinus and joined arteriovenous communications (AVCs),

an image of an AVC can be seen in figure A.11. They had diameters between 6 and 15 μm. Some AVCs passed through trabeculae and joined to the vasculature of next lymphatic lobule.

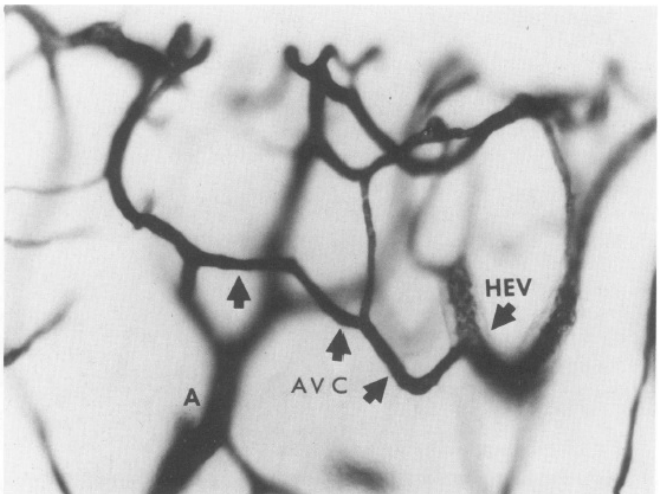

Figure A.11: AVC: Arteriovenous communications, A: artery, HEV: high endothelial venule (×220). This image was published in Anderson and Anderson [1975] Copyright 1975, American Society for invesitagtive pathology; Published by Elsevier Inc; All rights reserved.

Fenestrated and nonfenestrated capillaries were seen in both dog and rat lymph nodes [Anderson and Anderson, 1975; Belz and Heath, 1995b]. In rat nodes Anderson and Anderson [1975] observed that the fenestrated capillaries were surrounded by a thick layer of reticular fibres. From some of the nonfenestrated capillaries there extended pericyte processes [Anderson and Anderson, 1975]. Belz and Heath [1995b] saw that capillaries on the surface of medulla sinuses or that coursed through the sinus itself were nonfenestrated and that all the capillaries in the cortical parenchyma and the subcapsular sinus of the dog lymph node were nonfenestrated.

In the cortex of rat lymph nodes, the capillaries formed complex networks between 0.5 and 5 μm below the subcapsular sinus [Anderson and Anderson, 1975]. Similar networks were seen by Kowala and Schoefl [1986] in mouse popliteal nodes. They also noted that the networks over the follicles were less dense and near the lobules more dense. The capillaries were seen to drain into postcapillary venules with low endothelium, two to five of these in turn drained into larger HEVs [Anderson and Anderson, 1975; Kowala and Schoefl, 1986]. Capillaries were between 5 and 9 μm in diameter in mouse popliteal lymph nodes Kowala and Schoefl [1986].

The sinuses in the rat lymph node deep cortex had capillaries around them although the capillaries and lymphatic vessels never joined directly [Anderson and Anderson, 1975]. Anderson and Anderson [1975] also observed that capillaries near to where the cortex met the medulla connected to small venules that lead through the cortex to HEVs. Lower in the medulla, they connected to small venules that lead to

segmental veins [Anderson and Anderson, 1975]. Capillary networks surrounded medullary chords close to the medullary sinuses whereas the arterioles and venules were positioned more centrally within the cords [Belz and Heath, 1995b; Anderson and Anderson, 1975; Kowala and Schoefl, 1986]. The capillaries in dog lymph nodes were seen within 20 μm of the medullary sinuses [Belz and Heath, 1995b].

Belz and Heath [1995b] observed that the blood vessels in the medulla of dog lymph nodes drained into LEVs that ran close to the arteries. Kowala and Schoefl [1986] observed LEVs in the lobules of the mouse popliteal lymph nodes with diameters 10 to 17 μm and 40 to 50 μm. In the medulla of the mouse popliteal lymph nodes the LEVs were between 10 and 55 μm in diameter [Kowala and Schoefl, 1986]. In rat lymph nodes, postcapillary venules had diameters between 8 and 12 μm. They were separated from the intersitium by one layer of adventitial cells and reticular cell plates Anderson and Anderson [1975].

Anderson and Anderson [1975] saw HEVs in the lymphatic lobules of rat lymph nodes and leading from the subcapsular sinus to the medulla. Kowala and Schoefl [1986] observed that HEVs in the mouse politeal lymph node generally ran around the edges of lobules had diameters between 16 to 55 μm Kowala and Schoefl [1986]. The diameter of HEVs in rat lymph nodes increases beginning from about 8 μm and reaching 30 to 40 μm near where the cortex and medulla meet [Anderson and Anderson, 1975]. Within the deep cortex, venous plexuses drained into several vessels, which drained into the main trunks [Anderson and Anderson, 1975]. Three to five had high endothelium and two to three had flat endothelium [Anderson and Anderson, 1975]. In the medulla the HEVs became segmental veins with flat endothelium, which merge to the efferent vessels close to the hilus [Anderson and Anderson, 1975]. The diameters of the segmental veins were 50 to 150 μm and they were surrounded by a collagenous matrix containing reticular cell processes and fibroblasts [Anderson and Anderson, 1975].

A.4 Preliminary Imaging

The first scan of a perfused lymph node was made at the Diamond Light Source, Oxford, on beamline I13. Unfortunately, the images had a lot of edge effects and the node had separated from the wax. A slice from the scan can be seen in figure A.12. It was possible to see the perfused blood vessels and some less dense areas that could be lymph pathways.

Scans were made of the stained node using the Zeiss Xradia Versa 510 imaging system at the University of Southampton μ-vis Facility. The Versa has different lenses and can achieve a resolution of 700 nm. Various scans were made of the stained node, as seen in figure A.13. All the scans were made with settings of energy 60 kV and

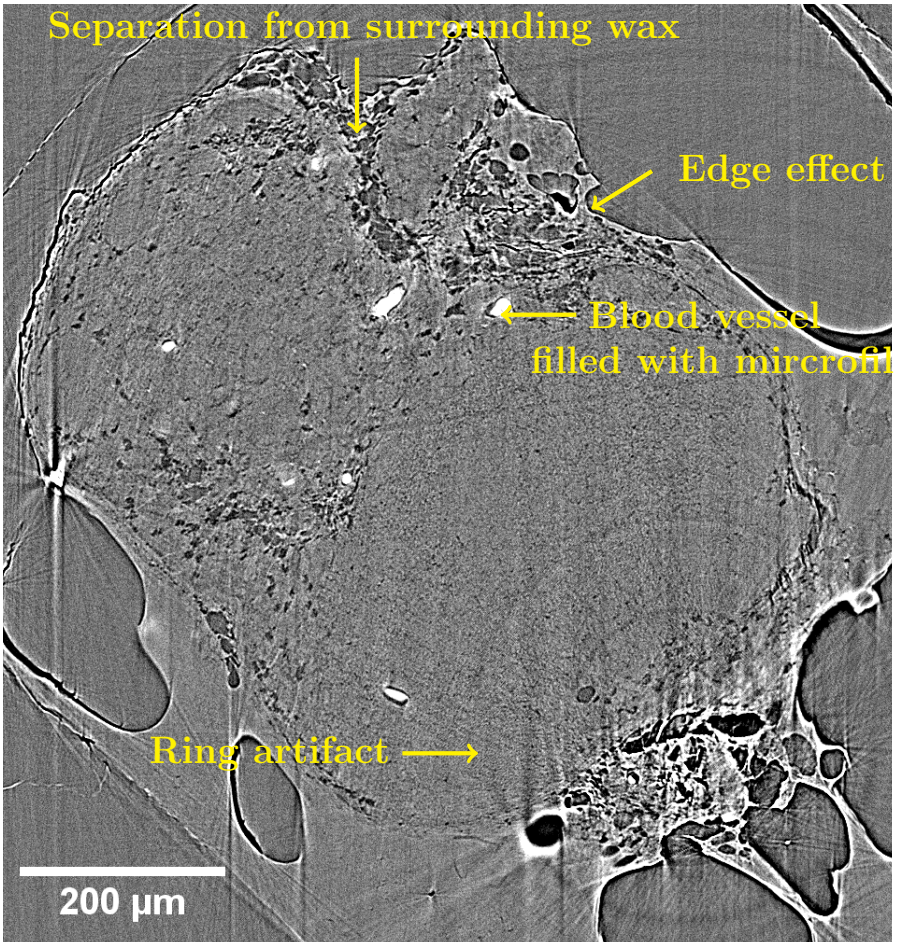

Figure A.12: Scan of lymph node with Microfil made at Diamond Light Source, Oxford. The scan was made at voltage 60 kV, current 115 μA with an exposure time of 1 second. The node has separated from the wax that it is embedded in and there are strong edge effects because of this. The thicker shorter bright white areas are blood vessels filled with Microfil. A ring artefact caused by the reconstruction, can be seen in the lower right corner. The bright white edge effects make it difficult to segment the blood vessels because they have the same grey scale value as the Microfil.

power 5 W. The first scan with the largest field of view had a exposure time of three seconds and used the 4X optic. The second and third scans used the 20X optic and an exposure time of 5 seconds. The field of view was decreased and the resolution increased for each scan by moving the detector away from the sample.

A scan was made of the perfused node using the Versa. The image was less noisy that previous scans. It was made using a 4X magnification lens, exposure time of 3 seconds, voltage of 80 kV and power 7 W. The scan took 9 hours. It had a resolution of 2.17 μm per pixel. The Microfil has caused streaks on the image. This scan, seen in figure A.14, is the least noisy and the blood vessels are more visible. It is also possible to distinguish the more dense tissue near the capsule from the less dense tissue near the hilus.

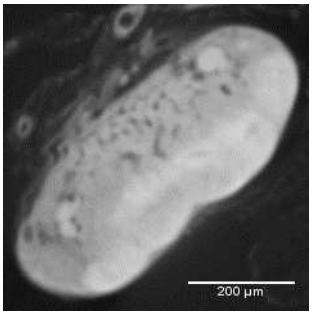

(a) 4X optic. Resolution 2.3799 μm. Exposure time 3 seconds. The lighter grey areas of the node indicate where the tissue is more dense. This is the cortex of the node. The slightly darker areas are the medulla and the small areas that are even darker are probably lymph pathways but may also be blood vessels.

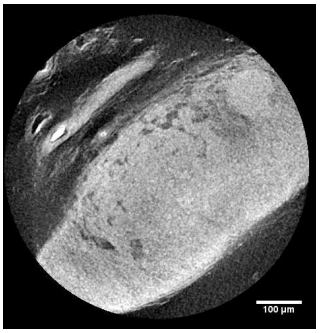

(b) 20X optic. Resolution 1.4471 μm. Exposure time 5 seconds. The bright white areas to the upper left of the image are probably red blood cells that were not flushed out during the preparation process. It is not easy to identify the cortex and the medulla in this image, but the dark areas within the node are either lymph pathways or blood vessels

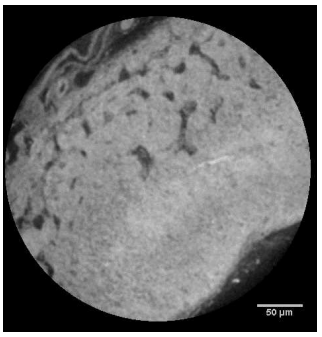

(c) 20X optic. Resolution 0.7235 μm. Exposure time 5 seconds. The white streak to the right of the centre of the image is most probably a blood vessel. The dark and light areas of this scan are easy to define, which will make segmentation easier.

Figure A.13: Node stained with PTA and scanned with Versa at different resolutions. All scans made with settings of energy 60 kV and power 5 W. The dark grey area surrounding the nodes is the wax that they are embedded in.

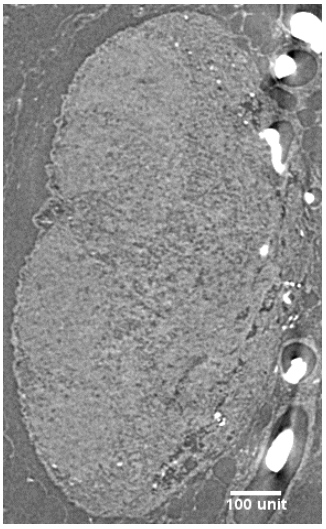

Figure A.14: Perfused node scanned with Versa with 4X magnification lens, exposure time of 3 seconds, voltage 80 kV and power 7 W. The bright white areas is the Microfil in the blood vessels. Most patches of Microfil have an area of dark grey around them, outlined by a lighter shade of grey. This shows where the Microfil has shrunk, as the lighter shade of grey is the wall of the vessel and the dark grey is the vessel lumen. The lymphatic tissue that makes up the node is a paler shade of grey to the wax surrounding it.

Higher resolution scans of the perfused, stained and unstained nodes have been made at the TOMCAT beamline at the Swiss Light Source (SLS), Switzerland. The resolution of the scans was 1 pixel to 0.65 μm. The lymph node in figure A.15a is

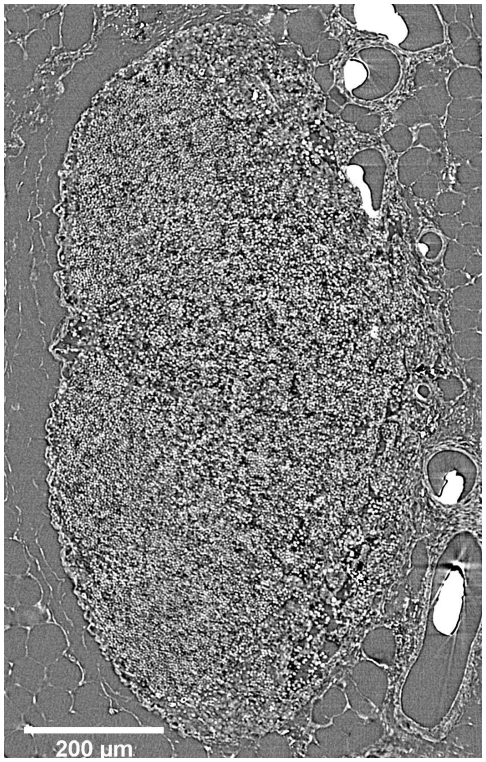

(a) Lymph node perfused with Microfil.

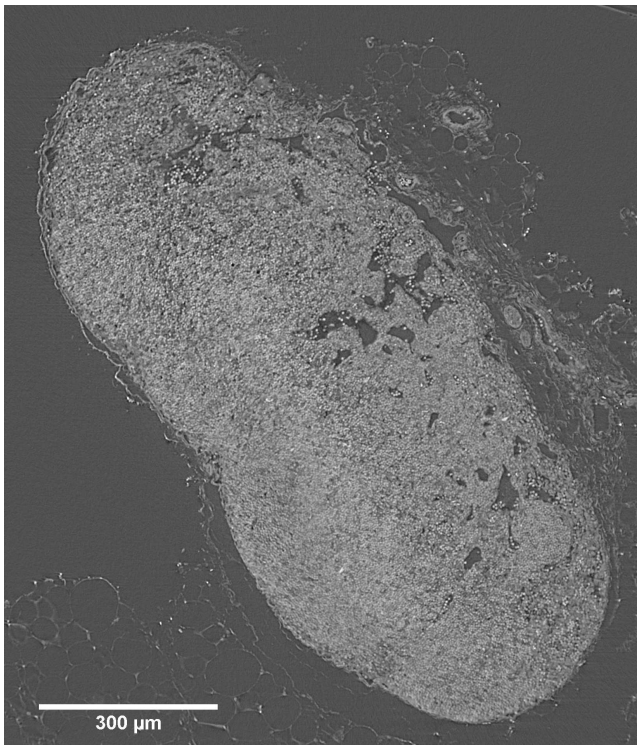

(b) Lymph node stained with PTA.

Figure A.15: Lymph nodes scanned at SLS with resolution 0.65 μm.

the same node as in figure A.14 and the node in figure A.15b is the same node as in figure A.13. The increased resolution allows us to see the internal structure much more clearly and see the individual cells. The future work will be carried out using these scans.

Bibliography

Abramson, D. I. and Dobrin, P. B., editors (1984). *Blood Vessels and Lymphatics in Organ Systems*. Academic Press, Inc.

Acheson, D. J. (1990). *Elementary Fluid Dynamics*. Oxford Applied Mathematics and Computing Science Series. Oxford : Clarendon Press ; New York : Oxford University Press.

Adair, T. H. and Guyton, A. C. (1983). Modification of lymph by lymph nodes. ii. effect of increased lymph node venous blood pressure. *American Journal of Physiology: Heart and Circulation Physiology*, 245:H616–H622.

Adair, T. H. and Guyton, A. C. (1985). Modification of lymph by lymph nodes iii. effect of increased lymph hydrostatic pressure. *American Journal of Physiology: Heart and Circulation Physiology*, 249:H777–H782.

Adair, T. H., Moffatt, D. S., Paulsen, A. W., and Guyton, A. C. (1982). Quatitiation of changes in lymph protein concentration during lymph node transit. *American Journal of Physiology: Heart and Circulation Physiology*, 243:H351–H359.

Albertine, K. H., Fox, L. M., and Omorchoe, C. C. C. (1982). The morphology of canine lymphatic valves. *Anatomical Record*, 202(4):453–461.

Ambrosi, D. and Mollica, F. (2002). On the mechanics of a growing tumor. *International Journal of Engineering Science*, 40(12):1297–1316.

Anderson, A. O. and Anderson, N. D. (1975). Studies on the structure and permeability of the microvasculature in normal rat lymph nodes. *Am J Pathol*, 80(3):387–418.

Andrews, P. and Timmis, J. (2006). *A Computational Model of Degeneracy in a Lymph Node*, volume 4163 of *Lecture Notes in Computer Science*, chapter 13, pages 164–177. Springer Berlin Heidelberg.

Arkill, K. P., Moger, J., and Winlove, C. P. (2010). The structure and mechanical properties of collecting lymphatic vessels: an investigation using multimodal nonlinear microscopy. *Journal of Anatomy*, 216(5):547–55.

Aukland, K. and Reed, R. K. (1993). Interstitial-lymphatic mechanisms in the control of extracellular fluid volume. *Physiological Reviews*, 73(1):1–78.

Auricchio, F., Conti, M., Ferrara, A., Morganti, S., and Reali, A. (2014). Patient-specific simulation of a stentless aortic valve implant: the impact of fibres on leaflet performance. *Computer Methods in Biomechanics and Biomedical Engineering*, 17(3):277–285.

Azuma, T. and Oka, S. (1971). Mechanical equilibrium of blood vessel walls. *American Journal of Physiology*, 221:1310–1318.

Badel, P., Rohan, C. P. Y., and Avril, S. (2013). Finite element simulation of buckling-induced vein tortuosity and influence of the wall constitutive properties. *Journal of the Mechanical Behavior of Biomedical Materials*, 26:119–126.

Bazigou, E., Xie, S., Chen, C., Weston, A., Miura, N., Sorokin, L., Adams, R., Muro, A. F., Sheppard, D., and Makinen, T. (2009). Integrin-alpha 9 is required for fibronectin matrix assembly during lymphatic valve morphogenesis. *Developmental Cell*, 17(2):175–186.

Bellhouse, B. J. and Talbott, L. (1969). The fluid mechanics of the aortic valve. *Journal of Fluid Mechanics*, 35:721–735.

Beltman, J. B., Maree, A. F., Lynch, J. N., Miller, M. J., and de Boer, R. J. (2007). Lymph node topology dictates t cell migration behavior. *J Exp Med*, 204(4):771–80.

Belz, G. T. and Heath, T. J. (1995a). Lymph pathways of the medial retropharyngeal lymph node in dogs. *J Anat*, 186 (Pt 3):517–26.

Belz, G. T. and Heath, T. J. (1995b). Pathways of blood flow to and through superficial lymph nodes in the dog. *J Anat*, 187 (Pt 2):413–21.

Bergel, D. H. (1961). The static elastic properties of the arterial wall. *Journal of Physiology*, 156(3):445–57.

Bertram, C., Macaskill, C., and Moore, Jr., J. E. (2011). Simulation of a chain of collapsible contracting lymphangions with progressive valve closure. *Journal of Biomechanical Engineering*, 133:011008–1–011008–10.

Bertram, C. D., Macaskill, C., Davis, M. J., and Moore, Jr., J. E. (2013a). Development of a model of a multi-lymphangion lymphatic vessel incorporating realistic and measured parameter values. *Biomechanics and Modeling in Mechanobiology*, pages 1–16.

Bertram, C. D., Macaskill, C., and Moore, Jr., J. E. (2013b). Incorporating measured valve properties into a numerical model of a lymphatic vessel. *Comput Methods Biomech Biomed Engin*.

Blatz, P. J. and Ko, W. L. (1962). Application of finite elastic theory to the deformation of rubbery materials. *Transactions of the Society of Rheology*, 6(1):223–251.

Bogle, G. and Dunbar, P. R. (2008). Simulating t-cell motility in the lymph node paracortex with a packed lattice geometry. *Immunol Cell Biol*, 86(8):676–87.

Bonanno, G., Coppo, S., Modregger, P., Pellegrin, M., Stuber, A., Stampanoni, M., Mazzolai, L., Stuber, M., and van Heeswijk, R. B. (2015). Ultra-high-resolution 3d imaging of atherosclerosis in mice with synchrotron differential phase contrast: a proof of concept study. *Scientific Reports*, 5:11980.

Burton, A. C. (1972). *Physiology and Biophysics of the Circulation*. Year Book Medical Publishers, Inc, 2nd edition.

Burton-Opitz, R. and Nemser, R. (1917). The viscosity of lymph. *American Journal of Physiology – Legacy Content*, 45(1):25–29.

Burvall, A., Lundström, U., Takman, P. A. C., Larsson, D. H., and Hertz, H. M. (2011). Phase retrieval in x-ray phase-contrast imaging suitable for tomography. *Optical Society of America*, 19:10359–10376.

Butler, M. G., Isogai, S., and Weinstein, B. M. (2009). Lymphatic development. *Birth Defects Res C Embryo Today*, 87(3):222–31.

Buxton, G. A. and Clarke, N. (2006). Computational phlebology: The simulation of a vein valve. *Journal of Biological Physics*, 32:506–521.

Caro, C. G., Pedley, T. J., Schroter, R. C., and Seed, W. A. (2012). *The Mechanics of the Circulation*. Cambridge University Press, New York, United States of America, 2nd edition.

Causin, P. and Malgaroli, F. (2015). A mathematical and computational study of microvascular districts: The mutual talk between vessels, capillary networks and tissue continua. In *Proceedings of the 4th International Conference on Computational and Mathematical Biomedical Engineering*.

Chan, C., Billard, M., Ramirez, S. A., Schmidl, H., Monson, E., and Kepler, T. B. (2013). A model for migratory b cell oscillations from receptor down-regulation induced by external chemokine fields. *Bull Math Biol*, 75(1):185–205.

Chugh, B. P., Lercha, J. P., Yua, L. X., Pienkowskic, M., Harrisone, R. V., Henkelmana, R. M., and Sleda, J. G. (2009). Measurement of cerebral blood volume in mouse brain regions using micro-computed tomography. *NeuroImage*, 47:1312–1318.

COMSOL Multiphysics (2013). *Structural Mechanics Module: Users Guide*.

Cornejo, S., Guzman, A., Valencia, A., Rodriguez, J., and Finol, E. (2014). Flow-induced wall mechanics of patient-specific aneurysmal cerebral arteries: Nonlinear isotropic versus anisotropic wall stress. *Proceedings of the Institution of Mechanical Engineers Part H-Journal of Engineering in Medicine*, 228(1):37–48.

Crivellato, E. and Mallardi, F. (1997). Stromal cell organisation in the mouse lymph node. a light and electron microscopic investigation using the zinc iodide-osmium technique. *J Anat*, 190 (Pt 1):85–92.

Davis, M. J., Rahbar, E., Gashev, A. A., Zawieja, D. C., and Moore, Jr., J. E. (2011). Determinants of valve gating in collecting lymphatic vessels from rat mesentery. *American Journal of Physiology: Heart and Circulation Physiology*, 301:H48–H60.

Deng, D., Jiao, P., Ye, X., and Xia, L. (2012). An image-based model of the whole human heart with detailed anatomical structure and fiber orientation. *Computational and Mathematical Methods in Medicine*, 2012:891070.

Dixon, J. B., Greiner, S. T., Gashev, A. A., Cote, G. L., Moore, Jr., J. E., and Zawieja, D. C. (2006). Lymph flow, shear stress, and lymphocyte velocity in rat mesenteric prenodal lymphatics. *Microcirculation*, 13.

Doll, S. and Schweizerhof, K. (2000). On the development of volumetric strain energy functions. *Journal of Applied Mechanics-Transactions of the Asme*, 67(1):17–21.

El-Bouri, W. K. and Payne, S. J. (2015). Multi-scale homogenization of the mass transport equation in periodic capillary networks. In *Proceedings of the 4th International Conference on Computational and Mathematical Biomedical Engineering*.

Figge, M. T., Garin, A., Gunzer, M., Kosco-Vilbois, M., Toellner, K. M., and Meyer-Hermann, M. (2008). Deriving a germinal center lymphocyte migration model from two-photon data. *J Exp Med*, 205(13):3019–29.

Földi, M., Földi, E., and Kubik, S., editors (2003). *Textbook of Lymphology for Physicians and Lymphodema Therapists*. Urban & Fischer.

Forrester, A., Sobester, A., and Keane, A. (2008). *Engineering design via surrogate modelling: a practical guide*. John Wiley & Sons.

Fratini, M., Bukreeva, I., Campi, G., Brun, F., Tromba, G., Modregger, P., Bucci, D., Battaglia, G., Span, R., Mastrogiacomo, M., Requardt, H., Giove, F., Bravin, A., and Cedola, A. (2015). Simultaneous submicrometric 3d imaging of the micro-vascular network and the neuronal system in a mouse spinal cord. *Scientific Reports*, 5:8514.

Fung, Y. C. and Tong, P. (2005). *Classical and Computational Solid Mechanics*. Advanced Series in Engineering Science - Volume I. World Scientific Publishing Co. Pte. Ltd.

Galarreta-Valverde, M. A., Macedo, M. M. G., and an dMarcel P. Jackowski, C. M. (2013). Three-dimensional synthetic blood vessel generation using stochastic l-systems. *Proc. SPIE 8669, Medical Imaging 2013: Image Processing*, 8669:86691I–1–86691I–6.

Gashev, A. A. (2002). Physiologic aspects of lymphatic contractile function, current perspectives. *Annals of the New York Academy of Sciences*, 979:178–187.

Gashev, A. A., Davis, M. J., Delp, M. D., and Zawieja, D. C. (2004). Regional variations of contractile activity in isolated rat lymphatics. *Microcirculation*, 11:477–492.

Gashev, A. A., Davis, M. J., and Zawieja, D. C. (2002). Inhibition of the active lymph pump by flow in rat mesenteric lymphatics and thoracic duct. *Journal of Physiology-London*, 540(3):1023–1037.

Girard, J. P., Moussion, C., and Forster, R. (2012). Hevs, lymphatics and homeostatic immune cell trafficking in lymph nodes. *Nat Rev Immunol*, 12(11):762–73.

Gnepp, D. R. and Green, F. H. Y. (1980). Scanning electron microscopic study of canine lymphatic vessels and their valves. *Lymphology*, 13:91–99.

Goldberg, D. E. (1989). *Genetic Algorithms in Search, Optimization, and Machine Learning*. Addison Wesley Longman, Inc.

Gonzalez, S. F., Lukacs-Kornek, V., Kuligowski, M. P., Pitcher, L. A., Degn, S. E., Turley, S. J., and Carroll, M. C. (2010). Complement-dependent transport of antigen into b cell follicles. *J Immunol*, 185(5):2659–64.

Gretz, J. E., Anderson, A. O., and Shaw, S. (1997). Cords, channels, corridors and conduits: critical architectural elements facihtating cell interactions in the lymph node cortex. *Immunological Reviews*, 156:11–24.

Gretz, J. E., Norbury, C. C., Anderson, A. O., Proudfoot, A. E., and Shaw, S. (2000). Lymph-borne chemokines and other low molecular weight molecules reach high endothelial venules via specialized conduits while a functional barrier limits access to the lymphocyte microenvironments in lymph node cortex. *J Exp Med*, 192(10):1425–40.

Griffith, B. E. (2006). An adaadapt, formally second order accurate version of the immersed boundary method. *Journal of Computational Physics*, 223:10–49.

Guyton, A. C. and Adair, T. H. (1985). *Lymph formation and its modification in the lymphatic system*, pages 13–42. Elsevier Science Publishers B. V.

Hart, J. D., Peters, G., Schreurs, P., and Baaijens, F. (2000). A two-dimensional fluid-structure interaction model of the aortic valve. *Journal of Biomechanics*, 33:1079–1088.

Hart, J. D., Peters, G., Schreurs, P., and Baaijens, F. (2003). A three-dimensional computational analysis of fluidstructure interaction in the aortic valve. *Journal of Biomechanics*, 36:103–112.

He, Y., Liub, H., Himenoa, R., Sunagaa, J., Kakushoa, N., and Yokotaa, H. (2008). Finite element analysis of blood flow and heat transfer in an image-based human finger. *Computers in Biology and Medicine*, 38:555–562.

Holzapfel, G., Gasser, T., and Ogden, R. (2000). A new constitutive framework for arterial wall mechanics and a comparative study of material models. *Journal of elasticity and the physical science of solids*, 61:1–48.

Howell, P., Kozyreff, G., and Ockendon, J. (2009). *Applied Solid Mechanics*. Cambridge Texts in Applied Mathematics. Cambridge University Press.

Hsieh, J. (2009). *Computed Tomography, Second Edition: Principles, Design, Artifacts, and Recent Advances*. SPIE and John Wiley & Sons, Inc., second edition.

Huisken, J., Swoger, J., Bene, F. D., Wittbrodt, J., and Stelzer, E. H. K. (2004). Optical sectioning deep inside live embryos by selective plane illumination microscopy. *Science*, 305:1007–1009.

Ikomi, F., Kawai, Y., and Ohhashi, T. (2012). Recent advance in lymph dynamic analysis in lymphatics and lymph nodes. *Annals of Vascular Diseases*, 5:258–268.

Jafarnejad, M., Woodruff, M., Zawieja, D., Carroll, M., and Moore, Jr., J. E. (2015). Modeling lymph flow and fluid exchange with blood vessels in lymph nodes. *Lymphatic Research and Biology*, 13:234–245.

Kampmeier, O. F. (1969). *Evolution and Comparative morphology of the Lymphatic System*. Charles C. Thomas.

Karch, R., Neumann, F., Neumann, M., and Schreiner, W. (1999). A three-dimensional model for arterial tree representation generated by constrained constructive optimization. *Computers in Biology and Medicine*, 29:19–38.

Kowala, M. C. and Schoefl, G. I. (1986). The popliteal lymph node of the mouse: internal architecture, vascular distribution and lymphatic supply. *J Anat*, 148:25–46.

Krige, D. G. (1951). A statistical approach to some basic mine valuation problems on the witwatersrand. *Journal of the Chemical, Metallurgical and Mining Society of South Africa*, 52:119–139.

Kunzelman, K. S., Einstein, D. R., and Cochran, R. P. (2007). Fluidstructure interaction models of the mitral valve: function in normal and pathological states. *Philosophical Transactions of the Royal Society B*, 362:1393–1406.

Lanciault, G. and Jacobson, E. D. (1976). The gastrointestinal circulation. *Gastroenterology*, 71(5):851–73.

Landis, E. N. and Keane, D. T. (2010). X-ray microtomography. *Materials Characterization*, 61:1305–1316.

Lauweryns, J. M. and Boussauw, L. (1973). The ultrastructure of lymphatic valves in the adult rabbit lung. *Cell and Tissue Research*, 143(2):149–168.

Lee, C., Lamart, S., and Moroz, B. E. (2013). Computational lymphatic node models in pediatric and adult hybrid phantoms for radiation dosimetry. *Phys Med Biol*, 58(5):N59–82.

Levick, J. R. (2009). *An introduction to cardiovascular physiology*. London : Hodder Arnold, 5th ed. edition.

Li, S. (2013). *Multiscale Simulations and Mechanics of Biological Materials*. John Wiley & Sons.

Macdonald, A., Arkill, K., Tabor, G. R., McHale, N. G., and Winlove, C. P. (2008). Modeling flow in collecting lymphatic vessels: one-dimensional flow through a series of contractile elements. *American Journal of Physiology: Heart and Circulation Physiology*, 295:H305–H313.

MacLaurin, J. (2011). *Tumour tissue mechanics*. PhD thesis, Oxford University.

MacLaurin, J., Chapman, J., Wyn Jones, G., and Roose, T. (2012). The buckling of capillaries in solid tumours. *Proceedings of the Royal Society A - Mathematical Physical and Engineering Sciences*.

Margaris, K. N. and Black, R. A. (2012). Modelling the lymphatic system: challenges and opportunities. *Journal of The Royal Society Interface*.

Mayer, J., Swoger, J., Ozga, A. J., Stein, J. V., and Sharpe, J. (2012). Quantitative measurements in 3-dimensional datasets of mouse lymph nodes resolve organ-wide functional dependencies. *Comput Math Methods Med*, 2012:128431.

Mazzoni, M. C., Skalak, T. C., and Schmid-Schönbein, G. W. (1987). Structure of lymphatic valves in the spinotrapezius muscle of the rat. *Blood Vessels*, 24:304–312.

McQueen, D. M., Peskin, C. S., and Yellin, E. L. (1982). Fluid dynamics of the mitral valve: physiologic aspects of a mathematical model. *American Journal of Physiology*, 242:H1095–H1110.

Meisner, J. K., Stewart, R. H., Laine, G. A., and Quick, M. C. (2007). Lymphatic vessels transition to state of summation above a critical contraction frequency. *American Journal of Physiology: Regulatory, Integrative and Comparative Physiology*, 293:R200–R208.

Mihara, M., Hara, H., Hayashi, Y., Narushima, M., Yamamoto, T., Todokoro, T., Iida, T., Sawamoto, N., Araki, J., Kikuchi, K., Murai, N., Okitsu, T., Kisu, I., and Koshima, I. (2012). Pathological steps of cancer-related lymphedema: histological changes in the collecting lymphatic vessels after lymphadenectomy. *PLoS One*, 7(7):e41126.

Miller, A. J., Ellis, A., and Katz, L. N. (1964). Cardiac lymph: Flow rates and composition in dogs. *American Journal of Physiology*, 206:63–6.

Moriondo, A., Boschetti, F., Bianchin, F., Lattanzio, S., Marcozzi, C., and Negrini, D. (2010). Tissue contribution to the mechanical features of diaphragmatic initial lymphatics. *The Journal of Physiology*, 588(20):3957–3969.

Morris, M. D. and Mitchell, T. J. (1995). Exploratory designs for computational experiments. *Journal of Statistical Planning and Inference*, 43(3):381–402.

Murray, C. D. (1926a). The physiological principle of minimum work applied to the angle of branching of arteries. *Journal of General Physiology*, 9:835–841.

Murray, C. D. (1926b). The physiological principle of minimum work. i. the vascular system and the cost of blood volume. *Proceedings of the National Academy of Sciences*, 12:204–214.

Nagai, T., Ikomi, F., Suzuki, S., , and Ohhashi, T. (2008). In situ lymph dynamic characterization through lymph nodes in rabbit hind leg: Special reference to nodal inflammation. *The Journal of Physiological Sciences*, 58:123–132.

Narracott, A., Keijsers, J., Leguy, C., Huberts, W., and van de Vosse, F. (2015). Fluid-structure interaction analysis of venous valve haemodynamics. In *Proceedings of the 4th International Conference on Computational and Mathematical Biomedical Engineering*.

Narracott, A. J., Zervides, C., Diaz, V., Rafiroiu, D., Lawford, P. V., and Hose, D. R. (2010). Analysis of a mechanical heart valve prosthesis and a native venous valve: Two distinct applications of fsi to biomedical applications. *International Journal for Numerical Methods in Biomedical Engineering*, 26:421–434.

Nipper, M. E. and Dixon, J. B. (2011). Engineering the lymphatic system. *Cardiovascular Engineering and Technology*, 2(4):296–308.

Ohashi, T., Ishii, Y., Ishikawa, Y., Matsumoto, T., and Sato, M. (2002). Experimental and numerical analyses of local mechanical properties measured by atomic force microscopy for sheared endothelial cells. *Bio-Medical Materials and Engineering*, 12(3):319–327.

Ohashi, T. and Sato, M. (2005). Remodeling of vascular endothelial cells exposed to fluid shear stress: experimental and numerical approach. *Fluid Dynamics Research*, 37(12):40–59.

Ohhashi, T. (2004). Lymphodynamic properties governing sentinel lymph nodes. *Ann Surg Oncol*, 11(3 Suppl):275S–8S.

Ohhashi, T., Azuma, T., and Sakaguchi, M. (1980). Active and passive mechanical characteristics of bovine mesenteric lymphatics. *American Journal of Physiology*, 239:H88–H95.

Ohtani, O. and Ohtani, Y. (2008). Structure and function of rat lymph nodes. *Archives of Histology and Cytology*, 71(2):69–76.

Ohtani, O., Ohtani, Y., Carati, C. J., and Gannon, B. J. (2003). Fluid and cellular pathways of rat lymph nodes in relation to lymphatic labyrinths and aquaporin-1 expression. *Archives of Histology and Cytology*, 66(3):261–272.

Olszewski, W. L. and Engeset, A. (1980). Intrinsic contractility of prenodal lymph vessels and lymph flow in human leg. *American Journal of Physiology: Heart and Circulation Physiology*, 239:H775–H781.

Paganin, D., Mayo, S. C., Gureyev, T. E., Miller, P. R., and Wilkins, S. W. (2002). Simultaneous phase and amplitude extraction from a single defocused image of a homogeneous object. *Journal of Microscopy*, 206:33–40.

Peskin, C. S. (1982). The fluid dynamics of heart valves: experimental, theoretical and computational methods. *Annual Review of Fluid Mechanics*, 14:235–259.

Pfeiffer, F., Kumar, V., Butz, S., Vestweber, D., Imhof, B. A., Stein, J. V., and Engelhardt, B. (2008). Distinct molecular composition of blood and lymphatic vascular endothelial cell junctions establishes specific functional barriers within the peripheral lymph node. *European Journal of Immunology*, 38:2142–2155.

Qui, Y., Quijano, R., Wang, S., and Hwang, N. (1995). Fluid dynamics of venous valve closure. *Annals of biomedical engineering*, 23:750–759.

Quick, C. M., Ngo, B. L., Venugopal, A. M., and Stewart, R. H. (2009). Lymphatic pump-conduit duality: contraction of postnodal lymphatic vessels inhibits passive flow. *American Journal of Physiology: Heart and Circulation Physiology*, 296:H662–H668.

Quick, C. M., Venugopal, A. M., Gashev, A. A., Zawieja, D. C., and Stewart, R. H. (2007). Intrinsic pump-conduit behaviour of lymphangions. *American Journal of Physiology: Regulatory, Integrative and Comparative Physiology*, 292:R1510–R1518.

Rahbar, E. and Moore, Jr., J. E. (2011). A model of a radially expanding and contracting lymphangion. *Journal of Biomechanics*, 44:1001–1007.

Rahbar, E., Weimer, J., Gibbs, H., Yeh, A. T., Bertram, C. D., Davis, M. J., Hill, M. A., Zawieja, D. C., and Moore, Jr., J. E. (2012). Passive pressure-diameter

relationship and structural composition of rat mesenteric lymphangions. *Lymphatic Research and Biology*, 10(4):152–63.

Reddy, N. P., Krouskop, T. A., and Newell Jr., P. H. (1975). Biomechanics of a lymphatic vessel. *Blood Vessels*, 12(5):261–78.

Reddy, N. P., Krouskop, T. A., and Newell Jr., P. H. (1977). A computer model of the lymphatic system. *Computers in Biology and Medicine*, 1977:181–197.

Renkin, E. M. and Michel, C. C., editors (1984). *Handbook of Physiology: Section 2: The Cardiovascular System*, volume Volume IV: Microcirculation, Part 1. American Physiological Society.

Roozendaal, R., Mempel, T. R., Pitcher, L. A., Gonzalez, S. F., Verschoor, A., Mebius, R. E., Andrian, U. H. v., and Carroll, M. C. (2009). Conduits mediate transport of low-molecular-weight antigen to lymph node follicles. *Immunity*, 30(2):264–276.

Rowan, J. O. (1981). *Physics and the circulation*. Adam Hilger Ltd.

Saltelli, A., Tarantola, S., Campolongo, F., and Ratto, M. (2002). *A Worked Example, in Sensitivity Analysis in Practice: A Guide to Assessing Scientific Models*. John Wiley & Sons, Ltd, Chichester, UK.

Scallan, J. P., Wolpers, J. H., and Davis, M. J. (2013). Constriction of isolated collecting lymphatic vessels in response to acute increases in downstream pressure. *J Physiol*, 591(Pt 2):443–59.

Schindelin, J., Arganda-Carreras, I., Frise, E., Kaynig, V., Longair, M., Pietzsch, T., Preibisch, S., Rueden, C., Saalfeld, S., Schmid, B., Tinevez, J.-Y., White, D. J., Hartenstein, V., Eliceiri, K., Tomancak, P., and Cardona, A. (2012). Fiji: an open-source platform for biological-image analysis. *Nature Methods*, 9:676–682.

Schmid-Schönbein, G. W. (1990). Microlymphatics and lymph flow. *Physiological Reviews*, 70(4):987–1028.

Schreiner, W. and Buxbaum, P. F. (1993). Computer-optimization of vascular trees. *IEEE Transaction on Biomedical Engineering*, 40:482–490.

Shepro, D., editor (2005). *Microvascular Research: Biology and Pathology*. Elsevier Academic Press.

Shipley, R. J. and Chapman, S. J. (2010). Multiscale modelling of fluid and drug transport in vascular tumours. *Bulletin of Mathematical Biology*, 72:1464–1491.

Skalak, T. C., Schmid-Schönbein, G. E., and Zweifach, B. W. (1984). New morphological evidence for amechanicsm of lymph formation in skeletal muscle. *Microvascular Research*, 28:95–112.

Sokolis, D. P. (2013). Experimental investigation and constitutive modeling of the 3d histomechanical properties of vein tissue. *Biomechanics and Modeling in Mechanobiology*, 12(3):431–451.

Sompayrac, L. (2012). *How the Immune System Works*. John Wiley & Sons, Ltd.

Spühler, J. H., Nilsson, T., Jansson, J., and Hoffman, J. (2015). Unified continuum ale finite element modelling of aortic valve dynamics. In *Proceedings of the 4th International Conference on Computational and Mathematical Biomedical Engineering*.

Stücker, O., Pons-Himbert, C., and Laemmel, E. (2008). Towards a better understanding of lymph circulation. *Phlebolymphology*, 15(1):31–35.

Suga, H. and Sagawa, K. (1972). Mathematical interrelationship between instantaneous ventricular pressure-volume ratio and myocardial force-velocity relation. *Annals of Biomedical Engineering*, 1(2):160–181.

Sun, W., Martin, C., and Pham, T. (2014). Computational modeling of cardiac valve function and intervention. *Annual Review of Biomedical Engineering*, 16:53–76.

Sunbuloglu, E., Bozdag, E., Toprak, T., and Islak, C. (2013). Experimental parameter estimation method for nonlinear viscoelastic composite material models: An application on arterial tissue. *Computer Methods in Biomechanics and Biomedical Engineering*, 16(12):1249–1261.

Swartz, M. A. and Fleury, M. E. (2007). Intersititial flow and its effect in soft tissues. *Annual Review of Biomedical Engineering*, 9:229–256.

Swartz, M. A. and Skobe, M. (2001). Lymphatic function, lymphangiogenesis and cancer metastasis. *Microscopy Research and Technique*, 55:92–99.

Takada, M. (1971). The ultrastructure of lymphatic valves in rabbits and mice. *American Journal of Anatomy*, 132(2):207–127.

Tomei, A. A., Siegert, S., Britschgi, M. R., Luther, S. A., and Swartz, M. A. (2009). Fluid flow regulates stromal cell organization and ccl21 expression in a tissue-engineered lymph node microenvironment. *The Journal of Immunology*, 183(7):4273–4283.

Tschanz, S. A., Salm, L. A., Roth-Kleiner, M., Barr, S. F., Burri, P. H., and Schittny, J. C. (2014). Rat lungs show a biphasic formation of new alveoli during postnatal development. *Journal of Applied Physiology*, 117:89–95.

Vajda, J. and Tomcsik, M. (1971). The structure of the valves of the lymphatic vessels. *Acta Anatomica*, 78(4):521–531.

Vatner, S. F. and McRitchie, R. J. (1975). Interaction of the chemoreflex and the pulmonary inflation reflex in the regulation of coronary circulation in conscious dogs. *Circulation Research*, 37(5):664–73.

Watson, D. J., Sazonov, I., Jr., J. E. M., Zawieja, D. C., and van Loon, R. (2015). Quantifiable smoothing of segmented lymphatic valves to determine the role of wavy features. In *Proceedings of the 4th International Conference on Computational and Mathematical Biomedical Engineering*.

Willard-Mack, C. L. (2006). Normal structure, function, and histology of lymph nodes. *Toxicol Pathol*, 34(5):409–24.

Wilson, J. T., Nepiyushchikh, Z., Zawieja, D. C., and James E. Moore, J. (2015a). Towards simulating movement and flow in the rat mesenteric lymphatic valve. In *Proceedings of the 4th International Conference on Computational and Mathematical Biomedical Engineering*.

Wilson, J. T., van Loon, R., Wang, W., Zawieja, D. C., and Jr., J. E. M. (2015b). Determining the combined effect of the lymphatic valve leaflets and sinus on resistance to forward flow. *Journal of Biomechanics*, pages ISSN 0021–9290.

Wilson, J. T., Wang, W., Hellerstedt, A. H., Zawieja, D. C., and Moore, J. E. (2013). Confocal image-based computational modeling of nitric oxide transport in a rat mesenteric lymphatic vessel. *J Biomech Eng*, 135(5):51005.

Woodruff, M. C., Herndon, C. N., Heesters, B. A., and Carroll, M. C. (2013). Contextual analysis of immunological response through whole-organ fluorescent imaging. *Lymphatic Research and Biology*, 11:121–127.

Zamir, M. (2001). Arterial branching within the confines of fractal l-system formalism. *Journal of General Physiology*, 118:267–275.

Zawieja, D. C. (2009). Contractile physiology of lymphatics. *Lymphatic Research and Biology*, 7(2):87–96.

Zulliger, M. A., Fridez, P., Hayashi, K., and Stergiopulos, N. (2004). A strain energy function for arteries accounting for wall composition and structure. *J Biomech*, 37(7):989–1000.

Zuther, J. E. (2009). *Lymphedema Management: The Comprehensive Guide for Practitioners*. Thieme Publishing Group.